High-Intensity, Picosecond-Pumped, Few-Cycle OPCPA

Christoph Skrobol

München, 2014

High-Intensity, Picosecond-Pumped, Few-Cycle OPCPA

Christoph Skrobol

Dissertation
an der Fakultät für Physik
der Ludwig-Maximilians-Universität
München

Vorgelegt von
Christoph Skrobol
geboren in Gräfelfing

München, 30.06.2014

Erstgutachter:	Prof. Dr. Stefan Karsch
Zweitgutachter:	Prof. Dr. Jens Biegert
Tag der mündlichen Prüfung:	27.08.2014

Zusammenfassung

Diese Arbeit befasst sich mit der OPCPA-Entwicklung für den PFS, ein System, dass erstmals Lichtpulse mit Pulsdauern von 5 fs (weniger als zwei optische Lichtzyklen) und einer Pulsenergie von mehr als 3 J [1, 2] bereitstellen soll. Damit sind Intensitäten von $10^{22}\,\mathrm{W/cm^2}$ im Fokus möglich. Die von Petawatt Field Synthesizer (PFS) verstärkten Lichtpulse werden bei der Erzeugung von hohen Harmonischen an Festkörperoberflächen eingesetzt, wodurch sich der Photonenfluß und die Photonenergie der erzeugten ultrakurzen XUV-Pulse im Vergleich zu der Erzeugung von hohen Harmonischen in Gasen deutlich erhöhen lässt [3–6].

Das PFS Projekt basiert auf einem modifizierten OPCPA-Konzept: Wenige Pikosekunden lange, hochintensive Pumppulse werden zur Verstärkung von sehr breitbandigen Signalpulsen in dünnen Kristallen, welche die Verstärkung der extrem großen Bandbreiten erlauben, eingesetzt. Die hohen Energien werden durch die hohen Pumpintensitäten, welche durch die kurze Pulsdauer der Pumppulse ermöglicht werden, garantiert. Die Pulsenergien in den letzten OPCPA Stufen erfordern große Aperturen der eingesetzten Kristalle. Als vielversprechendstes Kristallmaterial gilt heute DKDP, da dieses in Durchmessern von mehr als 100 mm erhältlich ist.

In dieser Arbeit wurde die Realisierbarkeit des modifizerten OPCPA Ansatzes sowohl experimentell als auch numerisch untersucht. Dabei wurde das Potential von DKDP große Bandbreiten zu verstärken, welche Pulsdauern von kleiner als 6 fs erlauben, demonstriert. Die Messergebnisse wurden mit den Resultaten eines Simulationsprogramms verglichen und zeigten dessen Funktionsfähigkeit. Mit Hilfe des Codes wurden numerische Machbarkeitsstudien zur Realisierung verschiedener OPCPA Designs für PFS durchgeführt. Die Studien zeigten, dass LBO Kristalle eine Alternative zu DKDP in den ersten Verstärkerstufen darstellen, da hier die Anforderung an die benötigte Kristallapertur nicht so groß ist wie in den letzten Stufen. Da LBO eine drei Mal höhere Nichtlinearität im Vergleich zu DKDP aufweist, können die ersten fünf geplanten DKDP Stufen durch nur zwei LBO Verstärkerstufen ersetzt werden. Experimente verifizierten das Potential von LBO Kristallen Bandbreiten, welche eine Pulsdauer von 5 fs unterstützen, zu verstärken. Messungen des zeitlichen Kontrasts der verstärkten Pulse bestätigten die erwartete Kontrastverbesserung aufgrund der kurzen Pumppulse. Die Skalierbarkeit der Pulsenergie (bis auf 10 mJ) und die Komprimierbarkeit des Signalpulses auf 7 fs wurde mit Hilfe eines abbildenden Vakuumsystems mit zwei LBO Stufen gezeigt.

Die durchgeführten Experimente verifizierten die Schlüsselpunkte des PFS Konzepts, wie die verstärkte Bandbreite, die Skalierbarkeit der Energie, die Komprimierbarkeit der verstärkten Pulse und die Verbesserung des zeitlichen Kontrasts. Physikalische Probleme, wie die Qualität der spektralen Phase des Signals, der zeitliche Jitter und die Qualität des Pumplaser, wurden aufgedeckt und analysiert.

Abstract

This work is dedicated to the OPCPA development for the Petawatt Field Synthesizer (PFS) which is aiming to become the first light source delivering petawatt-scale peak-power pulses with few-cycle pulse duration. The target parameters of PFS are pulse energies $> 3\,\mathrm{J}$ in combination with pulse durations of 5 fs [1, 2] leading to focused intensities of $10^{22}\,\mathrm{W/cm^2}$. Such pulses are an ideal driver for high harmonic generation (HHG) experiments at solid surfaces, which hold promise to increase both the photon flux and the photon energy of the generated ultra-short XUV pulses dramatically compared to what is available to date [3–6].

PFS is based on a modified OPCPA scheme: Few-picosecond, high-intensity pump pulses are utilized to amplify an ultra-broadband signal in thin nonlinear crystals which guarantee an extremely broad amplified bandwidth. The high pump intensities realizable due to the short pump-pulse duration ensure high gain levels allowing to reach the desired pulse energies. Owing to these high energies, large aperture nonlinear crystals are required in the last OPCPA stages. Currently, the DKDP crystal is the most promising candidate supporting free apertures of $> 100\,\mathrm{mm}$ and allowing for a sufficiently large amplification bandwidth.

The proof-of-principle experiments and numerical simulations performed in the scope of this thesis investigate the feasibility of this new OPCPA concept. The capability of DKDP to amplify bandwidths supporting pulse durations of less than 6 fs was demonstrated [7]. Furthermore, the experimental results were compared to simulations verifying the reliability of the simulation code which was then used for numerical design studies. These studies revealed that LBO crystals are a potential alternative to DKDP in the first stages of the PFS system, where the demands on crystal aperture are more relaxed. Owing to a three times higher nonlinearity of LBO, two LBO stages replace five OPCPA stages equipped with DKDP. Experiments verified the potential of LBO crystals to amplify bandwidths supporting pulse durations of 5 fs. A temporal-contrast measurement demonstrated the expected capability of short-pulse-pumped OPCPA systems to achieve an almost ideal temporal contrast on a timescale of a few picoseconds or longer. The scalability of the signal energy (up to 10 mJ) and the compressibility to few-cycle pulse durations (7 fs) was demonstrated with a vacuum imaging system housing two LBO stages.

The experiments verified all building blocks of the PFS concept, such as amplified bandwidth, sufficient high gain, compressibility of the signal pulses and the increase of temporal contrast due to the nonlinear amplification. Furthermore, physical issues that need to be resolved for further scaling such as the quality of the spectral phase of the signal beam, the temporal jitter between signal and pump and the quality of the pump beam have been identified and analyzed.

Contents

1 Introduction 1

1.1 PFS project 4

1.2 Thesis outline 6

I Theory and numerical modeling 9

2 Theory of OPA 11

2.1 Dipole moment, polarization 11

2.2 Coupled wave equations for pump, signal and idler 13

2.3 Phase mismatch 16

2.3.1 Crystal length 18

2.3.2 Wavevector mismatch 19

2.3.3 Conclusion 22

2.4 OPA phase 23

3 Tools for OPCPA modeling 25

3.1 Pseudo 3D simulations with SOPAS 25

3.2 3D simulations with Sisyfos 27

3.3 Comparison between SOPAS and Sisyfos 28

3.3.1 Signal with Gaussian-shape spectrum and quadratic phase 28

3.3.2 Comparison with experimental data 30
3.4 Conclusion 31

4 ps-OPCPA design for PFS 33
4.1 Walk-off compensation and tangential phase matching 33
4.2 Influence of beam and crystal parameters on OPCPA 36
4.2.1 Crystal material 37
4.2.2 Spectral phase of signal 39
4.2.3 Temporal jitter 40
4.3 OPA phase 42
4.4 Temporal contrast 44
4.5 Effects of n2: B-integral and self-phase modulation during amplification 45
4.6 Heat load in OPA crystals 48

5 OPCPA point design for PFS 49
5.1 First design: all DKDP 50
5.2 Optimized PFS design 52
5.2.1 Dispersion management of the broadband signal 54
5.3 Conclusion 56

II PFS system and experiments 57

6 PFS system setup 59
6.1 Frontend system 60
6.1.1 Spectral cleaning of the broadband signal pulses 62
6.2 Pump-laser system 65
6.3 OPCPA system 69
6.3.1 Temporal jitter between signal and pump pulse 69

7 OPCPA and compression experiments 73
7.1 Broadband ps-OPCPA operation in DKDP 74

7.2 OPCPA in LBO - beam propagation in air 79
7.2.1 OPCPA amplification in two LBO stages . . . 81
7.2.2 Compression test . . . 84
7.2.3 Characterization of the temporal contrast . . . 87
7.2.4 Conclusion . . . 88
7.3 OPCPA in vacuum 89
7.3.1 Results of 2-stage amplification in vacuum . . . 96
7.3.2 Compression of signal pulses . . . 99
7.3.3 Conclusion . . . 103

III Summary and outlook 105

8 Summary and outlook . . . 107
8.1 Outlook 109

IV Appendix 113

A Ultra-short light pulses . . . 115

B Benchmark of SOPAS . . . 119
B.1 Small-signal-gain measurements 120
B.2 Saturation measurements 121

C Numerical design studies . . . 123
C.1 Influence of beam and crystal parameters on OPCPA 123
C.1.1 Variation of parameters of the OPA crystal . . . 124
C.1.2 Variation of beam parameters . . . 125
C.2 Superfluorescence 135
C.3 Heat load in OPA crystals 139
C.3.1 Matlab-code used to calculate the heat distribution . . . 142

D Experimental OPCPA setups . . . 145
D.1 Experimental setup for measurements with DKDP 145

D.2 Experimental setup for measurements with two LBO stages in air 146

D.3 Experimental setup for measurements with two LBO stages in vacuum 148

E Tools for pulse characterization 153

E.1 Spectrum, energy and beam profile 153

E.2 Measurement of the pulse duration and phase of the broadband signal 157

E.2.1 X-FROG 157

E.2.2 Single-shot 5 fs SHG-FROG 159

E.3 Characterization of the temporal contrast 162

F SHG of the signal beam 165

G Publications 167

G.1 Broadband amplification by picosecond OPCPA in DKDP pumped at 515 nm 167

G.2 Simulations of petawatt-class few-cycle optical-parametric chirped-pulse amplification, including nonlinear refractive index effects 179

H Acknowledgments 203

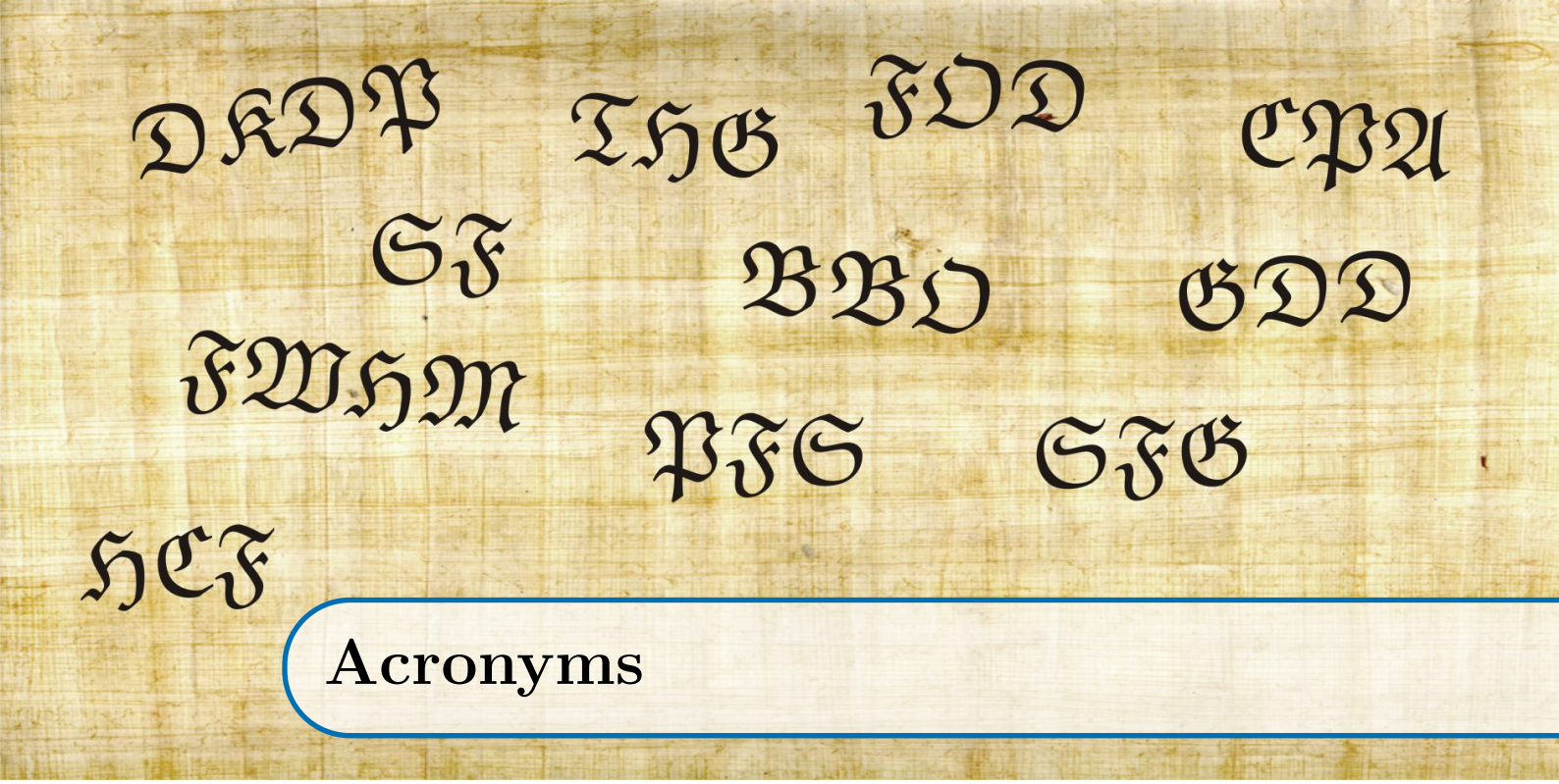

Acronyms

BBO Beta Barium Borate, beta $-$ BaB_2O_4
CLBO Cesium Lithium Borate, $CsLiB_6O_{10}$
CPA chirped pulse amplification
DFG difference frequency generation
DKDP Potassium Dideuterium Phosphate, KD_2PO_4
FOD fourth-order dispersion
FROG frequency resolved optical gating
FWHM full width at half maximum
GD group delay
GDD group-delay dispersion
HCF hollow-core fiber
HHG high harmonic generation
KDP Potassium Dihydrogen Phosphate, KH_2PO_4
LBO Lithium Triborate, LiB_3O_5
Nd:YAG neodymium-doped yttrium aluminum garnet, $Nd^{3+} : Y_3Al_5O_{12}$
OPA optical parametric amplification
OPCPA optical parametric chirped pulse amplification
PCF photonic crystal fiber
PFS Petawatt Field Synthesizer
PMT photo multiplier tube
PPLN periodically poled Lithium Niobate, $LiNbO_3$
SF self focusing
SFG sum frequency generation
SHG second harmonic generation
SPM self phase modulation

THG third harmonic generation
Ti:Sa titanium-sapphire, $Ti : Al_2O_3$
TOD third-order dispersion
Yb:YAG ytterbium-doped yttrium aluminum garnet, $Yb^{3+} : Y_3Al_5O_{12}$
XPW cross polarized wave generation

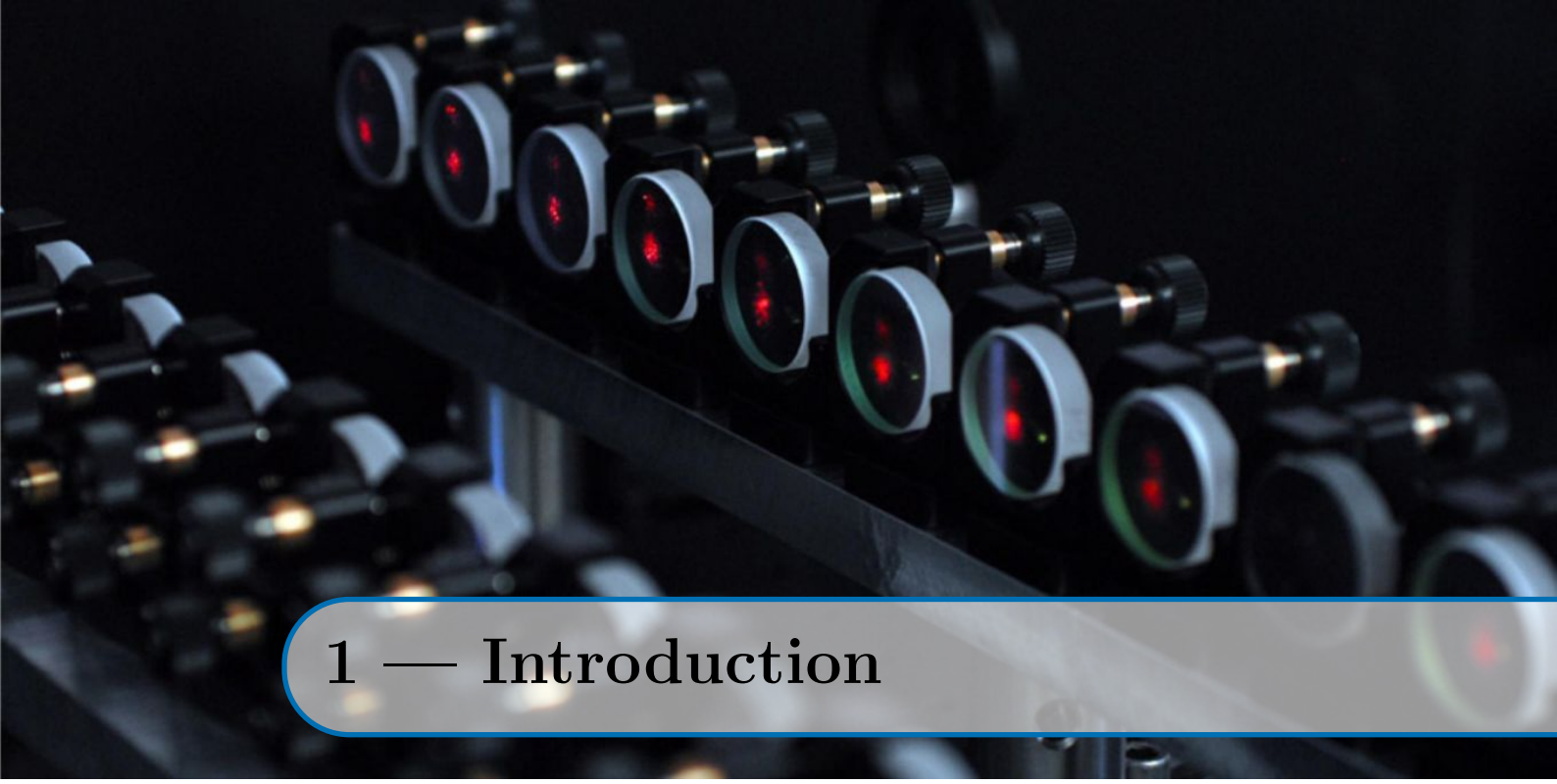

1 — Introduction

Since the first demonstration of a laser by T. H. Maiman [8] in 1960, laser physics experienced a rapid development. In 1961, just one year after the experiments of Maiman the frequency doubling (second harmonic generation (SHG)) of a ruby laser could be demonstrated in a quartz crystal [9]: the field of nonlinear optics was born. Over the last decades researchers have investigated different types of lasers with a huge variety of parameters and nowadays the laser became a powerful tool in many different fields of basic research. At the Laboratory for Attosecond Physics (LAP), located at the Max-Planck-Institut für Quantenoptik (MPQ) in Garching, few-cycle light pulses are applied for the generation of even shorter single-isolated XUV pulses via high harmonic generation (HHG) in gases [10]. The shortest pulses generated at the LAP reach pulse durations of only 80 as [11]. These ultra-short light pulses allow to resolve electron dynamics inside atoms and molecules for the first time [12].

As these experiments are based on the generation of high harmonics in noble gases, the intensity of the driving pulse is limited due to the ionization-induced saturation of the generation process at intensities beyond $10^{15}\,\mathrm{W/cm^2}$ [13]. Furthermore, the HHG process in gases exhibits a low conversion efficiency, which is on the order of 10^{-5} due to its highly nonlinear nature and in combination with the limited pulse intensity leads to very low XUV-photon flux [14, 15]. Consequently, alternative approaches for the generation have been investigated. One possibility to overcome these limitations is the HHG at solid surfaces [3–6]. The interaction of an ultra-intense light pulse with a solid surface leads to the formation of a surface plasma. The electrons at the plasma vacuum interface execute forced oscillations near the edge of an immobile step-like ion background driven by the ponderomotive force of the incident pulse [16]. Charge separation and corresponding electrostatic fields

give rise to the restoring force such that the whole surface starts oscillating in phase with the light field at relativistic velocities. Owing to the high electron density at the solid surface, the impinging light pulse gets reflected and Doppler-shifted. Two XUV pulses are generated per light cycle and their photon energy depends on the instantaneous relativistic γ-factor of the electron population which corresponds to the instantaneous electron velocity and therefore is linked to the current field amplitude of the light pulse. In the case of a few-cycle cosine pulse one XUV pulse is highly prominent such that by applying correct spectral filters a single attosecond pulse is obtained (cf. Figure 1.1). As the process is based on plasma formation there exists no limitation of the driving intensity of the light pulse. Higher intensities cause an increase of the conversion efficiency of the HHG predicted up to 10^{-2} [16]. A schematic sketch of a typical experimental configuration used for generation of attosecond pulses at solid surfaces is shown in Figure 1.1.

In order to drive solid-surface HHG experiments, few-cycle light pulses with intensities exceeding $10^{18}\,\mathrm{W/cm^2}$ are required. Light sources based on conventional laser amplification are not suited for the generation of high-energy few-cycle pulses due to their limited amplification bandwidth. While Ti:Sa oscillators with pulse durations below 10 fs with a few hundreds of nJ pulse energy have been demonstrated [17–20], amplified pulses with energies greater than a few microjoule will always suffer from gain narrowing preventing true few-cycle operation. At the high-

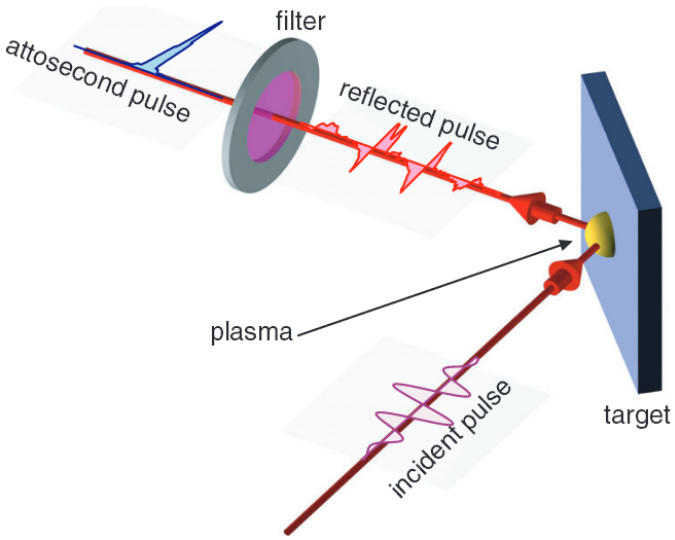

Figure 1.1: *Scheme showing the proposed experimental configuration for the generation of attosecond pulses using harmonics from overdense plasmas. This picture was created by Dr. G. D. Tsakiris and is subject to copyright of New Journal of Physics. It is published in [16] (Figure 7) and used with permission from NJP.*

est energy level currently achievable with Ti:Sa of several 10's of Joule, the limit is approx. $20 - 30\,\mathrm{fs}$ [21, 22]. In addition to the aforementioned systems, hybrid laser systems combining conventional laser schemes with nonlinear broadening techniques deliver pulse energies of several millijoule at sub-two-optical-cycle pulse durations [23, 24].

As a consequence, few-cycle pulses with high pulse energies have not yet been achieved with conventional laser technology. In order to generate light pulses in this extreme regime, systems based on the optical parametric chirped pulse amplification (OPCPA) technique are used and developed [25–27]. This technology combines chirped pulse amplification (CPA) with the optical parametric amplification (OPA) and allows the amplification of ultra-broad bandwidths supporting pulse durations in the few-cycle regime ($< 5 - 15\,\mathrm{fs}$) to pulse energies up to the J-level [2, 28–31]. The CPA principle [32, 33] is based on temporal pulse stretching leading to a drastic decrease of pulse intensity well below the onset of nonlinear effects during amplification. Afterwards, the light pulses are compressed back to short pulse durations increasing the peak power and intensity dramatically. OPA is a nonlinear amplification process based on three-wave mixing via the induced nonlinear polarization inside a crystal. In contrast to conventional lasers, the pump energy is not stored inside a medium, but transferred instantaneously by the pump beam (beam with highest photon frequency, ω_p) to the signal beam (ω_s). Owing to the energy conservation a third wave, the so called idler ($\omega_i = \omega_p - \omega_s$) has to be generated. The spectral bandwidth of an OPA is only determined by the phase mismatch between the three waves, which is the product of the wavevector mismatch ($\Delta k = k_p - k_s - k_i$) and the length of the nonlinear crystal. Phase matching can be achieved by different techniques such as angle phase matching (e.g. orthogonal polarizations of signal/idler and pump beam in birefringent crystals), temperature phase matching, quasi-phase matching or Čerenkov phase matching [34]. However, perfect phase match can only be achieved for a limited number (usually 1,2, or 3) of discrete wavelengths. Other wavelengths outside these perfect matched points experience a non-vanishing Δk the further their distance in wavelengths is. Minimizing Δk by either turning the crystal angle or minimizing its length can therefore help in keeping Δk below π for a broader overall bandwidth.

1.1 PFS project

In order to drive HHG from solid surfaces and gain insight into new physics of laser-matter interaction, a new light source is currently under development at the Max-Planck-Institut für Quantenoptik. Dubbed the Petawatt Field Synthesizer (PFS), it will deliver sub-two-optical cycle light pulses with a duration of 5 fs at pulse energies up to 3 J combined with unprecedented temporal contrast on the few-ps timescale at a repetition rate of 10 Hz [1,2]. With these parameters, intensities up to $10^{22}\,\mathrm{W/cm^2}$ should become feasible with few-cycle pulses for the first time. At these intensities the quality of the temporal contrast is of essential importance for the success of laser-matter experiments. Already at intensities greater than $10^{10}\,\mathrm{W/cm^2}$ multiphoton ionization becomes pronounced enough to turn a solid target into an expanding plasma. The hydrodynamic expansion of plasmas takes place on timescales longer than a few ps and consequently an intensity contrast of 12 orders of magnitude on a few-ps timescale as will be delivered by the PFS exclude that possibility. In order to reach the desired parameters, the only possible path is an advanced OPCPA approach.

The desired few-cycle regime, requires an ultra-broad bandwidth which has to be amplified in multiple consecutive OPCPA stages each trying to minimize the phase mismatch by using a non-collinear geometry [35] and applying thin nonlinear crystals. The high pulse energies call for large-aperture nonlinear crystals in the last OPCPA stages. To date, only Potassium Dihydrogen Phosphate, KH_2PO_4 (KDP) and Potassium Dideuterium Phosphate, KD_2PO_4 (DKDP) crystals are commercially available in the required aperture size of $> 100\,\mathrm{mm}$. However, DKDP is the favorite choice since it offers a broader transparency range (up to $2\,\mu\mathrm{m}$) leading to a reduced absorption of the idler beam. The small nonlinearity of DKDP crystals combined with the short interaction length in thin crystals results in a small gain, which however can be counter-balanced by using high pump intensities to drive the nonlinear interaction. The highest pump intensities can be achieved for short pump-pulse durations (τ) as the damage threshold of materials scales with $I_{damage} \propto \frac{1}{\sqrt{\tau}}$ in the nanosecond to picosecond range [36]. Consequently, the OPCPA stages of the PFS system are pumped by picosecond high intensity pump pulses from a CPA laser system. Furthermore, the short pump-pulse duration guarantees an intrinsically high temporal contrast on the few-picosecond time scale, as required in most high intensity laser-matter interaction scenarios.

In order to amplify the signal to pulse energies of $\sim 3\,\mathrm{J}$, a pump laser delivering a pulse energy of $4\,\mathrm{x}\,5\,\mathrm{J}$ for the frequency doubled beam, i.e. $4\,\mathrm{x}\,12\,\mathrm{J}$ for the funda-

mental beam, is required. Not many energy-efficient and thermally well-conducting laser gain materials support enough bandwidth for 1 ps pulses. In order to allow a repetition rate of 10 Hz, the laser medium needs to display good heat conductivity and low quantum defect, and should be pumped by a narrowband diode pump source. As the most promising solution to these requirements, the PFS pump laser was designed as a fully diode-pumped CPA system based on Yb-doped glass and ytterbium-doped yttrium aluminum garnet, $Yb^{3+} : Y_3Al_5O_{12}$ (Yb:YAG). Yb:YAG emits at a central wavelength of 1030 nm, yielding an OPCPA pump wavelength of 515 nm after frequency doubling.

The choice of DKDP as nonlinear crystal combined with the pump wavelength of 515 nm leads to a signal wavelength range of $700 - 1400$ nm for optimum phase-matching conditions. A schematic layout of the PFS is presented in Figure 1.2.

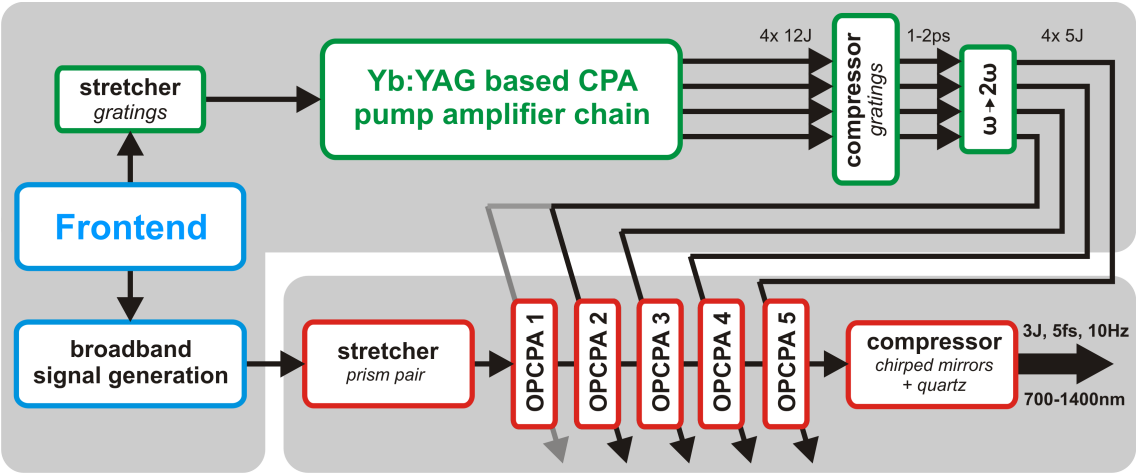

Figure 1.2: *Schematic layout of the PFS system. The frontend system generates the seed pulses for the CPA Yb:YAG pump laser and the broadband signal generation setup. The broadband signal is amplified in consecutive OPCPA stages pumped by picosecond short high-intensity frequency-doubled pump pulses. This picture is a modified version of the scheme presented in [37, 38] and used with the permission of the original authors.*

1.2 Thesis outline

This thesis is structured in three main parts:

- I Theory and numerical modeling
- II PFS system and experiments
- III Summary and outlook

In chapter 2 in the first part the theory of the OPCPA process is described by deriving the coupled wave equations describing the amplification process as used in simulations presented in this thesis. In addition, the effect of phase mismatch on the amplified bandwidth is discussed. Two simulation programs which were used for numerical studies are introduced in chapter 3. With the help of these codes different characteristics of OPCPA, which are relevant for an optimized amplification, are presented. Two different geometries of non-collinear OPCPA are explained. Furthermore, the most important results of a numerical study investigating the effect of different beam and crystal parameters on the amplification are discussed, followed by a study of the influence of the OPA phase on the signal compression and the enhancement of the temporal contrast due to the nonlinear amplification. In addition, the influence of n_2-effects and crystal heating due to linear absorption on the OPA process is discussed. In chapter 5 two point designs for the OPCPA chain for the PFS system are presented.

Since the main scope of this PhD thesis lies on the development and characterization of the broadband OPCPA and on the compression of the amplified signal pulses, the second part is dedicated to the PFS system and the OPCPA experiments. Here, chapter 6 gives an overview over the current status of the PFS system which was used for these experiments. The experimental results are presented in chapter 7. First the performance of a single DKDP stage is discussed. Then the amplification in Lithium Triborate, LiB_3O_5 (LBO) crystals is characterized, as LBO has the potential to be an alternative to DKDP crystals in the first stages of the PFS chain due to its higher nonlinearity and similar amplification bandwidth. Furthermore, the scalability of the amplified pulse energy and the compression to two optical cycles is demonstrated. These experiments are performed in an imaging vacuum system in order to reduce the limiting effects of nonlinear beam propagation of the high-intensity pump laser. Finally, the summary draws the conclusions from this experimental study.

In the third part of this thesis an outlook for the entire PFS system is presented describing the feasibility of the PFS concept and the remaining challenges.

Since the PFS is aiming for few-cycle pulse durations a brief mathematical description of ultra-short light pulses is presented in Appendix A. A comparison between experimental results and calculations performed with SOPAS is described in Appendix B. Appendix C is dedicated to numerical design studies. The experimental setups used for the measurements are described in detail in Appendix D. Technical and physical information about the diagnostics used for pulse characterization are given in Appendix E.

Part I

Theory and numerical modeling

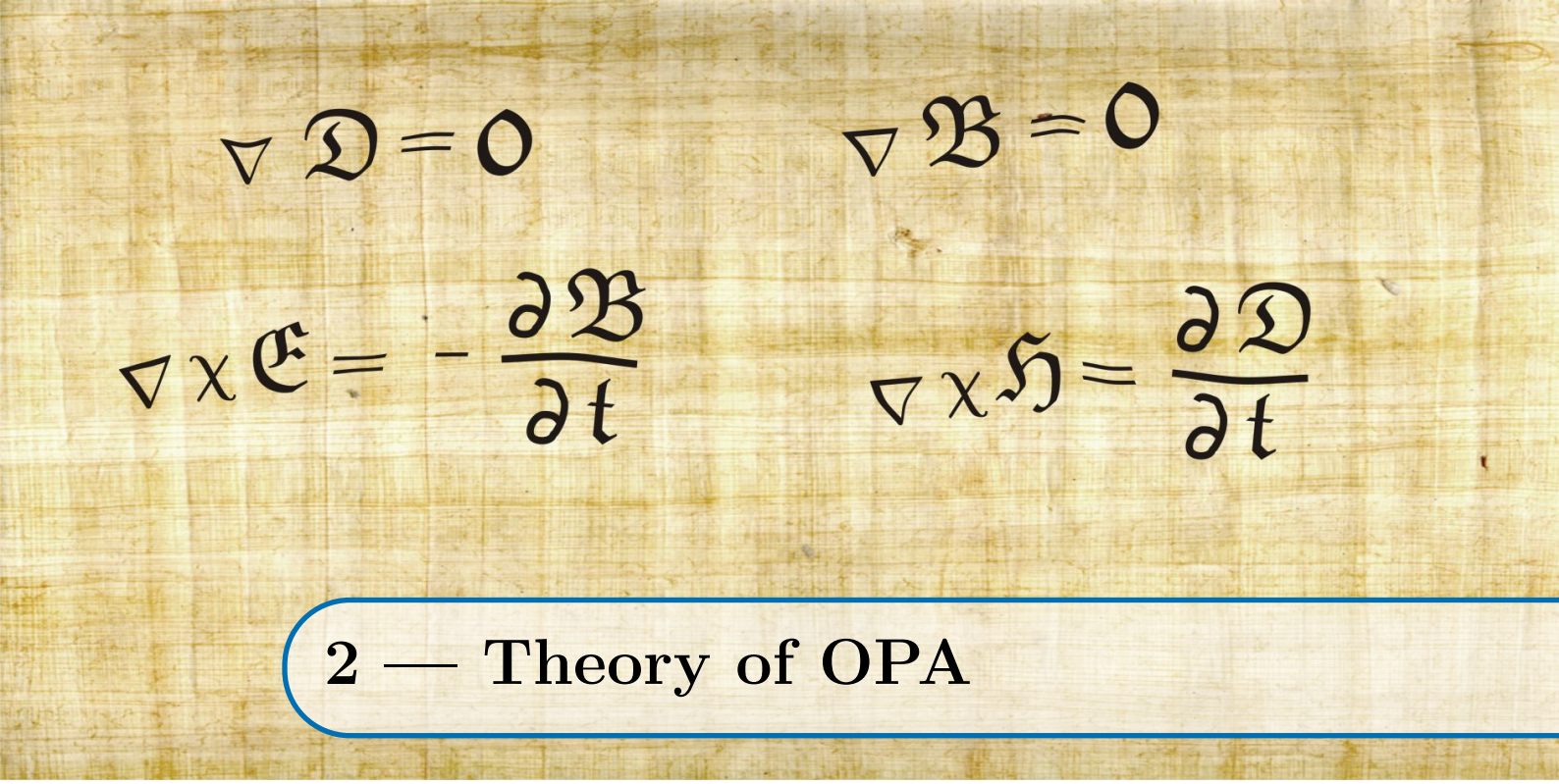

2 — Theory of OPA

As mentioned in the introduction, OPA is a three-wave mixing process where the waves are coupled to each other via the induced nonlinear polarization. Hence, OPA can be described by three coupled wave equations, one for each beam, which are derived in the following section. One of the main advantages of OPA is the possibility to amplify an ultra-broad bandwidth which is mainly limited by the phase mismatch. The amplified bandwidth is one of the key parameters for the PFS project and therefore the phase mismatch will be described in detail. The discussion in this chapter closely follows Ref. [39] and Refs. [26, 27, 34, 40].

2.1 Dipole moment, polarization

When an electromagnetic pulse propagates through material, a dipole moment is induced by its electric field $\mathbf{E}(t)$, which also determines the magnitude of the induced polarization. In the case of conventional optics (low field amplitude), the polarization exhibits a linear response to the external field. However, for high fields, the induced polarization becomes nonlinear and can be described by a series expansion:

$$\begin{aligned} \mathbf{P}(t) &= \epsilon_0 \left\{ \chi^{(1)}\mathbf{E}(t) + \chi^{(2)}\mathbf{E}^2(t) + \chi^{(3)}\mathbf{E}^3(t) + \ldots \right\} \\ &= \mathbf{P}^{(1)}(t) + \mathbf{P}^{(2)}(t) + \mathbf{P}^{(3)}(t) + \ldots \\ &= \mathbf{P}^{(1)} + \mathbf{P}_{NL} \end{aligned} \tag{2.1}$$

The quantity $\chi^{(1)}$ is known as linear susceptibility whereas $\chi^{(2)}$ and $\chi^{(3)}$ are the second- and third-order nonlinear susceptibilities. The first term $\mathbf{P}^{(1)}$ in Equation 2.1 describes the linear propagation whereas the higher order terms $\mathbf{P}^{(2)}(t) + \mathbf{P}^{(3)}(t) + \ldots \equiv \mathbf{P}_{NL}$ of the induced polarization define the nonlinear propagation.

For example, sum frequency generation (SFG) and OPA are second order effects whereas self phase modulation (SPM), cross polarized wave generation (XPW) and third harmonic generation (THG) relate to the third order polarization.

In the case of OPA, two laser beams (pump and signal) with frequencies ω_1 and ω_2 are sent into a nonlinear medium. The most simple ansatz for the optical field describing this situation is

$$\mathbf{E}(t) = E_1 e^{-i\omega_1 t} + E_2 e^{-i\omega_2 t} + c.c. \tag{2.2}$$

where *c.c.* is the complex conjugate. The induced second-order polarization which is generated by the propagation of this optical field through a second-order nonlinear medium ($\chi^{(2)} \neq 0$) is:

$$\begin{aligned} \mathbf{P}^{(2)}(t) &= \epsilon_0 \chi^{(2)} \mathbf{E}^2(t) \\ &= \epsilon_0 \chi^{(2)} \left\{ E_1^2 e^{-2i\omega_1 t} + E_2^2 e^{-2i\omega_2 t} + 2E_1 E_2 e^{-i(\omega_1+\omega_2)t} + 2E_1 E_2^* e^{-i(\omega_1-\omega_2)t} + c.c. \right\} + \dots \\ &\qquad\qquad \downarrow \qquad\quad \downarrow \qquad\quad \downarrow \qquad\qquad \downarrow \\ &\qquad \text{SHG of } E_1 \quad \text{SHG of } E_2 \qquad \text{SFG} \qquad\quad \text{DFG/OPA} \end{aligned} \tag{2.3}$$

This simple example shows that during the propagation of two optical waves through a nonlinear medium new frequency components are generated: $2\omega_1/2\omega_2$ second harmonic generation (SHG), $\omega_1 + \omega_2$ sum frequency generation (SFG) and $\omega_1 - \omega_2$ difference frequency generation (DFG) / optical parametric amplification (OPA). In the case of DFG/OPA the indices can be changed to $1 \rightarrow p$ and $2 \rightarrow s$ for pump and signal, respectively. A schematic picture of the OPA process is depicted in Figure 2.1.

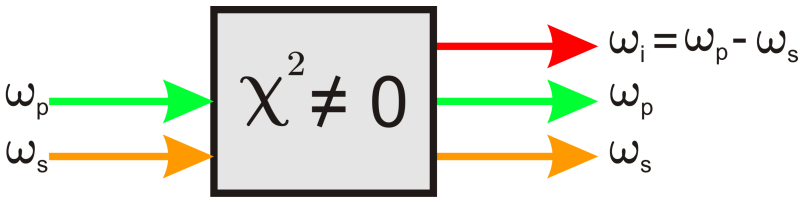

Figure 2.1: *Schematic picture of the OPA process. Two laser beams, pump and signal, are sent into a nonlinear medium with $\chi^{(2)} \neq 0$. In order to fulfill energy conservation a third beam, the so called idler, is generated with $\omega_i = \omega_p - \omega_s$.*

2.2 Coupled wave equations for pump, signal and idler

In order to derive the three coupled wave equations representing the optical parametric amplification process, it is common to start with Maxwell's equations without free charges ($\rho = 0$) and free currents ($\mathbf{j} = 0$):

$$\nabla \cdot \mathbf{D} = 0 \tag{2.4}$$

$$\nabla \cdot \mathbf{B} = 0 \tag{2.5}$$

$$\nabla \times \mathbf{E} = -\frac{\partial \mathbf{B}}{\partial t} \tag{2.6}$$

$$\nabla \times \mathbf{H} = \frac{\partial \mathbf{D}}{\partial t}, \tag{2.7}$$

where $\mathbf{D}$ is the displacement field, $\mathbf{B}$ is the magnetic field, $\mathbf{E}$ is the electric field and $\mathbf{H}$ is the magnetizing field. Under the assumption that the material is nonmagnetic ($\mathbf{B} = \mu_0 \mathbf{H}$) and nonlinear processes are allowed ($\mathbf{D} = \epsilon_0 \mathbf{E} + \mathbf{P}$), the most general form of the wave equation in nonlinear optics can be obtained from Maxwell's equations [39]:

$$\nabla \times \nabla \times \mathbf{E} + \frac{1}{c^2}\frac{\partial^2}{\partial t^2}\mathbf{E} = -\frac{1}{\epsilon_0 c^2}\frac{\partial^2 \mathbf{P}}{\partial t^2}. \tag{2.8}$$

The right hand side of Equation 2.8 contains the induced polarization $\mathbf{P}$ described in Equation 2.1.

To simplify this equation the following assumptions are made:

- **Assumption 1) transverse, infinite plane waves:** If $\mathbf{E}$ is a transverse, infinite plane wave, $\nabla \cdot \mathbf{E} = 0$ and therefore:

$$\nabla \times \nabla \times \mathbf{E} = \nabla (\nabla \cdot \mathbf{E}) - \nabla^2 \mathbf{E} = -\nabla^2 \mathbf{E}. \tag{2.9}$$

- **Assumption 2) Quasi-cw:** It is convenient to represent the electric field as a sum over its individual frequency components $\mathbf{E}(r,t) = \sum_n \mathbf{E}_n(\mathbf{r},t)$, where the summation is performed over positive frequencies since negative frequencies are included via the complex conjugated term (cf. Equation 2.2). For long light pulses (>ns) where dispersion can be neglected (quasi-cw) the second time derivative can be simplified to:

$$\frac{\partial^2}{\partial t^2} \rightarrow -\omega^2. \tag{2.10}$$

  However, for short pulses as in the case of the PFS system dispersion can not be neglected and consequently the second time derivative of the electric

field would not be constant as assumed in Equation 2.10 since the temporal phase contains terms which depend on higher orders of the time. Nevertheless, in the numerical simulation program, which was developed to model OPA in the frame of this thesis (cf. section 3.1), the crystals are cut into many thin slices. For one single crystal slice the interaction length is very short and therefore the effect of dispersion can be neglected for this short nonlinear step and assumption 2 can still be used. The influence of the dispersion on the light pulse is then simulated in a separate step.

With the assumptions 1 and 2 the general wave Equation 2.8 simplifies to:

$$\nabla^2 \mathbf{E}_n(\mathbf{r},t) + \frac{w_n^2}{c^2}\mathbf{E}_n(\mathbf{r},t) = -\frac{w_n^2}{\epsilon_0 c^2}\mathbf{P}_n(\mathbf{r},t) = -\frac{w_n^2}{\epsilon_0 c^2}\left(\mathbf{P}_n^{(1)}(\mathbf{r},t) + \mathbf{P}_{n,NL}(\mathbf{r},t)\right). \tag{2.11}$$

Furthermore, with $\mathbf{D} = \epsilon_0\mathbf{E} + \mathbf{P}^{(1)}$ and $\mathbf{D} = \epsilon_0\epsilon^{(1)}\mathbf{E}$, where $\epsilon^{(1)}$ is the real, frequency-dependent dielectric tensor, Equation 2.11 can be written as:

$$\nabla^2 \mathbf{E}_n(\mathbf{r},t) + \frac{w_n^2}{c^2}\epsilon^{(1)}\mathbf{E}_n(\mathbf{r},t) = -\frac{w_n^2}{\epsilon_0 c^2}\mathbf{P}_{n,NL}(\mathbf{r},t) \tag{2.12}$$

For solving this wave equation the following plane wave ansatz is used (cf. Equation 2.2):

$$\mathbf{E}_n(z,t) = E_n(z,t)e^{-i\omega_n t} + c.c. = A_n(z,t)e^{ik_n z}e^{-i\omega_n t} + c.c. \tag{2.13}$$

The fast oscillations of the electric field are described by the complex exponential functions and the envelope is defined by the complex amplitudes $E_n(z,t)$ and $A_n(z,t)$. Since the electric field is treated as an infinite transverse plane wave propagating in z-direction (assumption 1), the ∇^2 operator can be replaced by $\frac{d^2}{dz^2}$ (cf. Equation 2.9).

For reasons of simplicity only the OPA process is taken into account in the further text, i.e. $\mathbf{P}_{n,NL}(z,t) = \mathbf{P}^{(2)}_{OPA}(z,t) = 2\epsilon_0\chi^{(2)}E_1E_2^*e^{-i(\omega_1-\omega_2)t} + c.c.$. Different rules of symmetry, such as spatial symmetries of the nonlinear crystals or symmetry for lossless media can be applied which simplify the nonlinear susceptibility tensor to $\chi^{(2)} = 2d_{eff}$ [39] leading to:

$$\mathbf{P}^{(2)}_{OPA}(z,t) = 4\epsilon_0 d_{eff}E_1E_2^*e^{-i(\omega_1-\omega_2)t} + c.c. \tag{2.14}$$

More detailed information about the symmetry relations which are valid for different crystal structures is given in [34, 39].

The polarization for e.g. the idler beam is obtained by substituting Equation 2.13 for the signal and pump beam into Equation 2.14:

$$P_i(z,t) = 4\epsilon_0 d_{eff}A_pA_s^*e^{i(k_p-k_s)z-i\omega_i t} + c.c., \tag{2.15}$$

where $\omega_i = \omega_p - \omega_s$. Note, that in general $k_i \neq k_p - k_s$ because of the frequency dependent refractive index.

By substituting Equation 2.13 and Equation 2.15 into the simplified wave Equation 2.12 the idler beam is represented by:

$$\frac{d^2A_i}{dz^2} + 2ik_i\frac{dA_i}{dz} = \frac{-4d_{eff}w_i^2}{c^2}A_pA_s^*e^{i(k_p-k_s-k_i)z}.$$

Here, the nonlinear response of the medium driven by the signal and pump acts as a source term which appears on the right-hand side of this equation. As a further simplification it is assumed that the field amplitudes A_n vary only little within the distance of one wavelength so that the slowly varying amplitude approximation can be applied:

$$\left|\frac{d^2A_n}{dz^2}\right| << \left|k_n\frac{dA_n}{dz}\right|.$$

This and cyclic permutation of the three fields finally leads to the three coupled wave equations describing the nonlinear optical parametric amplification in the time domain:

$$\begin{aligned}
\frac{dA_s}{dz} &= i\frac{2\omega_s d_{eff}}{n_s c}A_i^*A_pe^{-i\Delta kz} \\
\frac{dA_i}{dz} &= i\frac{2\omega_i d_{eff}}{n_i c}A_s^*A_pe^{-i\Delta kz} \\
\frac{dA_p}{dz} &= i\frac{2\omega_p d_{eff}}{n_p c}A_sA_ie^{i\Delta kz}.
\end{aligned} \tag{2.16}$$

Here, $\Delta k = k_s + k_i - k_p$ denotes the wavevector mismatch.

Without further assumptions the wave equations can only be solved numerically. However, analytical solutions can be found by assuming that no pump depletion occurs during the amplification process, i.e. $A_p = const.$ [27]. In this regime, also known as the small-signal gain regime, the amplification is independent of the signal intensity. However, the OPCPA stages of the PFS operate in pump depletion in order to reach the highest efficiencies and output stabilities [41] and therefore a description of analytical solutions of the wave equations is not given in this work. Optimizations of the amplification stages therefore has to rely on the help of numerical simulations. Two different codes were used in the scope of this thesis in order to model the behavior of the OPA process. The SOPAS simulation program (section 3.1) which was developed by the author during the course of this thesis solves the coupled differential equations in the time domain. The Sisyfos code [42, 43] developed by Dr. Gunnar Arisholm (section 3.2) solves the wave equations in the frequency domain. Both programs are complementary, with Sisyfos acting as a benchmark for the simpler and faster SOPAS code.

2.3 Phase mismatch

The exponential term on the right hand side of the coupled wave equations (Equation 2.16) contains the so-called phase mismatch Δkz, where Δk is the wavevector mismatch and z the propagation length inside the crystal. The phase mismatch is one of the most important parameters in OPA: As can be seen from Equation 2.16, at a value of π it reverses the phase of the generated wave, leading to complete destructive interference. Therefore, it controls the spectral gain of the amplification, and consequently it determines the bandwidth and affects the maximum spectral efficiency of the process. In the following the influence of Δk and z on the amplification will be discussed.

In order to illustrate the effect of the phase mismatch on the amplification process, simulations with the SOPAS code with different Δkz values were performed for one representative set of pump, signal and idler wavelengths ($\lambda_s = 900\,\text{nm}$, $\lambda_i = 1204\,\text{nm}$ and $\lambda_p = 515\,\text{nm}$). The 3 mm thick DKDP crystal was pumped at an intensity of $100\,\frac{\text{GW}}{\text{cm}^2}$. The results of these simulations are presented in Figure 2.2. The energies for the pump (blue curve), signal (green curve) and idler beam (red curve) are calculated in dependence of the position inside the crystal for different phase mismatch values where L represents the crystal length. Figure 2.2(a) is the result for $\Delta kL = 0\,\text{rad}$, no phase mismatch. The entire pump energy can be transferred to the signal and the idler beams, 100 % efficiency is reached. After passing the point of full depletion the SFG process between signal and idler sets in and energy is transferred back to the pump beam in an oscillatory manner. In contrast, Figure 2.2(b) and Figure 2.2(c) show the case of a nonzero ΔkL. In this case the back conversion begins before the whole pump energy is depleted, the efficiency and gain are lower. In addition, it can be observed that the position inside the crystal when maximum conversion is reached shifts for the three different cases.

Moving to a more realistic picture, where the signal beam itself consists of a broad bandwidth instead of being monochromatic the process gets more complicated. A perfect phase match $\Delta kL = 0$ can only be obtained for a few wavelengths as Figure 2.3 shows for the case of a DKDP crystal with length $L = 3\,\text{mm}$ and $L = 5\,\text{mm}$. The phase mismatch for other spectral components is non-zero. In addition to the spectral phase mismatch, the simulated small-signal gain (independent of the signal input intensity) for a pump intensity of $100\,\text{GW/cm}^2$ is plotted over the signal wavelength in Figure 2.3. The longer crystal exhibits a larger phase mismatch for a given wavevector mismatch, and for increasing phase mismatch of a spectral component the spectral gain decreases. This behavior is evident from the comparison of Figure

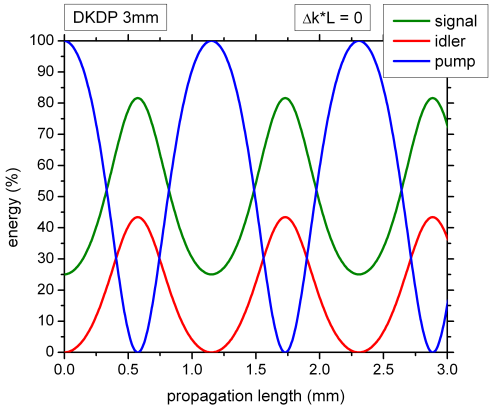

(a) $\Delta kL = 0\,\mathrm{rad}$

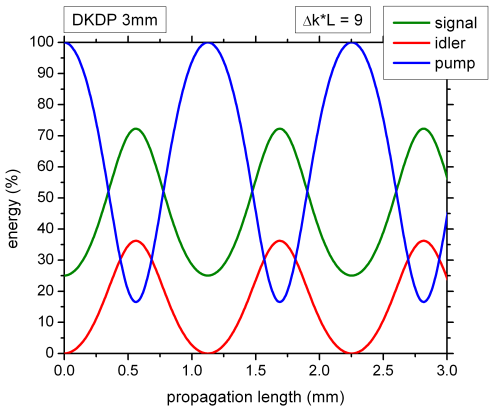

(b) $\Delta kL = 9\,\mathrm{rad}$

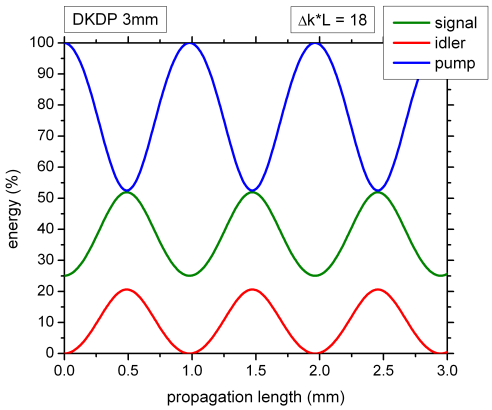

(c) $\Delta kL = 18\,\mathrm{rad}$

Figure 2.2: *Simulation of the relative pump (blue curve), signal (green curve) and idler (red curve) energy over the crystal length for different ΔkL values. Note that the initial signal energy is 25% of the pump, hence the sum of signal and idler after full conversion is 125%. (a) presents the case for $\Delta kL = 0\,\mathrm{rad}$, (b) the case for $\Delta kL = 9\,\mathrm{rad}$ and (c) for $\Delta kL = 18\,\mathrm{rad}$.*

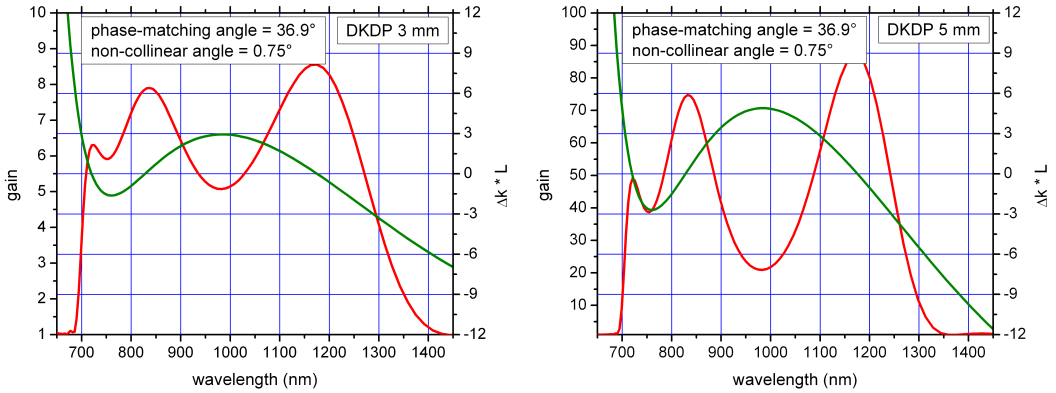

(a) DKDP, 3 mm (b) DKDP, 5 mm

Figure 2.3: *The simulated small-signal gain and phase mismatch for a* 3 mm *and* 5 mm *thick DKDP crystal is shown as a function of signal wavelength. The red curve corresponds to the small-signal gain, whereas the green curve represents the phase mismatch. The gain decreases for higher phase mismatch. Both simulation runs rely on the same pump and signal parameters for (a) a* 3 mm *and (b) a* 5 mm *thick crystal.*

2.3(a) and 2.3(b). In the spectral regions of too high phase mismatch amplification does not take place.

The simulations presented in Figure 2.2 show that the maximum efficiency and position inside the crystal when the highest efficiency is reached changes with the phase mismatch. From the calculation depicted in Figure 2.3 it follows that for broad bandwidths the phase mismatch is different for distinct spectral components. Combining these two results means that the maximum efficiency and its position inside the crystal varies for different spectral components. Finding the correct and best phase mismatch is always a compromise and a difficult task for a broad spectral bandwidth. The basic requirement for a broadband and efficient amplification in an OPA stage is a small phase mismatch for all frequencies along the signal spectrum in order to minimize the effects discussed. The phase mismatch is formed by two parameters: Δk wavevector mismatch and L the length of the crystal. In the following the possibilities to decrease each of these two parameters are discussed.

2.3.1 Crystal length

Figure 2.3 shows that for thinner crystals the phase mismatch gets smaller resulting in an increase of the amplified bandwidth and a less modulated spectral gain. However, the increase in bandwidth is obtained at the expense of the overall gain. Consequently, for an OPA there is a compromise between gain and amplified band-

width. In order to achieve an acceptable gain in the case of thin crystals, a higher pump intensity can be applied. The maximum possible pump intensity is limited by the damage threshold of the nonlinear material. The damage threshold scales with $I_{damage} \propto \frac{1}{\sqrt{\tau}}$ in the nanosecond to picosecond pulse duration regime [36]. Hence, shorter pump-pulse durations allow a higher pump intensity before damage occurs. Owing to the broad bandwidth of the PFS, crystal thicknesses of only a few millimeters are necessary. The pulse duration of the PFS pump laser is chosen to be 1 ps and its motivation is described in section 6.2. This pulse duration allows the operation of the OPCPA stages with pump intensities of $100\,\mathrm{GW/cm^2}$ which is a factor of ~ 3 below the threshold for damage of the used crystals. This figure was experimentally determined by performing tests with the compressed pump pulses of the PFS pump laser. These high pump intensities lead to prospective crystal thicknesses of $2 - 4\,\mathrm{mm}$ (cf. section 5.2).

2.3.2 Wavevector mismatch

Beside the possibility to improve the phase mismatch by shortening the crystal, as discussed in the previous section, another way to decrease the phase mismatch is the reduction of the wavevector mismatch. In section 2.2 the wavevector mismatch is defined as:

$$\Delta k = k_s + k_i - k_p.$$

In order to obtain an optimum amplification, this mismatch should be zero so that:

$$\begin{aligned} k_p &= k_s + k_i \\ \frac{n_p \omega_p}{c} &= \frac{n_s \omega_s}{c} + \frac{n_i \omega_i}{c} \end{aligned} \tag{2.17}$$

Different phase-matching techniques can be applied such as angle phase matching, temperature phase matching, quasi-phase matching or Čerenkov phase matching [34]. The PFS is based on angle phase matching thus this technique will be described in more detail in the following paragraph.

In the case of angle phase matching the birefringent nature of the OPA crystal is exploited. By changing the angle between the propagation direction and the crystal axis the refractive index of a birefringent medium for a beam with extraordinary polarization can be adjusted. In contrast, for ordinary polarization the refractive index is constant for all angles. Angle phase matching can be realized with two different geometries [27] at two different approaches for the beam polarizations.

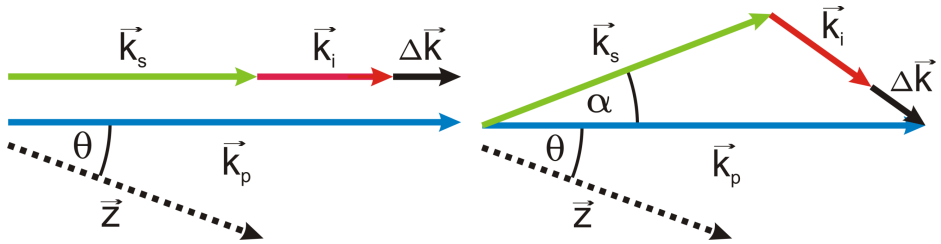

(a) collinear geometry (b) non-collinear geometry

Figure 2.4: *Two different geometries can be used for the angle phase matching technique: (a) collinear case: all beams are parallel and only the phase-matching angle θ is used to adjust minimal phase mismatch. (b) non-collinear case: pump and signal beam describe angle α. This introduces an additional degree of freedom to minimize the phase mismatch for a broader spectral region.*

- **OPA geometry:** In the collinear case, see Figure 2.4(a), all beams are propagating parallel. The angle θ between pump beam and the crystal axis is known as "phase-matching angle". In the case of a non-collinear geometry the signal and pump beam constitute a "non-collinear angle" α, see Figure 2.4(b). The additional degree of freedom introduced by α allows to obtain a smaller phase mismatch for more spectral components, which in turn leads to broader gain bandwidths. Hence, the PFS relies on the non-collinear phase matching concept. Applying the cosine rule the phase mismatch for the non-collinear case can be calculated as:

$$\Delta k = \sqrt{k_p^2 + k_s^2 - 2k_p k_s cos\alpha} - k_i. \tag{2.18}$$

- **Beam polarization:** Since three beams are involved in the process, at least two of them have the same polarization. For type-I phase matching these are the two lower frequency beams, while for type-II a high and a low frequency beam are equally polarized [39]. In addition, the pump beam usually has an extraordinary polarization. Consequently, by tilting the crystal axis relative to the pump beam the length of the k_p-vector can be adjusted in such a way to fulfill Equation 2.17 for a specific set of wavelengths. In comparison, a type-I arrangement exhibits a much broader amplification bandwidth compared to a type-II OPA as depicted in Figure 2.5. Here, the phase mismatch for a 5 mm thick DKDP crystal is plotted for different signal wavelengths at a non-collinear angle of 0.75°. In the case of type-I, the optimum phase-matching angle in terms of bandwidth and wavelength region is 36.9° and for type-II it is 55°. For type-II it is assumed that the signal has extraordinary and the idler ordinary polarization. However, the phase mismatch is not improved when the polarizations of signal ($e \rightarrow o$) and idler ($o \rightarrow e$) are changed. It

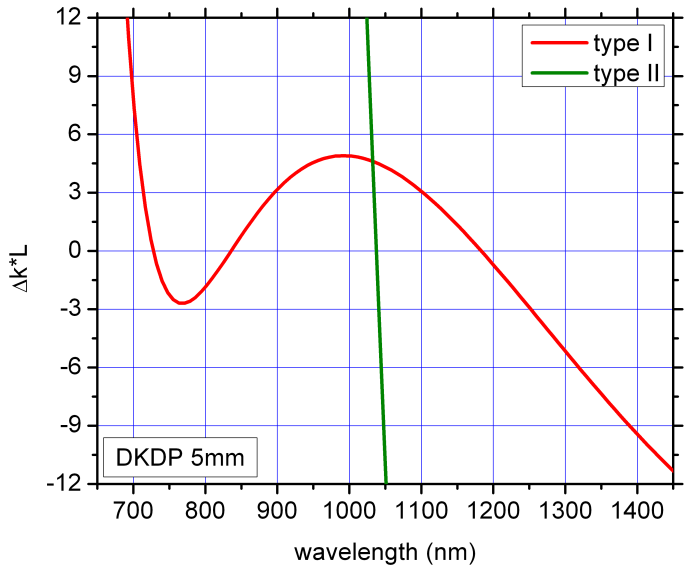

Figure 2.5: *Phase mismatch for type-I (red curve) and type-II (green curve) interaction.*

has to be mentioned that in the case of the type-II arrangement the phase mismatch can be further reduced leading to a slightly enhanced (by a few %) amplified bandwidth by using a collinear geometry. Nevertheless, since the gain bandwidth is much smaller for type-II than type-I, the OPCPA chain of the PFS is based on the type-I arrangement.

In summary, the broadest amplified bandwidth can be obtained for a type-I non-collinear OPCPA scheme in the case of PFS. For this arrangement the effect of the α and θ angle-tuning inside a 5 mm DKDP crystal pumped by 515 nm is shown in Figure 2.6. Subfigure (a) shows the change of ΔkL when only θ is varied and $\alpha = 0.75°$ is kept constant. The phase mismatch curve is shifted up and down so that the spectral region of perfect phase match moves to different wavelengths. In contrast, subfigure (b) presents the case of constant phase-matching angle $\theta = 36.9°$ and an altered non-collinear angle. The curve is not only shifted upwards/downwards but also tilted. By optimizing the non-collinear angle a very broad amplified bandwidth can be achieved when a small phase mismatch for some spectral parts is accepted. Therefore, finding the right set of phase-matching angle and non-collinear angle is a compromise between bandwidth and homogeneous amplification of the desired wavelength range. Table 2.1 presents the phase-matching and non-collinear angles for DKDP and LBO which are used in the PFS.

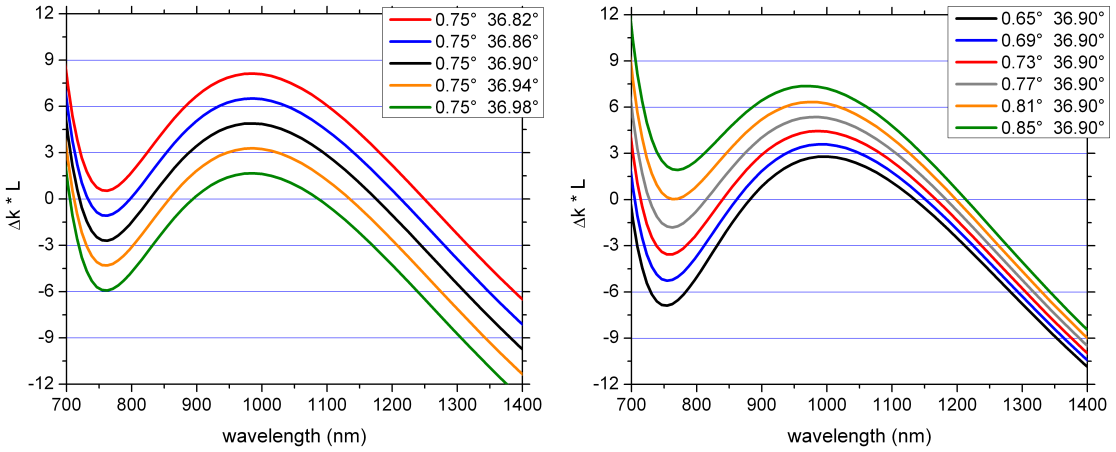

(a) phase-matching angle scan (b) non-collinear anlge scan

Figure 2.6: *The phase mismatch for different wavelengths is simulated for a* 5 mm *thick DKDP crystal: (a) the influence of the phase-matching angle* θ *on the phase mismatch, when the non-collinear angle* $\alpha = 0.75°$ *is kept constant; (b) the change of phase mismatch for different non-collinear angles and constant phase-matching angle* $\theta = 36.90°$.

	DKDP	LBO
phase-matching angle	$\sim 36.95°$	$\sim 14.45°$
non-collinear angle	$\sim 0.75°$	$\sim 1.1°$

Table 2.1: *Phase-matching and non-collinear angles for DKDP and LBO used in the PFS.*

2.3.3 Conclusion

As a result of the above considerations the bandwidth for the PFS amplification stages will be optimized by using short crystals at the best phase-matching condition in a non-collinear configuration. The resulting drop in gain is compensated by high pump intensities, necessitating a CPA pump laser. Nevertheless, there exists a trade-off between amplified bandwidth and gain. Ultra-high single-pass gain on the order of 10^5 has been demonstrated for narrow bandwidths [44, 45] whereas for broad bandwidths such as in the PFS system gains of only $1-2$ orders of magnitude per pass are expected. Consequently, the amplification of the broadband signal is performed in multiple subsequent OPCPA stages in order to reach the Joule-scale energy level.

2.4 OPA phase

The three coupled wave equations (cf. Equation 2.16) describing the OPA process are based on complex amplitudes which are formed by the time dependent real amplitudes and the complex temporal phases. By solving the imaginary parts of the coupled wave equations, three new coupled differential equations are obtained, which describe the evolution of the phases of signal, idler and pump during amplification. The derivation of these equations is well described in [46]. The amplification not only influences the real amplitudes but also the phases for non zero phase mismatch [46–48]. However, as discussed in section 2.3 for the amplification of ultra-broad bandwidths certain amounts of phase mismatch have to be tolerated and consequently the amplification of the signal beam leads to additional spectral phase distortions. The amount of this additional phase depends on the phase mismatch, the strength of the pump depletion and the intensity ratio between signal and pump [46].

In order to illustrate the meaning of the OPA phase, Figure 2.7 presents a simple example. A seed wave (red curve) is sent into a nonlinear crystal. As mentioned before, the pump and idler beam act as a source term for the amplification of the signal beam and therefore in the case of $\Delta k \neq 0$ a newly generated signal wave (blue curve) features a phase shift relative to the seed depending on Δk and the position inside the crystal the wave is generated (here, at 1.5). The sum of the seed and the newly generated wave form the amplified signal (black curve). It is obvious that the amplified signal is phase-shifted relative to the initial wave.

More detailed simulations showing the influence of the OPA phase on the compression of the signal pulse are presented in section 4.3.

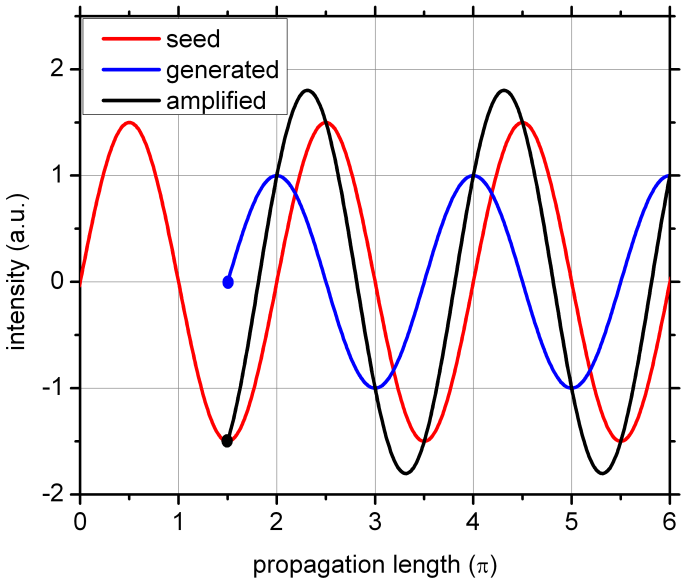

Figure 2.7: *Simple example illustrating the meaning of the OPA phase: initial seed (red curve), newly generated wave (blue curve) and amplified signal (black curve), which is the sum of both.*

3 — Tools for OPCPA modeling

As mentioned in section 2.2 the three coupled wave equations describing the OPA process can only be solved numerically. Therefore, in order to obtain a deeper insight into the OPCPA process, it is necessary to perform simulations. This chapter presents the two simulation codes which were used for the PFS development: SOPAS (**S**imulation of **O**ptical **P**arametric **A**mplifier **S**ystems) is a pseudo 3D code which was developed in the framework of this PhD work and is based on the split-step method, and is described in detail in section 3.1. The second program named Sisyfos (**Si**mulation **Sy**stem **f**or **O**ptical **S**cience) is a full 3D code written by Dr. Gunnar Arisholm [42, 43] which uses the Fourier space method to solve the coupled wave equations, described in section 3.2. The simpler SOPAS program allows for modeling multiple stages in a straight-forward way and can be adapted to particular problems of the PFS more easily since the source code is accessible. In comparison, Sisyfos grants more realistic simulations since it can handle measured beam profiles and phases and includes other nonlinear effects which can influence the OPA performance. A comparison between both codes is presented in section 3.3.

3.1 Pseudo 3D simulations with SOPAS

The SOPAS program (**S**imulation of **O**ptical **P**arametric **A**mplifier **S**ystems) is based on a code written by Dr. Franz Tavella [49]. One motivation for the improvement of the code was to reduce the calculation time dramatically in order to be able to optimize multiple OPCPA stages for the PFS system. The calculation of an OPCPA stage with the program from Dr. F. Tavella takes 8 hours and consequently it is not convenient to optimize 5 or 8 consecutive OPCPA stages as in the case of the PFS system. By changing the programing language from Mathematica to

Fortran and by optimization of the source code in terms of simulation time (reducing the number of calculations inside loops as much as possible) the time consumed for the modeling of one OPCPA stage was reduced to 30 seconds. The modeling of the optical parametric amplification is based on the Fourier split-step method [43]. The nonlinear, i.e. parametric process and the linear propagation are calculated in two separate steps for a thin crystal slice. The total length of the crystal is usually split into 1000 slices, which guarantees a sufficiently high accuracy of the simulation. The three coupled wave equations [27] describing the OPCPA process (see chapter 2) are solved in the time domain by a fourth-order Runge-Kutta solver independently in two dimensions (time and one transversal space coordinate). The solver is called up for each crystal slice and consequently it is optimized for a minimum of calculation time. In contrast to the nonlinear process, the linear propagation is treated in the frequency domain and k-space. The electrical field is Fourier transformed and the phase arising from linear propagation through the crystal is taken into account. Afterwards the field is Fourier transformed back to the time domain and real space where the next nonlinear step is calculated. This modeling principle is depicted in Figure 3.1.

The SOPAS program can handle the drift in space of the three beams relative to each other due to the non-collinear geometry. The pulse-fronts of all three beams are assumed to be parallel. Furthermore it is assumed that the pump beam is monochromatic and that the signal beam has only a second-order spectral phase. The complex amplitudes describing the fields are stored on a two dimensional grid with a temporal and one spatial coordinate. The energy of all pulses is calculated under the assumption of a rotational symmetry in space, hence the term "pseudo 3D". The wave equations are solved numerically, thus full pump depletion and back

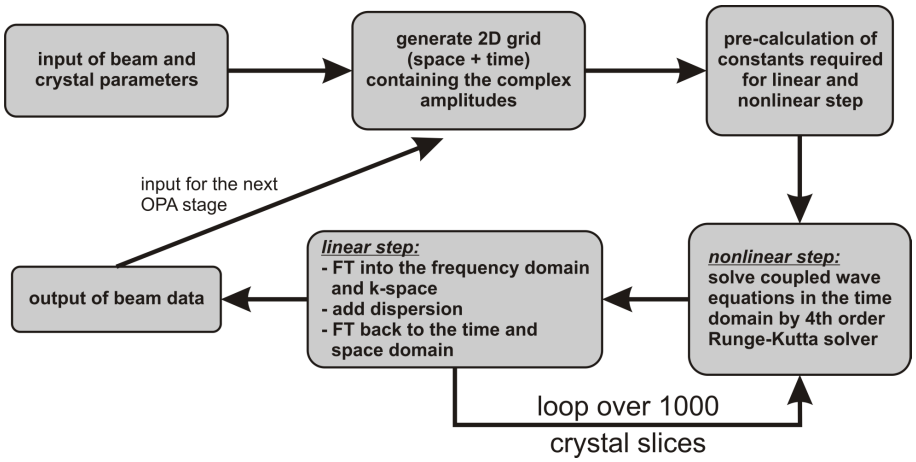

Figure 3.1: *Schematic scheme of the modeling principle of the SOPAS code.*

conversion can be modeled. The generation of superfluorescence is also taken into account, where the starting grid for the fluorescence is created with a random generator (method of stochastic fields [50]) and its amplitude is scaled with ϵA_p, where ϵ is an empirical factor [49] and A_p the root of the pump intensity. Furthermore, perfect phase match is assumed for the amplification of the generated fluorescence since the rate of transition from a pump photon to a fluorescence photon is higher in the direction of the smallest phase mismatch and therefore only in this case the fluorescence can be efficiently amplified from the quantum noise level [49].

Furthermore, the new code can handle higher-order super-Gaussian beam profiles in space and time for the signal and pump pulses and a measured signal input spectrum can be fed into the calculations. In addition, the program can reuse the simulation results from the previous run and therefore the modeling and optimization of a total OPCPA chain is easily realizable. The consecutive stages either can be pumped by a "fresh" pump beam or reuse the pump of the previous stage [51].

In order to show the validity of the simulation results, a comparison between the SOPAS simulations and experimental measurements was performed and is presented in Appendix B. Two aspects were investigated in particular, namely the amplified bandwidth in the small-signal-gain regime and the pump depletion and saturation behavior. From this investigation it was concluded that the SOPAS program is able to reliably model the small-signal and saturation behavior of the optical parametric amplification process. Furthermore, the SOPAS code was benchmarked with the Sisyfos program and the results are presented in section 3.3.

3.2 3D simulations with Sisyfos

In order to obtain a more detailed insight into the process of parametric amplification, more sophisticated simulations with Sisyfos (**Si**mulation **Sy**stem **f**or **O**ptical **S**cience) were performed. The code was developed by Dr. Gunnar Arisholm at the Forsvarets forskningsinstitutt, Norway [42, 43].

The program is based on the Fourier-space method. In contrast to the split-step method used by the SOPAS program (cf. section 3.1), the nonlinear and linear steps are not treated separately but solved within the same step. The coupled wave equations comprise the nonlinear amplification as well as the full dispersion, including walk-off and non-collinear geometry, and are solved in the frequency domain. The code handles the electric field in three dimensions which allows for an accurate analysis of the influence of the pump-beam profile on the amplified signal beam

and the change of the signal-beam profile due to strong saturation. Furthermore, it is capable to simulate pump depletion, tilted pulse fronts, diffraction, walk-off, nonlinear parasitic effects such as SHG of the idler, signal and pump beams and nonlinear refractive effects (n_2) such as self focusing (SF) induced by high pump intensities. Measured beam profiles and spectra as well as measured spectral phases can be loaded as input parameters. More detailed information about the structure and the mathematical background of the Sisyfos code is given in [42, 43, 52]. The code has demonstrated its versatility several times [53–57].

3.3 Comparison between SOPAS and Sisyfos

In order to compare both codes with each other and validate their simulation results two studies were performed: In the first investigation, a quadratically chirped signal pulse with a Gaussian spectral shape was assumed and the results of both programs are compared with each other. In the second study, the first stage of the vacuum OPCPA setup which is described in section 7.3 was modeled with both codes and the results are compared to the measured data.

3.3.1 Signal with Gaussian-shape spectrum and quadratic phase

The amplification of a Gaussian-shaped signal spectrum ($\lambda_0 = 880\,\text{nm}$, $\Delta\lambda = 280\,\text{nm}$) in a 4 mm thick LBO crystal was modeled with both codes. The nonlinear crystal was pumped by a 1.2 ps short pump pulse with an energy of 20 mJ. The pump beam diameter was set to 4.4 mm full width at half maximum (FWHM) leading to a pump intensity of 70 $\frac{\text{GW}}{\text{cm}^2}$. A seed energy of 20 μJ was assumed and the stretched FWHM signal pulse duration was 440 fs, which corresponds to a group delay (GD) difference between $700 - 1400\,\text{nm}$ of 900 fs for a quadratically chirped pulse. A non-collinear angle of 1.1° and a phase-matching angle of 14.45° were used.

The results of these simulations are presented in Figure 3.2 where the red curves correspond to the results achieved with the SOPAS code and the blue curves presents the data obtained with Sisyfos. Figure 3.2(a) shows the amplified signal spectra and Figure 3.2(b) presents the signal energy over the crystal length. It can be observed that the amplified spectra match well, but the predicted signal pulse energy differs by $\sim 15\%$. This is caused by the different calculation of the energy for the 2D and 3D code. The SOPAS code is assuming a rotational symmetry. Consequently, an asymmetric signal beam profile as it is expected for a non-collinear geometry results in a different energy compared to Sisyfos, where the full asymmetry is taken into

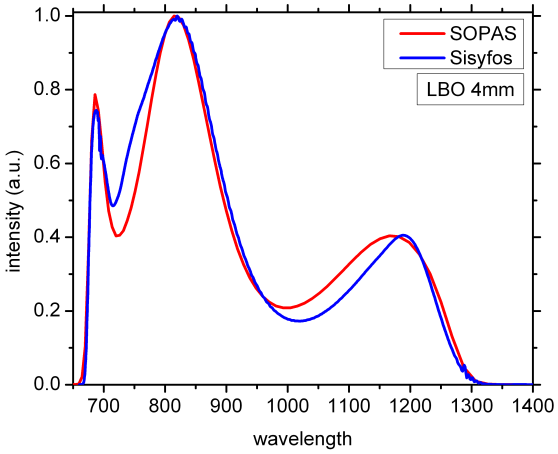

(a) amplified signal spectrum

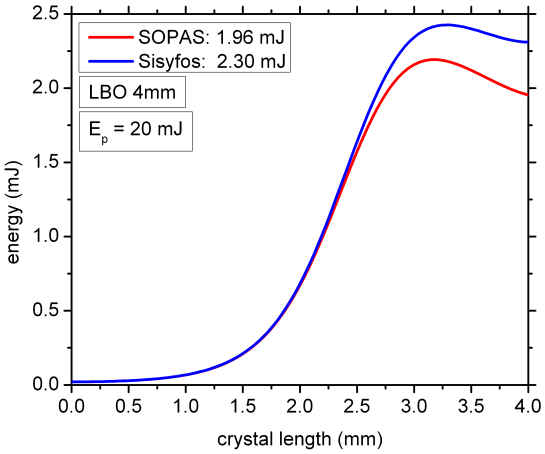

(b) signal energy vs. crystal length

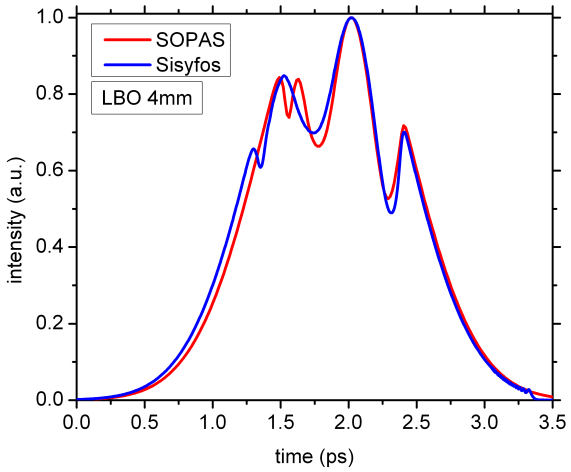

(c) temporal shape of pump pulse after OPCPA stage

Figure 3.2: *Comparison between the SOPAS (red curves) and the Sisyfos code (blue curves): (a) amplified signal spectrum; (b) signal energy versus the crystal length; (c) temporal shape of the pump pulse after the nonlinear crystal.*

account. Nevertheless, the saturation behavior is very similar for both codes. Figure 3.2(c) presents the temporal shape of the pump pulse after amplification clearly indicating the effect of pump depletion. Both codes show a very good agreement.

3.3.2 Comparison with experimental data

Here, the first stage of the vacuum OPCPA setup is modeled with the SOPAS and the Sisyfos codes. A detailed description of the experimental layout is given in section 7.3 and appendix D.3. A broadband signal spectrum, which is presented as green curve in Figure 3.3(a), was amplified in a 4 mm thick LBO crystal. The nonlinear crystal was pumped with 4.5 mJ and the pump-beam diameter was measured to 2.6 mm FWHM at the position of the crystal leading to a pump intensity of $\sim 100\,\frac{\mathrm{GW}}{\mathrm{cm}^2}$. The beam size of the signal beam was matched to the pump-beam size. A Gaussian-shape in space was assumed for the signal and pump beam in the simulations. The measured seed energy was 0.3 μJ and the measured GD of the signal pulse is depicted as blue curve in Figure 3.3(a) clearly indicating the presence of third-order dispersion (TOD) introduced by air and material. This GD was fed into the Sisyfos simulation. However, the SOPAS code can handle only quadratically chirped signal pulses and consequently for the SOPAS calculation the GD presented by the red curve in Figure 3.3(a) (only group-delay dispersion (GDD)) was used.

For the simulations the only adjustable parameters were the phase-matching angle and the relative timing between the signal and pump pulses. In the simulations a phase matching angle of 14.45° and a relative timing offset of 0.13 ps for SOPAS and $\sim$ 0.2 ps for Sisyfos was used. The relative timing differs in both simulations since the definition of the time zero for the signal beam are diverse in both codes. The measured amplified signal spectrum (green curve) as well as the calculated amplified spectra (red curve for SOPAS and blue curve for Sisyfos) are depicted in Figure 3.3(b). The spectral phase of the signal pulse has a significant influence on the amplified spectral shape as will be shown in more detail in subsection 4.2.2. Consequently, the spectrum obtained with SOPAS differs from the spectrum calculated with Sisyfos due to the difference in spectral phase. The GD used with Sisyfos is more flat in the infrared spectral part (900 − 1400 nm) compared to the GD used in the SOPAS code. Consequently, in the SOPAS code this spectral region sees a higher pump energy available than in the Sisyfos code (overlaps over a longer time with the pump pulse). This leads to a higher infrared spectral region for SOPAS compared to Sisyfos. Nevertheless, the amplified bandwidth is well reproduced with a slightly broader bandwidth in the visible part for the simulations compared to the measurements. The measurements show a smaller gain in the infrared part compared to the Sisyfos simulations. The origin of this discrepancy has not been clarified yet and needs further investigations. Figure 3.3(c) presents the calculated energy versus the crystal length. Signal energies of 203 μJ and 215 μJ are obtained with SOPAS and Sisyfos, respectively. The signal pulse energy measured in the experiment was 180 μJ. However, the highest SHG efficiency, which could be obtained in the experiments, was only 40% indicating a perturbation of the pump beam (cf. section 6.2),

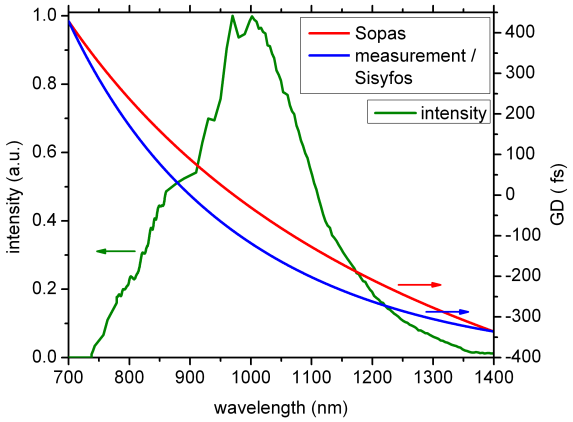

(a) input signal spectrum and GD

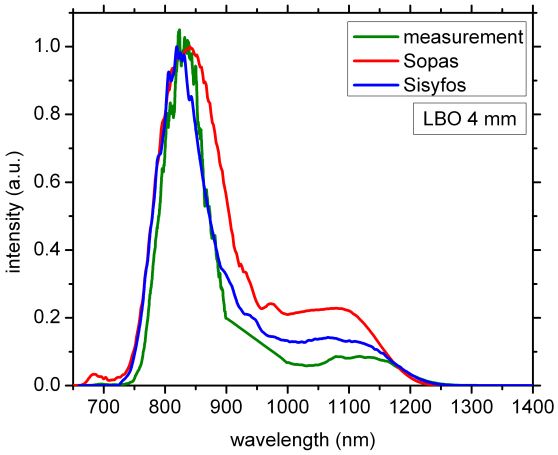

(b) amplified signal spectrum

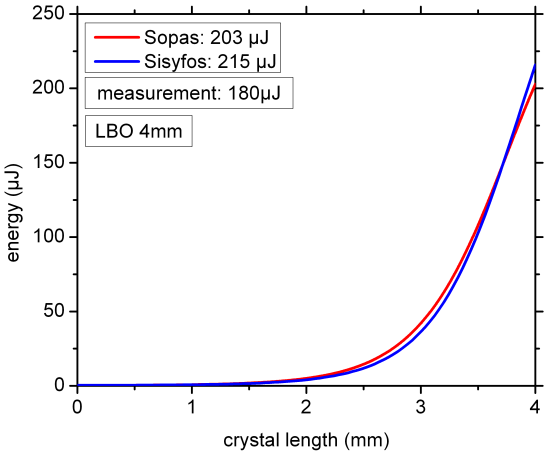

(c) energy vs. crystal length

Figure 3.3: *Comparison between SOPAS (red curves), Sisyfos (blue curves) and measurements (green curve): (a) shows the measured signal spectrum and GD used as an input for the simulations; (b) presents the measured amplified signal spectrum and the calculated spectra; (c) signal energy versus the crystal length.*

which consequently leads to a reduced efficiency for the OPCPA process as well. Therefore, a smaller pulse energy in the experiment is expected compared to the pulse energies obtained by the simulations.

3.4 Conclusion

Two different simulation programs were applied in the framework of this thesis. The "pseudo 3D" SOPAS code is based on the split-step model and can handle multiple consecutive OPCPA stages in a straight forward way (section 3.1) and is therefore the ideal choice for design studies of the PFS OPCPA chain. Furthermore, owing to the improvements and optimization of the code performed in the framework

of this thesis, which led to a reduced calculation time, parameter scans can be performed enabling the study of the dependence of the OPCPA process on various pulse parameters. However, more detailed simulations are performed with the Sisyfos code [42, 43] since it can treat realistic spectral phases, beam profiles as well as other perturbing nonlinear effects such as SF (cf. section 3.2). The comparison between simulations and measurements demonstrated the ability of both codes to model the behavior of the amplification process. The simulation of the amplified spectral bandwidth and the energy were treated correctly.

4 — ps-OPCPA design for PFS

After the introduction of the mathematical background of OPA and the description of the available simulation tools, this chapter is dedicated to general design principles which have to be considered during the development of a ps-OPCPA system. In the first part two different geometries which can be used for non-collinear type-I interactions are discussed. The second part presents the most important results of a numerical study investigating the influence of the pulse and crystal parameters on the OPCPA performance. In the third part the influence of the OPA phase on the compressed signal pulse is studied. The special requirement on the temporal contrast, arising from the intended PFS operation regime and application scope, will be discussed in part four. The fifth and six part are dedicated to the investigation of nonlinear effects like SF and side effects such as crystal heating due to the linear absorption of the pump and their influence on the OPCPA process.

4.1 Walk-off compensation and tangential phase matching

The OPCPA chain of the PFS is based on nonlinear birefringent crystals (cf. section 2.3). However, in a birefringent crystal the extraordinary beam exhibits a walk-off, i.e. k-vector and pointing vector (energy flow) do not point in the same direction any more. The angle between the k-vector and the pointing vector can be written as

$$\rho = -\frac{1}{n_e}\frac{\partial n_e}{\partial \theta}, \tag{4.1}$$

where n_e is the refractive index for extraordinary polarization and θ the phase-matching angle [58]. The negative sign indicates that the walk-off occurs in the

direction where the refractive index decreases. Depending on the crystal orientation two different arrangements are possible, which are shown in Figure 4.1. Here, Figure 4.1(a) presents the case where the walk-off leads to a shift of the pump beam towards the signal beam, which is called the "walk-off compensation scheme". The shift of the pump beam counterbalances the movements of the signal and pump beam relative to each other due to the non-collinear geometry. Consequently, the spatial overlap between pump and signal is enhanced over the crystal length. However, at the same time this leads to a decreased overlap of pump and idler beams. In comparison, Figure 4.1(b) depicts the second case named "tangential phase matching", where the crystal is rotated by 180° along the pump propagation direction. Now, the pump beam moves away from the signal beam and shifts towards the idler beam. In the case of the walk-off compensation scheme, the amplified signal beam overlaps much better with the initial input signal beam, leading to a better total beam quality. However, the tangential phase matching scheme results in a better total spatial overlap of all three beams leading, in general, to higher efficiencies [59]. Since the k-vector of the pump stays unaffected, the phase mismatch is the same for both cases.

In general it is favorable to operate the first stages of an OPCPA system where the extracted energy is low in the walk-off compensation regime in order to maintain the good spatial quality of the seed pulse. In the last stages the tangential phase-matching scheme should be applied in order to optimize the extraction of energy.

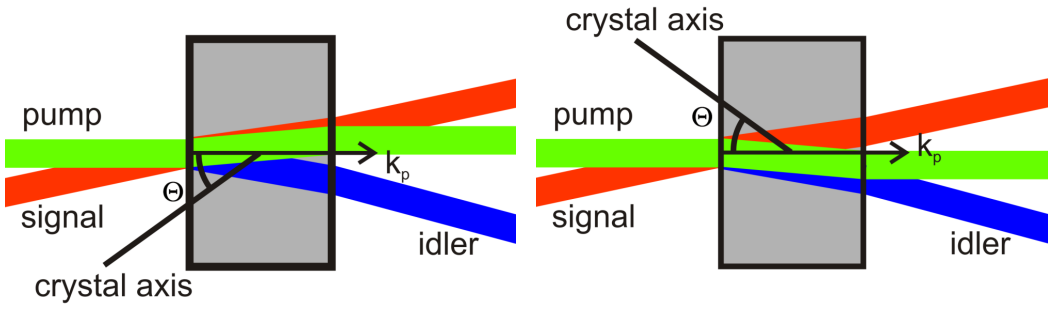

(a) walk-off compensation (b) tangential phase matching

Figure 4.1: *For the non-collinear geometry two different schemes can be applied. (a) presents the case where the walk-off leads to a shift of the pump beam towards the signal beam which is called walk-off compensation. (b) illustrates the case for a* 180° *rotated crystal which is known as tangential phase matching. Here, the walk-off of the extraordinary pump beam leads to a shift towards the idler beam.*

Table 4.1 presents the walk-off angles and the resulting angle between the pointing vectors of the signal and pump beam for both schemes in the case of PFS. In addition, the shift of pump beam relative to the signal beam per crystal length is shown. It is obvious that the influence of the beam shift on the OPA process is highest for small beam diameters and long nonlinear crystals. The highest relative beam shifts occurred in the experiments presented in section 7.1. Here, beam sizes on the order of $\sim 1.5 - 2\,\mathrm{mm}$ were used which for the DKDP crystal with a length of 7 mm resulted in $\sim 280\,\mu\mathrm{m}$ for the relative beam shift. This corresponds to 19% of the pump beam size and therefore cannot be neglected. However, no difference in terms of amplified signal spectrum, output energy or beam profile quality was detected between the two schemes in the experiments since the instabilities arising from pump fluctuations and signal-beam-profile variations overwhelmed the effect of the walk-off by far.

The largest spatial shifts in the point design for PFS (cf. section 5.2) will occur in the first and third stage, since the other OPCPA stages exhibit smaller beam shifts due to shorter crystal lengths. The first OPCPA stage is based on a 2.7 mm thick LBO crystal and a 3.3 mm thick DKDP crystal will be used in the third OPCPA stage. Consequently, a maximum spatial shift of $73\,\mu\mathrm{m}$ for the first stage and of $133\,\mu\mathrm{m}$ for the third OPCPA stage can be estimated. Compared to the planned beam sizes of 4.5 mm FWHM in the first stage and 70 mm FWHM in the third stage, these slippages are negligible and will not have any influence on the amplification process of the final PFS system. Owing to the small non-collinear angles and relatively large beam size in the PFS, both schemes can be used without the mentioned drawbacks.

		DKDP	LBO
non-collinear angle α		0.9°	1.1°
phase-matching angle θ		36.8°	14.45°
walk-off angle ρ		1.4°	0.45°
angle between pointing vectors of pump and signal	*wlk.*	0.5°	0.65°
	tan.	2.3°	1.55°
relative beam shift	*wlk.*	8.7 $\frac{\mu\mathrm{m}}{\mathrm{mm}}$	11.3 $\frac{\mu\mathrm{m}}{\mathrm{mm}}$
	tan.	40.2 $\frac{\mu\mathrm{m}}{\mathrm{mm}}$	27.1 $\frac{\mu\mathrm{m}}{\mathrm{mm}}$

Table 4.1: *Walk-off parameters and beam shift in LBO and DKDP as applied in PFS. Here, wkl. stands for walk-off compensation and tan. represents the tangential phase matching scheme.*

4.2 Influence of beam and crystal parameters on OPCPA

It is essential to have a substantiated knowledge about the process of amplification for an efficient optimization of an OPCPA system. In order to obtain such a deeper understanding, simulations investigating the dependence of the output performance of an OPCPA stage on different beam and crystal parameters were performed. These studies are presented in detail in appendix C.1. Here, only the most relevant results for PFS are discussed.

If not otherwise stated the simulations presented in the next sections are based on the following parameters: A 4 mm thick LBO crystal is used for the amplification of the broadband signal. The non-collinear angle is set to 1.1° and a phase-matching angle of 14.45° is assumed. The nonlinear crystal is pumped by a 20 mJ pump pulse with a pulse duration of 1.2 ps. The beam size of the pump is set to 4.4 mm FWHM resulting in an intensity of 70 $\frac{\mathrm{GW}}{\mathrm{cm}^2}$. The nonlinear crystal is seeded with the broadband signal generated by two subsequent hollow-core fiber (HCF)s (cf. red curve in Figure 4.2) and a seed energy of 20 μJ. The GD of the signal used for the simulations is taken from the measurements presented in section 7.3 and is shown as green curve in Figure 4.2. A signal-beam size of 4.4 mm FWHM is assumed. A Gaussian beam shape is used for the spatial profile of the signal and pump beam. Consequently, the simulations represent the tendencies of the OPCPA behavior but do not reproduce the complete realistic scenario. If not otherwise stated the simulations were performed with the SOPAS code.

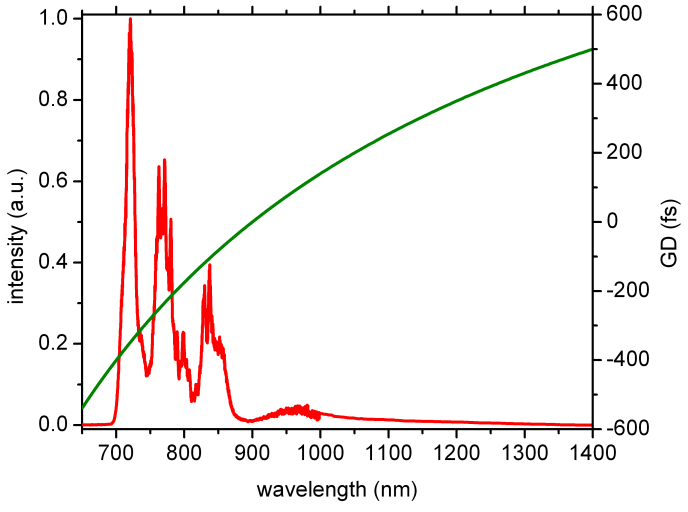

Figure 4.2: *Spectrum and GD used for the simulations as input parameters.*

4.2.1 Crystal material

The choice of the nonlinear crystal determines the amplified wavelength range (phase matching) and the possible gain per crystal length (effective nonlinearity, cf. chapter 2). Owing to the high nonlinear coefficient and the large gain bandwidth which can be supported by Beta Barium Borate, beta $-$ BaB_2O_4 (BBO) and LBO, these nonlinear crystals currently are widely used in existing OPA systems [28, 60–62]. In the last years periodically poled Lithium Niobate, $LiNbO_3$ (PPLN) has been used for parametric amplification in the mid-infrared spectral range in a number of systems [63–65] due to its very high nonlinearity which even exceeds the values of BBO. However, these crystals can only be grown in limited sizes up to a few centimeters in aperture for BBO and LBO and even less for PPLN. In order to construct an ultra-high peak power system based on OPCPA, which reaches up to the terawatt or even petawatt power level such as PFS, crystals supporting large apertures ($\geq 100\,\mathrm{mm}$) are needed for the last amplifier stages. KDP, DKDP [66] and Cesium Lithium Borate, $CsLiB_6O_{10}$ (CLBO) [67] are available in significantly larger sizes, although these crystals have a lower nonlinearity. It has been shown that CLBO and KDP support a similar gain bandwidth [68]. Owing to the fact that the gain bandwidth of DKDP exceeds that of KDP [66], most of the modern systems under development apply or plan to apply DKDP crystals for the last amplifier stages [69]. At the Institute of Applied Physics in Russia a system with 0.56 PW at pulse durations of 43 fs using DKDP as the nonlinear crystal is already in operation [44]. At the Rutherford Appleton Laboratory in Great Britain the "Vulcan 10 petawatt upgrade" is heading to reach 300 J at a pulse duration of 30 fs [70], where after two LBO-OPCPA stages the last amplification stage consists of two DKDP crystals. The last OPCPA stages of the PFS system will also apply DKDP. In the case of the 515 nm pump wavelength of the PFS system and the dispersion characteristics of DKDP the favorable and broadest bandwidth which can be amplified lies between $700 - 1400\,\mathrm{nm}$.

Simulations, to be presented in detail in section 5.1, show that due to the low nonlinearity of DKDP eight OPCPA stages are required to reach the desired parameters of PFS in terms of energy and bandwidth. In order to reduce the number of stages and the complexity of the system, it is favorable to find alternative nonlinear materials with higher nonlinearity replacing DKDP in the first stages, where the necessary aperture is between $10 - 60\,\mathrm{mm}$. Promising candidates are BBO and LBO. Figure 4.3 presents the results of simulations comparing these two crystals with each other. Two simulation runs with identical signal and pump parameters were performed: one run used a 1.6 mm thick BBO crystal ($\alpha_{internal} = 2.2°$ and $\theta = 24.08°$) and the second run was based on an LBO crystal ($\alpha_{internal} = 1.1°$ and $\theta = 14.45°$) with a thickness of 4.0 mm. Figure 4.3(a) presents the phase mismatch for both

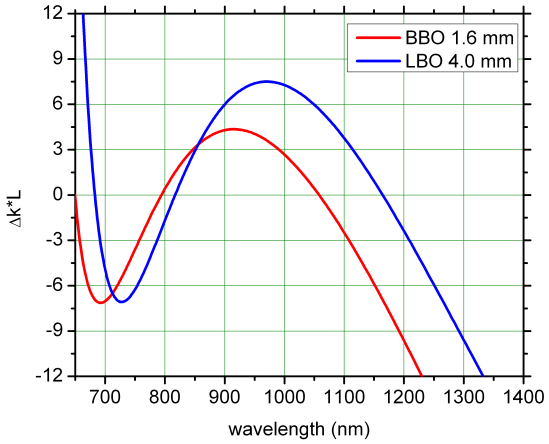

(a) phase mismatch

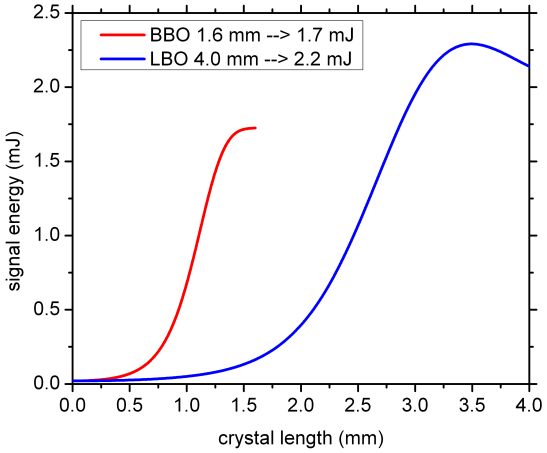

(b) signal energy vs. crystal length

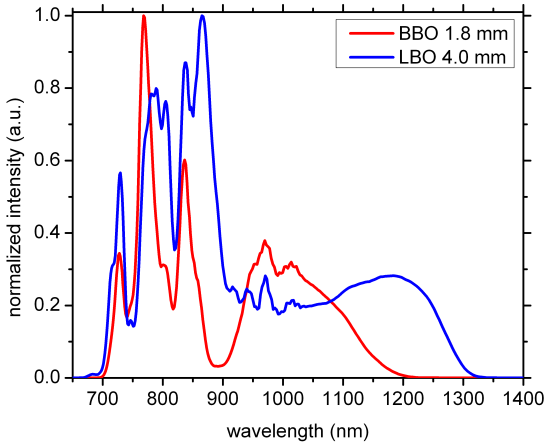

(c) normalized amplified signal spectrum

Figure 4.3: *Simulations comparing the performance of a BBO (red curves) and an LBO crystal (blue curves). The signal and pump parameters are identical in both simulations. (a) phase mismatch for both crystals; (b) the signal energy over the crystal length; (c) the normalized amplified signal spectra for both materials.*

crystals and Figure 4.3(b) shows the evolution of the signal energy during the propagation through the crystal, resulting in a signal output energy of 1.7 mJ in the case of BBO and a signal energy of 2.2 mJ for the case of an LBO crystal. Figure 4.3(c) presents the resulting normalized amplified signal spectra. The LBO crystal can support a much broader spectrum than the BBO crystal within the desired wavelength range of $700 - 1400$ nm. The amplified bandwidth of LBO is comparable to the supported bandwidth of DKDP and consequently LBO is the most promising replacement in the first OPCPA stages.

4.2.2 Spectral phase of signal

The influence of the spectral phase of the signal beam on a saturated OPA is investigated with Sisyfos simulations. Figure 4.4(a) shows three different group delays which where used in the calculations. In the case of the red curve the infrared tail of the spectrum is more compressed than the 700 − 900 nm part. Therefore, the infrared components overlap with a smaller part of the pump in time and consequently less pump energy contributes to the amplification. This leads to a reduced gain for the spectral components of 900 − 1300 nm compared to the blue part of the spectrum. In contrast, the green curve represents the opposite case. Here, the spectral components in the region of 700 − 900 nm are less chirped than the infrared components and consequently are less amplified. The blue curve presents a compromise between both cases. The amplified spectra presented in Figure 4.4(b) clearly reproduce the predicted behavior. Depending on the phase, the infrared tail of the spectrum can be enhanced or reduced relative to the blue part. This is a main difference to a laser where the spectral phase has no influence on the amplification behavior.

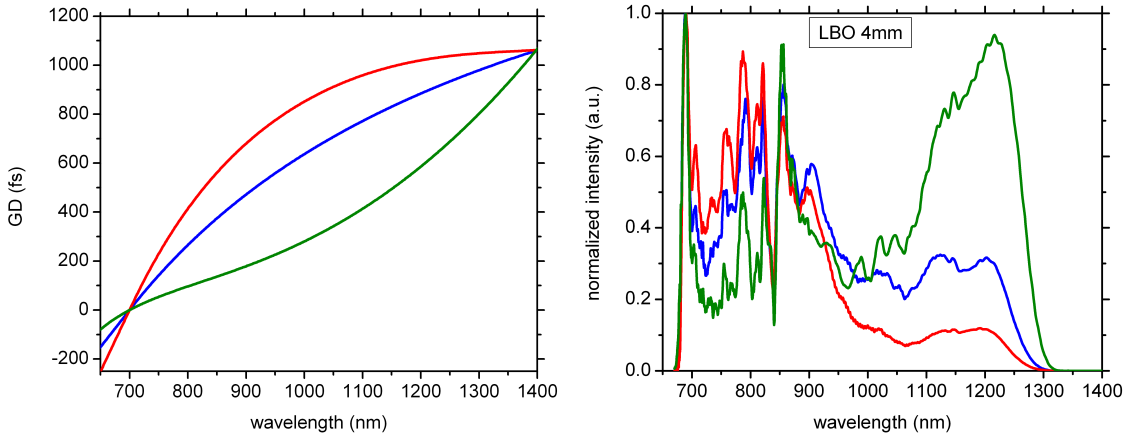

(a) group delay of signal pulse

(b) amplified spectra

Figure 4.4: *Simulations showing the effect of the spectral phase of the signal beam on the spectrum and the energy: (a) Group delays for the different simulation runs. The blue curve represents the case of a pure quadratic phase in the frequency domain at* $\lambda_0 = 920\,\mathrm{nm}$ *(*$\mathrm{GDD} = -790\,\mathrm{fs}^2$, $\mathrm{TOD} = 0\,\mathrm{fs}^3$, $\mathrm{FOD} = 0\,\mathrm{fs}^4$*), whereas the red and green curves depict the case of a phase with additional higher orders. The red curve (*$\mathrm{GDD} = -910\,\mathrm{fs}^2$, $\mathrm{TOD} = -850\,\mathrm{fs}^3$, $\mathrm{FOD} = 540\,\mathrm{fs}^4$*) is related to a spectral phase which can be compressed with* CaF_2 *and the green curve (*$\mathrm{GDD} = -380\,\mathrm{fs}^2$, $\mathrm{TOD} = 740\,\mathrm{fs}^3$, $\mathrm{FOD} = -3020\,\mathrm{fs}^4$*) corresponds to the spectral phase obtained after a prism stretcher. (b) Amplified spectra normalized to their peak values. The output energy varies by approx.* 10 %*. The red curve achieves the highest pulse energy and the green curve the lowest one.*

4.2.3 Temporal jitter

The nonlinear amplification is sensitive to the momentary pump intensity (cf. section 2.2). A change of the temporal overlap between the signal and pump results in a change of the momentary pump intensity the signal sees (cf. Figure 4.5) and consequently, leads to fluctuations of the amplified energy and to additional spectral variations for a chirped pulse. Obviously, the absolute timing accuracy requirements are more stringent for shorter pump and signal pulses, which poses a much greater challenge for PFS than for more traditional, ns-pumped OPCPA system. With its picosecond pump pulses, a timing jitter of just 100 fs can already have a very noticeable influence on the amplified spectrum as depicted in Figure 4.6. It presents the simulated effect of temporal jitter for different levels of amplification. For −100 fs, 0 fs and +100 fs pump-signal delays, Figure 4.6 shows both the amplified spectra and signal output energy. This is done for three different amplified signal energies below, at and above maximum energy transfer, respectively.

In the case of Figure 4.6(a), the LBO crystal length (3 mm) is terminated slightly before the OPCPA stage reaches the point of maximum efficiency, as can bee seen by comparing the insets of Figures 4.6 (a)-(c). Any timing jitter transfers into a spectral shift of the maximum gain. Figure 4.6(b) shows the same analysis for the crystal length (3.5 mm) set for maximum efficiency. The spectral shift is slightly less pronounced as more parts of the beam are in saturation. In Figure 4.6(c) the crystal length (4 mm) is chosen such that for all delay settings the energy transfer over-saturates. All three cases show a spectral shift of the gain window. The central part of the amplified spectrum remains stable whereas the spectral (and due to the chirp, also temporal) edges are most affected by the timing jitter and experience an intensity modulation. However, it can be observed that saturation leads to a more stable output in terms of energy and spectral shape. It is therefore favorable to sacrifice a bit of signal energy and work behind the point of maximum efficiency [41].

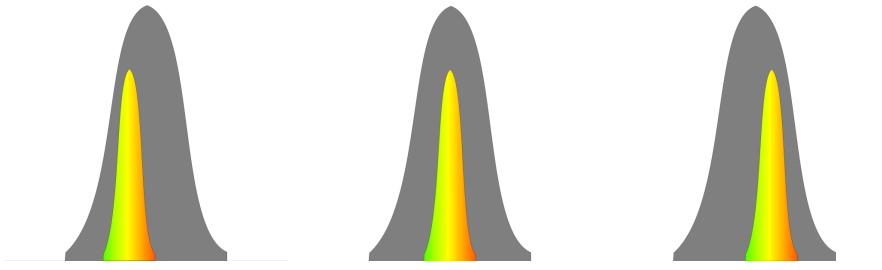

(a) signal pulse to early (b) perfect overlap (c) signal pulse to late

Figure 4.5: *Schematic illustration of the temporal jitter.*

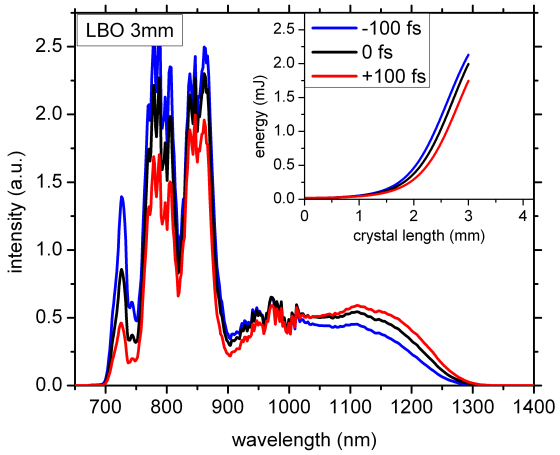

(a) before max. efficiency

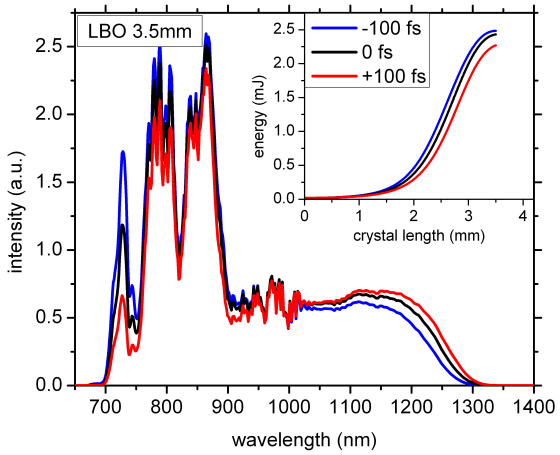

(b) maximum efficiency

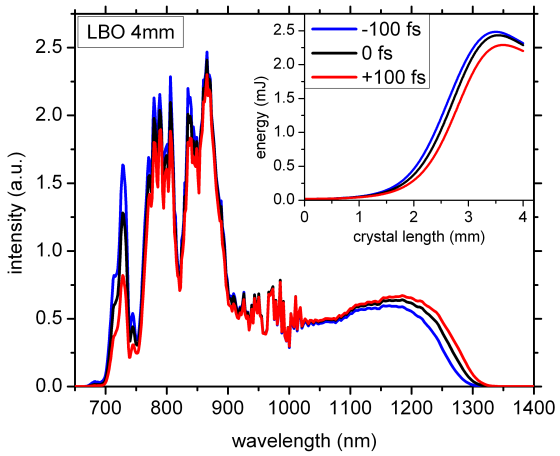

(c) saturation

Figure 4.6: *Simulations presenting the effect of temporal jitter on the amplified spectrum for different levels of amplification: (a) before the point of maximum efficiency; (b) maximum output energy; (c) past saturation regime.*

4.3 OPA phase

As described in section 2.4 the nonlinear amplification imprints an additional phase on the signal beam for non-zero phase mismatch. Simulations with Sisyfos investigating the additional spectral phase of the signal beam for different signal input energies, i.e. different levels of back conversion were performed. The results are shown in Figure 4.7. Broadband amplification in a 4 mm thick LBO crystal with a non-collinear angle of 1.1° and a phase-matching angle of 14.45° pumped at an intensity of $\sim 100\,\frac{\mathrm{GW}}{\mathrm{cm}^2}$ (i.e. 20 mJ pump energy) is modeled. The output spectrum of the XPW setup was taken as the seed spectrum (cf. section 6.1). Figure 4.7(a) presents the signal energy plotted over the crystal length, whereas Figure 4.7(b) depicts the amplified signal spectra. The OPA phase is presented in Figure 4.7(c). Here, the initial spectral phase as well as the dispersion introduced by the LBO crystal were subtracted from the phase of the amplified signal, resulting in the OPA phase. For small signal energies (≤ 10 nJ), i.e. before saturation, the OPA phase depends only on the pump intensity and the phase mismatch and consequently does not vary significantly in these simulations (red, black and blue curves). However, for signal energies ≥ 50 nJ, the OPA phase is changed, especially in the spectral regions where back conversion starts ($830 - 1050$ nm). The amount of introduced phase is high enough to have a significant effect on the temporal shape of the compressed pulse. Figure 4.7(d) depicts the Fourier transformation of the amplified spectrum obtained at an input signal energy of 200 nJ with the OPA phase (blue curve) and with compensated OPA phase, i.e. flat phase (red curve). The FWHM pulse duration is increased from 5.7 fs to 8.9 fs and in addition, side pulses can be detected leading to a strongly decreased peak intensity and reduced temporal contrast in the case of an uncompensated OPA phase. Consequently, the compressor of the broadband signal has to be adapted to compensate the additional spectral phase introduced due to optical parametric amplification in multiple stages in order to obtain the shortest pulse durations and highest peak intensities (cf. section 7.3).

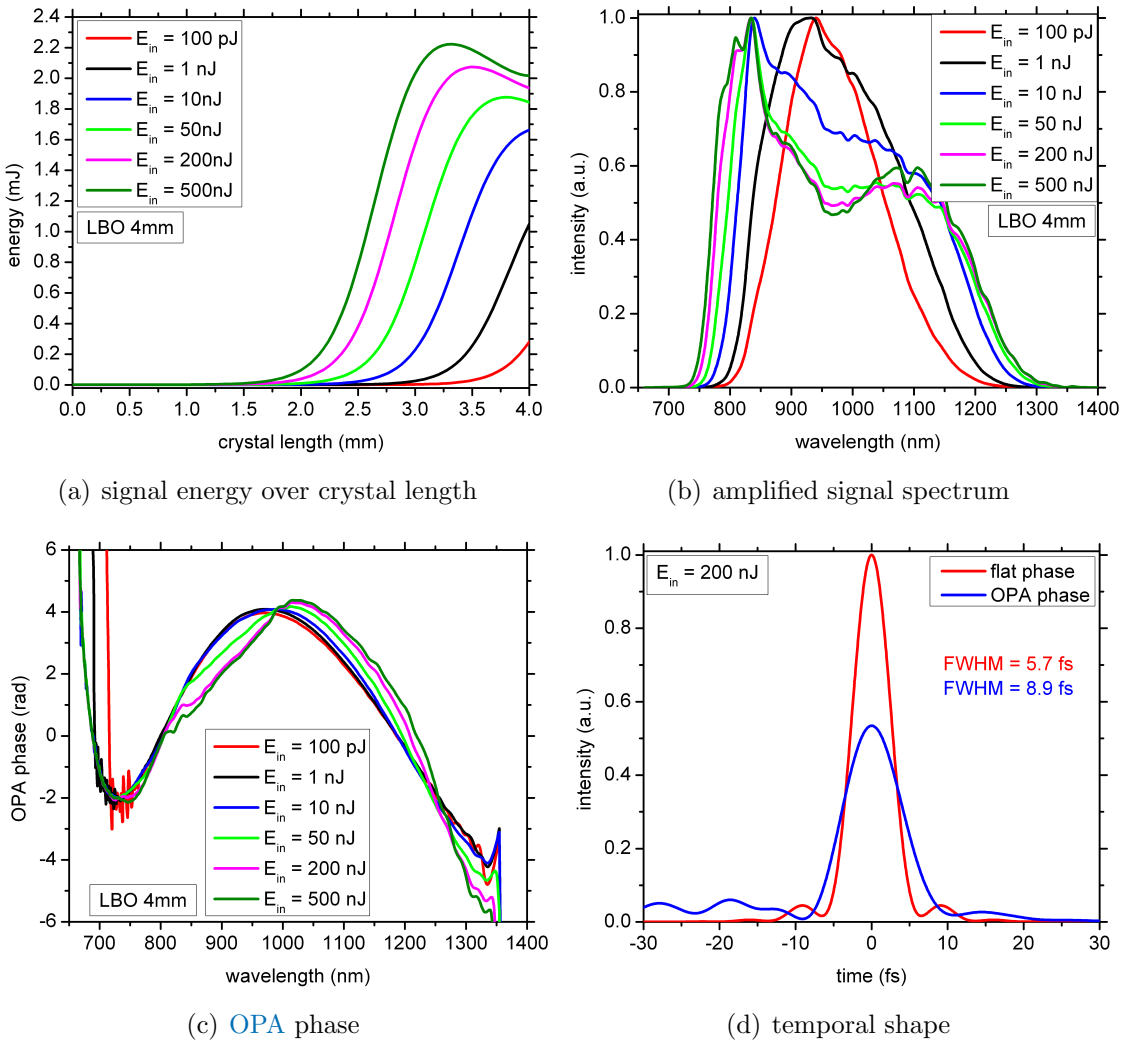

(a) signal energy over crystal length

(b) amplified signal spectrum

(c) OPA phase

(d) temporal shape

Figure 4.7: *Results of a simulation performed with Sisyfos investigating the amount of OPA phase due to amplification for different signal input energies, i.e. levels of back conversion. (a) depicts the evolution of the signal energy during the propagation through the nonlinear crystal. (b) presents the amplified signal spectra and (c) shows the spectral OPA phases for the different signal input energies. (d) depicts the effect of the OPA phase on the temporal shape of the compressed signal pulse for the 200 nJ case. The red curve corresponds to a full compression, i.e. flat spectral phase, whereas the blue curve demonstrates the influence of an uncompensated OPA phase. The pulse duration is increased by ∼ 56% and additional side pulses are generated leading to a decrease of the peak intensity by a factor of ∼ 2.*

4.4 Temporal contrast

As mentioned in the introduction, the PFS is aiming for HHG at solid targets. The temporal contrast of the amplified light pulses is of essential importance for the success of these experiments. Especially when working with focused intensities on the order of $10^{22}\,\frac{\mathrm{W}}{\mathrm{cm}^2}$ as the PFS is aiming for, an excellent temporal contrast is required so that the target is not affected by pre-pulses. This could happen at intensities greater than $10^{10}\,\frac{\mathrm{W}}{\mathrm{cm}^2}$, when multiphoton ionization becomes pronounced enough to turn a solid target into an expanding plasma. An intensity contrast of 12 orders of magnitude on a few-ps timescale would therefore exclude that possibility, but is extremely challenging to realize for any laser or light source.

The gain of an OPCPA strongly depends on the momentary pump intensity, consequently a pedestal and pre- or post-pulses which are located outside the temporal window of the pump are not amplified. Therefore, due to the amplification in an OPCPA stage the temporal contrast outside the pump time window is boosted by the gain. A proof-of-principle experiment demonstrating the increase of temporal contrast due to nonlinear amplification by picosecond pump pulses is presented in subsection 7.2.3. However, since the signal input energy is amplified from approx. $20\,\mu$J up to 3 J in PFS, the maximum gain-enhanced contrast enhancement is 10^5. Therefore, the remaining 7 orders of magnitude to reach 10^{12} have to be inherent to the seed pulse, which is ensured by an XPW stage in front of the OPCPA chain (cf. section 6.1).

In consequence, outside the pump window, OPCPA is very effective in improving the contrast, but this is not true inside, where not only all pre-pulses and pedestals see full gain, but also spontaneous superfluorescence might lead to a deterioration of the contrast on the sub-ps timescale. Fortunately, most of the hydrodynamic expansion of plasmas generated in the $10^{10} - 10^{15}\,\frac{\mathrm{W}}{\mathrm{cm}^2}$ regime takes place on longer timescales. Nevertheless, for the sake of completeness the influence of the superfluorescence is discussed in detail in appendix C.2.

4.5 Effects of n2: B-integral and self-phase modulation during amplification

As outlined before, in the PFS system the OPCPA stages are operated at an intensity of approx. 100 $\frac{\mathrm{GW}}{\mathrm{cm}^2}$. In this regime nonlinear propagation effects of the pump beam such as SPM and SF, which cause temporal and spatial modifications to the phase of the light pulses, cannot be neglected anymore. The "B-integral" is a common measure of the accumulated nonlinear phase due to propagation and is defined as [71]:

$$B = \frac{2\pi}{\lambda} \int_0^L n_2(z) I(z) dz, \tag{4.2}$$

where $n_2(z)$ is the nonlinear refractive index of the material, $I(z)$ the intensity of the light pulse along the propagation direction and L the propagation length. Depending on the initial beam quality the B-integral should be kept below < 3 in order to avoid nonlinear effects [71].

Table 4.2 presents the nonlinear refractive index n_2 for relevant materials at the fundamental and frequency-doubled PFS pump wavelengths. Owing to the lack of accurate information about the nonlinear refractive index in DKDP and LBO at a wavelength of 515 nm, the linear interpolation between published values at different wavelengths was employed. Based on these nonlinear refractive indices and Equation 4.2, the expected B-integrals for 1 m of air, 1 mm of fused silica, DKDP and LBO are summarized for an intensity of 100 $\frac{\mathrm{GW}}{\mathrm{cm}^2}$ in Table 4.3.

	515 nm	1030 nm	reference
air	$5.4 \cdot 10^{-19}\ \frac{\mathrm{cm}^2}{\mathrm{W}}$	$3.6 \cdot 10^{-19}\ \frac{\mathrm{cm}^2}{\mathrm{W}}$	[72]
fused silica	$3.0 \cdot 10^{-16}\ \frac{\mathrm{cm}^2}{\mathrm{W}}$	$2.7 \cdot 10^{-16}\ \frac{\mathrm{cm}^2}{\mathrm{W}}$	[73]
DKDP	$5.0 \cdot 10^{-16}\ \frac{\mathrm{cm}^2}{\mathrm{W}}$	$3.0 \cdot 10^{-16}\ \frac{\mathrm{cm}^2}{\mathrm{W}}$	[74, 75]
LBO	$4.8 \cdot 10^{-16}\ \frac{\mathrm{cm}^2}{\mathrm{W}}$	$2.0 \cdot 10^{-16}\ \frac{\mathrm{cm}^2}{\mathrm{W}}$	[76, 77]

Table 4.2: *Nonlinear refractive index n_2 for different materials and wavelengths. For the linear interpolation of n_2 at 515 nm the following values were used: for DKDP $n_2(335\,\mathrm{nm}) = 6 - 8 \cdot 10^{-16}\ \frac{\mathrm{cm}^2}{\mathrm{W}}$ and $n_2(1064\,\mathrm{nm}) = 3 \cdot 10^{-16}\ \frac{\mathrm{cm}^2}{\mathrm{W}}$ [74, 75], and for LBO $n_2(800\,\mathrm{nm}) = 3.4 \cdot 10^{-16}\ \frac{\mathrm{cm}^2}{\mathrm{W}}$ [77] and $n_2(1064\,\mathrm{nm}) = 2 \cdot 10^{-16}\ \frac{\mathrm{cm}^2}{\mathrm{W}}$ [76].*

	515 nm	1030 nm
air, 1 m	0.66	0.22
fused silica, 1 mm	0.37	0.17
DKDP, 1 mm	0.61	0.18
LBO, 1 mm	0.59	0.12

Table 4.3: *Estimated B-integral values for a pump beam with an intensity of* $100\,\frac{\mathrm{GW}}{\mathrm{cm}^2}$.

From this simple estimate, the following consequences can be drawn:

- The beam transport of the PFS pump laser can only be realized with reflecting optics since transmissive lense telescopes would cause B-integral contributions way above the limit of 3.
- Since the B-integral for 1 m propagation in air is comparable to 1 mm travel in optical materials, the beam transport of the pump laser to the OPCPA stages has to be realized in vacuum.
- DKDP crystal lengths of $2-4$ mm, as designed for the final PFS OPCPA stages results in a total B-integral of $1.2 - 2.4$ and therefore the nonlinear crystal introduces a significant amount of nonlinear phase shift of the pump. Note that this number only holds for the pump laser, and is dramatically lower for the seed due to its lower intensity and longer wavelength. However, the influence of the nonlinear propagation of the pump on the parametric amplification cannot be neglected and therefore was studied with Sisyfos simulations performed in collaboration with the group of Prof. J. Biegert at the ICFO-Institut de Ciències Fotòniques, Castelldefels, Spain. The results are discussed below.

Influence of the nonlinear refractive index on the OPCPA process: In order to estimate the effect of n_2 on the amplification process, a study with the Sisyfos code was performed. The simulations and results are published in [78]. An electronic reprint is attached in appendix G.2 with the permission of OSA.

The study was based on amplification in four consecutive DKDP stages which represent the last amplifiers for the PFS system (cf. chapter 6). The nonlinear refractive indices used for the simulations were $n_2 = 3 \times 10^{-16} \frac{\mathrm{cm}^2}{\mathrm{W}}$ for the signal and $n_2 = 5 \times 10^{-16} \frac{\mathrm{cm}^2}{\mathrm{W}}$ for the pump beam [78]. In summary the following conclusions can be drawn from this investigation:

- **pulse energy:** In the case of $n_2 = 0$ an output energy of 3.7 J is obtained, whereas in the case of $n_2 \neq 0$ the signal output energy is reduced to 3.29 J which corresponds to an decrease of 11.2%. While the exact percentage depends on the n_2 value chosen, the result clearly shows n_2 effects should be considered when designing OPCPA systems since the OPCPA interaction is sensitive to the nonlinear refractive index.

- **near and far field:** The near-field spatial profiles show little change due to n_2 effects, with the dominant feature being a narrowing in the plane of the non-collinear interaction due to the phase-front tilt between the pump, signal and idler. Figure 4.8(a) depicts the near-field spatial profile in the case of $n_2 \neq 0$. However, the far-field images are significantly different and the spatial phase induced by the n_2 effects reduces the peak of the far field by 30% when n_2 effects are included, as shown in Figure 4.8(b) and (c).

- **bandwidth and pulse duration:** The amplified signal spectra are presented in Figure 4.8(d). The amplified spectrum in the case of $n_2 = 0$ (blue curve) supports a Fourier-limited pulse duration of 4 fs. However, the simulations with n_2 effects show a narrowing of the spectral bandwidth of 129 nm compared to the results without n_2 effects at FWHM level (the peak at 700 nm is not taken into account). The Fourier-transform limit of this output signal spectrum (dashed red curve) is 4.7 fs, which corresponding to a 17.5% increase in the pulse duration.

Consequently, effects based on the nonlinear refractive index, occurring due to high pump intensities, reduce the performance of the OPCPA system.

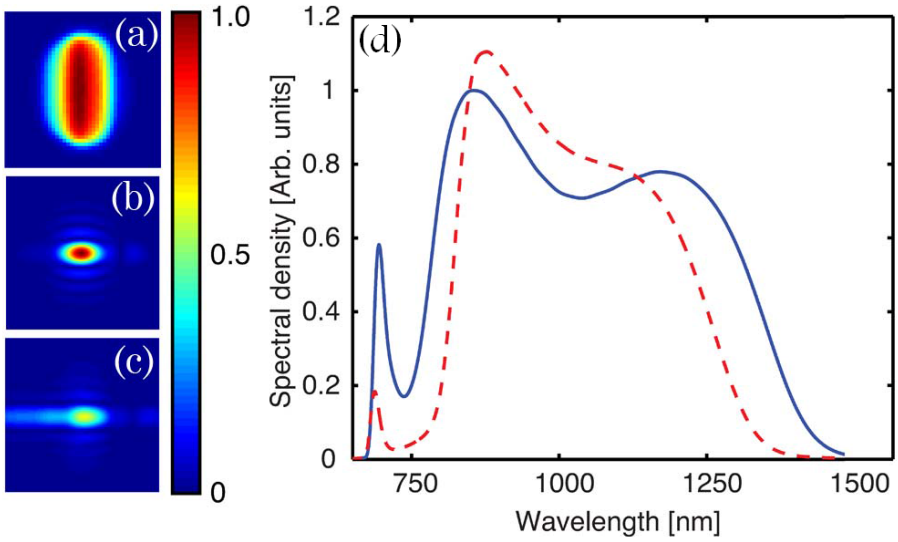

Figure 4.8: *Left, (a) near field of the output for $n_2 \neq 0$, (b) far field with $n_2 = 0$, and (c) far field with n_2 effects, showing a 30% decrease in peak intensity. Right, (d) comparison of the output spectra for the case without n_2 (solid curve) and with n_2 (dashed curve). A narrowing of the spectral bandwidth by 129 nm is observed at a FWHM level (peak at 700 nm is not taken into account). With n_2, the bandwidth of the output spectrum (normalized to the $n_2 = 0$ spectrum) represents a Fourier transform limit of 4.7 fs, corresponding to a 17.5% increase in the pulse duration. This picture is published in slightly modified form in [78] and used with permission from OSA.*

4.6 Heat load in OPA crystals

In an OPA the energy used for the amplification of the signal beam is directly delivered by the pump beam. No intermediate storage of the energy inside the crystal occurs. Consequently, only linear absorption during propagation through the crystal is responsible for heating. The rise of the crystal temperature leads to a change of the refractive index and consequently also to a change of the phase-matching conditions. Owing to the repetition rate of 10 Hz of the PFS the heat load is strongly reduced compared to kHz-OPCPA systems. An estimation presented in appendix C.3 shows that no detrimental effects due to crystal heating have to be expected for the OPCPA stages of the PFS.

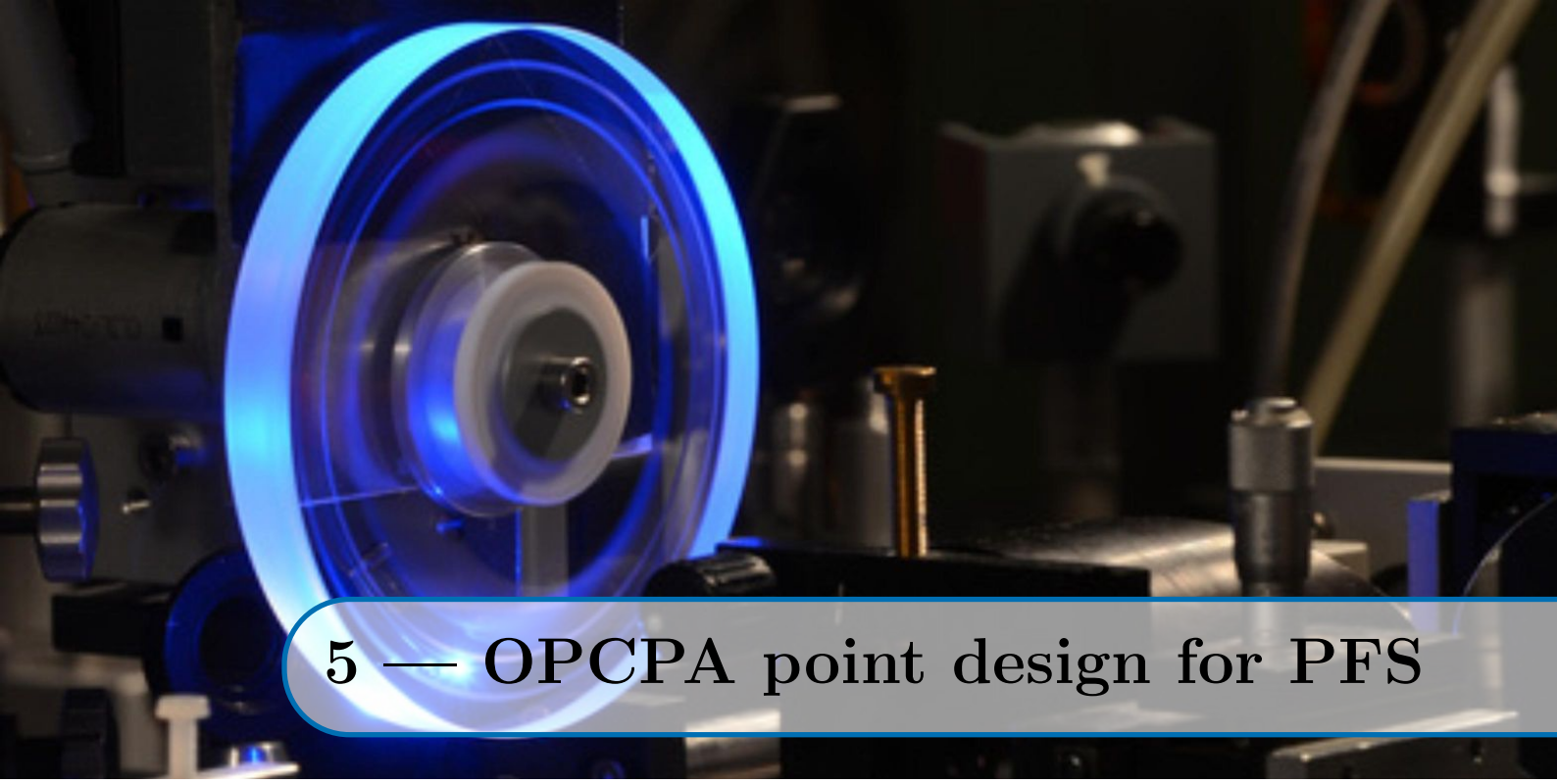

5 — OPCPA point design for PFS

As part of the team's effort to verify the basic PFS concept, in this thesis a numerical design study of the OPCPA amplifier chain was performed in order to prove that with high intensity, short picosecond pump pulses the desired PFS parameters of 5 fs pulse duration with $3-5$ J of pulse energy can be realized. A pump-laser system as originally conceived, consisting of four frequency doubled laser beams with 5 J of pulse energy each and a compressed pulse duration of 1.2 ps (as determined in the experiments cf. section 7.2) was taken as a basis for the design study. During the course of this work, it became clear that this energy level may not be reached within the allocated budget. However, due to the modular concept of the OPCPA amplifier, the results of this study still hold if the last stages are omitted.

Since in contrast to Sisyfos, the SOPAS code is able to simulate multiple OPCPA stages in a single run, it was used for the design study of the multiple-stage amplifier chain. The first design for PFS, as outlined in the proposal and slightly updated here, consisted of eight OPCPA stages based on DKDP and pumped by 4 x 5 J green laser pulses. In the course of this work in an effort to reduce the complexity of the PFS system, a second design study using LBO as the alternative crystal for the first stages before the beam becomes too large for the available crystal sizes was performed. It therefore employs just two LBO and three consecutive DKDP stages while maintaining the output energy and amplified bandwidth.

5.1 First design: all DKDP

As outlined before, PFS has to rely on DKDP despite its obvious drawbacks in its final amplification stages due to the insufficient size of other crystalline materials. Consequently, the most straightforward ansatz is based also on DKDP for the earlier stages. The overall first design study based on a simple 1D code performed by Prof. Dr. Stefan Karsch is published in [2]. A more detailed design study based on the pseudo-3D SOPAS code is presented in [7] and an electronic reprint is attached in appendix G.1 with the permission of OSA.

In this chapter, a modified version of the aforementioned design study with SOPAS is presented. Here, a pump beam with a 10th-order super-Gaussian geometry in space was used since in the final PFS system flat-top pump beams are expected (in [7], Gaussian beam profiles had been used). Furthermore, compared to the design presented in [7], in this study the OPCPA stages were operated in a less saturated regime, leading to a higher output energy at the expense of a smaller amplified bandwidth. Nevertheless, the crystal thickness was chosen such that with the given pump energy a broad amplified bandwidth supporting sub-two-optical cycle pulses was guaranteed. The first five stages share one pump beam, whereas stages $6-8$ were pumped by one 5 J beam each. The pulse durations of the pump and signal pulses were taken to be 1.2 ps and 1 ps FWHM, respectively. The pump peak intensity for each stage was fixed to 100 $\frac{\mathrm{GW}}{\mathrm{cm}^2}$. The non-collinear type-I geometry was applied with a phase-matching angle of 37.08° and an internal non-collinear angle of 0.92°. The simulations were performed using an experimentally measured signal spectrum.

Table 5.1 presents the parameters of the eight amplifier stages. In addition, the output energies and extraction efficiencies of the eight stages are shown. The signal spectrum and the resulting amplified spectra after each stage are presented in Figure 5.1. In a series of eight amplification stages the signal pulses reached a pulse energy of 3.4 J. The calculated Fourier-limited pulse duration supported by the spectrum after the eighth stage was 5.7 fs. Hence, the desired aims of the PFS are not fulfilled in terms of pulse durations.

OPCPA stage	1	2	3	4	5	6	7	8
pump energy	2 mJ	20 mJ	200 mJ	1 J	3.5 J	5 J	5 J	5 J
pump diameter FWHM	1.4 mm	4.4 mm	14 mm	32 mm	58 mm	70 mm	70 mm	70 mm
crystal length (DKDP)	8 mm	6.0 mm	5 mm	4.3 mm	4.1 mm	2.9 mm	2.1 mm	1.8 mm
output signal energy	0.2 mJ	2.9 mJ	30.5 mJ	175 mJ	691 mJ	1.55 J	2.48 J	3.43 J
extraction efficiency	9.7%	13.4%	13.8%	14.5%	14.7%	17.3%	18.5%	18.9%

Table 5.1: *Parameters used for the simulations of the system design study using DKDP in all stages. The extraction efficiency is defined as* $\frac{E_{out,signal}-E_{in,signal}}{E_{pump}}$.

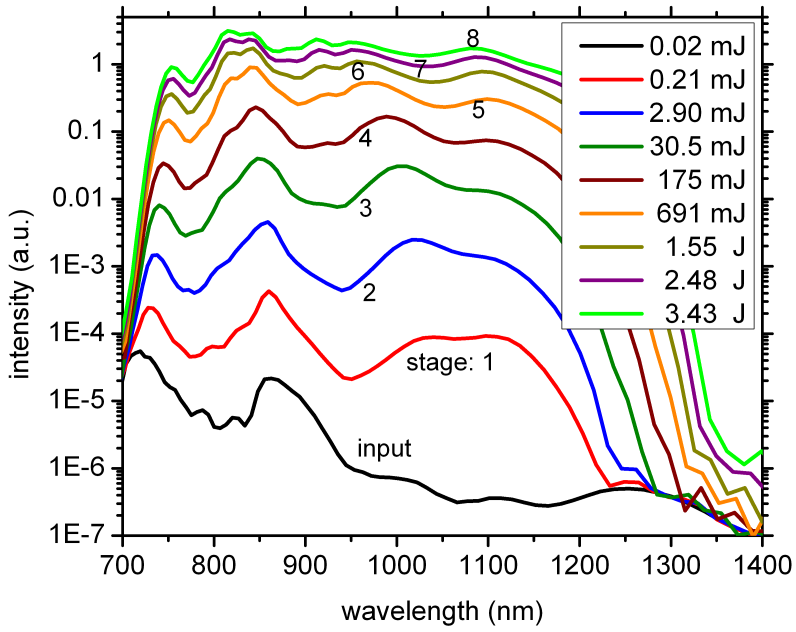

Figure 5.1: *Results of the purely DKDP-based OPCPA design study: Calculated amplified spectra for different OPCPA stages.*

5.2 Optimized PFS design

The first design study presented in section 5.1 consisted of eight OPCPA stages using DKDP as the OPCPA crystal. In order to reduce the complexity of the final PFS system, it is desirable to reduce the number of amplification stages. This reduction is only realizable when different nonlinear crystals with higher nonlinearity than DKDP are chosen. Owing to the high pump energy leading to large necessary apertures of the crystals in the last stages, a change of crystal material can only be realized in the first OPCPA stages where the demand on the crystal aperture is not as high. In section 4.2 different crystal materials have been compared in relation to DKDP. Since LBO is the most promising alternative, the second design was based on a hybrid solution consisting of LBO and DKDP stages. Recently, LBO crystals with an aperture of up to 65 mm have become available with promising results for further increase [79], which would permit the application of a pump energy of approx. 3.5 J. This is defined by the safety limit for the pump intensity of 100 $\frac{\mathrm{GW}}{\mathrm{cm}^2}$. Future crystal diameters up to $90-100$ mm would allow the use of the total available pump energy of 5 J for a flat-top pump beam. Table 5.2 presents the beam parameters for the hybrid design. These simulations were performed with the same parameters as the previous design study except the number of stages, pump energy and beam sizes. For LBO a phase-matching angle of 14.45° and an internal non-collinear angle of 1.1° was used. Owing to the higher nonlinear coefficient ($d_{eff,LBO} = 0.83\,\frac{\mathrm{pm}}{\mathrm{V}}$ compared to $d_{eff,DKDP} = 0.22\,\frac{\mathrm{pm}}{\mathrm{V}}$), two LBO stages now replace five stages of DKDP with a shared pump energy of ~ 3.5 J bringing down the system from 8 to 5 stages.

Figure 5.2 presents the amplified spectra for the different stages on a logarithmic scale. The obtained signal bandwidth is broader compared to the previous design. The total resulting signal energy is 3.59 J and the Fourier-limited pulse duration is 4.9 fs after the last OPCPA stage, corresponding to less than two optical cycles now fulfilling the design goals. The efficiency for the five OPCPA stages is presented in Table 5.2. An overall pump-to-signal conversion efficiency of $\sim 20\%$ can be expected.

OPCPA stage	1	2	3	4	5
pump energy	20 mJ	3.5 J	5 J	5 J	5 J
pump diameter FWHM	4 mm	55 mm	70 mm	70 mm	70 mm
crystal length	2.7 mm (LBO)	2.2 mm (LBO)	3.3 mm (DKDP)	2.3 mm (DKDP)	1.8 mm (DKDP)
output signal energy	4.35 mJ	663 mJ	1.53 J	2.53 J	3.59 J
extraction efficiency	21.7%	18.8%	17.3%	20.0%	21.3%

Table 5.2: *Parameters used for the simulations of the system design study with a combination of LBO and DKDP crystals. The extraction efficiency is defined as* $\frac{E_{out,signal}-E_{in,signal}}{E_{pump}}$.

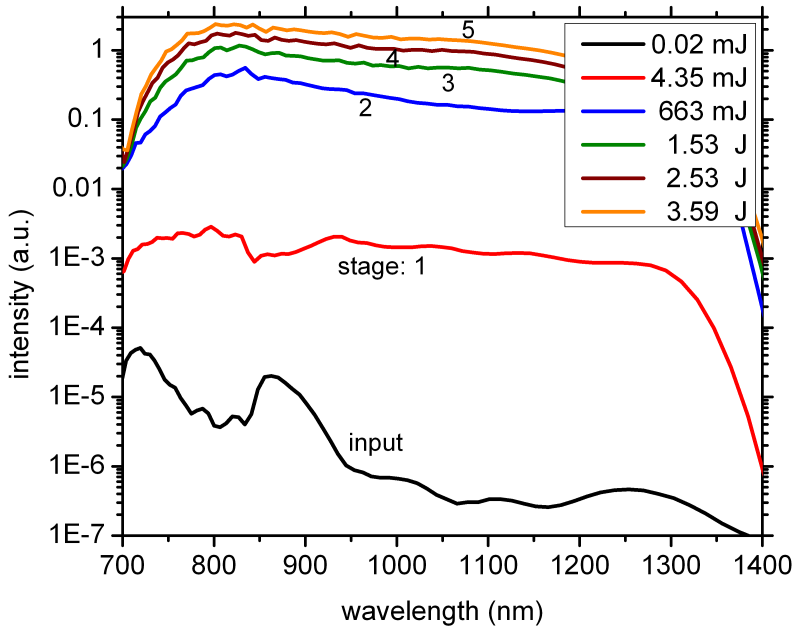

Figure 5.2: *Results of the OPCPA system design study: Calculated amplified spectra for different OPCPA stages of PFS.*

5.2.1 Dispersion management of the broadband signal

Since the amplification of the broadband signal of the PFS is based on the OPCPA technique, beside the optimization of the OPA, attention has to be paid to the stretching and compression (CPA) of the broadband signal pulses. In order to reach high peak intensities of the compressed pulses, the stretcher and compressor setup have to be matched to obtain a full pulse compression and consequently the shortest possible pulse duration. Here, the dispersion management for the optimized OPCPA design consisting of five stages (cf. section 5.2) is described.

The original design relied on a negatively chirped signal pulses since in this regime compression can be performed with bulk glass, which is available at large enough apertures that are required for the expected high pulse energies [1, 2]. Therefore, stretching was planned to be realized with a fused silica prism stretcher and for the compressor CaF_2 was chosen since it provides positive GDD over the full spectral range. The compression in the bulk material was planned to be incomplete in order to avoid SPM or SF and final compression was envisaged with chirped mirrors. This basic scheme is presented in Figure 5.3(a).

The amount and control of dispersion by chirped mirrors, has been vastly improved during the last years [80,81] leading to the possibility of pulse compression from the few-ps-range towards few-cycle durations based on chirped mirrors only [82]. With an all-chirped-mirror compressor it is feasible to perform the pulse stretching with material leading to a much simpler stretcher setup compared to a prism stretcher. Furthermore, simulations presented in section 4.2 showed that in saturated OPCPAs the spectral phase of the stretched broadband signal strongly influences the spectral shape of the amplified signal. Consequently, not only the total amount of dispersion introduced by stretcher and compressor has to be controlled, but also the spectral phase of the signal beam in the OPCPA stages. These considerations lead to a new dispersion scheme for the PFS system as schematically shown in Figure 5.3(b). The broadband signal pulses are stretched by 10 m of air and 25 mm of CaF_2 resulting in a GD depicted as red curve in Figure 5.3(c). Chirped mirrors (**TOD**) in front of the OPCPA stages (blue curve in Figure 5.3(c)) compensate the higher orders of the stretcher in order to obtain a linear group delay in the frequency domain (black curve) leading to an enhanced amplification of the infrared spectral part compared to the case without counterbalancing the higher orders (cf. section 4.2). After amplification in two LBO stages additional chirped mirrors (**LBO 1-2**) compensate the dispersion introduced by the crystals and the amplification, i.e. OPA phase, again leading to a linear group delay in the frequency domain as shown in Figure 5.3(d). The dispersion and OPA phase introduced by the third stage is compen-

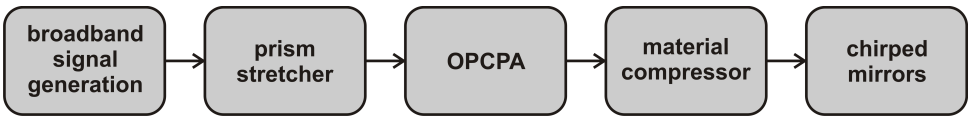

(a) original dispersion scheme

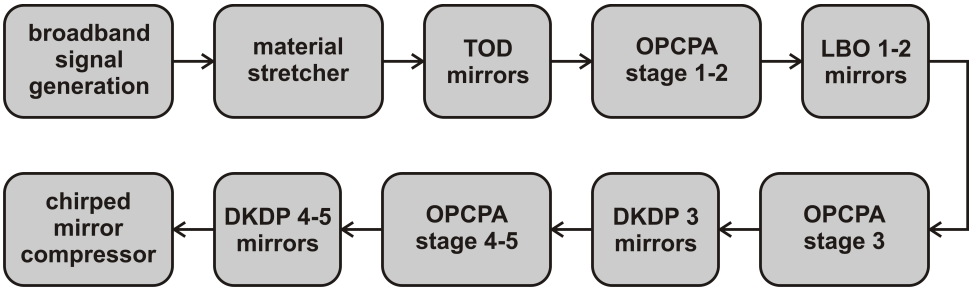

(b) improved dispersion scheme

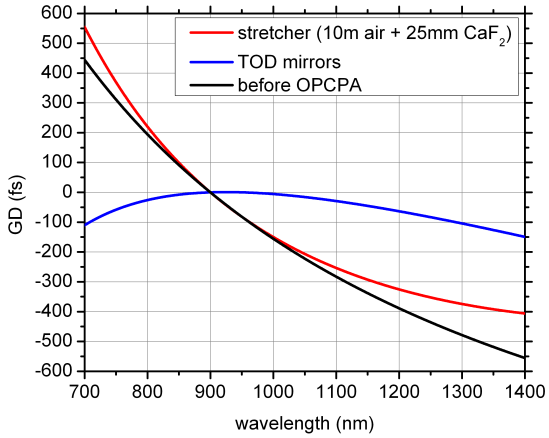

(c) GD before OPCPA stages

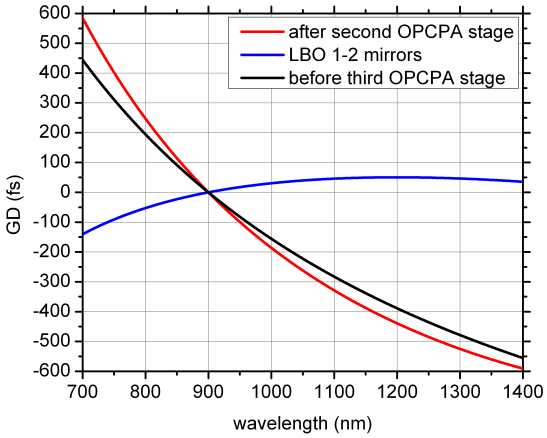

(d) GD after second stage

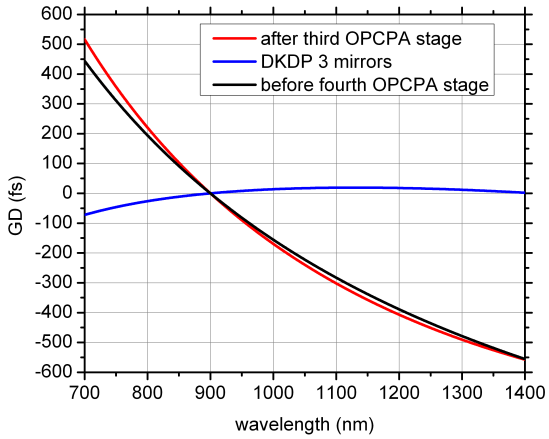

(e) GD after third stage

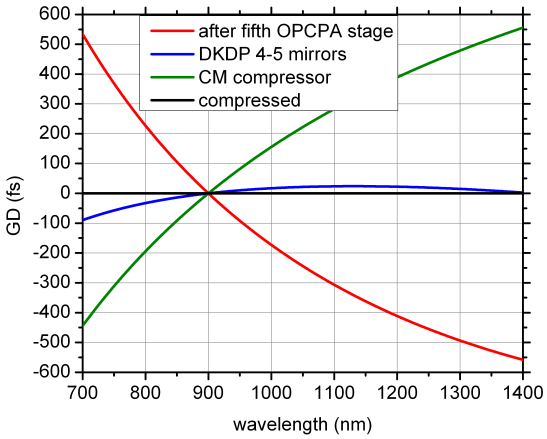

(f) GD after OPCPA chain

Figure 5.3: *Dispersion schemes for the broadband signal of the PFS system. (a) depicts the originally planned dispersion layout. (b) displays the dispersion management based on an all chirped mirror compressor. (c)-(f) show the group delays and target designs for the chirped mirrors for the dispersion scheme presented in (b) at different locations of the OPCPA chain.*

sated by chirped mirrors (**DKDP 3**) before the fourth stage (cf. Figure 5.3(e)). The compensation of the dispersion introduced by the fourth and fifth stage is combined (**DKDP 4-5**, blue curve in Figure 5.3(f)) since the dispersion of one crystal is too small to be counterbalance by one pair of double-angle chirped mirrors. The residual linear group delay is compensated by a chirped mirror compressor shown as the green curve in Figure 5.3(f). The main advantage of chirped mirrors just counterbalancing the individual OPCPA stages is the high flexibility since independent from the current status of the system the **TOD** and compressor mirrors are kept unchanged.

5.3 Conclusion

The design studies show that the desired pulse duration of sub-two cycles for the compressed signal pulse is realizable via a picosecond pumped OPCPA system as it will be implemented in the PFS system. Unfortunately the original goal of 5 J of pulse energy presented in [1, 2] does seem too ambitious in hindsight. However, output energies of > 3 J are predicted by both design studies. It has to be mentioned that in these design studies no n_2 effects were included. The investigation of the influence of the nonlinear refractive index on the OPCPA process, described in section 4.5, identified that a decrease of the pulse energy and an increased Fourier-limited signal pulse duration has to be expected in the real scenario. However, even these simulations showed that with the n_2 effects considered, a signal spectrum supporting the desired pulse duration of less than two optical cycles and a signal-pulse energy in the few-Joule range can be obtained. Therefore, in conclusion all studies show that the concept of the PFS system [1, 2] is a promising route towards few-cycle pulses with ultra high peak intensities.

Part II

PFS system and experiments

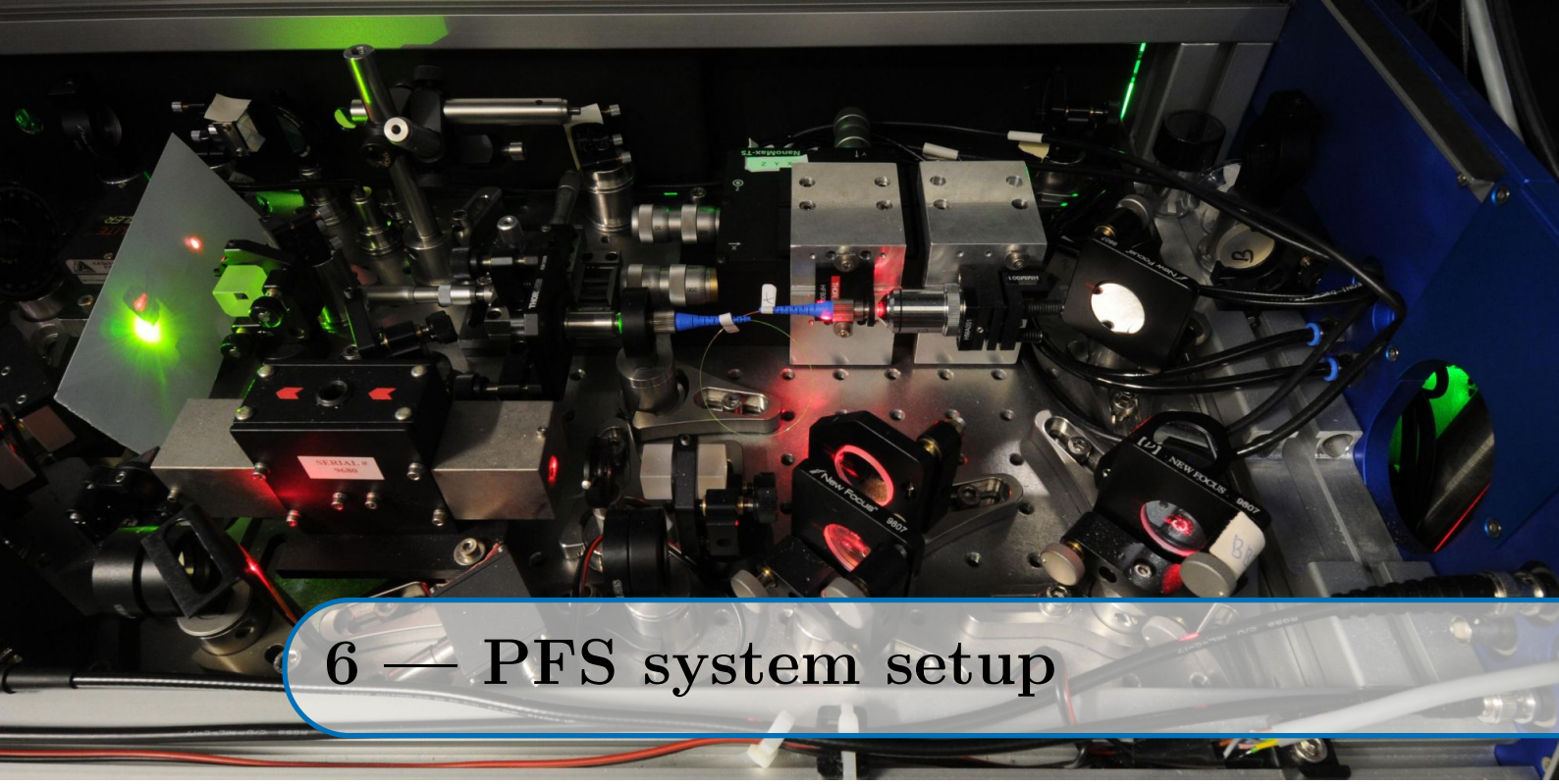

6 — PFS system setup

In preparation for the experimental results, this chapter gives an overview of the PFS system. The detailed setup of each different OPCPA campaign is presented separately in Appendix D since it was adapted several times to fit the changing requirements.

The initial projected configuration of the PFS system is presented in Figure 6.1, which is a combination of the layouts presented in [37] and [38]. This is done to best convey the basic novel design principles of PFS, although changes to this initial design have been and will be made during the construction phase. The system can be divided into three major parts:

- The **frontend system** delivers the seed pulses for both the Yb:YAG pump-laser chain and the broadband OPCPA chain. Both pulses are produced by a common titanium-sapphire, $Ti : Al_2O_3$ (Ti:Sa) master oscillator in order to provide optical synchronization.

- The **Yb:YAG pump laser** is intended to produce four picosecond laser beams with an energy of 5 J each at 515 nm, which pump the OPCPA stages. The pump-laser chain itself is a fully diode-pumped CPA system with a targeted repetition rate of 10 Hz.

- **OPCPA system:** The broadband seed pulses generated by the frontend are stretched and afterwards amplified to the J-level in multiple non-collinear OPCPA stages based on LBO and DKDP. After the OPCPA stages the amplified pulses are compressed to the few-cycle regime.

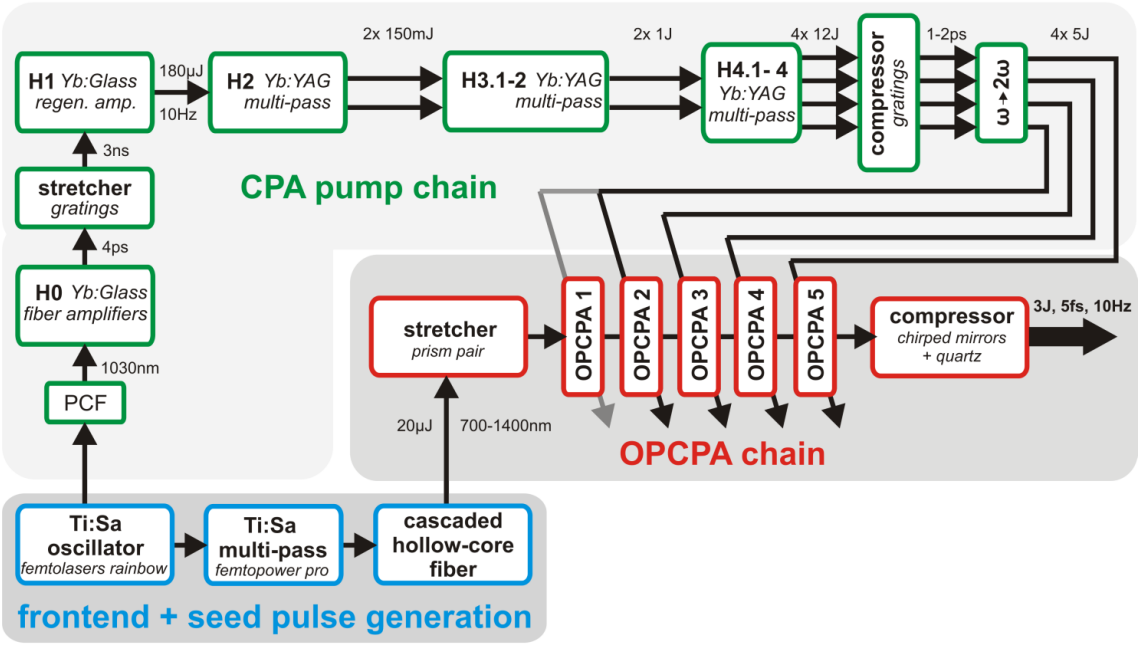

Figure 6.1: *Projected layout of the PFS system. This scheme is a combination of the layouts presented in [37] and [38] and used with permission from the original authors.*

6.1 Frontend system

The frontend provides two optically synchronized seed pulses for the OPCPA and pump-laser chains. A sketch of the setup is depicted in Figure 6.2. Both seed pulses originate from the same master oscillator (Femtolasers Rainbow, 250 mW, $620 - 950$ nm, < 7 fs, 70 MHz) by selecting two different pulses from the same oscillator train in order to minimize the temporal jitter between both pulses. Different pulses are selected in order to pre-compensate for the much longer optical path in the pump laser as compared to broadband seed generation setup. The seed pulse for the pump is soliton self-frequency-shifted [83–85] to the central wavelength of the amplification band of Yb:YAG in a photonic crystal fiber (PCF) in order to optimize the seed energy in the Yb:YAG spectral range (1030 nm) [86]. For the OPCPA seed generation, the remaining beam is stretched with material and chirped mirrors to a pulse duration of 10 ps for further amplification. Spectral and phase shaping is performed in a Dazzler (Fastlite). The pulses are amplified to 2 mJ in a 10-pass "FEMTOPOWER compact PRO" Ti:Sa amplifier. After the 6^{th} pass the repetition rate is reduced from 70 MHz to 1 kHz by a pockels cell. For compression, a hybrid prism/chirped mirror scheme is used in order to mitigate the effects of SPM in the last prism that often plague pure prism compressors. Therefore, a double prism

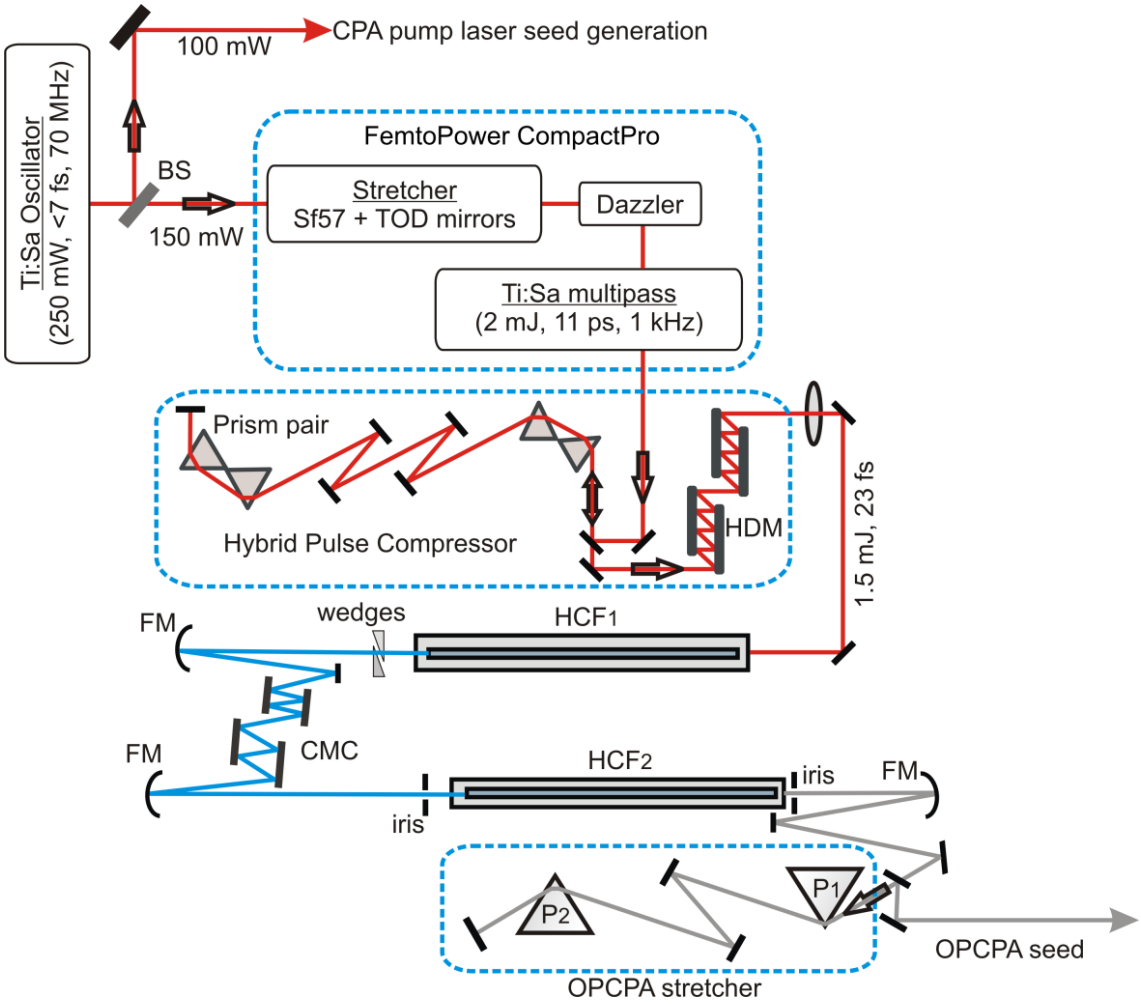

Figure 6.2: *Schematic sketch of the frontend system. The description is given within the text. This picture is a modified version of the layout presented in [37] and used with permission from the original author.*

pair precompresses the laser pulses, whereas the final pulse shortening is performed with chirped mirrors (**HDM**).The resulting pulses have an energy of 1.5 mJ, and a duration of 23 fs at a repetition rate of 1 kHz. Gain narrowing in the Ti:Sa amplifier leads to a final bandwidth of 60 nm FWHM centered at ~ 800 nm.

Since the specifications for PFS call for sub-two-cycle pulses, the Femtopower output pulses have to be aggressively broadened spectrally. This operation is performed by SPM in two cascaded hollow-core-fiber compressors. The first hollow-core fiber, (**HCF1**, 300 μm core diameter) filled with neon at a pressure of 2.3 bar, broadens the spectrum to $500 - 1000$ nm. The broadened pulses are compressed with a double-angle chirped-mirror compressor (**CMC**) [82] to approximately 5 fs. In order to reach the desired OPCPA wavelength range of $700 - 1400$ nm, a second hollow-core fiber (**HCF2**) is implemented for further broadening into the infrared region. It is

filled with 3.3 bar of neon and has a core diameter of 250 μm. The output spectrum after the second HCF spans from $300 - 1400$ nm containing $\sim 30\,\mu$J of pulse energy within the relevant range of $700 - 1400$ nm.

In order to match the pump-pulse duration ($\sim$ 1 ps) at the OPCPA stages, the broadband signal pulses are stretched in a prism stretcher (cf. section 6.3). The spectrum is cut below $\sim$ 680 nm by the second prism leading to a seed spectrum for the OPCPA as depicted in Figure 6.3. This spectrum supports a Fourier-limited pulse duration of 4.7 fs.

More detailed information about the frontend system can be found in Izhar Ahmand's PhD thesis [37] and in Ref. [87].

6.1.1 Spectral cleaning of the broadband signal pulses

Owing to its creation in an SPM process, the signal spectrum features strong intensity modulations in the wavelength range of $700 - 1000$ nm (cf. Figure 6.3) resulting in a degradation of the temporal contrast on a time scale of a few hundreds of femtoseconds. Simulations and experimental data, described in subsection 7.2.1, show that these intensity variations are not smoothed out by saturation as first expected, but enhanced by the amplification in the OPCPA stages. Consequently, it is necessary to generate a broadband seed pulse with a smooth spectral shape before the optical parametric amplification. Two different approaches improving the signal

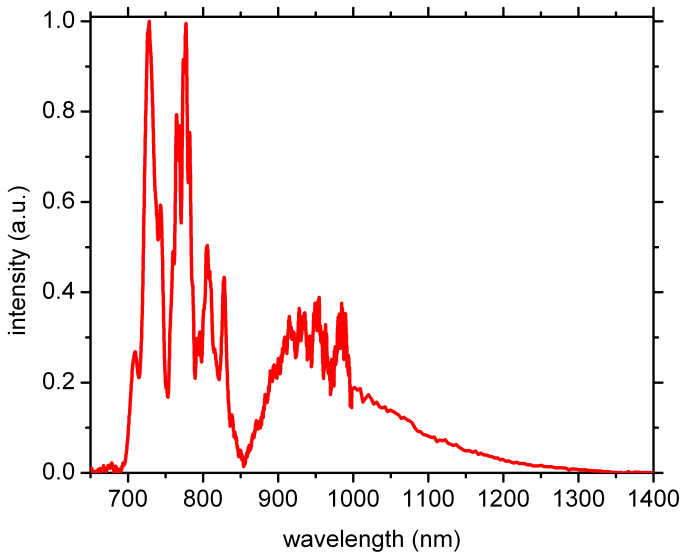

Figure 6.3: *Spectrum of the broadband signal pulse after the prism stretcher generated in two cascaded HCF's. The spectrum is cut at* $\sim$ 680 nm *by the second prism of the stretcher and exhibits a pulse energy of* 20 μJ.

spectrum are currently being developed by Alexander Kessel as part of his PhD thesis with the help of Sergei Trushin, Andreas Münzer and Alexander Kastner. Therefore, only a brief overview is given here.

- **Pulse cleaning by XPW:** This pulse-cleaning technique is based on cross polarized wave generation (XPW), a four-wave-mixing process, in which a new pulse is generated in the same spectral region as the input beam ($\omega = \omega+\omega-\omega$) [88] but with orthogonal polarization. The separation of the newly generated pulse from the input pulse can be done by using a crossed polarizer setup. The efficiency of this process is proportional to I^3 for the small signal case and therefore perfectly suited for pulse cleaning of compressed pulses as it has been demonstrated already in many laboratories, see e.g. [89–91]. Strong spectral intensity modulations of a compressed pulse lead to temporal wings and pre- and post-pulses in time with much weaker peak intensity than the main pulse. Consequently, the pedestal and side-pulses experience much less conversion than the main pulse due to the strong intensity dependence of the nonlinear process. This temporal clipping and the resulting fast rising and falling edges translate to much less modulations in frequency space. Therefore, the pulse is cleaned in the temporal as well as in the spectral domain.

  The schematic layout of the XPW setup of the PFS is presented in Figure 6.4(a). After the generation of the broadband signal in the two cascaded HCFs, the pulse is compressed with chirped mirrors and quartz wedges. The XPW process takes place in a 2 mm thick BaF_2 crystal. The cross-polarized beam is separated from the input beam by a polarizer. The obtained smooth signal spectrum is plotted in Figure 6.4(b). Owing to the limited efficiency of

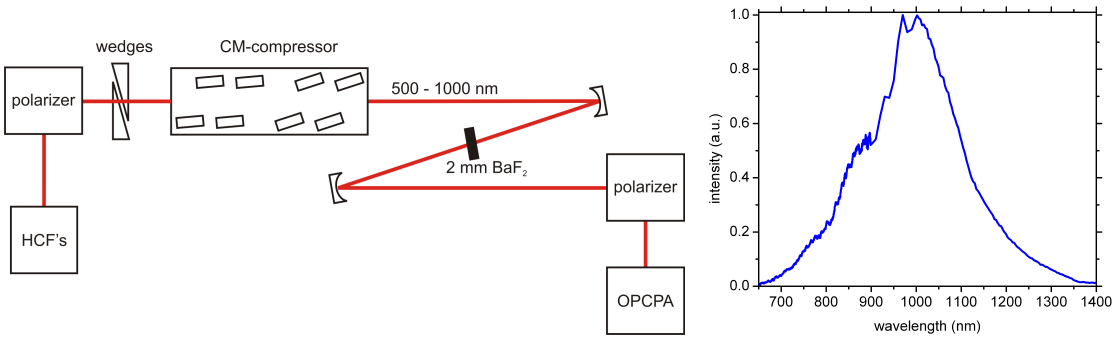

(a) schematic XPW layout (b) smoothed XPW spectrum

Figure 6.4: *Broadband signal-pulse cleaning by XPW in BaF_2: (a) The schematic layout of the XPW setup implemented in the PFS system; (b) The smoother output spectrum. All spectral intensity modulations are removed (cf. Figure 6.3).*

the XPW process, the available seed energy for the OPCPA stages dropped from $\sim 20\,\mu$J without pulse cleaning to $\sim 0.3\,\mu$J with XPW. Further results and more detailed information are given in [92].

- **non-collinear idler generation:** An alternative approach to the aforementioned signal generation in two HCFs followed by pulse cleaning in an XPW stage, is the generation of a background free, broadband idler in a non-collinear OPA. Owing to the non-collinear geometry, required to support the desired broad bandwidth, the idler pulse is generated with an angular dispersion which can be compensated by a combined telescope-grating setup [93]. In the case of the PFS, the compressed pulses of the Femtopower (800 nm, 2 mJ, 25 fs) are used to generate synchronized pump (400 nm) and broadband seed pulses for the DFG stage from one single laser pulse. The spectral broadening of the seed pulses is performed in a single HCF ($500 - 1000$ nm). The resulting idler generated by non-collinear DFG in a $200\,\mu$m thin BBO crystal provides the desired wavelength range of $700 - 1400$ nm. The main difference compared to the generation of a broadband seed in two HCFs is that the pulse broadening relies on one HCF only and consequently the intensity and phase modulations due to SPM are less pronounced. The DFG process then shifts the broadened visible spectrum into the required infrared spectral region and therefore pulses with a much smoother spectrum are obtained to seed the OPCPA stages.

  First experiments already demonstrated promising results [94]. An improved setup is currently under development [95]. Pulse energies of up to $3\,\mu$J have been obtained. Higher pulse energies can be expected in future experiments by reducing the losses in the beam transport from the Femtopower to the idler generation setup resulting in higher pump energies. Despite the angular dispersion compensation setup a residual angular chirp of ~ 1 mrad in the wavelength range of $700 - 1150$ nm is present, but this may be largely compensated in the future by adding a wedge of suitable material and apex angle.

Both approaches show the ability to generate a signal beam with a smooth spectrum in the desired wavelength range of $700 - 1400$ nm. The idler-generation approach is more favorable in terms of output energy, but still suffers from a residual angular chirp and more residual spectral modulations. At the time of the last OPCPA experiments (cf. section 7.3) the XPW setup was further developed than the idler-generation scheme and consequently the OPCPA experiments were preformed using pulses from the XPW output as a seed.

6.2 Pump-laser system

The pump laser of the PFS is a fully diode-pumped CPA system based on Yb:YAG. It is intended to deliver 1 ps, high-energy pump pulses (4 x 12 J in the fundamental beams) for the OPCPA chain at a repetition rate of 10 Hz.

- **CPA:** The desired short pulse duration combined with the desired high pulse energy can only be realized with a CPA [32, 33] based laser system since for non-CPA systems the peak intensity is limited due to nonlinear propagation effects. Therefore, pump-laser systems which are not based on CPA, allow on the one hand ultra high pulse energies of hundreds of Joules at pulse durations on the order of nanoseconds [44, 70] or on the other hand pulse energies of a few Joules with pulse durations on the order of 80 ps however the realization of high energies and short pulse durations at the same time is not possible for these systems. Consequently, the PFS pump laser is based on the CPA principle.

- **Diode pumping:** The high pulse energy combined with the repetition rate of 10 Hz requests a high wall-plug efficiency and a minimized thermal load of the laser crystal. Owing to the smaller bandwidth of diodes compared to flash lamps the absorption bands of the active medium can be better matched with diodes. This allows an efficient usage of the pump radiation for the amplification leading to an increased wall-plug efficiency and to a reduced loss of pump energy to heat. Consequently, the PFS pump laser is based on diode pumping.

- **Laser material:** A laser medium with good thermal properties allowing high efficiencies is favorable for the amplification of laser pulses to high pulse energies at a repetition rate of 10 Hz. Ti:Sa systems which are based on optical pumping by a frequency doubled, flash lamp pumped neodymium-doped yttrium aluminum garnet, $Nd^{3+} : Y_3Al_5O_{12}$ (Nd:YAG) laser are not suited for pumping the OPCPA chain of the PFS due to their low wall-plug efficiency of only 0.1%. In contrast, laser materials such as Yb:YAG and Nd:YAG can be pumped directly by diodes leading to high efficiencies. Since Yb:YAG exhibits a larger amplification bandwidth compared to Nd:YAG, pulse durations of only 1 ps are realizable compared to > 10 ps in the case of Nd:YAG. Furthermore, the good thermal properties of Yb:YAG allow repetition rates of 10 Hz. Consequently, the PFS pump laser is based on Yb:YAG as laser material.

A schematic layout of the currently installed parts of the pump-laser system is depicted in Figure 6.5 [38]. The seed pulses generated by the frontend are preamplified

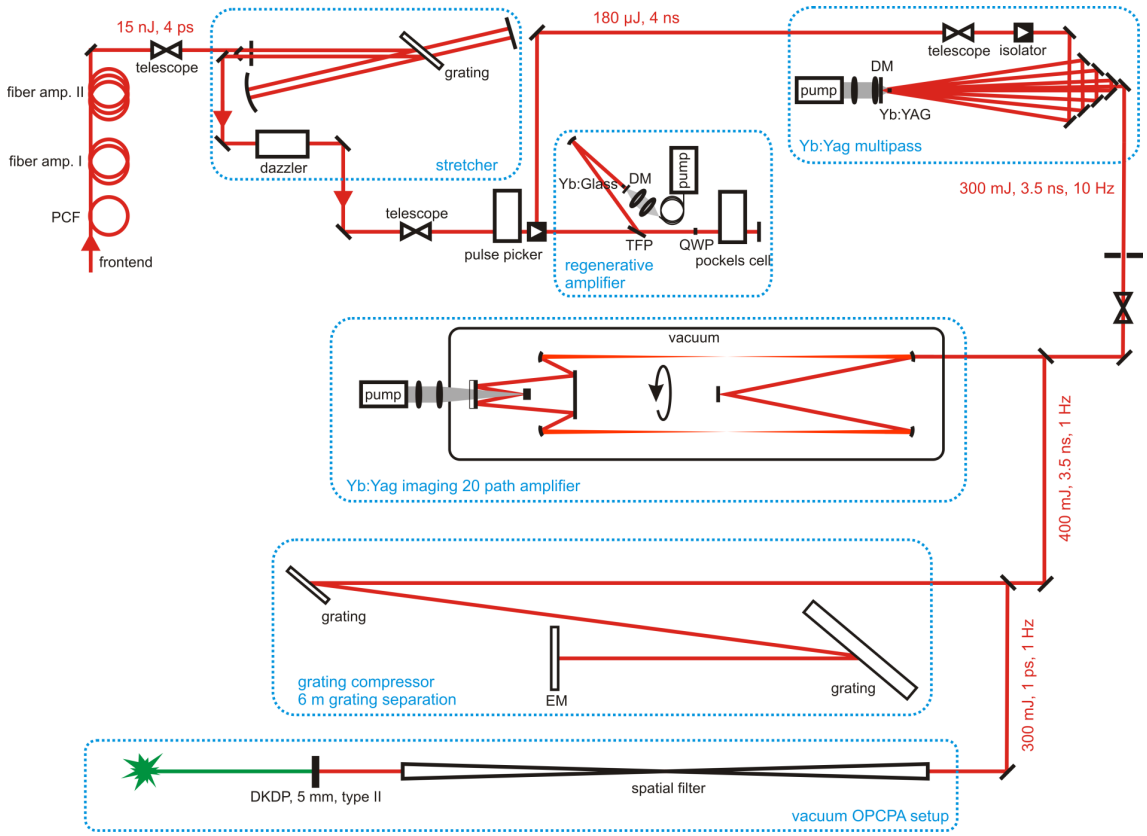

Figure 6.5: *Schematic sketch of the pump laser chain. The description is given within the text. This figure is a modified version of the layout presented in [38] and used with permission from the original author.*

in two consecutive CW diode-pumped Yb-doped fiber amplifiers to 14 nJ with a pulse duration of 5 ps at a repetition rate of 70 MHz (Institute for Applied Physics, Jena, Germany). The pulses are stretched to 4 ns in an all-reflective grating stretcher in a double-pass configuration which reduces the bandwidth to 4 nm due to spectral clipping at the grating. A Dazzler is used for spectral shaping in order to reduce the effect of gain narrowing in the subsequent amplifiers and for spectral-phase shaping for an optimum compression. Before the amplification of the stretched pulses in the regenerative amplifier, a pulse picker (fast pockels cell in combination with a faraday rotator) reduces the repetition rate from 70 MHz to 10 Hz. The laser pulses are amplified during approximately 120 round trips in a broadband Yb:glass regenerative amplifier from < 10 nJ to 180 μJ while keeping their input bandwidth and excellent beam profile. Further amplification is performed in an 8-pass Yb:YAG amplifier in bow-tie geometry to 300 mJ. The bandwidth is reduced to 3.5 nm due to the residual gain narrowing which cannot be fully compensated by the spectral shaping with the Dazzler. In order to improve the quality of the beam profile before further amplification, the beam is clipped with a hard aperture and imaged

onto the next amplifier with the drawback of loosing 60% of the pulse energy. The subsequent 20-pass Yb:YAG amplifier is based on relay imaging and maintains the spectral width and the good beam profile [96]. On a single-shot basis an output pulse energy of $> 1\,\mathrm{J}$ is reached. However, at this energy level damage occured at one dichroic mirror in the amplifier limiting the output energy to 400 mJ at 1 Hz repetition rate. After the final OPCPA campaign the dichroic mirror was replaced by a more resiliently coated specimen now allowing an output energy of 1 J on a daily basis.

The amplified pulses are compressed in a compressor with a grating separation of approximately 6 m. Their spectrum is shown in Figure 6.6(a) recorded at full power of the imaging amplifier. It supports a Fourier-limited pulse duration of 750 fs. At the beginning only a SHG autocorrelator was available to measure the pulse duration. Owing to the unknown spectral phase, the pump pulses could not be fully compressed resulting in a pulse duration of $1 - 1.6\,\mathrm{ps}$ FWHM. As a remedy, the autocorrelator was upgraded to a single-shot SHG-frequency resolved optical gating (FROG)-setup by spectrally resolving the autocorrelation trace with an installed imaging spectrometer. The obtained spectral-phase information now allowed for full compression by optimizing the compressor and compensating the residual phase with the Dazzler. A pulse duration of 840 fs was obtained on a daily basis (cf. Figure 7.14). Since the grating compressor imprints stripes on the beam profile of the pump laser, a spatial filter for cleaning the near-field is necessary. The smoothed output pulses were frequency doubled in a 5 mm thick DKDP crystal (type II). While frequency doubling the output of the 8-pass amplifier, conversion efficiencies of up to 50% were demonstrated [38]. This value could not be reproduced with the 20-pass imaging amplifier, where efficiencies of only $\sim 40\%$ were achieved. The spectrum of the frequency-doubled beam (full amplification in the 20-pass imaging amplifier) is presented in Figure 6.6(b). It seems that the modulated intensity profile of the pump laser (observable on burn paper shots) combined with an aberrated wave front (observable during measurements of the focusbility) are the reasons for the reduced conversion efficiency.

The beam size of the pump laser is reduced after frequency doubling in order to obtain a pump intensity of approx. $100\,\frac{\mathrm{GW}}{\mathrm{cm}^2}$ at the OPCPA crystals. These high intensities lead to a significant contribution of nonlinear phase-propagation effects in air and material as described in section 4.5. Consequently, the beam transport is realized with only reflective components. As a further consequence of these high intensities for OPCPA experiments in air the maximum energy is limited to $\sim 40\,\mathrm{mJ}$ at 515 nm due to strong SF (cf. section 7.2). In order to make full use of the available

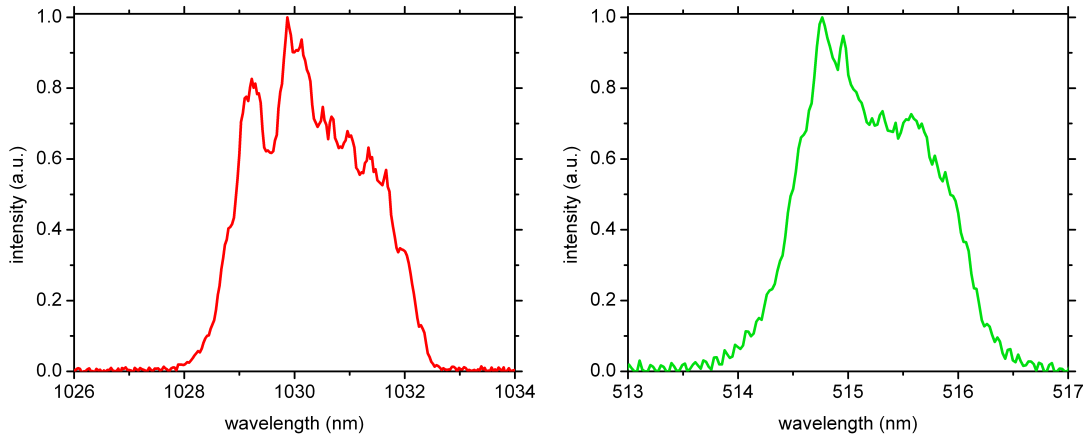

(a) fundamental pump spectrum (b) frequency doubled pump spectrum

Figure 6.6: *Measured pump spectra at full energy: (a) Spectrum of the fundamental beam after compression; (b) spectrum of the frequency-doubled beam.*

pump energy, a vacuum OPCPA system had to be installed (cf. section 7.3). Since different aspects of the OPCPA process are investigated with different pump-laser parameters such as energy, beam profile and pulse duration, these parameters are described in the corresponding sections of chapter 7.

More details about the CPA Yb:YAG pump-laser chain can be found in the PhD theses of Sandro Klingebiel [38] and Christoph Wandt [97]. Some detail aspects of the pump-laser system can also be found in the publications [98–100].

6.3 OPCPA system

As already introduced in chapter 1 and section 2.3, the OPCPA chain of the PFS is based on the non-collinear geometry scheme in order to amplify broadband pulses supporting few-cycle pulse durations. As an example for an experimental setup of a non-collinear OPA Figure 6.7 depicts a photograph of an OPA stage in operation. For better visibility of the beams, here a blue pumped OPA is shown which amplifies a broadband seed in the visible wavelength range [101]. Therefore, the generated idler lies in the NIR spectral range and is observed as a red beam.

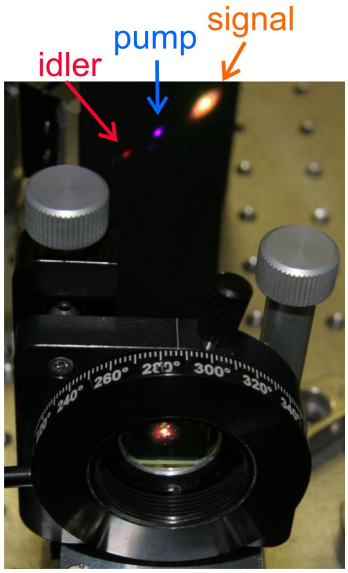

Figure 6.7: *Photograph of a non-collinear OPA in operation. For better visibility of the beams, here a blue pumped OPA stage is shown.*

6.3.1 Temporal jitter between signal and pump pulse

As mentioned in subsection 4.2.3, a temporal jitter between pump and signal can lead to both fluctuations in energy and spectrum of the amplified seed pulse. Despite the optical synchronization, such a behavior was observed in all experimental OPCPA campaigns, hinting at an unforeseen source of timing jitter. In order to measure the timing jitter on a single-shot basis, a cross-correlation technique [102] with spectral encoding was implemented. It is based on SFG between a compressed and a strongly chirped pulse. A change in the relative delay between both pulses shifts the wavelength of the SFG signal since the compressed pulse (pump laser, $\tau = 1\,\mathrm{ps}$) overlaps with different spectral components of the chirped pulse (uncompressed Femtopower pulse, $\Delta\lambda = 60\,\mathrm{nm}$, $\tau = 10\,\mathrm{ps}$), as indicated in Figure 6.8 [37]. The setup implemented in the PFS system is described in detail in [37,38,100]. Note

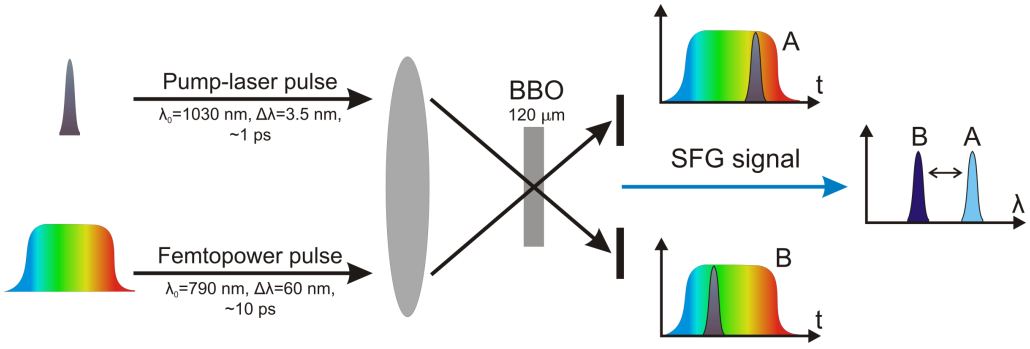

Figure 6.8: *Principle of the modified cross correlation technique [102] implemented to characterize the level of temporal synchronization between signal and pump pulse. This picture is a slightly modified version of the schematic drawing found in [37] and used with permission from the original author. The cases **A** and **B** correspond to two different arrival times at the BBO crystal for imperfect temporal synchronization of the pulses relative to each other. The compressed short pulse overlaps with a different spectral component of the stretched broadband pulse leading to a shift of the wavelength of the resulting SFG signal.*

that despite the fact that the shortest pulse is 1 ps long, it supports a much better time resolution. The spectrometer (Avantes AvaSpec-2048) used for detecting the SFG has a spectral resolution of 0.06 nm which leads in combination with the calibration factor of the cross-correlator of 533 fs/nm [38] to an accuracy of 32 fs/px for the temporal jitter measurement. However, the centroid position can be determined with sub-pixel resolution [103] and therefore the accuracy is further improved to $\sim$ 10 fs depending on the signal-to-noise ratio [38]. The results of this investigation, presented in Figure 6.9(a), proved that the instabilities observed in the OPCPA experiments originated from a temporal jitter of the order of 400 fs rms.

The source of the jitter was located inside either the compressor or stretcher of the pump laser. When both components were bypassed, the measured jitter (15 fs rms) approached the instrument resolution limit. It turns out that while small pointing fluctuations introduce nearly opposite path changes before and after a reflection off a mirror, canceling out any delay jitter, this is not the case for reflection on a grating or transmission by a prism in the dispersion plane, as has been shown in [100]. This finding came somewhat unexpected, and caused a large delay without much progress for the OPCPA development. In order to minimize the pointing fluctuations, mainly originating from air turbulence, the stretcher was rebuilt inside an air tight box reducing the temporal jitter to $\sim$ 200 fs rms as depicted in Figure 6.9(b). An active stabilization system (motorized delay unit) [100] was installed in order to compensate the slow drift observable in Figure 6.9(b) and therefore

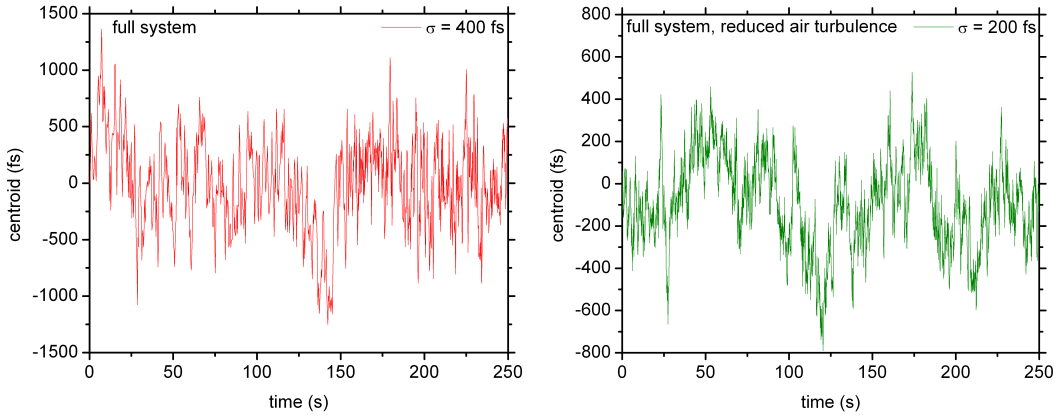

(a) full system (b) full system, reduced air turbulence

Figure 6.9: *Results of the temporal-jitter measurement. (a) depicts the temporal jitter measurements without any improvements of the PFS system. The level of jitter was* 400 fs *rms. (b) presents the improved temporal jitter with reduced air fluctuations. A jitter of* 200 fs *rms was detected. The pictures and the measurements are originally presented in the PhD thesis of Izhar Ahmad [37] and Sandro Klingebiel [38] and used with permission from the original authors.*

the temporal jitter was decreased to 100 fs rms as presented in Figure 6.10. This level was small enough thus that the first proof-of-principle OPCPA experiments could be performed. Currently, also the compressor is being enclosed in a vacuum vessel in order to reduce the pointing fluctuations due to air turbulences further (cf. section 8.1).

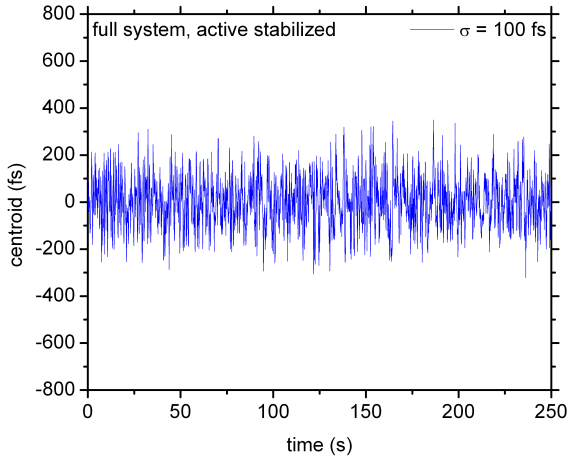

Figure 6.10: *Temporal-jitter measurement with working active stabilization system. A residual jitter of* 100 fs *rms was detected. The pictures and the measurement are originally presented in the PhD thesis of Izhar Ahmad [37] and Sandro Klingebiel [38] and used with permission from the original authors.*

7 — OPCPA and compression exp.

In order to prove the validity of the PFS concept, the nonlinear amplification dynamics in thin LBO and DKDP crystals, pumped on a picosecond timescale, were studied. These proof-of-principle experiments were designed to detect any possible "show-stoppers" that might jeopardize the PFS concept in part or as a whole. Additionally, the experimental studies target several other important aspects of the PFS concept, such as the compressibility of the amplified ultra-broadband signal pulses and the expected high temporal contrast.

Since during the course of this work the pump laser was only reliably working up to the 400 mJ-level, the experiments presented in this work were restricted to one or two OPCPA stages. The detailed setup of each different OPCPA campaign is presented in Appendix D. The various tools for pulse characterization, which were used in these experiments, are described in Appendix E. Throughout this thesis, the OPCPA setup evolved through the following general steps:

- **Single DKDP stage:** The first OPCPA experiments were performed with a single DKDP stage in order to verify the amplified bandwidth predicted by the simulations (cf. section 5.1). In addition, the results of the small-signal gain and saturation measurements were compared with simulations performed with SOPAS in order to check the validity of the simulation results (cf. Appendix B).

- **Two LBO stages located in air:** In order to investigate the performance of LBO as an alternative to DKDP, an experiment with two consecutive LBO stages was performed. In addition, the compressibility of the amplified signal beam as well as the improved temporal contrast due to the nonlinear amplification was studied. As already mentioned in section 6.2, the high intensities of the pump laser resulted in a high B-integral during propagation in air. This limited the maximum pump energy to 40 mJ at 515 nm for these experiments. At higher energy, strong SF in air led to damage of optical components.

- **Two LBO stages located in vacuum:** Since the LBO experiment in air showed the good performance of LBO, these experiments aimed at demonstrating the scalability in terms of output energy. In order to remove the restrictions to pulse energy due to nonlinear propagation in air, a vacuum system for two OPCPA stages was installed to allow higher energies for the experimental campaign. A total energy of ~ 90 mJ for the frequency-doubled pump beam was used to pump the two stages. The pulse compression after amplification was realized by an all chirped mirror compressor.

7.1 Broadband ps-OPCPA operation in DKDP

Broadband amplification in DKDP had never been investigated before. This chapter reports the first successful demonstration of that novel approach. In a first test, the small-signal gain was characterized in a 3 mm crystal in order to verify the accuracy of the simulation results and to demonstrate broadband amplification. The second experiment used a 7 mm thick DKDP crystal to reach the saturation regime.

The results of these measurements are published in [7] in slightly modified form. An electronic reprint is attached in appendix G.1 with the permission of OSA.

Pulse parameters used for amplification

The experimental setup used for these measurements is described in appendix D.1. Here, the relevant pulse parameters are presented. For these measurements a small fraction ($\sim 800\,\mu$J) of the total available pump-laser energy at 515 nm was used with a FWHM duration of 2 ps, i.e. slightly longer than the best achievable performance, since in this way the relative influence of the timing jitter (130 fs in this experiment) could be reduced.

The signal spectrum which seeded the OPCPA stage is presented in Figure 7.1 (black curve). It has a spike at 720 nm, which is approximately two orders of magnitude

higher than the spectral intensity at 1000 nm. This peak was attenuated in a 2 mm thick RG1000 bandpass. The spectrum after the RG1000 filter is also shown in Figure 7.1 (red curve). The energy of the broadband signal after the RG1000 filter was 4.5 μJ. It has to be mentioned that the measured spectra presented in this section were smoothed (adjacent averaging over 10 points) with the spectrometer software (Avantes) in order to reduce spectral intensity modulations, which arose due to strong SPM inside the HCFs (cf. section 6.1).

The pump pulses were combined with the broadband signal pulses in a DKDP crystal in the non-collinear geometry to allow for the broadest bandwidth and to separate the beams after amplification. The internal non-collinear angle between the pump and signal was 0.75°.

The pump and signal beams were focused to obtain near-Gaussian beam profiles in the OPCPA crystal with FWHM beam diameters of $\sim$ 1.5 mm and 1.4 mm, respectively.

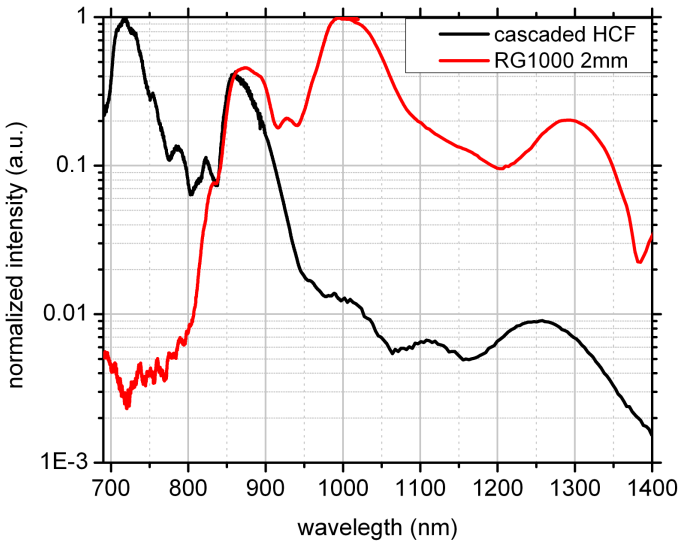

Figure 7.1: *Broadband input signal spectra, normalized to the peak values, at the output of cascaded hollow core fibers (black) and after a* 2 mm *thick bandpass filter (RG1000) shown in red. This picture is published in [7] and used with permission from OSA.*

DKDP small-signal gain

The small-signal gain was investigated at different phase-matching angles in a 3 mm thick DKDP crystal. For this the signal energy was reduced to 20 nJ using a variable neutral-density filter in order to avoid saturation of the OPCPA process. The seed was stretched to a pulse duration of $\sim$ 300 fs FWHM.

The results of this gain measurement are shown in Figure 7.2(a) for three different phase-matching angles, 36.8°, 36.9° and 37.0°, respectively. In addition, the unamplified and amplified spectra for a phase-matching angle of 37.0° are presented in Figure 7.2(b). The presented values for the phase-matching angles were derived from a comparison with simulations (cf. Appendix B). Owing to the usual uncertainty in the cut-angle information provided by the crystal manufacturers the phase-matching angle cannot be experimentally determined with the available tools in the laboratory. The measured gain curves were averaged over 100 shots to eliminate the effect of shot-to-shot instabilities. Since the spectrum of the signal pulse was artificially suppressed below 800 nm using a bandpass filter, no reliable gain information for this region could be extracted from the experiment. Nevertheless, calculations predict that the gain curve extends down to 700 nm (cf. Figure 2.3). As can be seen from the measured curves, very broadband amplification was achieved with a significant gain over a bandwidth of 500 nm for a phase-matching angle of 37.00°. Moreover, the gain curve is very sensitive to the phase-matching angle and changes its shape significantly when the angle is slightly detuned. When the phase-matching angle

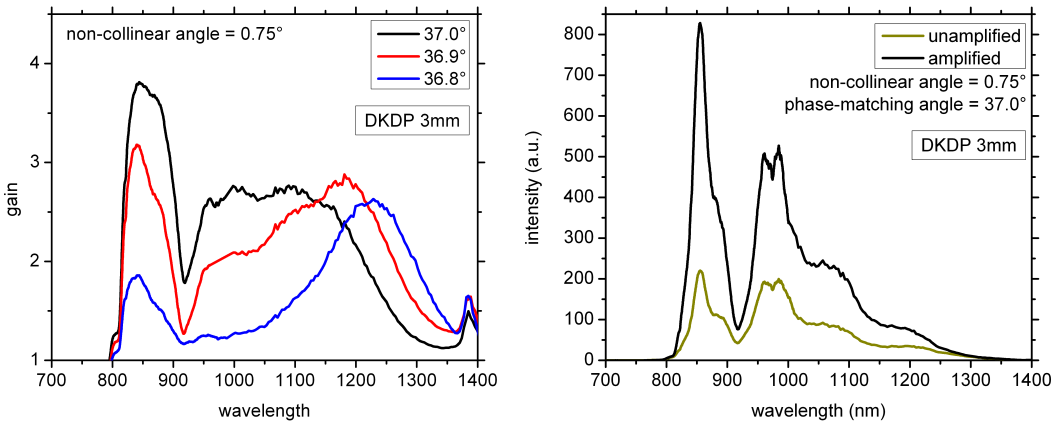

(a) small-signal gain (b) signal spectrum for 37.0∘

Figure 7.2: *(a) Investigation of the small-signal gain: Measured gain for a 3 mm thick DKDP crystal for three different phase-matching angles 36.8°, 36.9° and 37.0°. This picture is published in [7] and used with permission from OSA. (b) presents the unamplified and amplified spectrum for the case of a phase-matching angle of 37.0°.*

was reduced, the amplification extended more and more into the near infrared region and even reached 1400 nm in this experimental setup. In addition, a narrow dip was observed in the measured gain curves around 920 nm. This is a combination of a very weak seed intensity in this spectral range and the way of spectral detection, since this region is situated at the edge of the sensitivity range of the visible spectrometer which therefore introduces high noise levels and delivers inaccurate measurements (cf. Appendix E). The dip in the middle of the gain curves for the phase-matching angles of 36.80° and 36.90° respectively, is a result of the characteristic phase-matching curve of DKDP.

DKDP saturated gain

For this study a 7 mm thick DKDP crystal was installed in the same setup as above. The signal-pulse duration after the RG1000 filter was matched to the pump-pulse duration (green curve in Figure 7.3) in order to optimize the extraction efficiency by increasing the prism separation of the double-prism stretcher. A GD between $700 - 1400$ nm of ~ 1.5 ps was measured, cf. Figure 7.3.

The phase-matching angle (36.95° from simulations) and the relative timing between signal and pump were adjusted for amplification in the infrared tail with its maximum at 1100 nm. Figure 7.4(a) shows the input and the amplified spectra and Figure 7.4(b) presents the spectral gain. The amplification in the 7 mm long DKDP

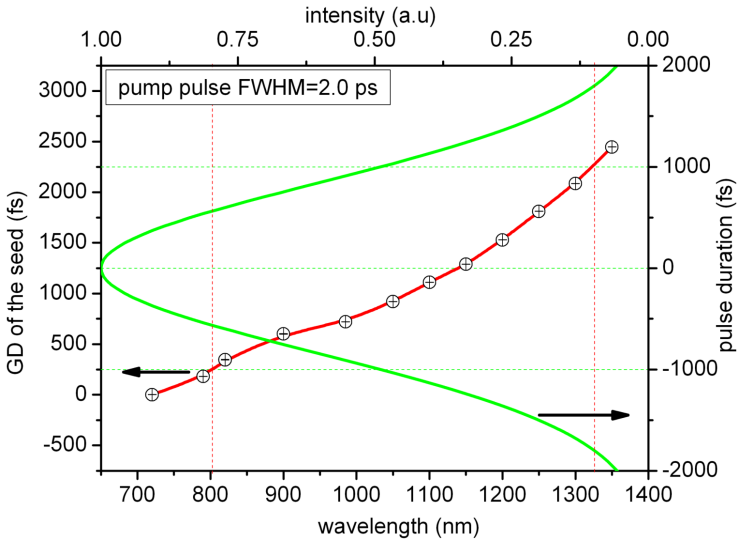

Figure 7.3: *Measured GD of OPCPA signal (red curve) for the measurements using the full signal energy: The central part of the signal* ($800 - 1325$ nm) *is stretched to fit in the FWHM duration of the pump pulse (green curve). This picture is published in [7] and used with permission from OSA.*

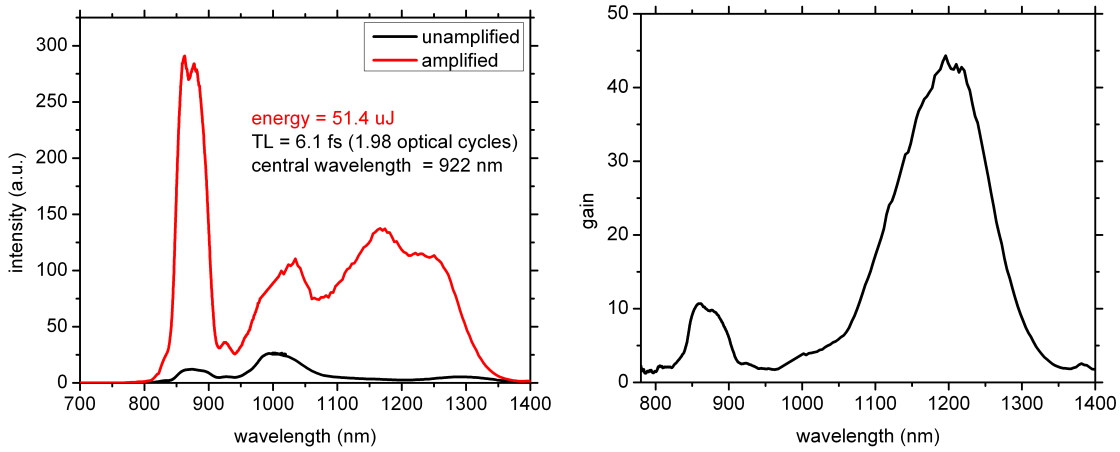

(a) signal spectrum (b) spectral OPCPA gain

Figure 7.4: *(a) The amplified (red curve) and unamplified (black curve) spectra, using* 7 mm *DKDP under saturation condition. (b) Spectral gain of the amplification process extracted from (a). These pictures are published in [7] and used with permission from OSA.*

crystal covered the range from $830 - 1310$ nm (measured at the 10% level). Below 800 nm no gain was observed due to the suppression of the signal by the RG1000 filter. Even without the spectral part from $700 - 800$ nm the amplified spectrum supported a Fourier-limited pulse duration of 6 fs, which corresponds to a two-cycle pulse.

Conclusion

The measurements demonstrated that DKDP crystals, which can be produced with large apertures, pumped at 515 nm and an intensity of 100 $\frac{\mathrm{GW}}{\mathrm{cm}^2}$, are able to amplify a bandwidth supporting pulse durations shorter than 6 fs [7].

7.2 OPCPA in LBO - beam propagation in air

The simulations, presented in section 5.2, revealed that LBO is a promising alternative to DKDP crystals. Consequently, measurements investigating the performance of two LBO stages in terms of bandwidth and gain were performed. Unlike the previous amplification-only studies, in this campaign the full OPCPA concept including compression and contrast measurements was realized.

Pulse parameters used for amplification

The experimental setup used for these experiments is described in appendix D.2. Here, the relevant pulse parameters are presented.

Pump beam: Strong SF in air limited the usable pump energy. A total pump energy of 42 mJ directly after the doubling crystal was determined as a safe regime leading to a pump energy of 5.3 mJ and 31.3 mJ measured in front of the first and second stages, respectively. At higher pump energies the SF resulted in damage of the optical components. The measured beam profiles at the first stage with very low pump energy, i.e. no effects of SF and with full energy of 5 mJ are presented in Figure 7.5(a), and (b), respectively. A modification and steepening of the beam profile caused by SF in air is obvious. Figure 7.5(c) shows the pump at the second LBO stage at full energy. The FWHM beam sizes of the pump at the first and second OPCPA stages at full energy were $0.9 \times 1.2\,\mathrm{mm}^2$ and $1.3 \times 1.4\,\mathrm{mm}^2$, respectively. The pulse duration after the compressor was ~ 1.2 ps and the timing jitter between the pump and signal pulses was measured to $100 - 120$ fs rms.

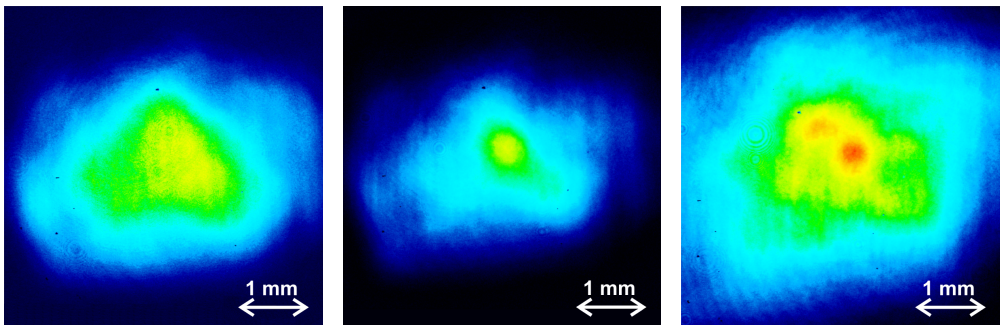

(a) 1st stage: low energy (b) 1st stage: high energy (c) 2nd stage: high energy

Figure 7.5: *Measured pump-beam profiles at the position of the OPCPA crystals: (a) profile at the first stage at low energy. No nonlinear propagation effects were observed; (b) profile at the first stage at a pulse energy of* 5 mJ*. The influence of SF is clearly visible; (c) profile at the second stage at full energy* (31 mJ)*.*

Signal beam: Figure 7.6(c) shows the seed spectrum for this experiment generated in two subsequent HCFs (black curve). Owing to strong SPM inside the HCFs, the signal spectrum was strongly modulated around 800 nm which corresponds to the central wavelength of the driving pulse. In contrast to the experiments described in appendix 7.1, no spectral smoothing was used before plotting the spectra. In order to compensate the higher orders of the stretcher and the compressor material (CaF_2), chirped mirrors were installed after the prism stretcher. The chirped mirrors were designed such that after two LBO stages the pulses can be compressed by propagating through ~ 30 mm of CaF_2. The spectral phase of the signal pulse in

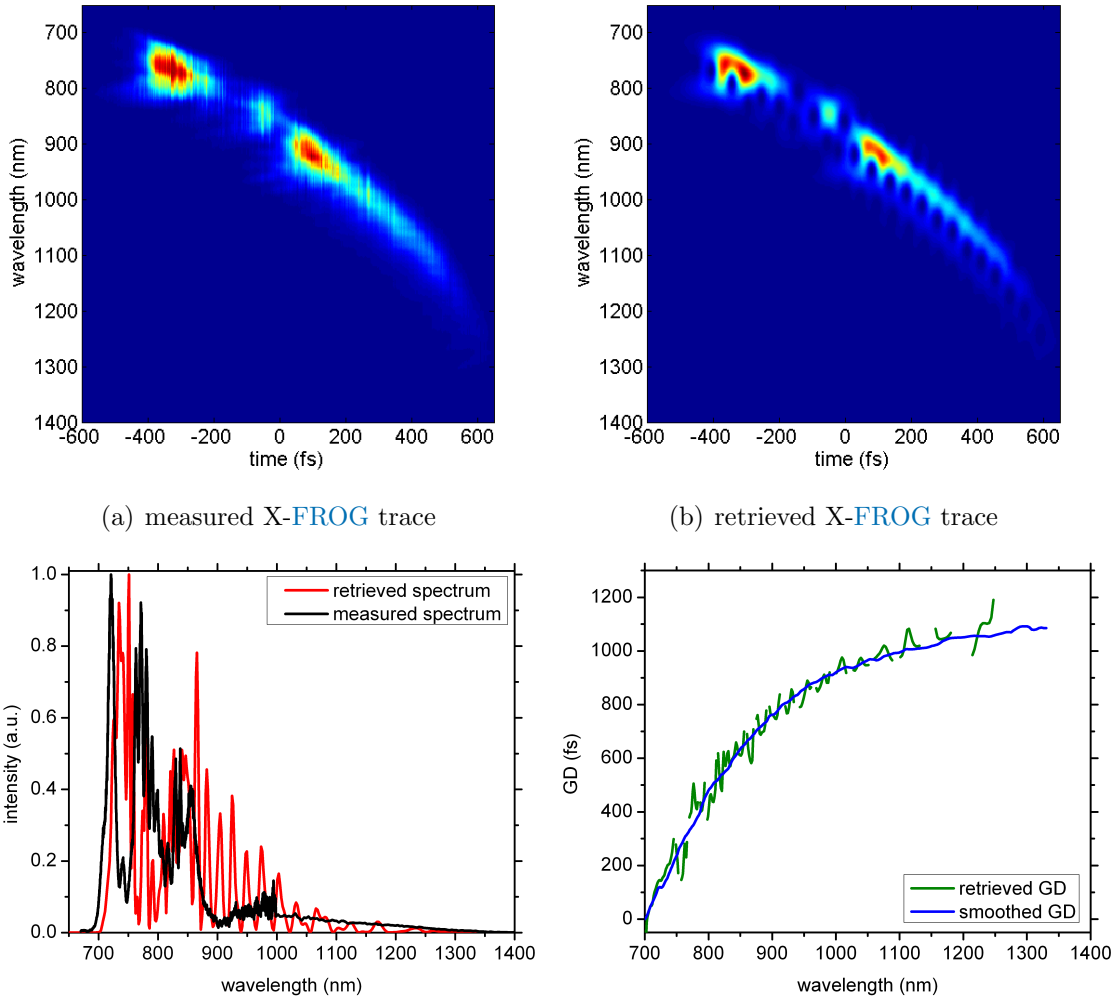

(a) measured X-FROG trace

(b) retrieved X-FROG trace

(c) spectra

(d) retrieved and smoothed GD

Figure 7.6: *Temporal characterization of the seed with the X-FROG: (a) measured FROG trace; (b) retrieved FROG trace; (c) shows the measured spectrum in front of the OPCPA crystals (black curve) and the retrieved spectrum (red curve); (d) presents the retrieved (green curve) and smoothed GD (blue curve).*

front of the first OPCPA stage was characterized with the X-FROG presented in appendix E.2. Figure 7.6(a) shows the measured FROG trace. Energy fluctuations of the seed pulse led to a fluctuating SFG signal during the measurement, which can be observed as vertical strips in the measured trace. The retrieved FROG trace depicted in Figure 7.6(b) represents the best fit of the FROG algorithm resulting in a modulated spectrum and phase. The retrieved spectrum is shown in Figure 7.6(c) and the retrieved GD is presented as green curve in Figure 7.6(d). It has to be mentioned that smoothing (Gauss-filter) of the measured FROG trace does not decrease the modulations in the retrieved trace. By smoothing the GD (blue curve in Figure 7.6(d)) the artifacts introduced by the retrieval are removed, however with the drawback that real GD modulations of the seed underlying these artifacts are lost. The total GD difference between $700 - 1400\,\text{nm}$ was $1100\,\text{fs}$ and was hence well matched to the pump-pulse duration. The beam size of the signal beam was matched to the pump-beam size in the first and second stages. The seed energy after the prism stretcher and the chirped mirrors amounted to $10\,\mu\text{J}$.

Nonlinear crystals: The nonlinear amplification was performed in two LBO crystals with 4 mm and 2 mm crystal length for the first and second stages, respectively. The internal non-collinear angle was 1.1° and a phase-matching angle of $\sim 14.45°$ was used for the nonlinear interaction.

7.2.1 OPCPA amplification in two LBO stages

The results of the amplification measurement are presented in Figure 7.7: signal spectrum without amplification (green curve), after amplification in the first stage (red curve) and the final spectrum after amplification in both stages (blue curve). The measured spectra are shown on linear (Figure 7.7(a)) and logarithmic (Figure 7.7(b)) scales. In the first stage, a bandwidth ranging from $720 - 1250\,\text{nm}$ was amplified. The second stage delivered a broader amplified bandwidth, $690 - 1350\,\text{nm}$, compared to the first stage due to the use of a thinner crystal. In addition, the second stage was operated closer to the point of back conversion leading to a further increase of bandwidth. The amplified bandwidth is even broader than the one achieved with DKDP (cf. section 7.1), and the Fourier-limited pulse duration of the amplified signal spectrum after the second OPCPA stage is 5 fs. The amplified energy after the first stage reached $312\,\mu\text{J}$ and the second stage boosted the energy up to 4.1 mJ. Figure 7.8(a) presents the measured beam profile of the unamplified signal beam after the OPCPA chain whereas Figure 7.8(b) shows the beam profile of the amplified signal at the same location. It is obvious that the intensity profile of the pump (cf. Figure 7.5(c)) was imprinted on the signal beam.

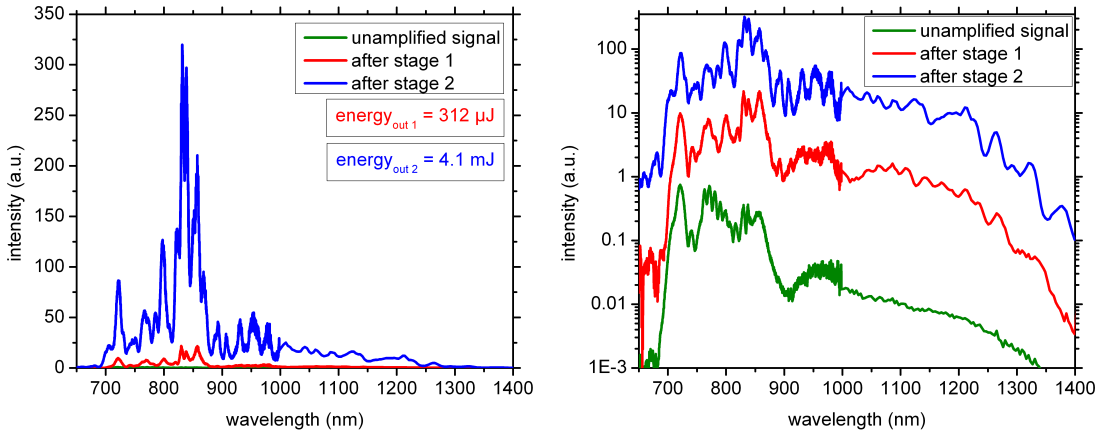

(a) signal spectra: linear scale (b) signal spectra: logarithmic scale

Figure 7.7: *Measured signal spectra for the unamplifed case (green curve), after the first OPCPA stage (red curve) and the final spectrum after amplification in two LBO stages (blue curve). The final spectrum supports a Fourier-limited pulse duration of* 5 fs. *(a) presents the spectra on a linear scale; (b) shows the spectra on a logarithmic scale.*

The measured spectra are compared to the results of a Sisyfos simulation. The calculations were based on the real scenario by taking the measured pump and signal energies, beam sizes, crystal thicknesses, and the measured seed spectrum and phase. The only fitting parameters were the phase-matching and non-collinear angle as well as the relative timing between signal and pump. The results are presented in Figure 7.9(a) and 7.9(b) for the first and second stages, respectively. The overall bandwidth is well reproduced by the simulations. However, the blue part differs from the measured spectra in both stages. For the simulations the smoothed group delay presented as the blue curve in Figure 7.6(d) was used. As mentioned before,

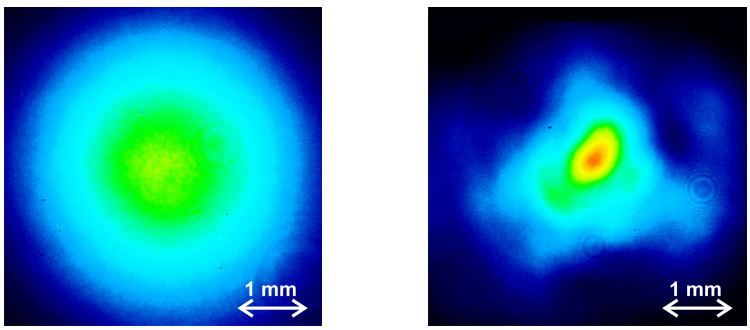

(a) unamplified case (b) amplified case

Figure 7.8: *Measured signal-beam profiles without amplification (a) and after amplification (b) in two OPCPA stages. The pump-beam profile (cf. Figure 7.5(c)) is imprinted on the signal-beam profile.*

the smoothing not only removed the artifacts introduced by the retrieval but also phase modulations of the seed pulse are lost. Since the spectral phase of the seed has a noticeable influence on the amplified spectrum (cf. simulations presented in subsection 4.2.2) the difference of the spectral phase used in the simulations and in the measurements might be a reason for the discrepancy in the amplification of the blue part. Furthermore, the nonlinear beam propagation of the pump in air results not only in SF but also affects the temporal shape of the pump pulse. However,

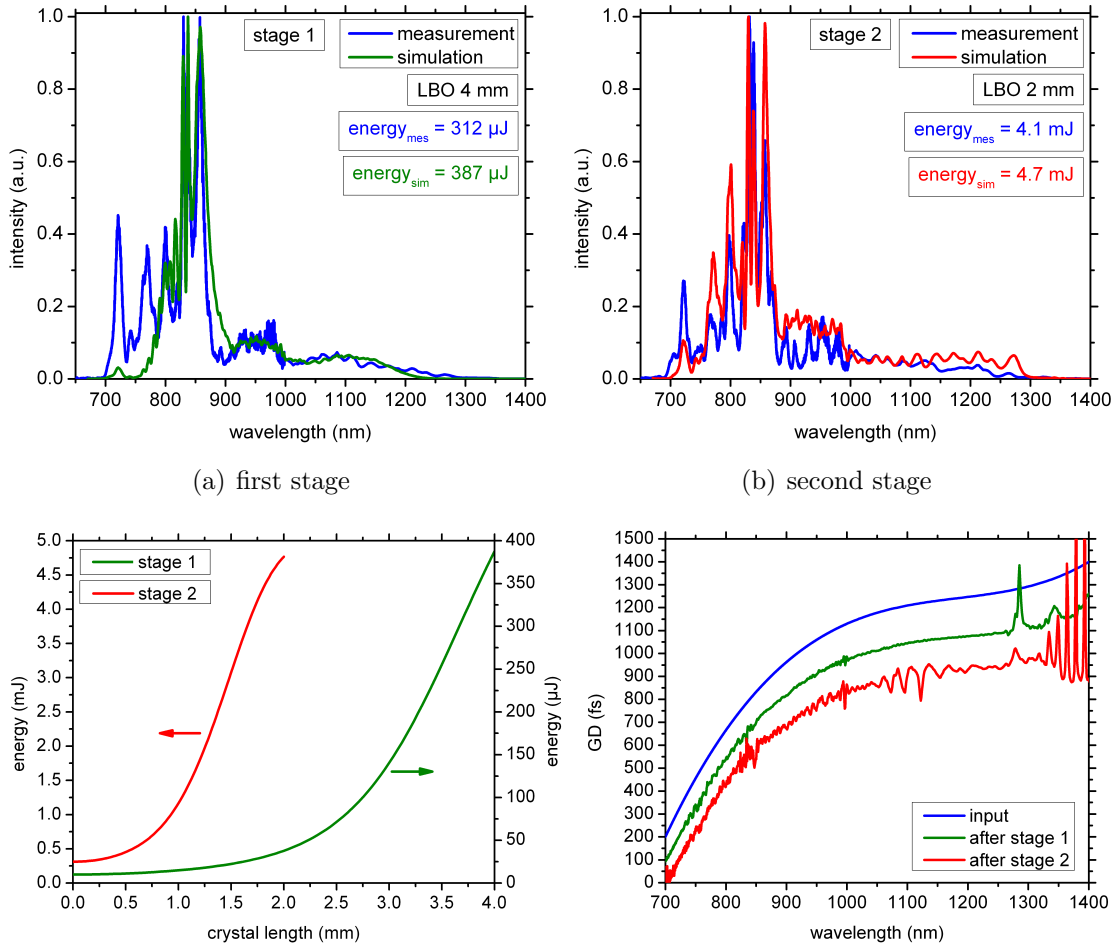

(a) first stage

(b) second stage

(c) signal energy over crystal length

(d) signal group delay

Figure 7.9: *Results of the Sisyfos simulation: (a) measured (blue curve) and simulated (green curve) spectra of the first OPCPA stage. For this simulation a phase-matching angle of $\theta = 14.63°$ and a non-collinear angle of $\alpha = 1.09°$ was used; (b) measured and simulated spectra of the second stage for $\theta = 14.45°$ and $\alpha = 1.1°$; (c) signal energy over the crystal length for the first (green curve) and second stages (red curve); (d) simulated group delay for the seed (blue curve) and after the first (green curve) and second stages (red curve). For better visibility the GD for the seed and after the first stage are shifted vertically.*

the simulations are based on a Gaussian-shaped pump in time, since no diagnostic was available to determine the temporal shape of the frequency-doubled pump. A difference in the temporal intensity profiles for simulation and measurement leads to different amplified spectra for a chirped seed. However, it can not be clarified which of these two effects has more influence on the discrepancy in the blue part. The simulated signal energies over the crystal length are presented in Figure 7.9(c) for both stages. The nonlinear process in the second stage is close to saturation. The simulated energy in the first stage is 1.24 times higher than the measurement and the energy of the second stage varies by 1.15 in the same direction. This inconsistency can also be explained by the slight discrepancies between simulations and measurements.

It is noticeable that in the measurements as well as in the simulations the modulations of the seed spectrum are not smoothed when the amplification is saturated but even enhanced. These enhanced modulations are caused by the OPA phase (cf section 4.3). Figure 7.9(d) presents the simulated GD of the seed (blue curve) and of the amplified signal after the first and second stages (green and red curves). It is obvious that the smooth input group delay gets modified during amplification: The more the amplification is driven into saturation, the more the modulated spectrum leads to a modulation of the GD due to the OPA phase. The modulated GD now affects the amplification and leads to a further modulation of the spectrum. Therefore, this loop avoids smoothing of the spectrum in saturation and leads to enhanced spectral intensity variations.

7.2.2 Compression test

In a first test the unamplified signal was compressed by propagation through CaF_2 and characterized with the single-shot SHG-FROG described in appendix E.2.2. Figure 7.10 (a), (b) and (c) presents the measured FROG traces for three thicknesses of CaF_2: 25 mm, 28 mm and 30 mm. Figure 7.10 (d), (e) and (f) shows the retrieved FROG traces. The retrieved spectral phases are depicted in Figure 7.10(g) and the resulting temporal shapes are presented in Figure 7.10(h). The shortest pulse duration (7 fs FWHM) is obtained for a material thickness of 28 mm. The design of the chirped mirrors, which were installed before the OPCPA stages, was based on the assumption of a compressed seed pulse after the second HCF and for a CaF_2 thickness of 30 mm. Therefore, the dispersion introduced by the propagation through the second HCF and the SPM process was not taken into account. A part of this uncompensated phase was counterbalanced by reducing the thickness of CaF_2 by

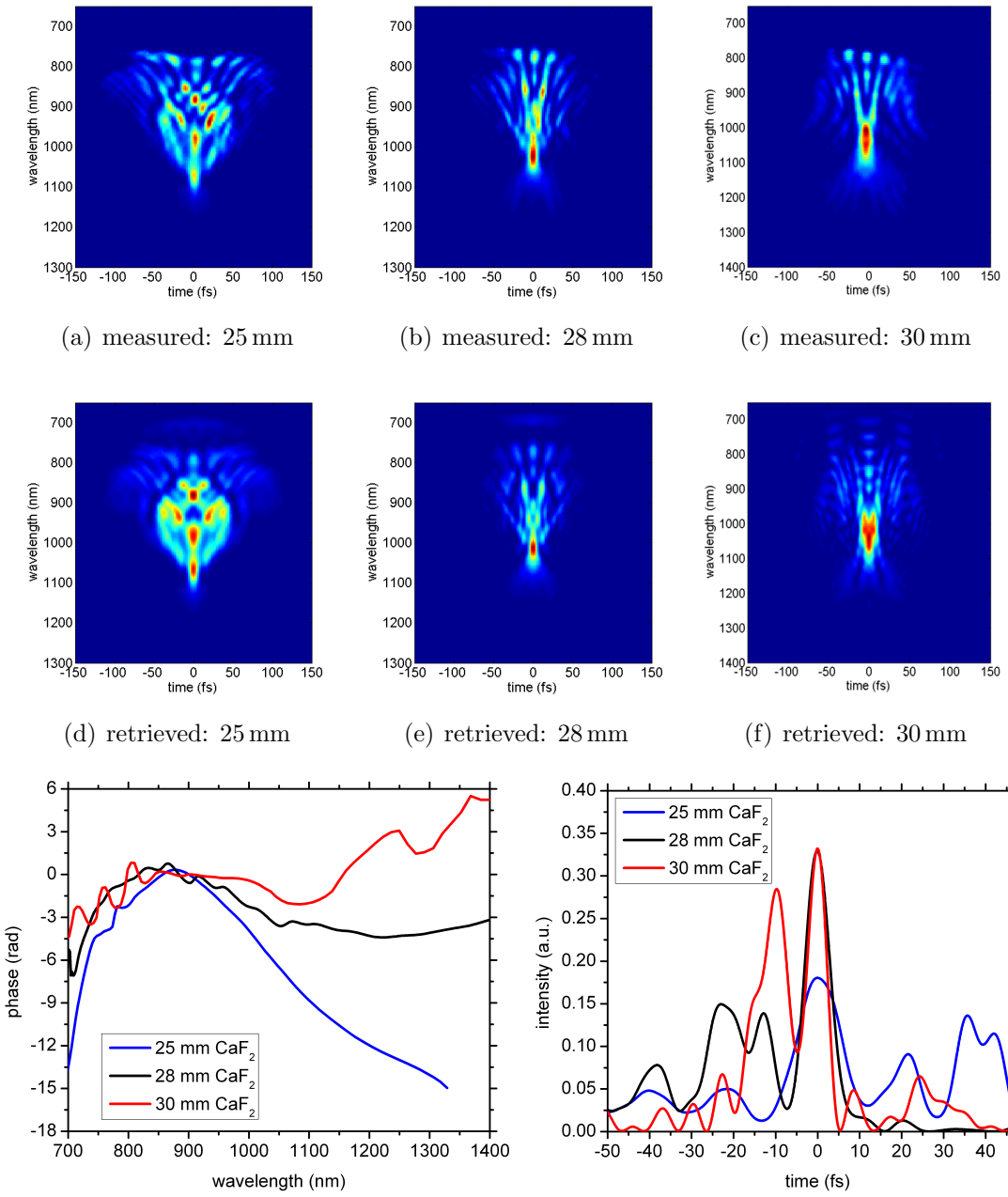

(a) measured: 25 mm (b) measured: 28 mm (c) measured: 30 mm

(d) retrieved: 25 mm (e) retrieved: 28 mm (f) retrieved: 30 mm

(g) retrieved phase (h) retrieved temporal shape

Figure 7.10: *Compression of unamplified signal: (a), (b) and (c) measured FROG traces for* 25 mm, 28 mm *and* 30 mm *of* CaF_2*; (d), (e) and (f) retrieved FROG traces. (g) retrieved phases for the three cases; (h) retrieved temporal shapes.*

2 mm however, a residual oscillating phase was still present leading to side shoulders in the time domain.

After the compression of the unamplified pulse, the temporal shape of the signal after amplification in two stages was characterized. The amplified pulse was attenuated

with wedges before compression in order to avoid SPM in the compressor material. The measured and retrieved FROG traces for 28 mm of CaF_2 are presented in Figure 7.11(a) and Figure 7.11(b), respectively. The measured FROG trace features strong oscillations due to the modulated signal spectrum and phase, influencing not only the spectral domain but also the temporal one. The retrieved spectrum and GD are depicted in Figure 7.11(c). The input spectrum was not well retrieved since the resolution of the SHG-FROG is too low to resolve the spectral modulations in detail. The high-order fluctuations of the GD are a combination of the uncompensated phase mentioned above and the additional OPA phase imprinted by the nonlinear

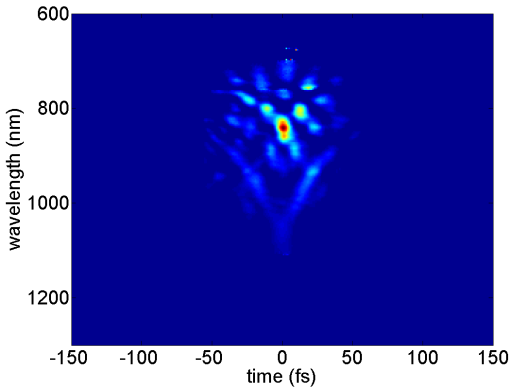

(a) measured FROG trace

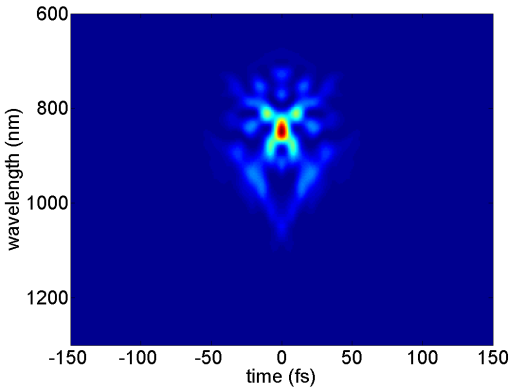

(b) retrieved FROG trace

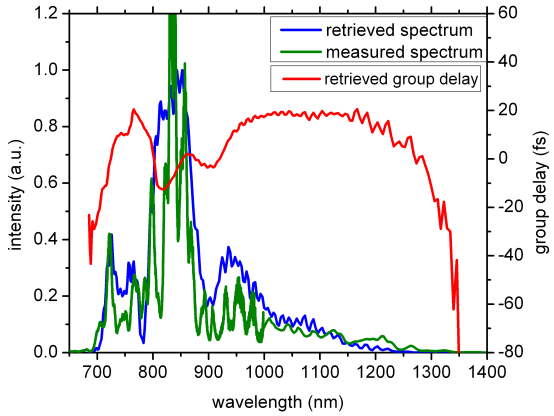

(c) retrieved spectrum and GD

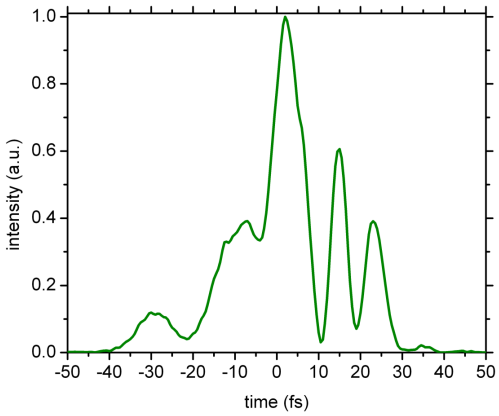

(d) retrieved temporal shape

Figure 7.11: *Pulse duration characterization with the single-shot SHG-FROG: (a) measured FROG trace; (b) retrieved FROG trace. The modulated FROG trace is a result from the strongly modulated signal spectrum. (c) retrieved spectrum (blue curve), measured spectrum (green curve) and retrieved GD (red curve). (d) presents the retrieved temporal shape. The FWHM pulse duration of the main peak is* 9 fs *with additional two side peaks and a shoulder. The FROG error was* 1.2% *for a grid size of* 512 x 512 *points.*

amplification. This modulated GD results in two side pulses and a shoulder in time as shown in Figure 7.11(d), which depicts the retrieved temporal profile. The FWHM pulse duration of the main peak is 9 fs while the total pulse structure lasted for approx. 70 fs. Further flattening of the GD with new chirped mirrors would have led to a better suppression of the side pulses and shorten the main pulse however, the lack of experimental time due to the ongoing pump-laser development (20-pass Yb:YAG imaging amplifier) prevented a next iteration of these mirrors.

7.2.3 Characterization of the temporal contrast

Picosecond-pumped OPCPA systems such as the PFS are expected to have an intrinsically good temporal contrast on the picosecond time scale since pre- or post-pulses outside the temporal pump window will not experience amplification and therefore the ratio between these pulses and the main light pulse will increasing with pulse energy (cf. section 4.4). Consequently, one major task of this thesis was to experimentally demonstrate this expected behavior.

The temporal contrast of the compressed signal pulse was characterized by a Sequoia third-order autocorrelator from Amplitude Technologies as described in appendix

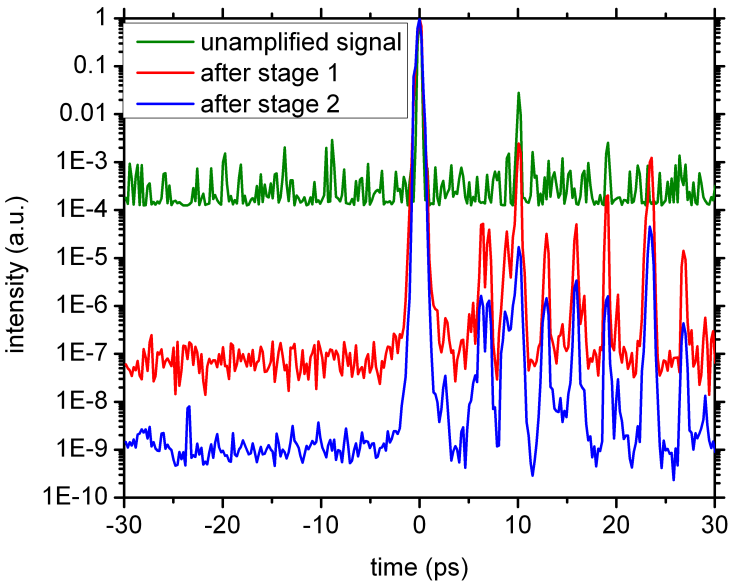

Figure 7.12: *Temporal contrast measurements performed with the Sequoia third-order autocorrelator. The green curve represents the temporal profile with an unamplified signal pulse, and the red and blue curves after one and two stages, respectively. By comparing the intensity ratios of the main pulses to the post pulses at* 10 ps *(cf. Table 7.1) the improvement of the temporal contrast due to short-pulse-pumped OPCPA systems is evident.*

	unamplified signal	amplification in one stage	amplification in two stages
relative intensity of main pulse	1	1	1
relative intensity of post pulse	2.8×10^{-2}	2.5×10^{-3}	1.7×10^{-5}
ratio $\frac{\text{mainpulse}}{\text{postpulse}}$	35.7	4×10^{2}	5.9×10^{4}

Table 7.1: *Temporal contrast measurements with the Sequoia third order autocorrelator. Intensities of the main peaks, the post pulses at* 10 ps *and their ratio for the three different cases.*

E.3. It has to be mentioned that the Sequoia cannot detect the full bandwidth of the signal pulse and therefore represents the temporal contrast only for a part of the signal spectrum ($760 - 840$ nm). The results of the measurements are presented in Figure 7.12. The green curve demonstrates the temporal contrast of the unamplified signal pulse. The improved temporal contrast after the first OPCPA stage is depicted by the red curve, and the blue curve shows the contrast after amplification in two stages. The signal-pulse energy in the unamplified and single-stage cases was below the required minimal pulse energy for the autocorrelator (1 mJ) in order to achieve its full dynamic range of 10^9 (cf. appendix E.3). Consequently, it was not useful to evaluate the ratio of the main peaks and the background for these two cases (time range -30 ps to -10 ps). Nevertheless, the expected contrast improvement is clearly visible by comparing the intensity ratio of the main peaks and the post pulse at ~ 10 ps. Table 7.1 lists the intensities of the main pulse and post pulse and their ratio for the different energies. Owing to the short pump-pulse duration of 1.2 ps, even the small post-pulse at ~ 2.5 ps was reduced which can be seen by comparing the red and blue traces.

7.2.4 Conclusion

The measurements with two LBO stages demonstrated the feasibility of LBO as an alternative to DKDP crystals. Amplified bandwidths supporting Fourier-limited pulse durations of 5 fs are obtained by amplification in 4 mm and 2 mm thick LBO crystals. A total signal energy of 4.1 mJ is reached. Furthermore, the compressibility of these amplified pulses was demonstrated by measurements performed with the single-shot SHG-FROG. Pulse compression in 28 mm of CaF_2 led to a pulse duration of 9 fs for the main peak, however, the residual phase led to strong side pulses. Measurements performed with a third-order autocorrelator proved the expected feature of picosecond-pumped OPCPA systems in terms of an inherently good temporal contrast, which was reached even on the picosecond time scale.

7.3 OPCPA in vacuum

The proof-of-principle OPCPA experiments with DKDP and LBO described in section 7.1 and section 7.2 exposed no physical "show-stopper" or limitation of the planned PFS concept in terms of bandwidth and gain. However, the nonlinear beam propagation in air resulted in SF which limited the usable pump energy to $\sim$ 40 mJ at 515 nm. In order to apply the full pump energy of currently 90 mJ and up to 500 mJ at a later stage, a vacuum system containing two OPCPA stages was planned and installed. Working in vacuum reduces the accumulated B-integral significantly, thereby allowing higher pump energies and the usage of a pump-laser-imaging system for maintaining the beam profile over long propagation distances. After the installation of the vacuum system, OPCPA experiments in two LBO stages were performed. Finally the amplified signal pulses were compressed by an all-chirped-mirror compressor. The results of this study are presented in the current section.

Pulse parameters used for amplification

The vacuum setup used for these measurements is described in appendix D.3. Here, the relevant pump, seed and crystal parameters are presented.

Pump laser: The beam profile of the fundamental pump beam at the position of the SHG crystal is shown in Figure 7.13(a) (FWHM $18 \times 17\,\mathrm{mm}^2$) leading to a peak intensity of $\sim 100\,\frac{\mathrm{GW}}{\mathrm{cm}^2}$. The stripes on the left side of the profile were

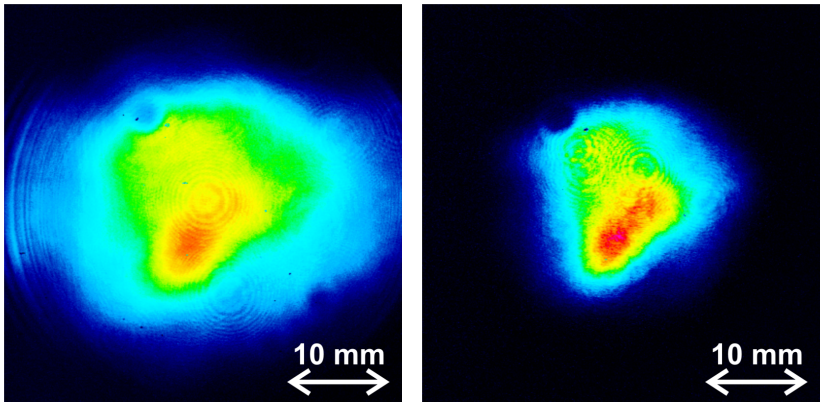

(a) fundamental beam (b) frequency-doubled beam

Figure 7.13: *Beam profiles of the pump laser at the position of the SHG crystal. (a) depicts the beam profile of the fundamental beam. (b) shows the profile of the frequency-doubled laser measured with color filters in order to suppress the fundamental beam.*

introduced by clipping at the optics of the imaging system for the beam-profile measurement. The asymmetric shape was already present after the pump compressor and was maintained due to the imaging system. In addition, the beam profile of the frequency-doubled beam at the same position measured with color filters is depicted in Figure 7.13(b). The first OPCPA stage was pumped by $4.5 \pm 0.4\,\mathrm{mJ}$ (measured over 30 shots) and for the second stage a pump energy of $81 \pm 7.3\,\mathrm{mJ}$ was available, resulting in pump intensities of $\sim 90\,\frac{\mathrm{GW}}{\mathrm{cm}^2}$ and $\sim 120\,\frac{\mathrm{GW}}{\mathrm{cm}^2}$, respectively.

The pump-pulse duration was measured after the grating compressor with the single-shot pump SHG-FROG and the results are presented in Figure 7.14. The measured FROG trace was well retrieved and a pulse duration of 840 fs was measured, which is 1.08 times longer than the Fourier-limited pulse duration of 780 fs. Compressed pump pulses are favorable since they are less sensitive to variations of the GDD originating from pointing fluctuations before the compressor than partially compressed

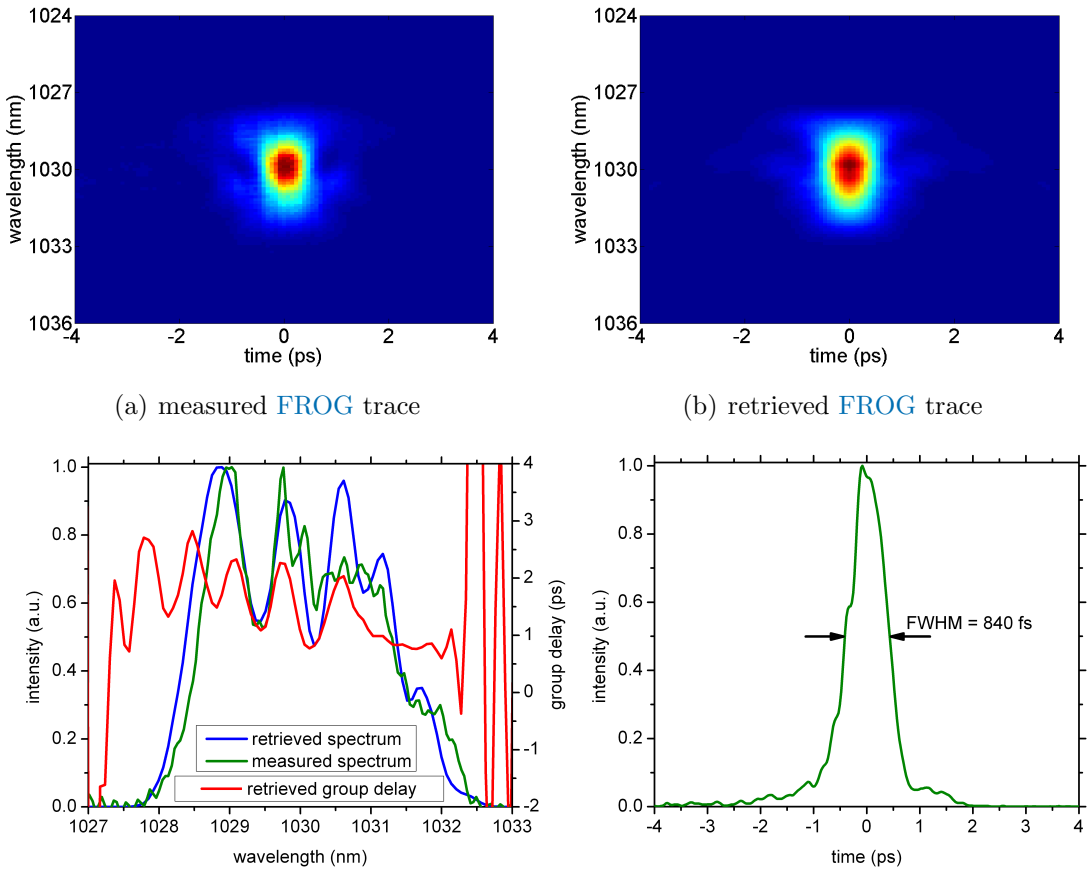

(a) measured FROG trace

(b) retrieved FROG trace

(c) retrieved spectrum and GD

(d) retrieved temporal shape

Figure 7.14: *FROG measurements of the pump laser: (a) Measured FROG trace; (b) retrieved FROG trace; (c) retrieved spectrum (blue curve) and GD (red curve); (d) temporal shape with a FWHM pulse duration of* 840 fs.

pulses which were used in the previous experiments, i.e. 1.2 ps [38]. Shot-to-shot variations of the pulse duration are minimized for compressed pulses.

Signal beam: The experiments with LBO revealed that the signal-beam quality in terms of spectral modulations had to be improved since amplification even enhanced these modulations (cf. subsection 7.2.1). Consequently, an XPW pulse-cleaning stage was implemented by Sergei Trushin, Andi Münzer and Alex Kessel parallel to the installation of the vacuum system. A short description of this pulse-cleaning setup is given in section 6.1. The cleaned signal spectrum is shown in Figure 7.15(a). The improvement of the signal spectrum was obtained at the cost of pulse energy which dropped to $\sim 0.3\,\mu$J from $10\,\mu$J without XPW. Figure 7.15(b) shows the measured signal-beam profile (FWHM $1.8\,\mathrm{x}\,1.5\,\mathrm{mm}^2$) at the location of the first LBO crystal.

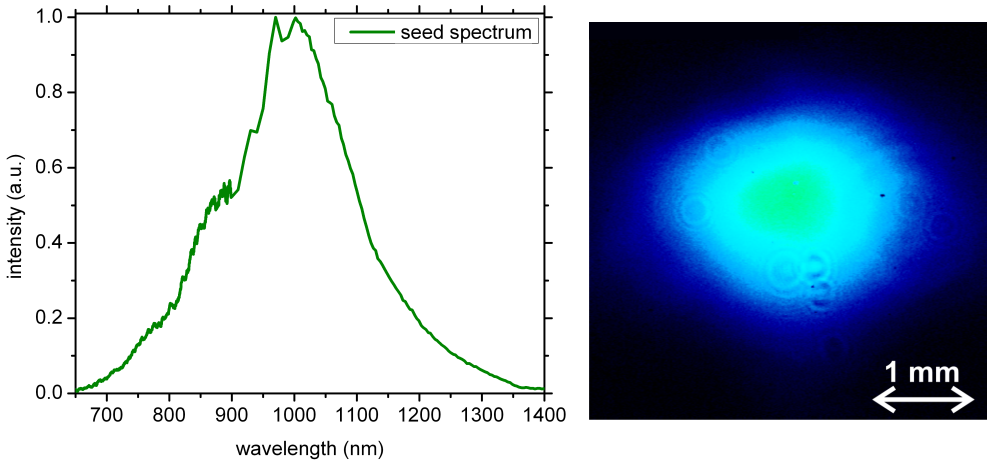

(a) seed spectrum (b) beam profile

Figure 7.15: *Broadband seed: (a) spectrum measured in front of the OPCPA stages; (b) beam profile at the location of the first OPCPA crystal with a FWHM beam size of* $1.8\,\mathrm{x}\,1.5\,\mathrm{mm}^2$.

Nonlinear crystals: The original layout aimed at amplification in two LBO stages with 4 mm and 2 mm crystal thickness, respectively. Unfortunately the reduced seed energy after the XPW resulted in a change of the amplification dynamics. Simulations presented in Figure 7.16 show that in order to counterbalance the reduced seed energy the best scheme in terms of bandwidth consists of two 4 mm thick LBO crystals (black curve). The blue curve in Figure 7.16(a) corresponds to the case of a 5 mm and the red curve to a 6 mm thick crystal in the first stage. Owing to the 2 mm thick second crystal, the second stage is not working in the regime of back conversion

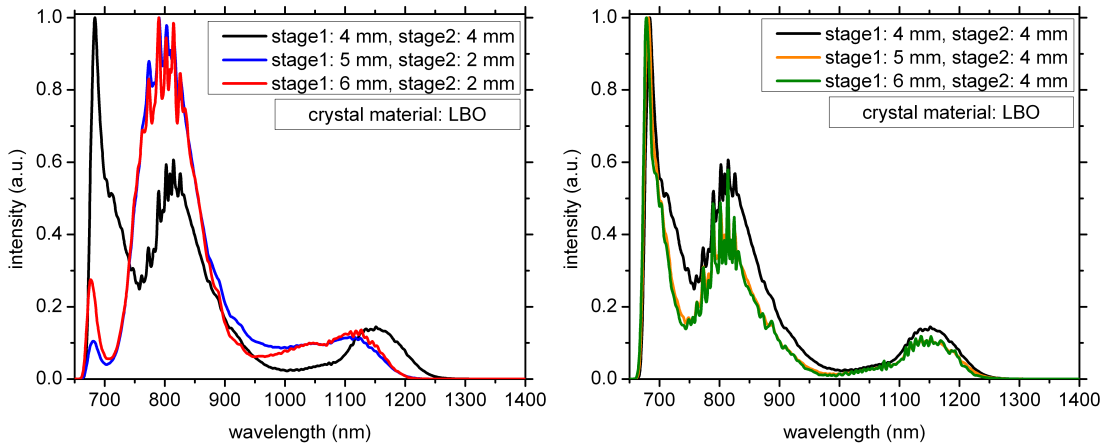

(a) case 1: 4 mm and 4 mm thick crystals
case 2: 5 mm and 2 mm thick crystals
case 3: 6 mm and 2 mm thick crystals

(b) case 1: 4 mm and 4 mm thick crystals
case 4: 5 mm and 4 mm thick crystals
case 5: 6 mm and 4 mm thick crystals

Figure 7.16: *Simulation of the amplified bandwidth for different crystal thicknesses: the black curve represents the optimum choice in terms of bandwidth and consists of two* 4 mm *thick LBO crystals. (a) The blue curve uses a combination of* 5 mm *and* 2 mm *thick crystals. The red curve is based on amplification in a* 6 mm *thick crystal in the first stage and a* 2 mm *crystal in the second stage. (b) The orange curve corresponds to* 5 mm *and* 4 mm *thick crystals and the green curve show the case for* 6 mm *and* 4 mm *thick crystals.*

and therefore the bandwidth is smaller compared to the case with two 4 mm thick crystals where back conversion is reached. Furthermore, a 4 mm thick crystal in the second stage leads to a strongly oversaturated amplification in the cases of a 5 mm (orange curve) or 6 mm (green curve) crystals in the first stage resulting in a more modulated spectrum than for the case of two 4 mm crystals as depicted in Figure 7.16(b). The energies of these cases differs by $\pm \sim 15\%$. Therefore, the experiments were performed with two 4 mm thick LBO crystals.

Unfortunately, the available 4 mm crystals had a smaller clear aperture than the planned 2 mm crystal, which led to a slight cut of the pump and signal beams in the second stage. Both crystals were cut for a phase-matching angle of 14.4° and the applied internal non-collinear angle in the experiments was 1.1°.

Dispersion management: The experiments were performed in the positive dispersion regime as shown in Figure 7.17(a). In total the signal beam was stretched by 2 mm of BaF_2 (XPW crystal), $\sim$ 2 mm of fused silica (polarizer), 19.5 m of air (propagation distance from the XPW setup to the vacuum system) and 5 mm of CaF_2 (vacuum window). The resulting GD of the signal beam is presented as the blue curve in Figure 7.17(b). In order to counterbalance the higher orders (mainly TOD) of the spectral phase, improving the nonlinear amplification in the infrared part, double-angle chirped mirrors [82] were designed and installed in front of the first OPCPA stage (**TOD** mirrors cf. Figure 7.17(a)) resulting in a GD presented as red curve in Figure 7.17(b).

After the LBO stages the spectral phase is modified by additional 5 mm of CaF_2 (vacuum window) and $\sim$ 10 m of air. The compressor mirrors (6 pairs of PC515) were designed such to compensate the total dispersion without XPW stage in com-

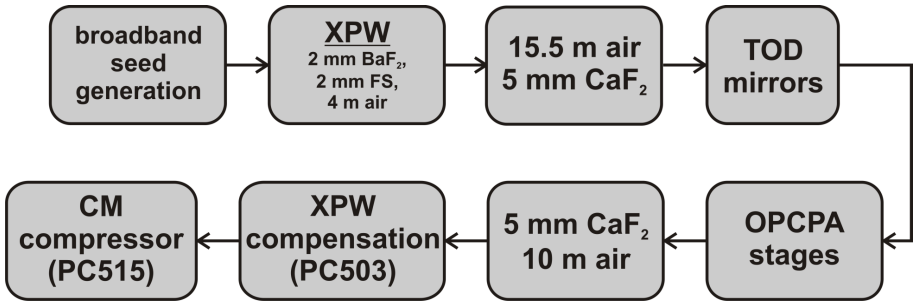

(a) Dispersion scheme

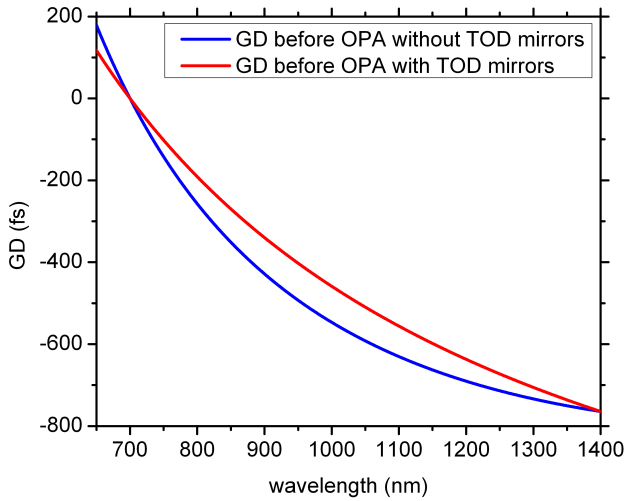

(b) GD before OPA

Figure 7.17: *(a) Dispersion scheme for the OPCPA measurements in vacuum; (b) Calculated group delay in front of the first OPCPA stage with TOD mirrors (red curve) and without TOD mirrors (blue curve).*

bination with the mentioned **TOD** mirrors. Their calculated GD for one reflection is presented in Figure 7.18(a). The dispersion introduced by the XPW is compensated by additional chirped mirrors (1 pair of PC503, cf. Figure 7.18(b)). However, X-FROG measurements of the compressed seed pulse showed that the **TOD** mirrors imprinted strong phase oscillations on the spectral phase of the signal beam. The FROG trace with installed **TOD** mirrors (Figure 7.19(a)) clearly indicates a strongly disturbed phase compared to the case without these mirrors (Figure 7.19(b)). Tuning of the angle of incidence on these mirrors did not reduce these phase oscillations. Furthermore, this oscillating phase led to a modulated amplified spectrum as depicted in Figure 7.20. Consequently, these **TOD** mirrors were removed for the

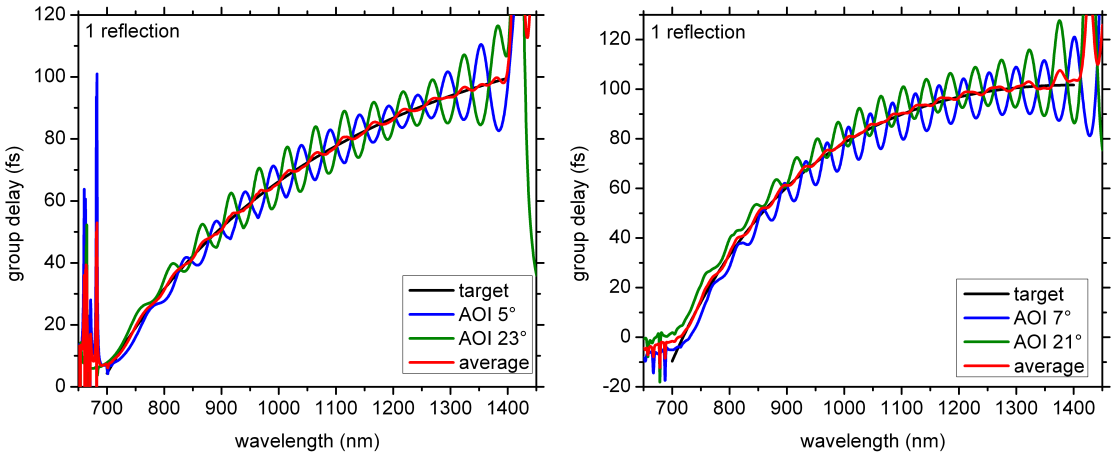

(a) PC515 (b) PC503

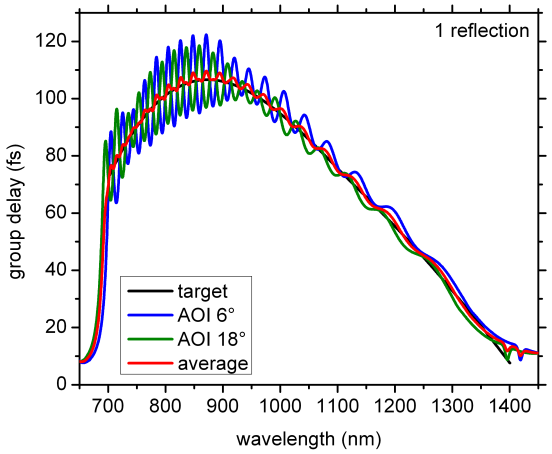

(c) PC518

Figure 7.18: *Theoretical GDs of the chirped mirrors used for pulse compression for one reflection. The black curve presents the target curve, green curve and blue curve show the GD for different angle of incidences and the red curve depicts the average of the latter cases, i.e.* $(GD_{AOI1} + GD_{AOI2})/2$. *(a) GD of the PC515 mirror design, (b) for the PC503 mirror design and (c) for the PC518 mirror design.*

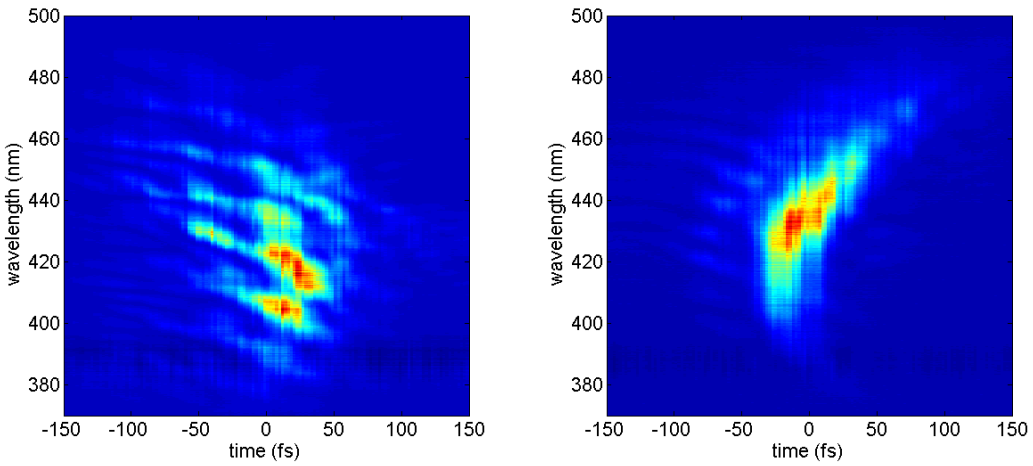

(a) X-FROG with **TOD** mirrors (b) X-FROG without **TOD** mirrors

Figure 7.19: *X-FROG measurements with the **TOD** mirrors installed (a) and without mirrors (b).*

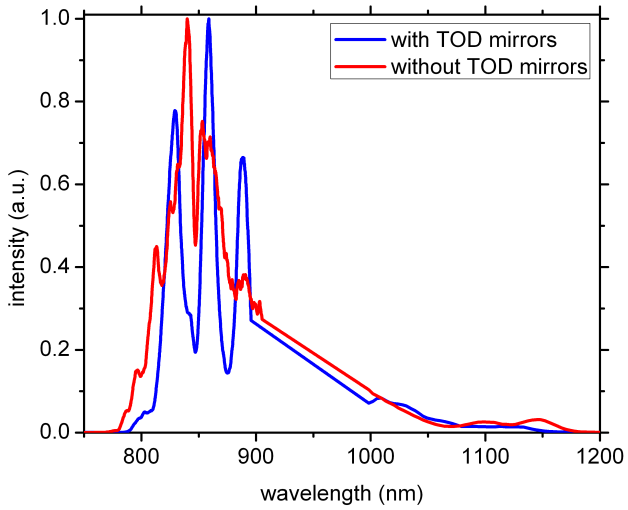

Figure 7.20: *Amplification of the broadband seed in the first OPCPA stage with installed **TOD** mirrors (blue curve) and without these mirrors (red curve).*

measurements. In order to replace these mirrors for compression, new chirped mirrors (1 pair of PC518) were designed based on the retrieved GD from the X-FROG measurement (Figure 7.19(b)) which is presented in Figure 7.18(c). Since during the time of delivery of these mirrors the OPCPA stages already were optimized for the dispersion without **TOD** mirrors, such as phase-matching and non-collinear angle and relative timing, these mirrors were installed after the amplification stages for the compression tests.

7.3.1 Results of 2-stage amplification in vacuum

Figure 7.21 presents the obtained signal spectra of these OPCPA experiments. Figure 7.21(a) plots the signal spectra on a linear scale and Figure 7.21(b) on a logarithmic scale. The green curve demonstrates the unamplified signal spectrum (not visible on the linear scale since the signal energy is too low), the red curve shows the amplified signal after the first stage and the blue curve depicts the final signal spectrum after amplification in two stages. The spectra were averaged over 15 shots, in order to reduce the effect of instabilities. Owing to the spectral smoothing of the signal spectrum in the XPW setup, the amplified spectra featured no strong modulations. The shape with the dips at 720 nm and at $1000 - 1100$ nm is an outcome of the phase mismatch in LBO (cf. Figure 4.3(a)).

The input-signal energy of $0.3\,\mu$J was amplified to $180 \pm 80\,\mu$J (averaged over 30 shots) in the first stage and further boosted to 9.8 ± 1.9 mJ (averaged over 30 shots) in the second stage. Owing to the small input-signal energy, the first stage was not operating under optimized conditions, which led to a relatively small output energy. The residual temporal jitter of 120 fs combined with pump-energy fluctuations of 9% std resulted in relatively large energy instabilities. In total, a pump-to-signal efficiency of $\sim$ 12% was demonstrated. The Fourier-limited pulse duration of the signal spectrum after the first stage was 6 fs. The amplification in the second stage increased the spectral bandwidth by amplification of the spectral wings and consequently resulted in a shortened Fourier-limited pulse duration of 4.7 fs.

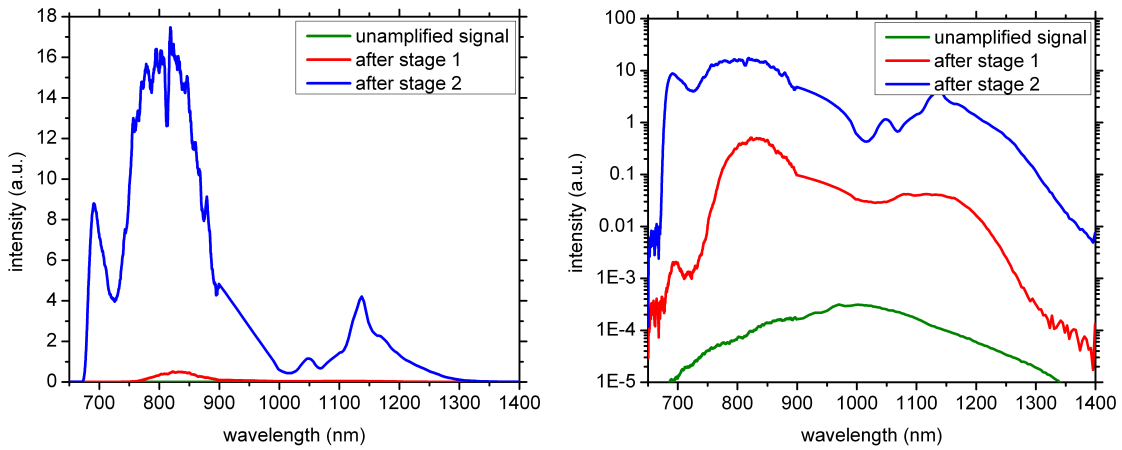

(a) signal spectra: linear scale

(b) signal spectra: logarithmic scale

Figure 7.21: *Broadband signal spectra, (a) linear, (b) logarithmic scale: unamplifed case (green curve), spectrum after amplification in the first OPCPA stage (red curve) and the finally obtained spectrum after amplification in two LBO stages (blue curve). The final spectrum supports a Fourier-limited pulse duration of* 4.7 fs.

Figure 7.22(a) presents the amplified signal-beam profile with a FWHM aperture of $5.6\,\mathrm{x}\,6.8\,\mathrm{mm}^2$ measured $\sim 4\,\mathrm{m}$ after the second OPCPA stage. The signal beam featured a reasonable focusability as shown in Figure 7.22(b) with astigmatism as the main aberration. The signal beam was focused with an $f = 400\,\mathrm{mm}$ silver mirror and captured at the focus position resulting in an FWHM beam size of $53\,\mathrm{x}\,40\,\mu\mathrm{m}^2$. In contrast, a perfect Gaussian beam with a FWHM beam size of $5.6\,\mathrm{x}\,6.8\,\mathrm{mm}^2$ focused with an $f = 400\,\mathrm{mm}$ lens would result in a far field beam size of $28\,\mathrm{x}\,24\,\mu\mathrm{m}^2$ FWHM.

SHG of the signal beam at a wavelength of 500 nm was detected during these measurements. Since the energy ratio between the fundamental and the SHG beam was 5.5×10^3 there was no detrimental influence on the OPA process. A more detailed analysis of SHG of the signal is discussed in Appendix F.

The measurements are compared to a simulation performed with Sisyfos. Here, the only fitting parameters were the phase-matching and non-collinear angle as well as the relative timing between signal and pump. Other parameters were based on the real scenario by taking the measured pump and signal energies, beam sizes, crystal thicknesses, and the measured seed spectrum (cf. Figure 7.15(a)) and phase (cf. blue curve in Figure 7.17(b)). The results are presented in Figure 7.23(a) and 7.23(b) for the first and second stages, respectively. The overall bandwidth is remarkably well reproduced for both stages. However, the infrared tail in the first stage experiences a higher amplification in the simulations compared to the measurements and in the second stage the spectral region from $700 - 800\,\mathrm{nm}$ differs from the measurements as

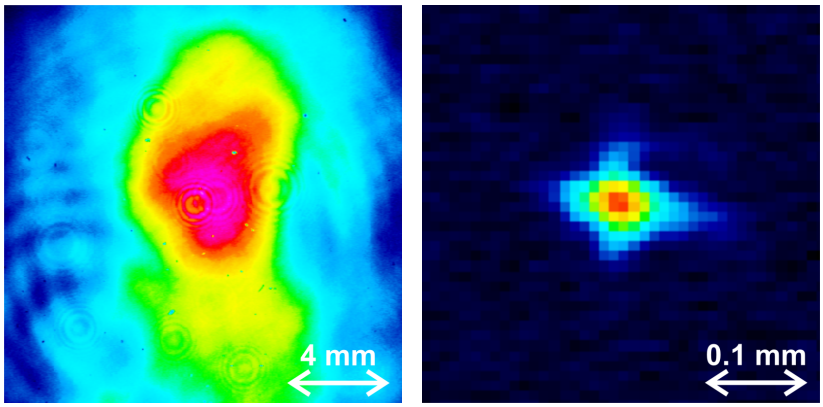

(a) amplified signal beam (b) focus of signal beam

Figure 7.22: *Beam profiles of the signal after amplification in two stages. (a) depicts the beam profile of the signal beam measured* 4 m *after the second stage. (b) shows the beam profile in the far field with a FWHM size of* 53x40 $\mu\mathrm{m}^2$.

well. The origin of these discrepancies is yet not fully understood. The evolution of the signal energy inside the crystals is shown in Figure 7.23(c) for both stages. As expected the first stage does not reach backconversion due to the small seed energy. In contrast, the second stage is over saturated. The simulated energy of the first stage is a factor of 1.19 higher than the energy obtained from the measurements and 1.09 times higher in the case of the second stage. However, the highest SHG efficiency which was obtained in the experiments was only 40%. As mentioned in section 6.2 wavefront aberrations of the fundamental beam were detected as origin for the reduced conversion efficiency. During the SHG these wavefront aberrations

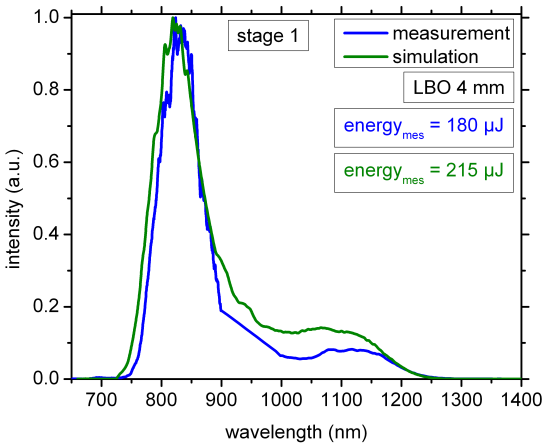

(a) first OPCPA stage

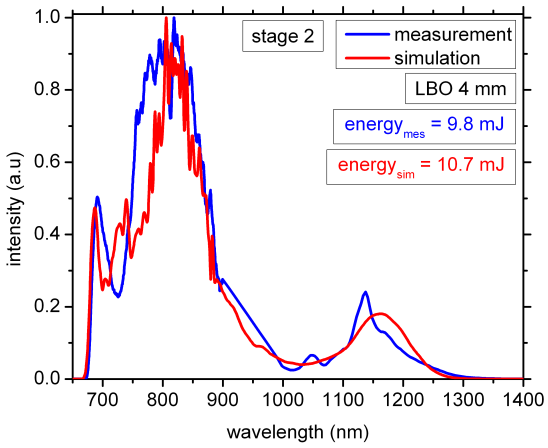

(b) second OPCPA stage

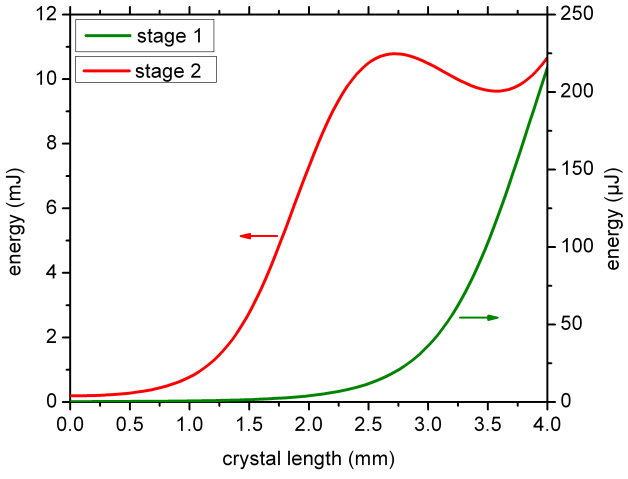

(c) signal energy over crystal length

Figure 7.23: *Comparison between the measurements and a Sisyfos simulation: Measured (blue curve) and simulated (green curve) spectra of the first OPCPA stage (a) and of the second stage (red curve) (b) . For both stages a phase-matching angle of $\theta = 14.45°$ and a non-collinear angle of $\alpha = 1.1°$ was used in the simulations. (c) signal energy over the crystal length for both stages.*

are transferred to the frequency-doubled beam and consequently lead to a reduced efficiency for the OPCPA process as well. However, since the second stage uses larger beam sizes than the first stage, wavefront aberrations of the pump beam are less pronounced and therefore have a reduced influence on the OPA performance compared to the first stage leading to a better energy match of the simulations and the measurements for the second stage.

7.3.2 Compression of signal pulses

As mentioned before the signal beam was compressed with a chirped-mirror compressor. The unamplified compressed signal pulses were characterized with the X-FROG, whereas the amplified pulses were measured with the single-shot SHG-FROG (cf. appendix E.2).

Unamplified signal pulses: The results of the X-FROG scan are presented in Figure 7.24. The agreement between the measured and retrieved traces is remarkable. The measured spectrum (green curve) is well reproduced by the retrieved spectrum (blue curve). The retrieved temporal profile has an FWHM pulse duration of 5.8 fs which is 1.16 times longer than the Fourier-limited pulse duration of 5.0 fs.

Amplified signal pulses: After the demonstration of the compressibility of the unamplified signal, the amplified pulses after two stages were characterized. It has to be mentioned that during the time of the compression experiments of the amplified pulse the spectrum and energy of the seed decreased and consequently, also the amplified spectrum changed compared to the pure amplification experiments (cf. Figure 7.21). Amplified pulse energies of ~ 10 mJ were obtained although a smaller bandwidth was amplified. Later on, damaged silver mirrors in the XPW setup were detected as the source for this detrimental behavior however the construction of the pump compressor prevented a repeat of the compression measurements. In order to avoid damage of the optical components inside the SHG-FROG, the pulse energy was reduced with a wedge and a neutral-density filter, which introduced additional dispersion. The results of this measurement are presented in Figure 7.25. The obtained signal-pulse duration was 14.2 fs, (Figure 7.25(d)), which was significantly longer than the pulse duration for the unamplified case. Since the retrieved GD manifests a positive slope (negative GDD in the frequency domain), the increase of pulse duration was not the result of the additional spectral phase introduced by the filter which introduces only positive GDD in that spectral range (cf. Figure 7.25(c)). In fact, the longer pulse duration and larger spectral group delay was a consequence of the OPA phase as expected (cf. section 4.3).

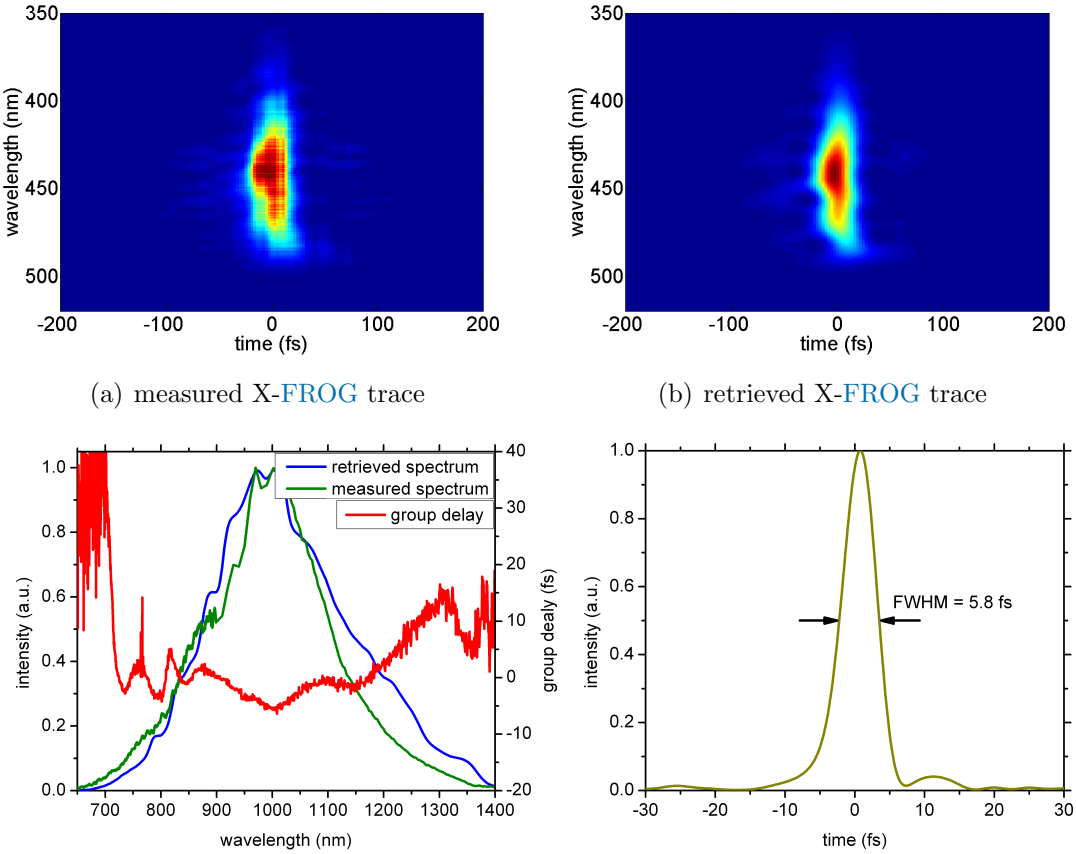

(a) measured X-FROG trace

(b) retrieved X-FROG trace

(c) retrieved spectrum and GD

(d) retrieved temporal shape

Figure 7.24: *X-FROG measurements of the unamplified signal pulse. (a) shows the measured frog trace; (b) presents the retrieved frog trace; (c) shows the retrieved (blue curve) and the measured spectrum (green curve). The retrieved GD is represented by the red curve. (d) presents the retrieved temporal shape with an FWHM pulse duration of* 5.8 fs.

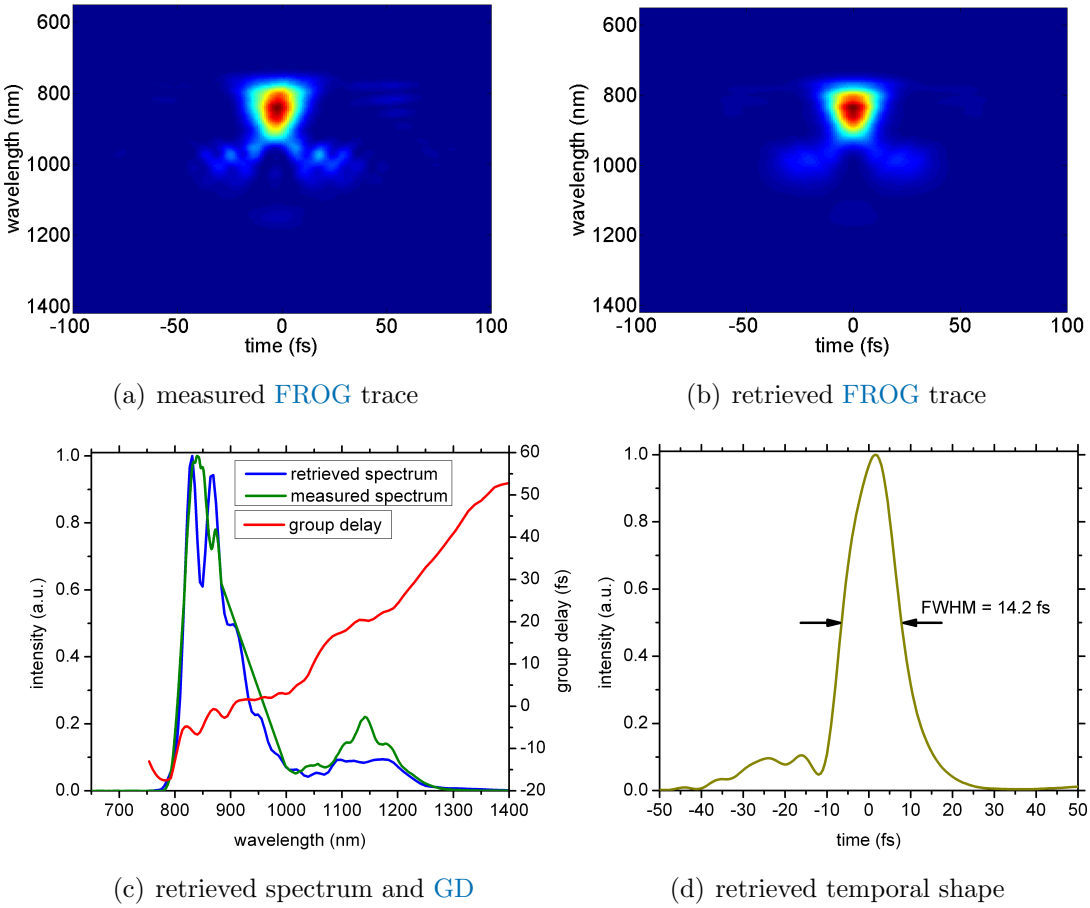

(a) measured FROG trace

(b) retrieved FROG trace

(c) retrieved spectrum and GD

(d) retrieved temporal shape

Figure 7.25: *Single-shot SHG-FROG measurements of the amplified signal pulse. The dispersion control was performed only with chirped mirrors as in the case of the unamplified pulse except with an additional neutral-density filter. (a) measured FROG trace; (b) retrieved FROG trace; (c) retrieved (blue curve) and the measured spectrum (green curve). The retrieved GD is represented by the red curve. (d) presents the retrieved temporal shape with an FWHM pulse duration of* 14.2 fs.

In order to optimize the compression by counterbalancing the additional phase introduced by the nonlinear amplification, new chirped mirrors replacing the two PC518 mirrors were designed in consideration of the measured GD presented in Figure 7.25(c). Furthermore, fused silica wedges were implemented allowing a finer dispersion control. Figure 7.26(a) presents the results of the FROG measurement. The measured FROG trace is well reproduced by the retrieval. Furthermore, the measured (green curve) and retrieved signal spectrum (blue curve) show a good agreement. The temporal shape features an FWHM pulse duration of 7 fs which is close to two optical cycles and 1.16 times longer than the Fourier-limited pulse duration. Since the newly manufactured chirped mirrors did not fully match the target design, a contribution of uncompensated higher-order phase was still present,

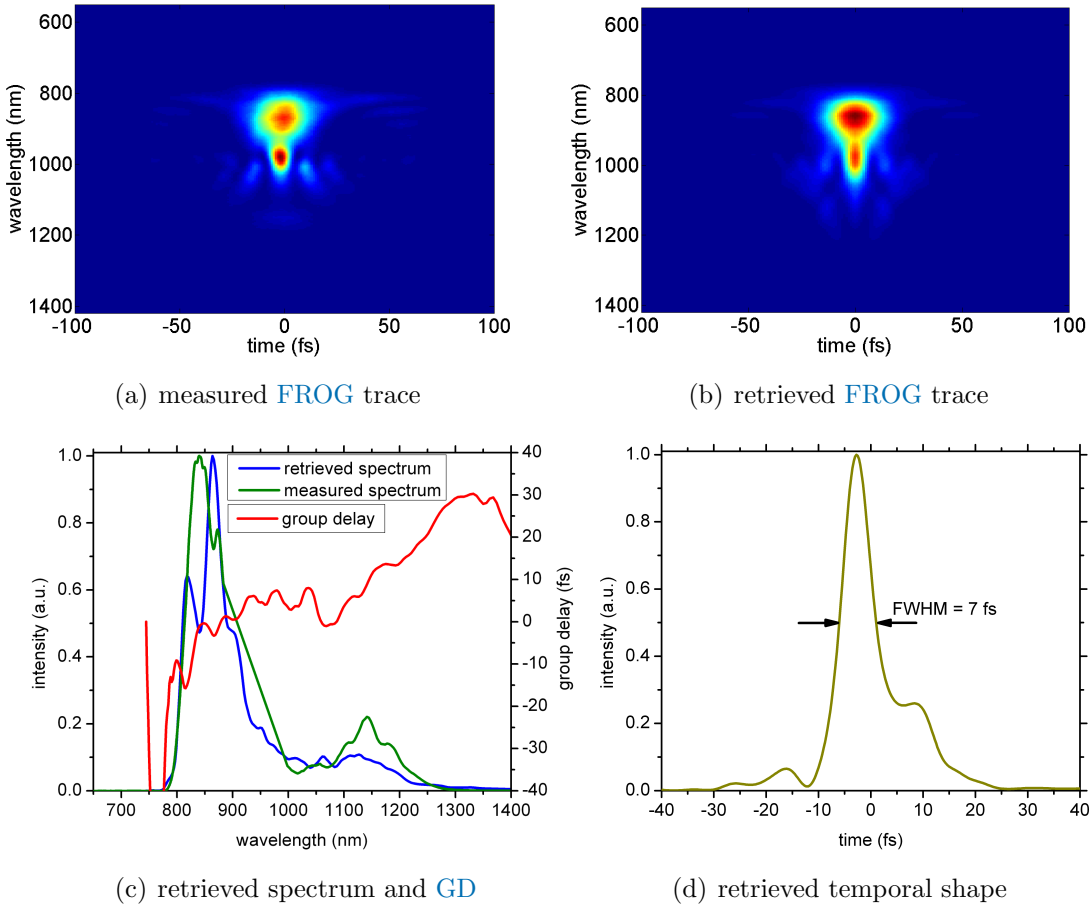

(a) measured FROG trace

(b) retrieved FROG trace

(c) retrieved spectrum and GD

(d) retrieved temporal shape

Figure 7.26: *Optimized single-shot SHG-FROG measurements of the amplified signal pulse. In these measurements the spectral phase is optimized with additional fused-silica wedges compared to Figure 7.25. (a) measured FROG trace; (b) retrieved FROG trace. The FROG error was* 1% *for a grid size of* 512 x 512 *points; (c) retrieved (blue curve) and the measured spectrum (green curve). The retrieved GD is represented by the red curve. (d) retrieved temporal shape.*

which manifested itself as a shoulder in the temporal shape and prevented compression to the Fourier limit of 6 fs. In order to estimate the uncertainty of the FROG retrieval, the measured FROG trace was evaluated several times with the Femtosoft Frog 3 program. The algorithm tries to minimize the FROG error as much as possible and thereby the algorithms can converge to different local minimum for the different retrieval runs. The different retrievals of the same FROG trace featured a pulse-duration variation of ± 0.5 fs. The retrievals differed only in the retrieved spectrum, however the spectral phase was the same for all retrievals. The retrieval, which matched the measured spectrum best, is depicted in Figure 7.26.

7.3.3 Conclusion

The experiments demonstrated the scalability of the amplified signal energy up to 10 mJ. An amplified bandwidth of $680 - 1200$ nm on the 10% level supporting a Fourier-limited pulse duration of 4.7 fs was demonstrated. Furthermore, the pulses showed a good focusability and compressibility as well. A pulse duration of 7 fs was obtained by compression with an all-chirped-mirror compressor. The throughput of the compressor was 70% leading to a compressed pulse energy of 7 mJ. Combined with the temporal shape presented in Figure 7.26(d) a peak intensity of 0.65 TW was demonstrated. Future chirped mirrors with a reduced number of reflections will allow a higher throughput. However, design and production of chirped mirrors takes around 4-12 weeks, so it is not practical to go through many iterations of CM design during the course of this thesis, given the long lead time it took to get the first OPCPA results. Therefore, an additional spectral-phase shaper would be favorable in order to optimize the compression and increase the flexibility in case modifications in the OPCPA chain need to be accomodated. As an alternative Fastlite, the manufacturer of acousto-optic programmable dispersive filters, offers a Dazzler based on Calomel (Hg_2Cl_2) covering more than the PFS bandwidth ($650 - 1400$ nm). The device is able to compensate its own crystal dispersion and still offers a programmable GD of 2 ps. Therefore, even the full stretching could be realized by this shaper. The flexibility of phase shaping comes at the costs of signal-pulse energy (10% efficiency), which however, can be compensated by an additional OPCPA stage acting as a pre-amplifier. With such a device, close to Fourier-limited pulse durations will be realizable.

As will be described in appendix C.1, tilted pulse fronts between the signal and pump beam mainly imprint a spatial chirp on the signal beam and detriment the spatial quality. In order to keep the first experiments in vacuum as simple as possible, a pulse-front-matching setup was not implemented. For further experiments using higher pump energies and consequently applying larger beam sizes, a pulse-front-matching setup will be implemented.

Part III

Summary and outlook

8 — Summary and outlook

The PFS project will deliver few-cycle light pulses (5 fs) combined with pulse energies up to the J-level (> 3 J) for the first time. In order to reach these demanding parameters, the PFS is based on a modified OPCPA scheme in which thin crystals enable the amplification of ultra-broad bandwidths supporting pulse durations in the few-cycle regime. 1 ps short pump pulses allow the use of high pump intensities and therefore facilitates high gains despite the short crystal lengths. An additional advantage of short pump-pulse durations is the achievable intrinsically good temporal contrast which is required for the expected peak intensities of 10^{22} W/cm^2. In this work the building blocks of this novel concept such as amplified bandwidth, sufficient high gain, compressibility of the signal pulses and the increase of temporal contrast due to the nonlinear amplification were investigated and verified.

In order to optimize the parameters of the nonlinear amplification and to perform a design study of the multiple staged OPCPA chain of the PFS, an existing simulation program was further developed and improved. As a result the calculation time for one OPCPA stage is reduced from 8 hours to 30 seconds enabling design studies for the PFS system in a remarkably short time. The simulations led to a re-design of the OPCPA layout making use of LBO as a very promising alternative to DKDP crystals in the first nonlinear stages where the available crystal size is not the limiting factor. Owing to the three times higher nonlinearity of LBO compared to DKDP, the estimated eight DKDP OPCPA stages pumped by 20 J of total pump energy are reduced to five stages. The first two stages are equipped with LBO crystals pumped by one 5 J beam and the residual three pump beams are used to pump three high-energy DKDP stages.

One of the main aims of this thesis was to demonstrate the amplification of ultrabroad bandwidths supporting few-cycle pulse durations in thin DKDP crystals. The broadband signal pulses generated in two cascaded HCFs were amplified in a single OPCPA stage equipped with DKDP crystals of different thickness. The nonlinear interaction was pumped with picosecond pump pulses at an intensity of 100 $\frac{\mathrm{GW}}{\mathrm{cm}^2}$. Even a 7 mm thick DKDP crystal supported an amplified bandwidth of $830 - 1310$ nm at a 10% level, allowing for a Fourier-limited pulse duration of 6.1 fs. This is a very encouraging result for the further development of the PFS project since the point design of the OPCPA chain (compare chapter 5) aims for crystal thicknesses of DKDP of only $1.8 - 3.3$ mm allowing even broader amplified bandwidths.

In a two-stage OPCPA experiment the performance of LBO crystals was investigated. Amplification was performed in two consecutive LBO stages with 4 mm and 2 mm crystal thickness, respectively. Strong SF of the pump laser in air limited the usable total pump energy for these experiments to ~ 40 mJ at 515 nm. Nevertheless, the amplified spectrum supports a Fourier-limited pulse duration of 5 fs and the energy is boosted to 4 mJ. The amplified broadband pulses were compressed with 28 mm of CaF_2. The retrieved FWHM pulse duration for the main peak is 9 fs. In addition, the contrast enhancement due to the nonlinear amplification was investigated. The temporal contrast is enhanced in each OPCPA stage and even post pulses located 2 ps after the main peak experience a significantly reduced amplification leading to a very good temporal contrast on the picosecond time scale.

A vacuum imaging system containing two OPCPA stages was designed and constructed in order to apply the full available pump energy and avoid limitations by SF. This measure increases the usable pump energy to ~ 90 mJ for the frequency-doubled beam. Cleaning of the strongly modulated signal spectrum is performed in an XPW setup implemented in front of the vacuum system. Within two LBO stages with 4 mm crystal thickness each, the signal energy is boosted to 10 mJ. The bandwidth of the amplified pulse supports a Fourier-limited pulse duration of only 4.7 fs. Compression of the broadband signal is performed with an all-chirped-mirror compressor. 16 reflections on double-angle chirped mirrors compress the positively chirped signal pulses to 7 fs. A peak intensity of 0.65 TW is obtained when taking into account the temporal shape and the throughput of 70% of the compressor.

The presented experimental results demonstrate the feasibility of short-pulse-pumped (1 ps) OPCPA systems based on thin nonlinear crystals to push the frontiers of the current state-of-the-art light parameters to the sub-two-optical cycle regime combined with high pulse energies reaching the Joule-level. They prove the feasibility of the concept of the modified OPCPA approach applied in the PFS system and are very promising for the future success of the project since no physical "show-stoppers" were encountered.

8.1 Outlook

Since the conclusion of the last OPCPA experiments, some changes and improvements of the PFS system were performed:

- **Frontend system:** The XPW setup was moved closer to the output of the two cascaded HCFs in order to shorten the propagation distance. This leads to an improved stability on a shot-to-shot basis and furthermore to a more reliable output from day to day.

  The output of the idler generation setup was used as a seed for an OPCPA test measurement performed with the vacuum setup with two LBO stages. The obtained amplified spectra are presented in Figure 8.1 on a linear scale (a) and a logarithmic scale (b). It can be observed that the amplified spectra do not exhibit fast and strong modulations. The slow modulation is a result of the phase-matching conditions of LBO. The amplified bandwidth supports a Fourier-limited pulse duration of 5.3 fs. The seed pulses are amplified from 3 μJ to $\sim$ 7 mJ. Consequently, the idler generation has the potential for a seed source for the OPCPA chain of the PFS. However, the effect of the residual chirp on the focusability and the compression of the amplified pulses still has to be checked.

  In addition to the XPW and idler-generation setup, a new alternative scheme for the broadband seed generation based on collinear DFG is currently investigated. The spectrally broadened output of one HCF is sent to an XPW stage which generates a smoothed signal pulse. The transmitted fundamental beam is used as a pump. Collinear DFG of the two input beams is performed in the subsequent BBO crystal. Owing to cascaded nonlinear processes, a smooth spectrum in the wavelength range of $700 - 1400$ nm is obtained with efficiencies close to 10%. An energy of 5 μJ is demonstrated at a pump energy of 60 μJ. Further upscaling of the energy is possible since the total energy avail-

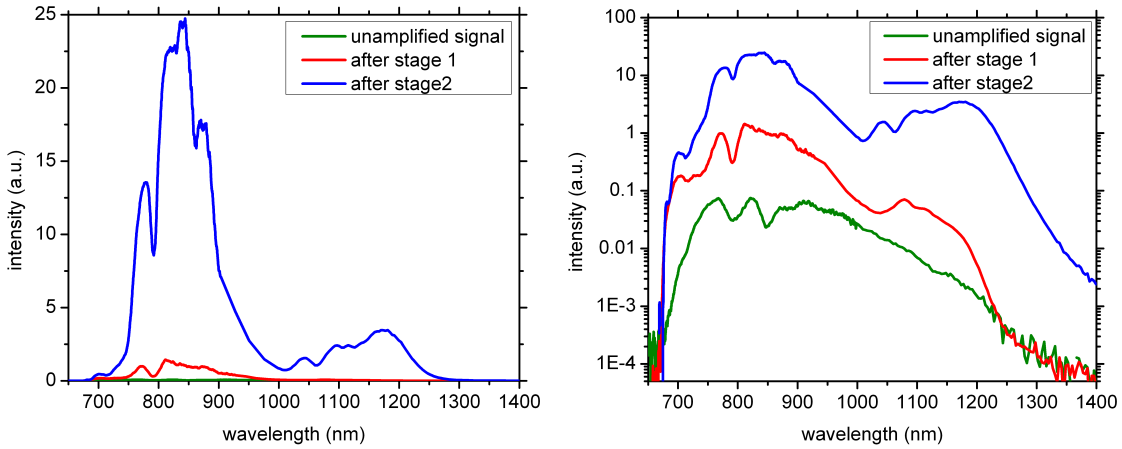

(a) signal spectra: linear scale

(b) signal spectra: logarithmic scale

Figure 8.1: *Amplification of the output seed of the idler generation setup in two LBO stages: unamplifed case (green curve), spectrum after amplification in the first OPCPA stage (red curve) and the finally obtained spectrum after amplification in two LBO stages (blue curve). (a) presents the spectra in a linear scale. (b) instead shows the same spectra in a logarithmic way.*

able after the HCF is 300 μJ. In order to understand the processes occuring in the BBO crystal, simulations are carried out. However, a full picture of the nonlinear interactions has not yet been obtained and more simulations and measurements are required. Nevertheless, a first experimental test where the output of this setup is used to seed the OPCPA chain will be performed in the upcoming OPCPA campaigns that are scheduled just after the installation of the vacuum compressor.

- **Pump-laser system:** The dichroic mirror of the 20-pass imaging Yb:YAG amplifier, which limited the output energy to 400 mJ due to damage was replaced by a specimen with a more resilient coating. Therefore the output energy was recently increased to 800 mJ at 1 Hz repetition rate.

  The grating compressor of the pump laser was reinstalled in vacuum in order to reduce the timing jitter between signal and pump beam at the OPCPA crystals and to minimize effects due to the nonlinear beam propagation further. Figure 8.2 depicts the schematic layout of the vacuum compressor. The timing jitter without active stabilization is reduced to 103 fs rms. Consequently, for a further decrease of this level more measurements are necessary in order to detect the origin of the residual jitter.

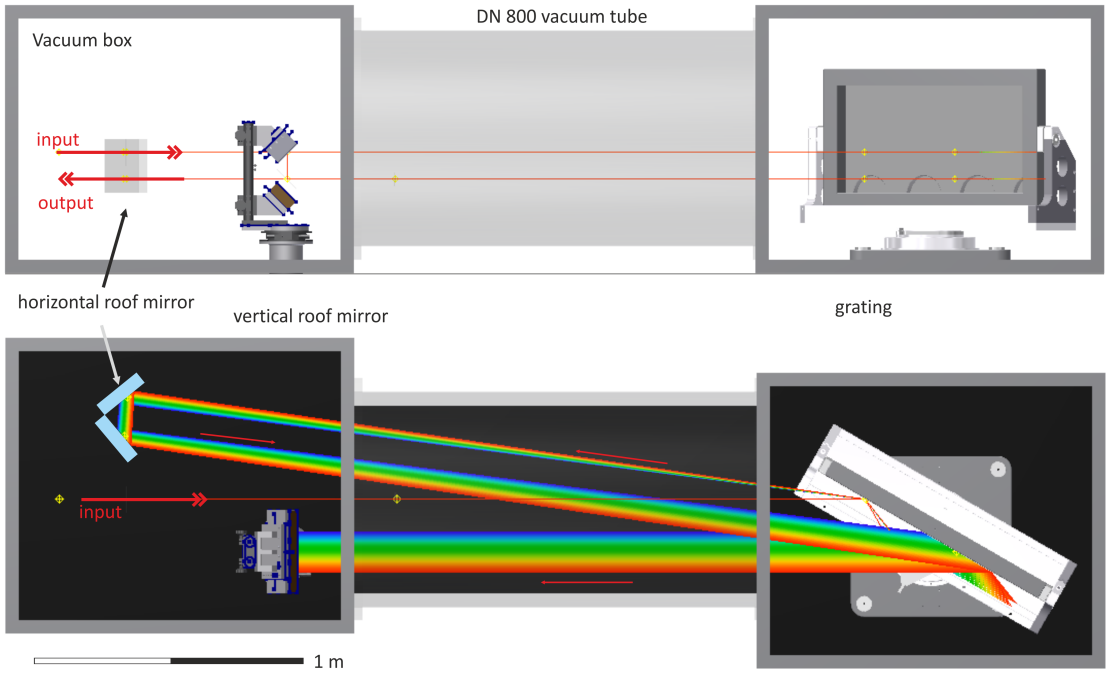

Figure 8.2: *Schematic layout of the vacuum compressor for the pump laser. This picture is originally presented in the PhD thesis of Sandro Klingebiel [38] and used with permission from the original author.*

- **OPCPA chain:** Since the OPCPA vacuum system was already designed for a 1 J fundamental pump pulse energy, no rearrangements of the system have to be performed. The two LBO stages will be pumped by $\sim 400\,\mathrm{mJ}$ in total for the frequency-doubled pump beam which is predicted to result in an amplified signal energy of $\sim 50\,\mathrm{mJ}$. However, due to the enlarged beam apertures in the second stage compared to the experiments presented in this thesis, a pulse-front-tilting setup for the pump laser will be implemented in order to maintain a good spatial signal beam profile.

In order to boost the amplified signal energy further, the pump energy has to be increased for future experiments. An additional imaging Yb:YAG amplifier, which is expected to be in operation by the end of 2014, will boost the fundamental pump energy up to 10 J leading to a frequency-doubled pump energy of 5 J pumping three OPCPA stages: two LBO stages and one DKDP stage. In order to keep the construction costs low, the existing OPCPA vacuum system will be extended by an additional OPCPA stage. Signal-pulse energies of $0.75 - 1\,\mathrm{J}$ are expected resulting in 200 TW pulses. These energies and powers are already close to the desired parameters the PFS system is aiming for and will allow HHG at solid surfaces.

The vacuum system for the pump compressor can support pulse compression for two 10 J pump-laser beams and consequently, a second 10 J Yb:YAG amplifier stage will be implemented in 2015. The total available pump energy will be doubled to 10 J at 515 nm and is applied to pump four OPCPA stages. The upgraded pump energy allows signal energies of ~ 2 J and boosts the power up to 400 TW.

Part IV

Appendix

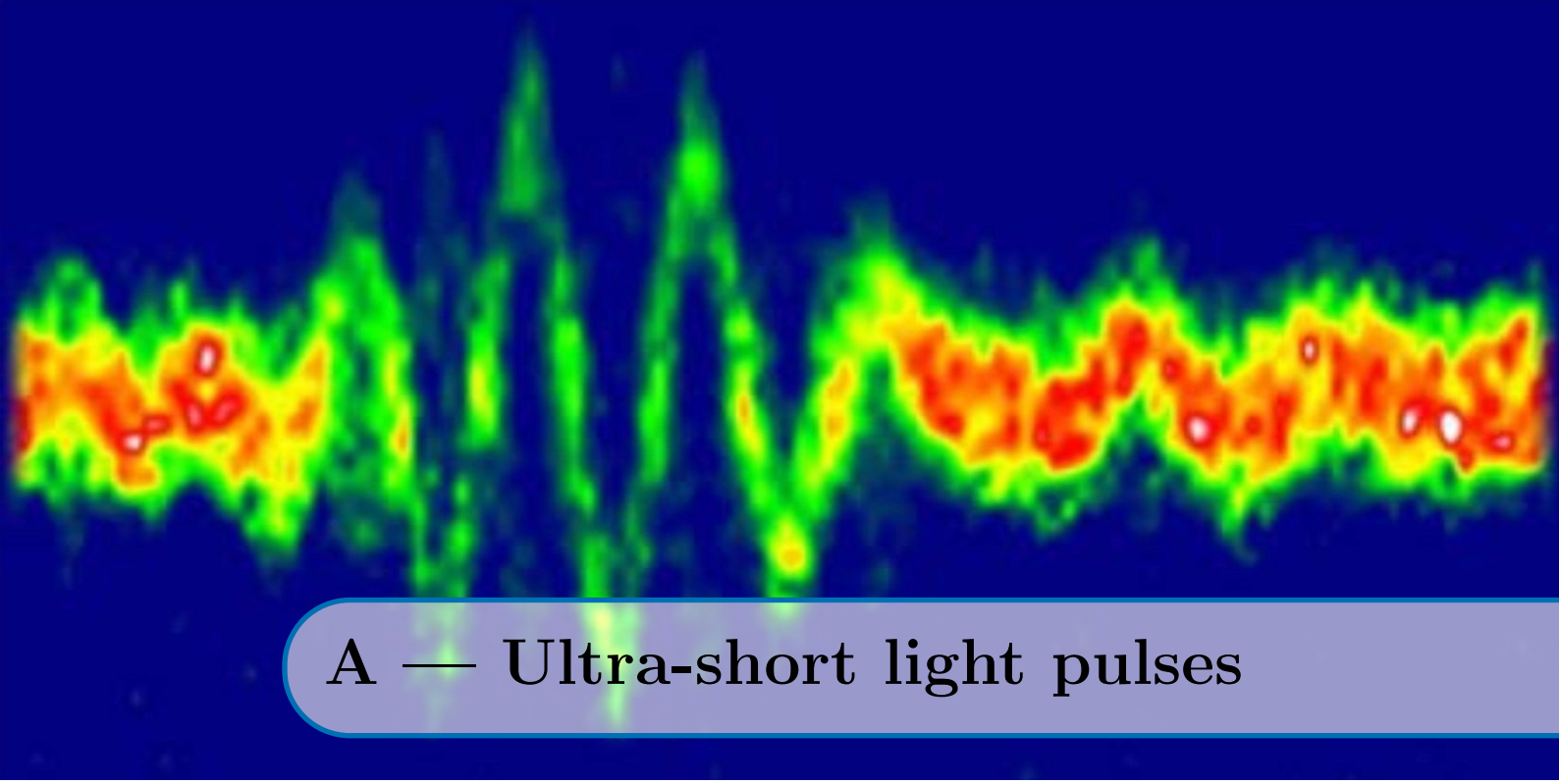

A — Ultra-short light pulses

The PFS system is aiming for ultra-short light pulses in the sub-two-cycle regime (5 fs). This chapter is dedicated to the mathematical description of such pulses. It follows the books by R. Trebino [104] and J. C. Diels and W. Rudolph [105].

A light pulse can be described by its electric field defined in space and time $E(x, y, z, t)$. Since in this chapter the interests lies on the temporal characteristics of short light pulses only the dependence of the electric field on the time coordinate $E(t)$ is taken into account.

The temporal electric field describing short light pulses can be written as:

$$E(t) = \frac{1}{2}\sqrt{I(t)}e^{i(\omega_0 t - \Phi(t))} + c.c,$$

where $I(t) = |E(t)|^2$ and $\Phi(t)$ are the temporal intensity and temporal phase, respectively. ω_0 is the rapidly varying carrier angular frequency and $c.c$ stands for the complex conjugate. It has to be mentioned that some definitions in literature include the carrier frequency ω_0 into the temporal phase $\Phi(t)$. It is convenient to describe the electric field as a complex function for reasons of mathematical simplicity. However, the temporal electric field is a real quantity and consequently the complex conjugate has to be added, although in the following treatment it is omitted for the sake of simplicity.

Especially for short pulses it is beneficial to describe the light pulse in the frequency domain and not in the temporal domain. Similar to the definition of the temporal electric field, the field in the frequency domain can be written as:

$$E(\omega) = \sqrt{S(\omega)}e^{-i\varphi(\omega)},$$

where $S(\omega) = |E(\omega)|^2$ and $\varphi(\omega)$ are the spectrum and the spectral phase of the light pulse.

The temporal domain and the frequency domain are connected to each other via the Fourier transformation (FT) and the Fourier back transformation (FT^{-1}):

$$\begin{aligned} E(\omega) &= \frac{1}{\sqrt{\pi}} FT[E(t)] \\ E(t) &= \frac{1}{\sqrt{\pi}} FT^{-1}[E(\omega)]. \end{aligned}$$

The basic principle of generating very short pulses is based on the superposition principle of wave mechanics, which states that temporal energy localization is obtained when mutually coherent waves are superimposed in time (cf. Figure A.1). The interplay between constructive and destructive interference in a superposition of monochromatic light waves in the time domain relates to a train of short pulses [16]. The Fourier transformation which is the mathematical description of wave superposition dictates that confinement in time gets more pronounced for a larger number of properly phased spectral components of comparable amplitudes. Furthermore, the shortest pulse duration, i.e. Fourier-limited pulse duration, is obtained for a flat or linear spectral phase, i.e. $\frac{\partial \varphi}{\partial \omega} = constant$.

If the derivative of the spectral phase is not constant the pulse is longer than its Fourier-limited pulse duration, the pulse is stretched in time. Consequently, the spectral phase has a major influence on the temporal pulse shape. It is common to

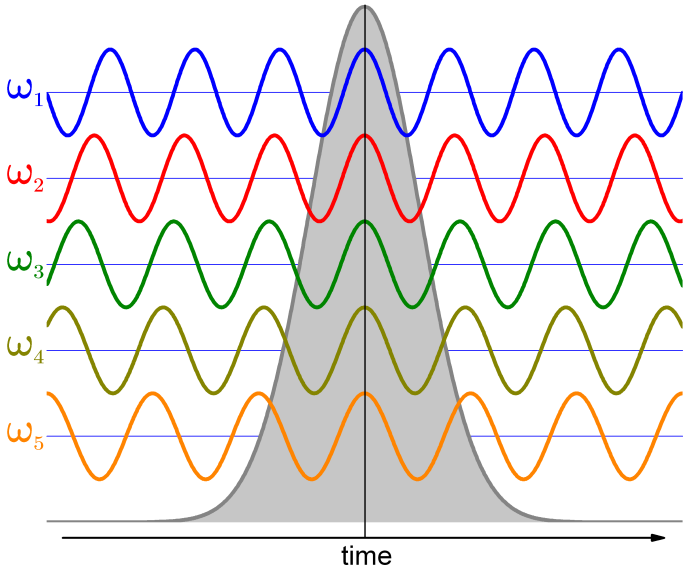

Figure A.1: *Superposition of monochromatic light waves in time.*

describe the spectral phase as a Taylor expansion around the carrier frequency ω_0:

$$\varphi(\omega) = \sum_{m=0}^{\inf} \frac{(\omega - \omega_0)^m}{m!} \left(\frac{\partial^m}{\partial \omega^m} \varphi(\omega) \right)_{\omega=\omega_0}$$

The derivatives of the spectral phase are known as dispersion coefficients:

- the first derivative $\frac{\partial}{\partial \omega}\varphi(\omega)|_{\omega=\omega_0}$ is called group delay GD
- the second derivative $\frac{\partial^2}{\partial \omega^2}\varphi(\omega)|_{\omega=\omega_0}$ is the group-delay dispersion GDD
- the third derivative $\frac{\partial^3}{\partial \omega^3}\varphi(\omega)|_{\omega=\omega_0}$ is known as the third-order dispersion TOD
- the fourth derivative $\frac{\partial^4}{\partial \omega^4}\varphi(\omega)|_{\omega=\omega_0}$ is the fourth-order dispersion FOD
- and higher orders.

Figure A.2 depicts the effect of the first four dispersion coefficients on the temporal pulse shape and on the temporal electric field for a 5 fs short light pulse with a central wavelength of $\lambda_0 = 920\,\text{nm}$. The upper row shows the temporal intensities which are normalized to their peak values on a linear scale, whereas the middle row presents the intensity on a logarithmic scale (red curves). The thin black curve presents the temporal shape for the case of a compressed pulse (cf. Figure A.2(a)). The lower row depicts the temporal amplitude (green curve) and the temporal electric field (blue curve). The GD shifts the pulse in time whereas the GDD chirps the pulse and consequently increases the pulse duration (5 fs $\rightarrow$ 12.4 fs). The TOD mainly leads to an asymmetry of the pulse shape and the fourth-order dispersion (FOD) results in pulse stretching and enhanced wings and consequently to a decrease of the temporal contrast.

In order to achieve compressed pulse durations of a few femtoseconds, an accurate control of the spectral phase is required. This control can be realized by a variety of different setups such as stretchers or compressors based on prisms [106] and gratings [107] or by material [108] and chirped mirrors [109]. For example the phase introduced by propagation through material can be written as $\varphi(\omega) = \frac{x}{c}\omega n(\omega)$, where c is the speed of light, x is the propagation length through the material and $n(\omega)$ is the frequency-dependent refractive index. In addition, programmable spectral phase shapers, e.g. liquid-crystal modulators [110] or accousto-optic programmable dispersive filters [111] are currently well established which allow for a finer control of dispersion in a reduced group-delay range compared to the aforementioned techniques. The phase introduced by consecutive components add up and in the ideal case a flat/linear total phase is achieved at the target position of the laser-matter experiment.

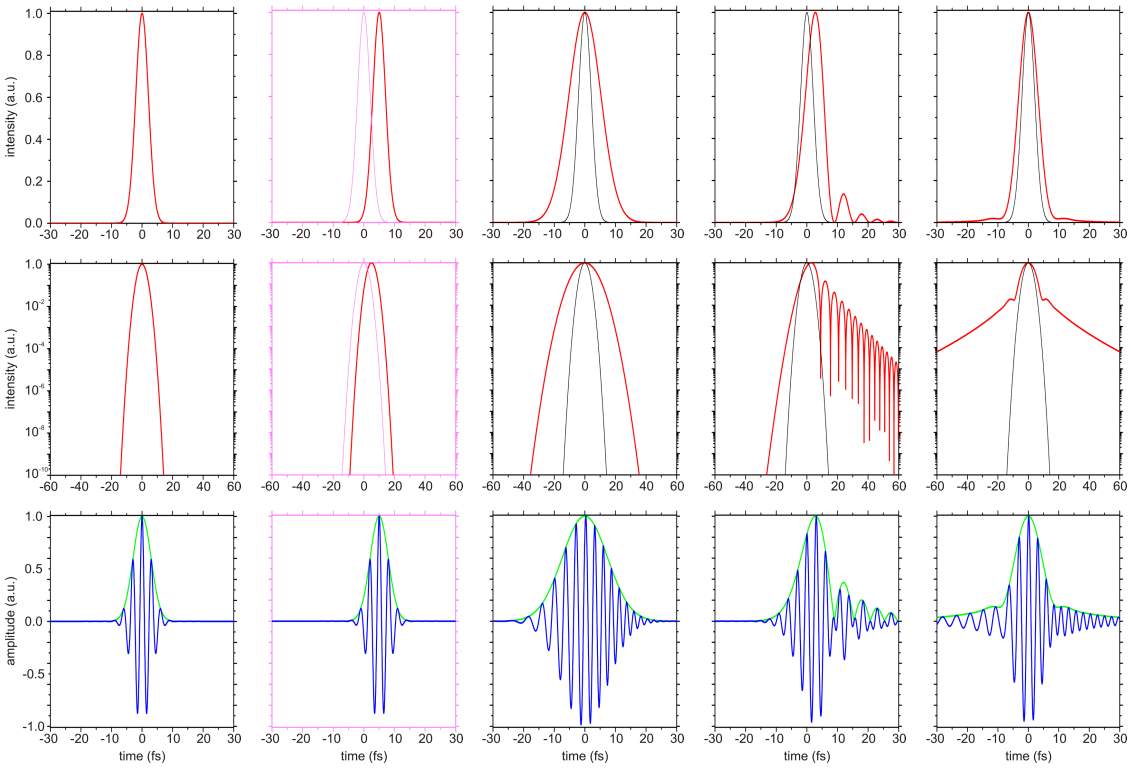

(a) flat phase (b) GD = 5fs (c) GDD = 20fs^2 (d) TOD = 100fs^3 (e) FOD = 500fs^4

Figure A.2: *Influence of the different dispersion coefficients on the temporal pulse shape and the temporal electric field of a* 5 fs *Gaussian light pulse with a central wavelength of* $\lambda_0 = 920\,\mathrm{nm}$*: (a) case of a compressed pulse, i.e. flat phase, (b)* GD $= 5\,\mathrm{fs}$*, (c)* GDD $= 20\,\mathrm{fs}^2$*, (d)* TOD $= 100\,\mathrm{fs}^3$*, (e)* FOD $= 500\,\mathrm{fs}^4$*.*

B — Benchmark of SOPAS

In order to show the validity of the simulation results, a comparison between the SOPAS simulations and experimental measurements was performed. To prove the validity of the simulations, two aspects were investigated in particular, namely the amplified bandwidth in the small-signal-gain regime and the pump depletion and saturation behavior. The calculations were based on the real scenario by taking the measured pump and signal energies, beam sizes, crystal thicknesses and the non-collinear angle. The only adjustable parameter was the phase-matching angle. Owing to the usual uncertainty in the cut-angle information provided by the crystal manufacturers, this assumption was justified.

The following results are published in [7] in a slightly modified form. An electronic reprint is attached in appendix G.1 with the permission of OSA. In the publication the simulations were performed with a Gaussian-shaped seed spectrum. In contrast, the simulations presented here are based on a measured input spectrum.

Information about the experimental setup and a discussion of the experimental results are given in detail in section 7.1 and in [7]. A pump energy of $\sim 800\,\mu$J was used for these experiments. The pump-pulse duration was 2.1 ps and the pump-beam diameter inside the DKDP crystal was measured to $\sim 660\,\mu$m FWHM. The signal-beam size was matched to the pump-beam size. For the small-signal-gain measurements a 3 mm thick DKDP was seeded with the stretched broadband signal generated in two subsequent HCFs (cf. Figure 7.1). In contrast, the saturation measurements were performed in a 5 mm thick DKDP crystal, which was seeded with a narrow-band compressed signal pulse ($\tau = 31$ fs, $\lambda_0 = 780$ nm, $\Delta\lambda = 45$ nm).

B.1 Small-signal-gain measurements

The measured small-signal-gain curves at different phase-matching angles for a 3 mm thick DKDP crystal are shown in Figure B.1. Alongside these, Figure B.1 also shows the results of the simulations that correspond to the experimental scenario, represented by the dotted lines. Since the spectrum of the signal pulse was artificially suppressed below 800 nm using a low-pass filter, no reliable gain information for this region could be extracted from the experiment. In addition, a narrow dip was observed in the measured gain curves around 920 nm which on one hand was a result of a very weak signal input energy at that wavelength and on the other hand originated from the way of spectral detection resulting in inaccurate measurements in this wavelength range (cf. appendix E.1). The calculations agree well with the measured gain curves both in absolute values and shape except for the blue curve in the red part of the spectrum. The origin of this discrepancy has not yet been understood. Nevertheless, the dependence on the phase-matching angle is also closely reproduced. The dip in the middle of the gain curves for the phase-matching angles of 36.80° and 36.90°, which is due to the characteristic phase-matching curve of the DKDP, is also well rendered.

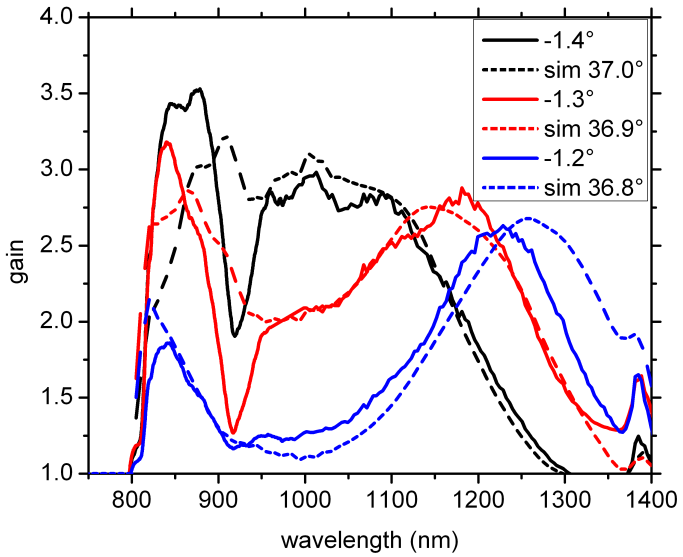

Figure B.1: *Investigation of the small-signal gain: Measured gain (solid lines) versus calculated gain (dotted lines) for a 3 mm thick DKDP crystal for three different phase-matching angles. The crystal was cut for a phase-matching angle of 37.1°, according to the manufacturer. The angles for the experimental curves are given as the deviation from the nominal cut angle. For the calculation an offset in the phase-matching angle has been chosen to achieve the best possible fit with experiment.*

B.2 Saturation measurements

A narrow-band compressed signal pulse ($\tau = 31\,\text{fs}$, $\lambda_c = 780\,\text{nm}$, $\Delta\lambda = 45\,\text{nm}$) was used to investigate the amplification behavior in saturation. The output pulse energy E_{out} was measured as a function of the input energy E_{in}, determining the extracted energy $E_{out} - E_{in}$. The results are presented in Figure B.2. The measured temporal profile of the signal pulse is shown in the inset of Figure B.2, clearly indicating the presence of a pre/post-pulse with an intensity of approximately 10% of the main pulse. Since the temporal profile was characterized with an SHG-FROG it was not possible to distinguish between pre- and post-pulses. However, in the simulations this pedestal was taken into account as a post pulse. The OPA gain started to be saturated at $E_{in} > 0.5\,\mu\text{J}$. The calculations are consistent with the measured data.

Therefore, it was concluded that the SOPAS program is able to reliably model the small-signal and saturation behavior of the optical parametric amplification process.

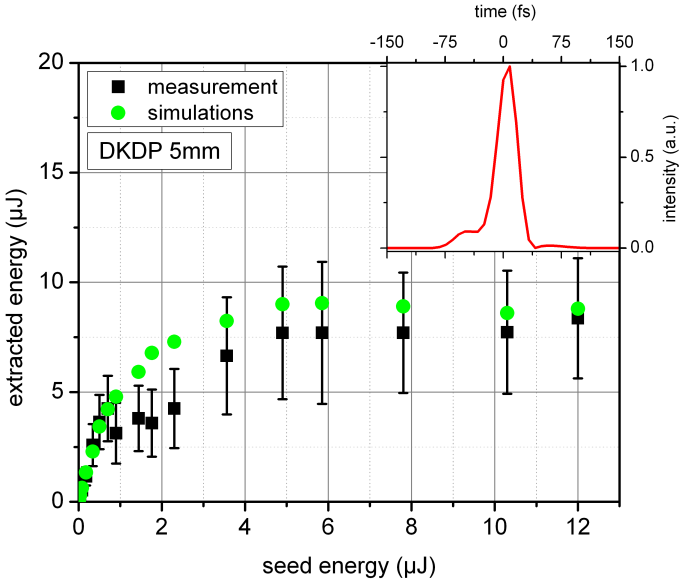

Figure B.2: *Extracted energy vs. input signal energy: The black squares represent the measurements using a* 31 fs *input pulse (the temporal profile of which is shown in the inset). The error bars of the measured data are the standard deviation of 100 shots, which originate both from the temporal jitter and the shot-to-shot pump-energy fluctuation. The green circles show the results for the calculation.*

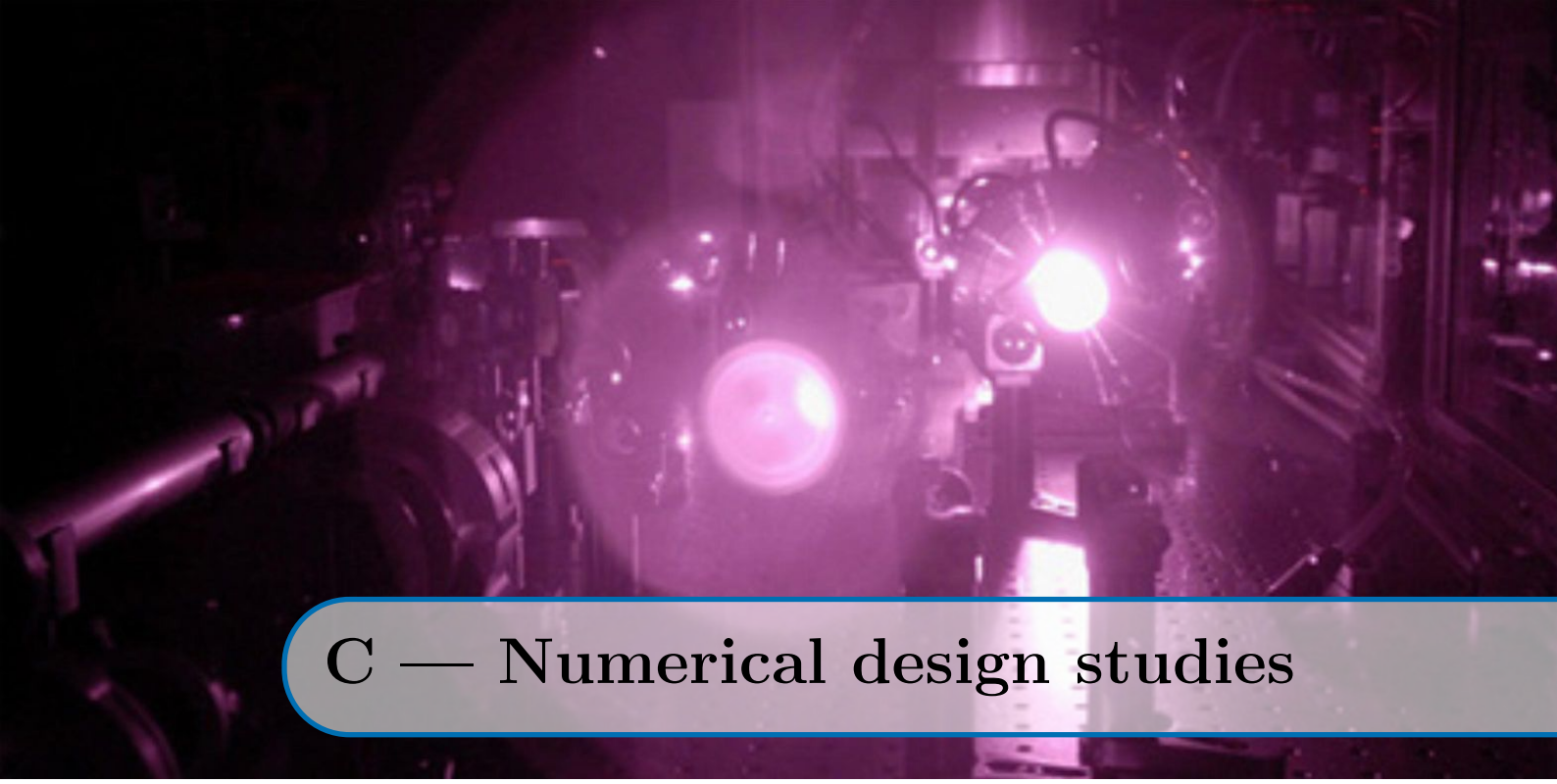

C — Numerical design studies

C.1 Influence of beam and crystal parameters on OPCPA

As already mentioned in section 4.2 it is essential to have a substantiated knowledge about the process of amplification for an efficient optimization of an OPCPA system. Especially for nonlinear processes, small changes in the input parameters can have a large influence on the output performance of a system. Here, the results of simulations investigating the dependence of the output performance of an OPCPA stage on different beam and crystal parameters are presented. Some of these results have been discussed already in section 4.2.

Some of the parameters are fixed by the experimental setup and the system design, others can be adapted. In order to obtain a better illustration of the dependencies, this section is supported by simulations. If not otherwise stated the simulations presented in the next section are based on the following parameters: A 4 mm thick LBO crystal is used for the amplification of the broadband signal. The non-collinear angle is set to 1.1° and a phase-matching angle of 14.45° is assumed. The nonlinear crystal is pumped by a 20 mJ pump pulse with a pulse duration of 1.2 ps. The beam size of the pump is set to 4.4 mm FWHM resulting in an intensity of 70 $\frac{\mathrm{GW}}{\mathrm{cm}^2}$. The nonlinear crystal is seeded with the broadband signal generated by two subsequent HCFs (cf. red curve in Figure C.1) and a seed energy of 20 μJ. The GD of the signal used for the simulations is taken from the measurements presented in section 7.3 and is shown as green curve in Figure C.1. A signal-beam size of 4.4 mm FWHM is assumed. A Gaussian-beam shape is used for the spatial profile of the signal and

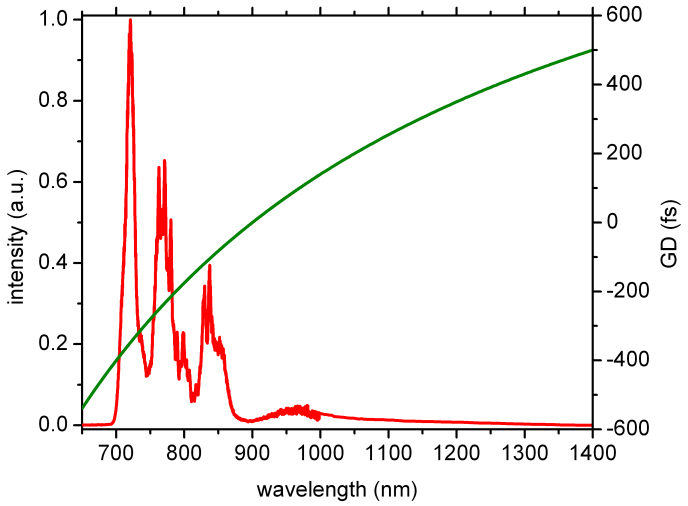

Figure C.1: *Spectrum and GD used for the simulations as input parameters.*

pump beam. Consequently, the simulations represent the tendencies of the OPCPA behavior but do not reproduce the complete realistic scenario. These parameters correspond to the first OPCPA stage of the vacuum OPCPA chain (cf. section 7.3) as it was originally planned. If not otherwise stated the simulations were performed with the SOPAS code.

C.1.1 Variation of parameters of the OPA crystal

Crystal material

The choice of the nonlinear crystal determines the amplified wavelength range (phase matching) and the possible gain per crystal length (effective nonlinearity, cf. chapter 2). A detailed investigation of different crystals and their performance in the case of PFS is presented in section 4.2.

Non-collinear angle and phase-matching angle

The phase-matching angle in combination with the non-collinear angle defines the amplified bandwidth range (cf. section 2.3). By changing these angles the amplification can be shifted to different spectral parts (cf. Figure 2.6).

Crystal length

The crystal length should be chosen as short as possible in order to increase the amplified bandwidth since the phase mismatch scales with ΔkL (cf. section 2.3). On the other hand, too short a crystal length fails to reach the point of maximum efficiency for a given signal and pump intensity. In the point-design simulations presented in chapter 5 the intensity of the pump is usually fixed to the highest

possible value in terms of damage threshold hence the crystal length is optimized for highest output energy stability beyond the saturation point on the negative slope of the gain curve (cf. simulation regarding pump energy in the next section and [41, 112]).

C.1.2 Variation of beam parameters

Variation of the signal energy

The input energy of the signal beam is determined by the seed-generation process. In general, high initial signal energies are favorable since for higher seed energy the detrimental effect of the superfluorescence on the temporal contrast can be minimized (cf. appendix C.2). Figure C.2 depicts the influence of the seed energy on the output energy of an OPCPA. Figure C.2(a) shows the evolution of the signal energy over the crystal length for different signal input energies. A change of the seed energy leads to a changed amplification dynamic. For small seed energy the OPA is operated in the small-signal regime and with increasing input energy the process is starting to saturate and than driven into back conversion. The influence of the seed energy on the output energy changes for these different regimes as depicted in Figure C.2(b). In the small-signal regime the output energy depends on the seed energy in a linear way whereas in the region of back conversion ($E_{\mathrm{s,in}} \geq 5\,\mu\mathrm{J}$) this influence is strongly reduced.

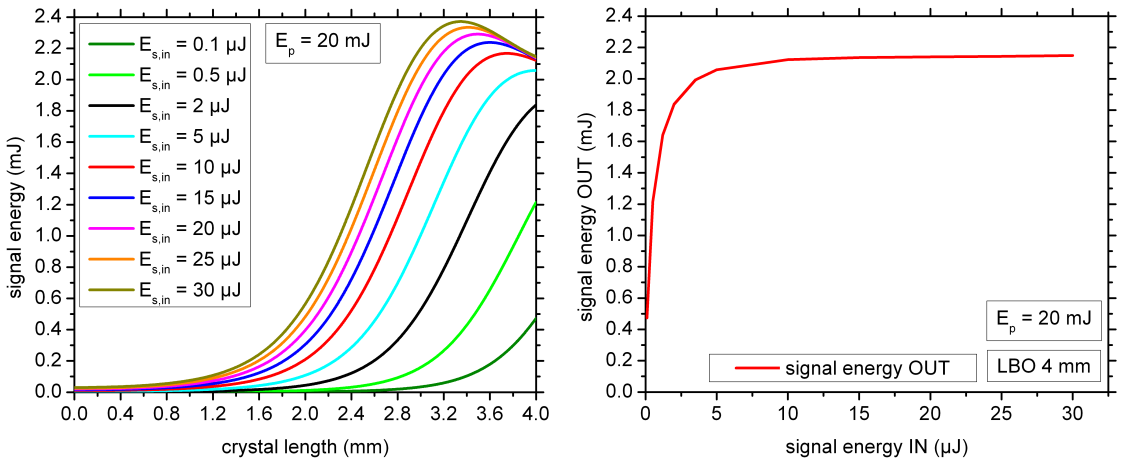

(a) energy vs. crystal length

(b) ouput energy vs. input energy

Figure C.2: *The effect of signal input energy on the amplification process: (a) signal energy inside the crystal for different signal input energies, (b) amplified output energy as a function of the signal input energy.*

Variation of the pump energy

The energy of the pump-laser system required for the OPCPA stages is defined by the desired maximum signal energy. In the case of PFS, a signal energy of $\sim 3\,\mathrm{J}$ calls for a total pump energy of 20 J at 515 nm under the assumption of an overall conversion efficiency of 15 % in the OPCPA chain. Figure C.3 shows the results of the simulation investigating the influence of the pump energy on the output performance of an OPCPA stage. Figure C.3(a) depicts the dependence of the output signal energy (blue curve) and conversion efficiency (red curve) on the pump energy. The efficiency is defined as the ratio between the extracted signal energy to the input pump energy i.e. $\eta = \frac{E_{sig,Out} - E_{sig,In}}{E_{pump,In}}$. Note that in the point designs for PFS described in chapter 5 efficiencies of $\sim 15 - 20\%$ were demonstrated which are much higher than the efficiencies presented here. Since the design studies are based on flat-top pump beams much higher efficiencies can be expected compared to the case of a Gaussian-shaped pump. Figure C.3(b) demonstrates the signal energy during propagation inside the crystal for three different pump energies (19 mJ, 20 mJ and 21 mJ), corresponding to a pump-energy fluctuation of 5 %. The inset of Figure C.3(b) shows the signal-energy fluctuations at different crystal positions, i.e. $\frac{E_{sig}(E_p=21\,\mathrm{mJ}) - \mathrm{E_{sig}(E_p=19\,mJ)}}{2 \times E_{sig}(E_p=20\,\mathrm{mJ})}$. The stability of the signal is increased for stronger back conversion, the highest instabilities occur before saturation sets in (cf. 2.4 mm). It can be observed that the point of maximum conversion efficiency ($\sim$ 3.4 mm) does not coincide with the point of maximum stability (cf. also [41]). Therefore, a trade-off between stability and efficiency is inherent to the OPCPA process.

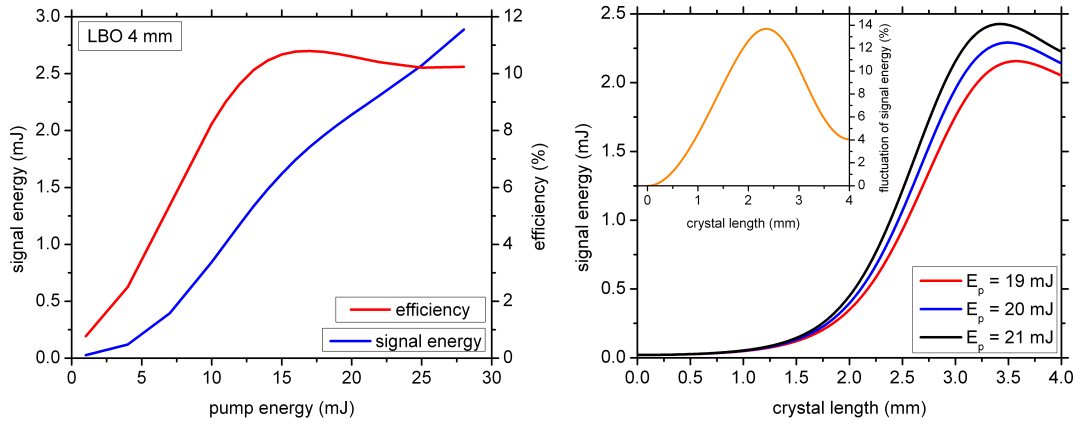

(a) signal energy vs. pump energy

(b) signal energy vs. crystal length

Figure C.3: *(a) Dependence of the output signal energy on the pump energy (blue curve), and the resulting efficiency (red curve). (b) Signal energy inside the crystal for different pump energies. The inset shows the fluctuations of the signal energy at different crystal positions.*

Variation of spatial parameters

The signal-beam size can be used to optimize the efficiency of the OPCPA process. Figure C.4(a) shows the results of a simulation investigating the influence of the signal-beam size on the signal energy. The maximum efficiency can be reached for a signal-beam size of $\sim 7\,\mathrm{mm}$ FWHM, slightly larger than the pump-beam size ($\sim 4.4\,\mathrm{mm}$), in the case of a 4 mm thick crystal. For smaller beam sizes the signal intensity is increased and therefore back conversion is reached at shorter crystal lengths (cf. blue and green curves) resulting in a reduced output energy at the end of the crystal. In addition, these small beam sizes lead to a reduced spatial overlap with the pump beam and consequently less pump energy contributes to the amplification which decreases the signal energy further. For larger beam diameters the signal intensity is reduced so that the amplification does not reach saturation.

By changing the pump-beam size the pump intensity can be easily controlled in the experiment. The pump intensity is chosen such that the highest efficiency and stability is reached for the available crystal length and signal and pump energy. Figure C.4(b) shows the behavior of the OPCPA process for a change of pump-beam size and therefore pump intensity. The beam size of the pump was increased from 3.9 mm to 5.9 mm FWHM, which results in a change of the intensity of $90 - 40\,\frac{\mathrm{GW}}{\mathrm{cm}^2}$. The signal-beam size was matched to the pump-beam size in all calculation runs leading to a change of intensity since the signal energy was fixed to $20\,\mu\mathrm{J}$. For smaller pump-beam diameters and therefore higher pump intensities, the maximum achievable signal energy rises. However, back conversion is reached at shorter crystal length leading to a reduced signal energy at the end of the nonlinear crystal. For larger beam diameters and smaller intensities the amplification does not reach saturation so that the efficiency is reduced. Here, a pump-beam diameter of 4.4 mm corresponding to a pump intensity of $70\,\frac{\mathrm{GW}}{\mathrm{cm}^2}$ is the ideal choice in terms of efficiency and stability. As described in section 2.2 and shown in Figure C.4(b), the OPA process strongly depends on the local pump intensity and therefore spatial modulations of the pump beam are transferred to the signal beam and decrease the quality of its intensity beam profile [41]. This behavior was observed in the OPCPA experiments described in chapter 7. In addition, the modulations of the pump beam affect the conversion efficiency of the amplification. Distortions of the pump laser can originate from the pump-laser amplifiers or compression gratings and are further aggravated by nonlinear effects during propagation through air and material. An evacuated imaging beam transport system (cf. appendix D.3) was designed and installed for the last experiments in order to avoid such problems.

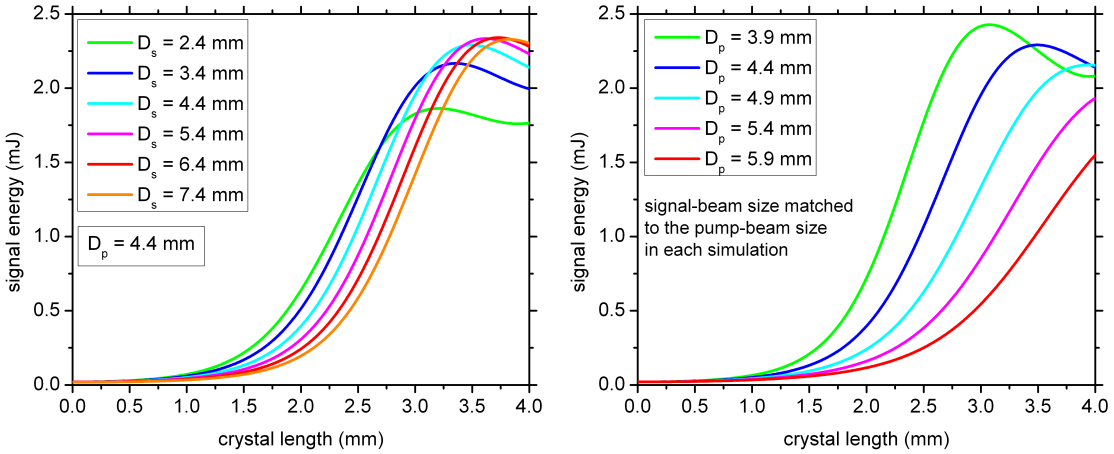

(a) signal-beam size (b) pump-beam size

Figure C.4: *Simulations presenting the influence of the signal-beam and pump-beam size on the nonlinear amplification: (a) effect of the signal-beam size for fixed input energies of pump and signal beam on the amplification; (b) influence of a pump-beam size variation on the nonlinear process.*

Furthermore, the strong dependence of the OPA gain on the instantaneous pump intensity causes another effect on the output: Variations of the spatial overlap between pump and signal lead to an unstable amplified signal output. Alterations of the spatial overlap are mainly an outcome of beam-pointing fluctuations arising e.g. from unstable mounts, air turbulences or on a longterm scale from temperature variations. For example, the beam-pointing fluctuations of the PFS pump laser measured over 1000 shots is $\sim 3\,\mu$rad std. [38] and the pointing fluctuations of the signal beam were too small to be detected (overlapped with beam-profile variations). However, since the beam sizes in the OPCPA stages of the PFS are quite large (> 6 mm FWHM) the measured pointing fluctuations are low enough to have negligible effect on the spatial overlap. Furthermore, such small pointing fluctuations don't influence the phase-matching conditions [7].

Variation of spectral parameters

The actual input spectrum of the seed is determined by the details of its generation process (cf. section 6.1). Here, the influence of the signal spectrum on the OPA process in saturation is investigated. Figure C.5(a) shows the two different input spectra used for these simulations: (i) a measured spectrum and (ii) a Gaussian spectrum in the frequency domain. The Gaussian spectrum is centered at 900 nm or 2.1 PHz with a Gaussian width of 0.4 PHz. Figure C.5(b) presents the corresponding normalized amplified spectra. The amplified bandwidth is similar in both cases. The Fourier-limited pulse duration for the case of a Gaussian-shaped input spectrum is

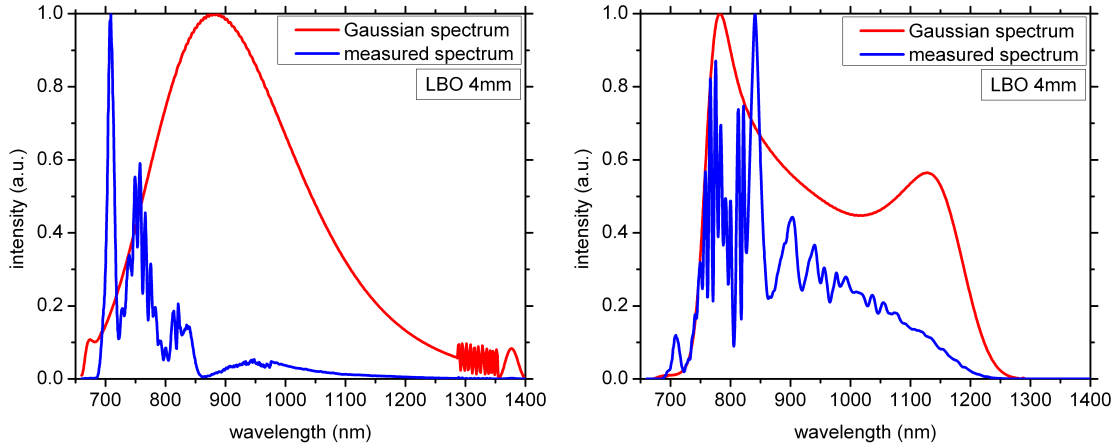

(a) unamplified spectra

(b) amplified spectra

Figure C.5: *Simulation with two different input spectra: (i) measured spectrum in front of the first OPCPA stage (blue curve) and (ii) a Gaussian spectrum in the frequency domain (red curve); (a) input spectra for the simulation, (b) amplified spectra.*

5.2 fs and for the case of the measured input spectrum 5.5 fs. However, modulations of the input spectrum (blue curve) are strongly enhanced in the amplified pulse for a saturated OPA whereas a smooth input spectrum results in a clean amplified spectrum (red curve). A modulated spectrum leads to side pulses in the time domain and consequently decreases the temporal contrast as well as the peak intensity. Consequently, already during the generation process of the broadband signal care has to be taken about the shape and smoothness of the spectrum. This is the reason for implementing a very complex seed generation scheme as described in section 6.1.

Variation of temporal parameters

Depending on the matching between pump-pulse and signal-pulse durations the amplified spectrum and energy are changed. Figure C.6 presents the results of a simulation investigating this behavior. The amplified spectrum and energy for a saturated OPA were simulated for different signal group delays which are depicted in Figure C.6(a). For all three cases the spectral phase is pure quadratic in the frequency domain. Figure C.6(b) displays the amplified signal spectra for these cases. In addition, the Fourier-limited pulse durations of these spectra and the obtained signal energies are depicted. For a less stretched signal pulse (green curve) the temporal overlap between signal and pump is reduced compared to the case of a stronger chirped signal pulse (red curve). Consequently, less pump energy contributes to the amplification and therefore the output energy is smaller (1.72 mJ). However, due to

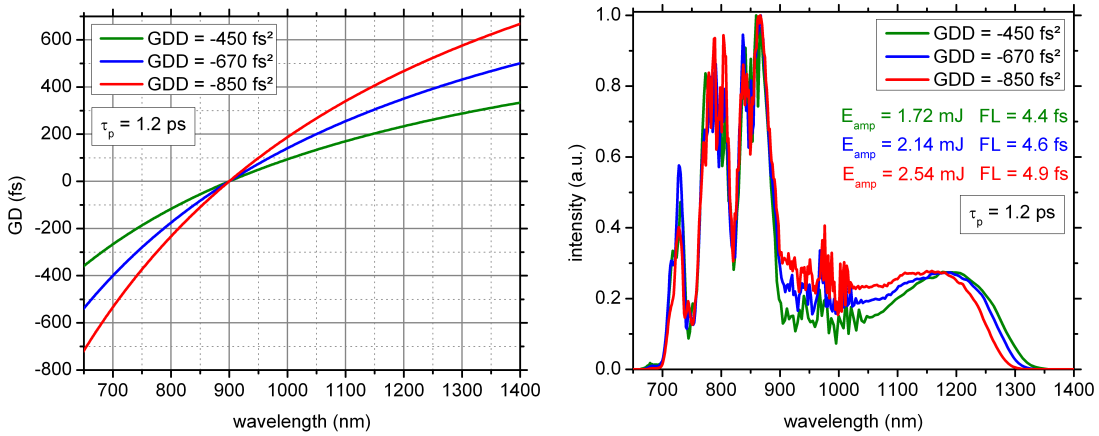

(a) group delay (b) amplified spectra

Figure C.6: *The effect of the signal-pulse duration on the amplification. The group delay taken into account in these simulations was linear in the frequency domain. (a) Group delays used for the simulation. The green curve corresponds to a GDD of* $-450\,\mathrm{fs}^2$ *at* $900\,\mathrm{nm}$*, the blue curve to a GDD of* $-670\,\mathrm{fs}^2$ *and the red curve to* $-850\,\mathrm{fs}^2$*; (b) amplified spectra for these group delays. The spectra were normalized to the peak.*

the shorter pulse duration, the spectral components of the signal pulse see a more uniform pump intensity, which leads to a broader amplified bandwidth compared to the case of a longer pulse, where the wavelengths at the edges of the spectrum are amplified by a reduced pump intensity. It has to be mentioned that the latter effect only occurs for chirped signal pulses. Furthermore, a shorter signal-pulse duration is less sensitive to temporal jitter, given a constant and longer pump duration. The blue curve represents a compromise between these aspects.

In the previous simulation the duration of the whole signal pulse was varied. A more compressed signal pulse experiences less gain than a strongly chirped pulse. This behavior is also valid for a signal pulse with a spectral phase, which is formed not only by GDD but also contains components of TOD and FOD resulting in locally compressed spectral parts. The results of a Sisyfos simulation investigating the influence of the signal group delay on the amplified spectrum are presented in subsection 4.2.2. Since the SOPAS code can only handle a quadratical shaped phase (cf. section 3.1), this study was performed with Sisyfos. The simulations show that the spectral phase of the signal pulse has a major influence on the spectral shape and the energy of the amplified pulse in a saturated OPA. Depending on the phase, the infrared tail of the spectrum can be enhanced or reduced relative to the blue part. This is a main difference to a laser where the spectral phase has no influence on the amplification behavior.

Figure C.6(b) indicates that the nonlinear amplification is sensitive to the temporal overlap between the signal and pump pulses. Consequently, an unstable temporal overlap leads to fluctuations of the amplified energy of an OPA and to additional spectral variations for a chirped pulse. Obviously, the absolute timing accuracy requirements are more stringent for shorter pump and signal pulses, which poses a much greater challenge for PFS than for more traditional, ns-pumped OPCPA system. With its sub-picosecond pump pulses, a timing jitter of just 100 fs can already have a very noticeable influence on the amplified spectrum. The results of a numerical study investigating the influence of a timing jitter on the amplification are presented in subsection 4.2.3. The simulations show that the detrimental effect of the timing jitter can be reduced for a saturated OPA. Therefore, also from this point of view it is favorable to sacrifice a bit of signal energy and work behind the point of maximum efficiency [41].

Spatio-temporal effects: tilted pulse fronts

In non-collinear OPCPA geometries the k-vector of the signal and pump beam constitute an angle and hence their pulse fronts are tilted relative to each other. A schematic sketch illustrating this behavior is depicted in Figure C.7(a). Obviously, depending on the position in y-direction the temporal overlap of both pulses changes. However, a change in the temporal overlap of pump and signal leads to a variation

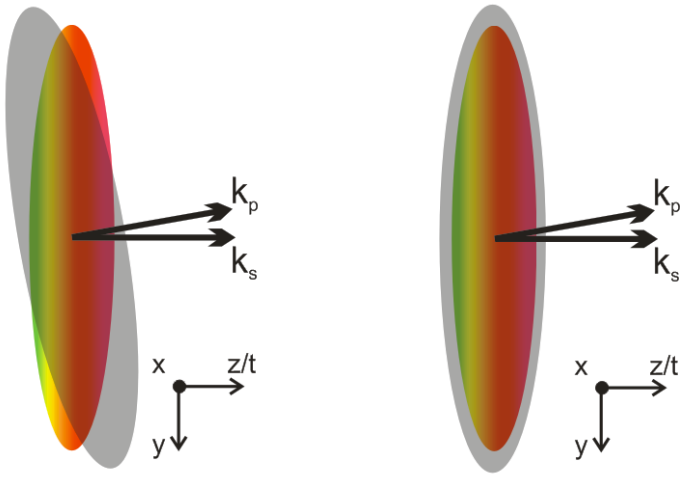

(a) non-parallel pulse fronts (b) parallel pulse fronts

Figure C.7: *Schematic sketch (a) for pulse fronts perpendicular to the k-vectors as it is the general case for a non-collinear geometry and (b) for parallel pulse fronts, i.e. pump pulse front is tilted.*

of the gain as it was shown in the previous section. Consequently, the beam profile of the amplified signal gets asymmetric, since at the edges of the signal beam in y-direction the temporal overlap with the pump pulse is reduced. Furthermore, for a chirped signal a spatial chirp is imprinted during amplification owing to the angle between the pulse fronts. Especially for femtosecond-short pumped OPCPA systems based on BBO where large non-collinear angles ($> 2.5°$) are used this effect has to be taken into account [93]. However, despite the small non-collinear angles used in the PFS, the non-parallel pulse fronts play a major role since the applied beam sizes are large compared to the spatial length of a 1 ps pump pulse ($\sim 300\,\mu$m).

Consequently, simulations investigating the effect of tilted pulse fronts on the OPCPA process were performed with Sisyfos. In order to observe the effect, two simulation runs were performed: in the first simulation the pulse fronts of pump and signal were perpendicular to their k-vectors as it is the general case for a non-collinear geometry (cf. Figure C.7(a)). However, in the second simulation the pulse front of the pump beam was tilted in order to match the pulse front of the signal pulse i.e. parallel pulse fronts (cf. Figure C.7(b)). The simulations were based on a 2.5 mm thick LBO crystal, with a non-collinear angle of 1.1° and a phase-matching angle of 14.45°. A FWHM pump-beam size of 8 mm and a signal-beam size of 6 mm were assumed which correspond to the largest beam sizes used in the experiments so far (cf. second stage of the LBO measurements located in vacuum, section 7.3). The nonlinear crystal was pumped at 100 $\frac{\mathrm{GW}}{\mathrm{cm}^2}$ in the simulations. The pulses were traveling along the z/time-direction and the non-collinear geometry was placed in the y-z plane (cf. Figure C.7).

Figure C.8 shows the spatial and signal-phase-space distribution of the input pulses and Figure C.9 presents the results. The pictures on the left side correspond to the case of matched pulse fronts, i.e. parallel pulse fronts, whereas the pictures in the right column show the results for pulse fronts perpendicular to their k-vectors. In the first row, Figures C.8(a-b) present the initial beam profile of the signal beam (x-y plane) whereas the second, Figures C.8(c-d), and third row, Figures C.8(e-f) represent the side-view, i.e. the beam profiles of signal and pump in the y-t plane of the signal. Figures C.9(a-b) depict the beam profile (x-y plane) of the amplified signal clearly indicating an asymmetric profile in the case of pulse fronts perpendicular to k. The spectra at three different y-positions (−2.1 mm, 0 mm and +2.1 mm) for both cases are shown in Figures C.9(c-d). For non-parallel pulse fronts, a spatial chirp can be detected since depending on the y-position the relative temporal overlap between signal and pump varies. In the case of matched pulse fronts, the spectrum at the position $y = 0$ is broader, since the amplification reached a higher level of

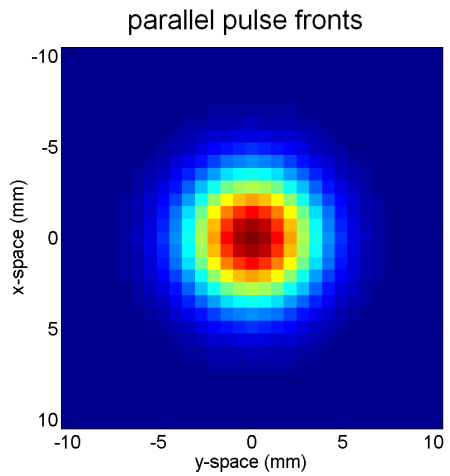

(a) initial beam profile

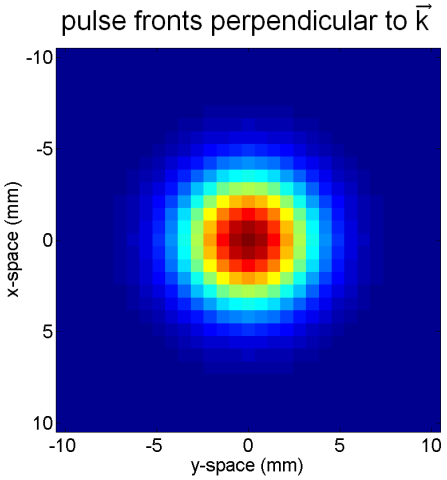

(b) initial beam profile

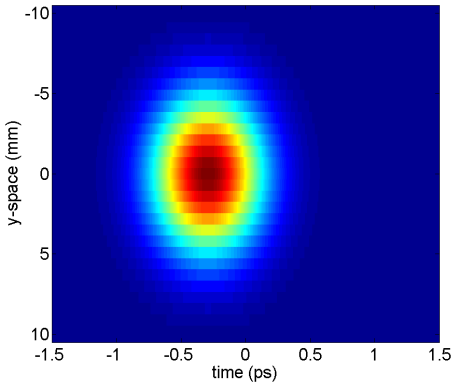

(c) y-t signal phase space: pump

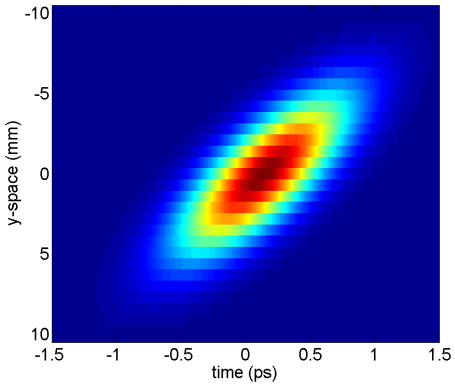

(d) y-t signal phase space: pump

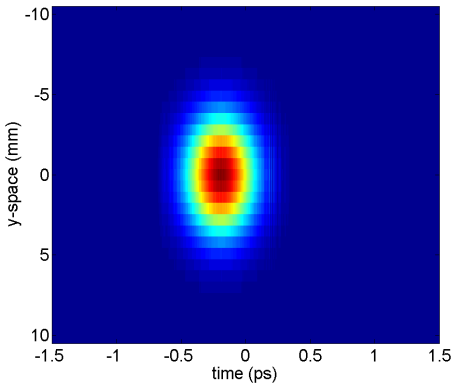

(e) y-t signal phase space: signal

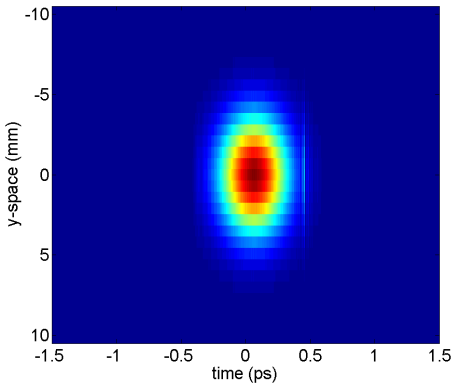

(f) y-t signal phase space: signal

Figure C.8: *Input parameters for the simulation investigating the difference between parallel pulse fronts of pump and signal and pulse fronts constituting an angle. The pictures on the left side correspond to the case of parallel pulse fronts, whereas the right column presents the results in the case of pulse fronts perpendicular to their k-vectors. (a), (b) initial beam profile (x-y plane), (c), (d) pump beam in the y-t signal-phase space. (e), (f) side view of the signal beam.*

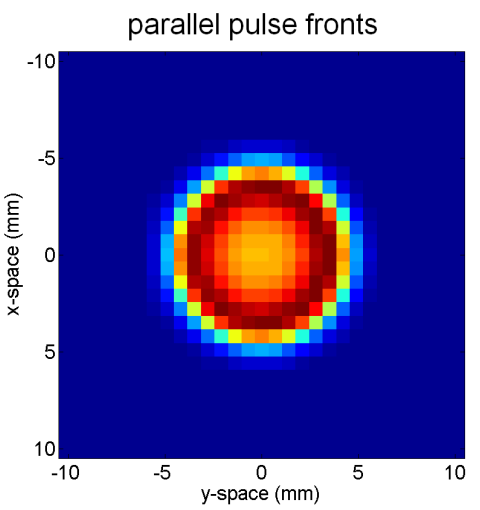

(a) amp. beam profile

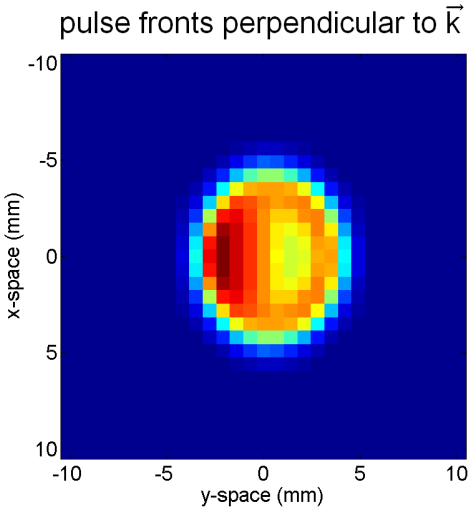

(b) amp. beam profile

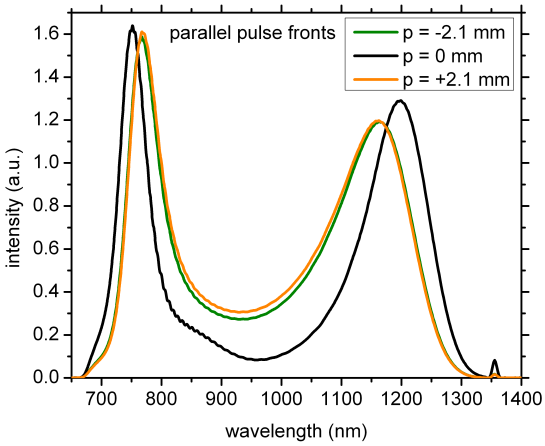

(c) spatial chirp

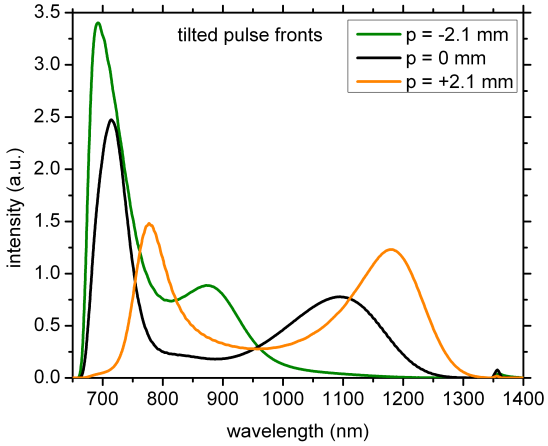

(d) spatial chirp

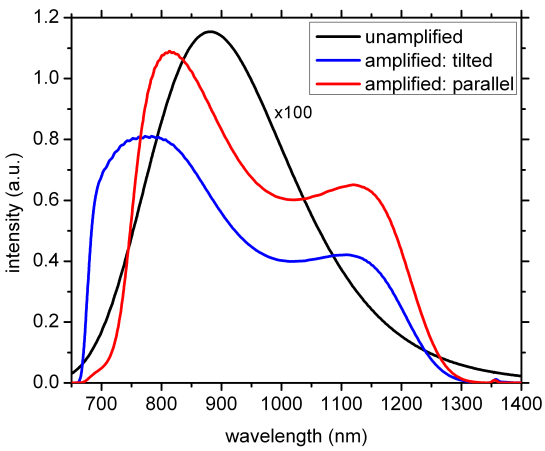

(e) total spectrum

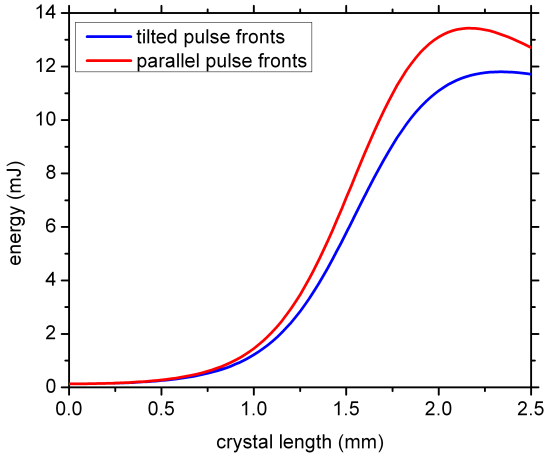

(f) signal energy

Figure C.9: *Results of the simulation: (a), (b) beam profile of the amplified signal. (c), (d) spectra at three different y-positions, (e) obtained total spectra and (f) signal energy along the crystal length for both cases.*

saturation compared to the two other positions. The total spectrum obtained for both cases is presented in Figure C.9(e). In addition, the unamplified spectrum is shown as black curve and for better visibility it was increased by a factor of 100. In the case of non-parallel pulse fronts the amplified bandwidth is larger compared to the case with parallel pulse fronts. The signal energy along the crystal length is depicted in Figure C.9(f). The difference between both cases is $\sim$ 10%, with a higher efficiency obtained for parallel pulse fronts.

In summary, already at beam sizes of 8 mm FWHM and picosecond pump pulses a degradation of the signal-beam quality is to be expected. In order to avoid such effects, the pulse fronts of the signal and the pump beam have to be matched. This can be realized by tilting the pulse front of the pump with two transmission gratings which are aligned with a small angular tilt relative to each other and imaging these gratings onto the OPA stage [101]. The angular chirp introduced by this setup due to the non-parallel gratings results in a tilted pump pulse front and therefore can be used to match the pulse fronts of signal and pump inside the nonlinear crystal.

C.2 Superfluorescence

Similar to the amplified spontaneous emission in conventional laser systems, fluorescence photons which are generated at the beginning of the nonlinear crystal of an OPA are further amplified by the pump beam during their propagation through the crystal, to form the so-called superfluorescence. These fluorescence photons are created even when no signal is present since their generation is based on quantum fluctuations of the electromagnetic field [113–116]. Since the superfluorescence is not compressible it leads to a pedestal which reduces the temporal contrast of the signal pulse. The duration of this pedestal is defined by the used pump-pulse duration. Simulations with the SOPAS code were performed in order to investigate the decreasing effect of the superfluorescence on the temporal contrast.

The strength of the superfluorescence is defined by the small-signal gain in the OPA stage and hence by the pump intensity, the crystal length and the nonlinearity of the crystal. For example, the dependence of the superfluorescence on the pump intensity is presented in Figure C.10(a). For this simulation a 4 mm LBO crystal was assumed. The intensity was varied by changing the pump-beam size, whereas the pump-pulse duration of 1.2 ps and the pump energy of 20 mJ were kept constant. Furthermore, the simulations were performed with a blocked signal beam. The energy of the superfluorescence obtained at the end of the nonlinear crystal increases with rising pump intensity. At a pump intensity of 100 $\frac{\mathrm{GW}}{\mathrm{cm}^2}$ a superfluorescence energy of 3 nJ can

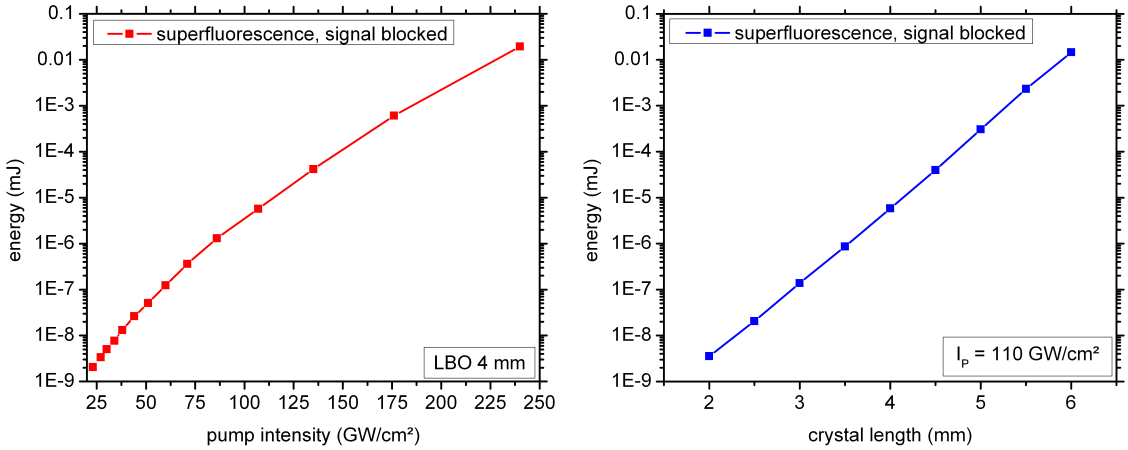

(a) dependence on pump intensity

(b) dependence on crystal length

Figure C.10: *Results of a simulation performed with SOPAS investigating the dependence of the level of superfluorescence on (a) the pump intensity and (b) the crystal length. Both simulations were performed with an LBO crystal and a blocked signal beam. For (b) the pump intensity was fixed to* $\sim 110\,\frac{\mathrm{GW}}{\mathrm{cm}^2}$*. More details about the used simulation parameters are given within the text.*

be expected. A second simulation presented in Figure C.10(b) shows the dependence of the superfluorescence on the crystal length. Here, a constant pump intensity of $\sim 110\,\frac{\mathrm{GW}}{\mathrm{cm}^2}$ was assumed. Again, it can be observed that for increasing crystal length and therefore greater small-signal gain, the superfluorescene becomes stronger.

However, the situation is different if the signal beam is not blocked. The level of superfluorescence mainly is still determined by the small-signal gain, however the decrease of the temporal contrast also depends on the gain of the signal beam as is shown in Figure C.11. Here, the results of a simulation investigating the decrease of temporal contrast for different pump intensities are depicted. A signal input energy of $1\,\mu\mathrm{J}$ and a pulse duration of 1.0 ps was used. The pump-pulse duration was set to 1.2 ps. Figure C.11(a) presents the amplified signal energy on a mJ-scale as well as the obtained superfluorescence energy on a nJ-scale for different pump intensities. Figure C.11(b) shows the evolution of the signal energy during propagation through the nonlinear crystal for different cases. The energy ratio between the amplified signal and the superfluorescence, which is therefore a measure for the temporal contrast, is depicted in Figure C.11(c). With increasing pump intensity the amplification of the signal beam is driven more and more into saturation leading even to back conversion at high pump intensities. In contrast, the energy of the superfluorescence is growing exponentially. At pump intensities where no or only low saturation effects occur ($< 70\,\frac{\mathrm{GW}}{\mathrm{cm}^2}$) the signal beam and the superfluorescence

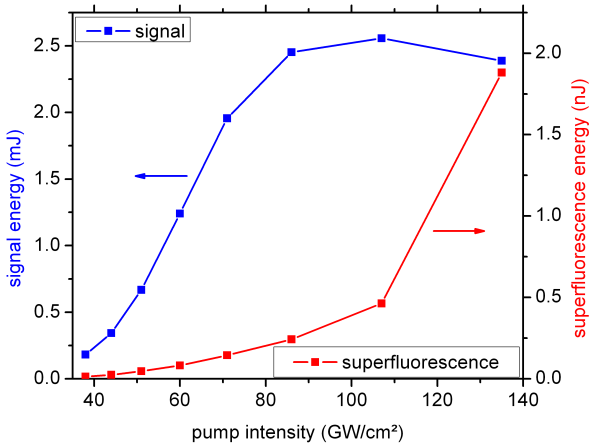

(a) pump intensity

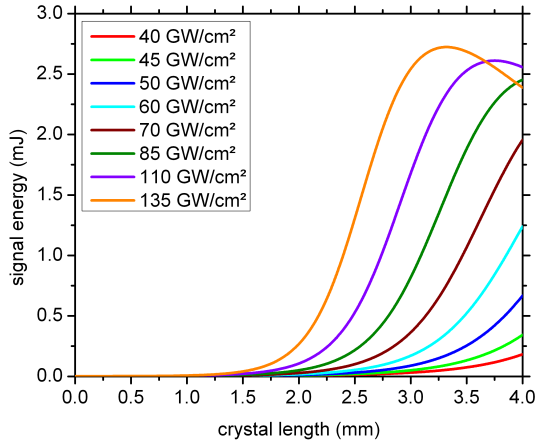

(b) pump intensity

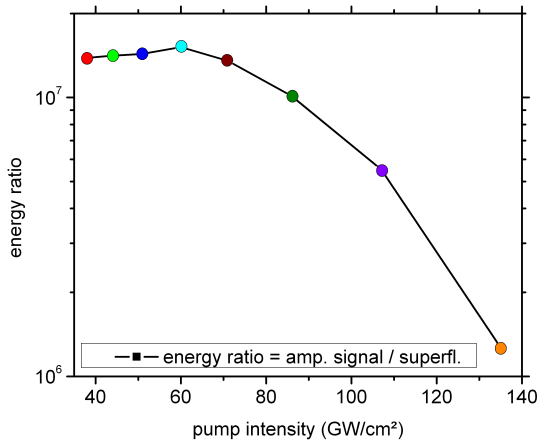

(c) crystal length

Figure C.11: *Influence of the superfluorescence on the temporal contrast. (a) shows the amplified signal energy and the superfluorescence energy for different pump intensities obtained in a* 4 mm *thick LBO crystal. (b) depicts the signal energy over the crystal length for these cases whereas (c) shows the resulting energy ratio between the signal beam and the superfluorescence.*

experience a similar gain and consequently the energy ratio stays constant. However, for higher pump intensities the gain for both beams differ, where the signal beam experiences less gain than the superfluorescence due to saturation and back conversion. Therefore, the energy ratio is starting to decrease and consequently the temporal contrast will degrade. However, as described earlier, slight back conversion increases the energy stability of the signal beam and the amplified bandwidth. Consequently, there exists a trade-off between the temporal contrast and an optimized OPA process.

The decreasing influence of the superfluorescence on the temporal contrast can be minimized by using higher seed input energies for the signal beam. Figure C.12 depicts this behavior. Here, amplification in a 4 mm thick LBO crystal pumped at 70 $\frac{\mathrm{GW}}{\mathrm{cm}^2}$ was assumed. At seed energies of 1 μJ saturation starts and at 10 μJ the regime of back conversion is reached. The energy ratio between the signal and the superfluorescence is dramatically enhanced for higher seed input energies. Consequently, the PFS system is aiming for relatively high seed energies of $0.5 - 20\,\mu$J for the first stage minimizing the energy ratio between the signal and the superfluorescence to $> 10^6$ and therefore leading to an enhanced contrast at the end of the OPCPA chain as well. Since the superfluorescence is not compressible the intensity ratio and therefore the temporal contrast will be even higher ($> 10^8$ on a picosecond time scale) for a compressed signal.

Furthermore, short pump pulses are desired since the time span over which the contrast could be compromised by superfluorescence is shorter as well. In general, shorter pump-pulse durations lead to higher pump intensities but at the same time to shorter crystal lengths, so that the overall gain and therefore the generation of superfluorescence is kept constant. Therefore, the benefit of a pump duration of only 1 ps as used in the PFS is the greatly improved temporal contrast.

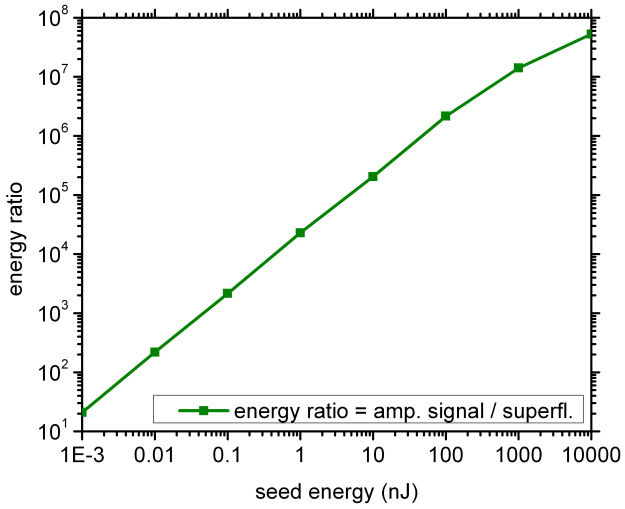

Figure C.12: *Energy ratio between the signal and the superfluorescence for different seed input energies. Seeding the OPA stage with higher energies minimizes the detrimental influence of the superfluorescence on the temporal contrast.*

C.3 Heat load in OPA crystals

In this section the heat load in the OPA crystals of the PFS which can be expected is investigated. The last OPCPA stages of the PFS will be pumped by 5 J at 10 Hz resulting in an average power of only 50 W. Under the assumption of typical absorption coefficients for DKDP $\alpha_{DKDP} \approx 0.005 \frac{1}{\text{cm}}$ at a wavelength of 532 nm [117] the absorbed power in a 4 mm thick crystal is 100 mW. A rough estimation of the heat distribution inside the crystal triggered by the absorption of the pump laser is presented in Figure C.13. This estimate is based on the formulas given in [118] and more information about the Matlab-code developed to study that issue can be found in appendix C.3.1. Only radial heat flow was taken into account as it is the case for an OPA stage installed in vacuum where the heat is only removed by the crystal mount. The crystal has an aperture of 130 mm and is pumped by a flat-top pump beam (77 mm FWHM) with an energy of 5 J, a pulse duration of 1 ps and a repetition rate of 10 Hz. The thermal conductivity for DKDP is $\kappa \approx 2 \frac{\text{W}}{\text{mK}}$ [117]. Based on these parameters the temperature in the center of the crystal rises by 2 K compared to the temperature at the edges of the crystal. However, the temperature difference which is relevant for the OPA process is the temperature change between the center of the light pulse and its boundary, which is ~ 1 K (radius = 38.5 mm).

Beside the absorption of the pump laser, the idler absorption can play an important role as a heat source as well. It has to be mentioned that the IR transmission of DKDP crystals above 1400 nm sensitively depends on the purity of deuteration. Even small amounts of light hydrogen will lead to strong IR absorption. Since for increasing deuteration level the cut off for transmission is shifted to higher wavelengths [119] it is important to use DKDP crystals with high deuteration level in order to reduce the absorption of the idler. Furthermore, an absorbed idler leads to a limitation of the amplified signal bandwidth. Figure C.14 shows measured transmission curves for two DKDP crystals used for the experiments. The transmission starts to decrease for wavelengths of ≥ 1600 nm. For a signal wavelength of 700 nm the corresponding idler wavelength is 1985 nm ($\lambda_{pump} = 515$ nm), which experiences a transmission of only $9 - 30$ %. Especially in the last power amplifier stages, the idler beam can contain a couple of mJs of pulse energy in the absorbed spectral region leading to a heat source comparable to the pump. Consequently, temperature changes of $2 - 5$ K can be expected depending on the absorpted power from the idler beam.

By using the formulas for the temperature dependent refractive indices of DKDP (page 86 in [117]) the influence of the temperature change on the phase mismatch

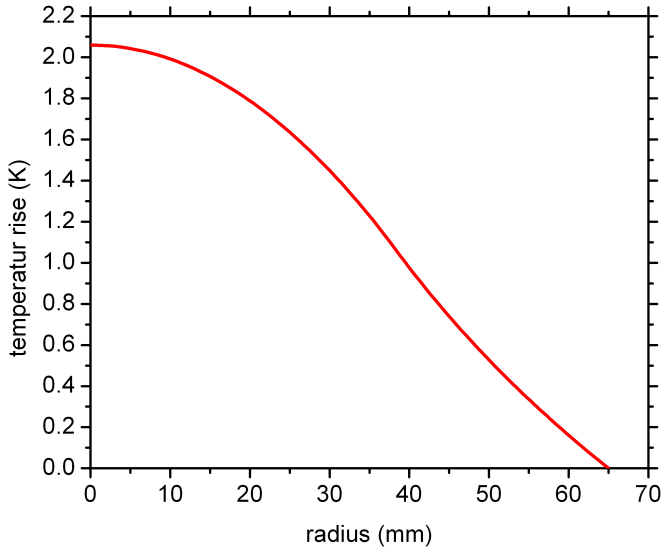

Figure C.13: *Calculation of the heat distribution inside a DKDP crystal. Only radial heat flow and absorption of the pump was taken into account. The simulated crystal had an aperture of* 130 mm *and was pumped by a flat-top pump beam (*$w =$ 38.5 mm*) with an energy of* 5 J*, a pulse duration of* 1 ps *at a repetition rate of* 10 Hz*. The thermal conductivity for DKDP is* $\kappa \approx 2\,\frac{\mathrm{W}}{\mathrm{mK}}$*. The temperature increase is* 2 K*.*

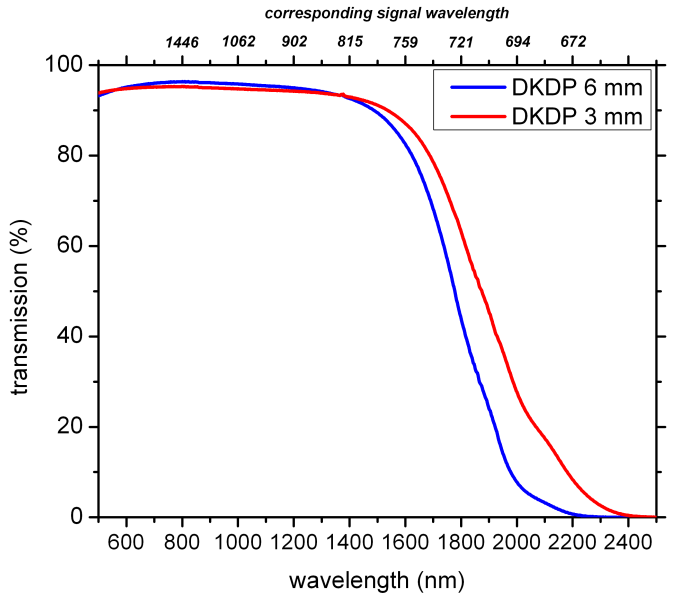

Figure C.14: *Measurement of the transmission of DKDP (deuteration level of* 96%*) for two different crystal lengths. The transmission starts to decrease at* $\sim 1.6\,\mu$m*.*

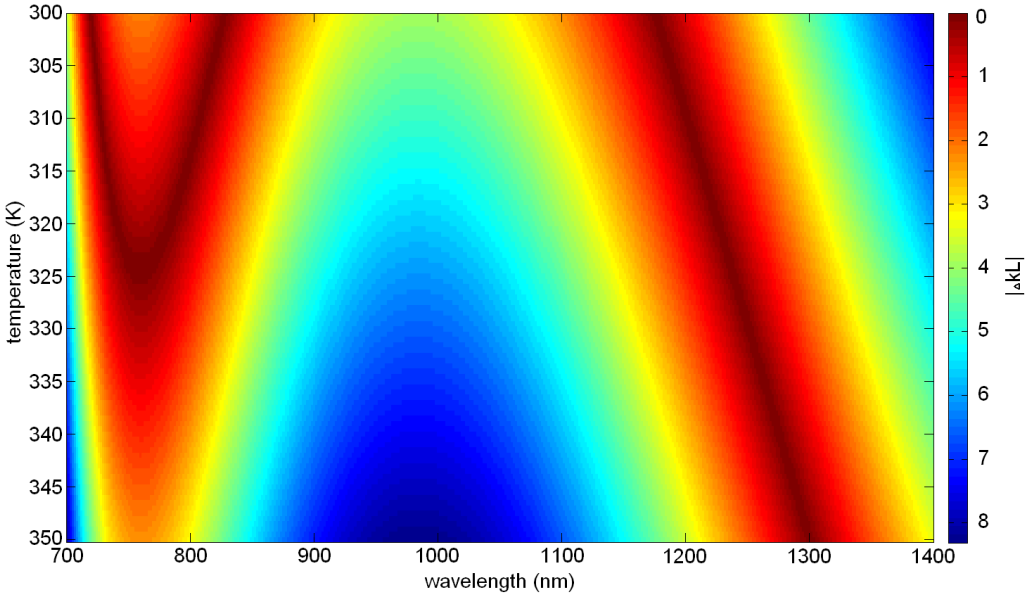

Figure C.15: *Change of the phase mismatch for different crystal temperatures. A non-collinear angle of* 0.75° *and a* 4 mm *thick DKDP crystal cut at a phase-matching angle of* 36.9° *was assumed for this calculation. For better visibility of the colormap the absolute phase mismatch is presented. The red regions correspond to perfect phase match, whereas spectral components in the blue regions are not amplified due to too high phase mismatch.*

was estimated. Figure C.15 shows the simulated phase mismatch at different temperatures for a non-collinear angle of 0.75° and a 4 mm thick DKDP crystal cut at a phase-matching angle of 36.9°. It has to be mentioned that for better visibility of the colormap the absolute phase mismatch is presented here, i.e. $|\Delta kL|$. Regions shaded in red correspond to perfect phase match, whereas spectral components located in the blue regions will not be amplified. Owing to the radial temperature distribution inside the nonlinear crystal, the phase-matching condition changes across the crystal diameter mainly leading to a spatial chirp of the amplified signal pulse.

Figure C.16 depicts the phase-matching curves at 300 K (red curve) and 305 K (blue curve). The shift to higher phase-mismatch values can be counterbalanced by a slightly different phase-matching angle ($\sim 0.01°$). However, such a small change in the phase-matching condition does not have an observable influence on the OPA process.

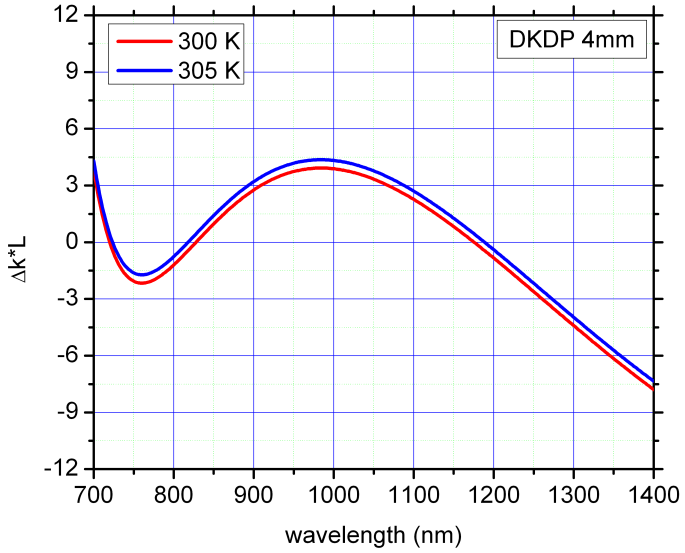

Figure C.16: *Phase-matching curve for two different temperatures:* 300 K *red curve and* 305 K *blue curve for a* 4 mm *thick DKDP crystal.*

C.3.1 Matlab-code used to calculate the heat distribution

In this section the matlab-code which models the heat distribution inside a DKDP crystal is presented. The original formulas are given in [118]. The following assumptions are made for the calculations:

- only the pump-laser beam is taken into account
- the intensity of the pump laser remains constant during propagation through the crystal
- the beam has a flat-top spatial profile with 2w diameter
- the temporal profile is Gaussian with a FWHM of τ.

Equation 2 and 5 of the publication [118] combined with the listed assumptions lead to the effective heat-density:

$$h_0 = \frac{\tau\sqrt{\pi}}{2\sqrt{ln2}} I_0 \alpha f,$$

with I_0 the maximum intensity, α the absorption coefficient and f the repetition rate of the laser.

The calculated h_0 is set into equation 4 in [118]:

$$\begin{aligned} \Delta T(r) &= \frac{h_0}{4\kappa}(w^2 - r2) - \frac{h_0 w^2}{2\kappa} Ln\left(\frac{w}{r_0}\right) \qquad r < w \\ \Delta T(r) &= \frac{-h_0 w^2}{2\kappa} Ln\left(\frac{w}{r_0}\right) \qquad r \geq w \end{aligned}$$

where κ is the heat conductivity, r_0 the radius of the crystal and w the beam radius in order to obtain the heat distribution inside the crystal.

In the following the source code is presented.

```
% Program to calculate the temperature distribution inside a crystal
% It follows the publication: S. Seidel and G. Mann,
% "Numerical modeling of thermal effects in nonlinear
%  crystals for high average power second harmonic generation"
%  SPIE, 2989: 204-214, May 1997
%
% for a flat-top beam in space:
% h0(z) = f(reprate) * integral(dt) alpha * I(z,t)
%
% for a Gaussian beam in time with pulse duration t (FWHM) the integral is:
% -->  h0(z) = t sqrt(pi) / (2 sqrt (ln2) ) * I0(z) * alpha * f
%
% for our calculation we assume a constant I0 (independant from z)
%
% Equation 4 in the publication is true for the temperature distribution
%
%
%
  I0 = 102e9;     % intensity (W/cm^2)
  alpha = 0.005;  % absorption coefficient  (1/cm)
  f = 10;         % repetition rate  (1/s)
  t = 1e-12;      % pulse duration FWHM  (s)
  k = 2e-2;       % heat conductivity  (W / K / cm)    % DKDP
  w = 3.85;       % beam size (cm)
  D = 13;         % diameter crystal (cm)
  r0 = D/2;   % radius crystal (cm)

  N1 = 100;       % number of points
  r = linspace(0, r0, N1);    % radius-vector
%
  h0 = t * sqrt(pi) / 1.66510922 * I0 * alpha * f;
%
  for i1=1:1:N1
    if r(i1) < w
```

```
    ln = log(w/r0) / log(exp(1));
    DT(i1) = h0/(4*k) * (w^2 - r(i1)^2) - h0*w^2 / (2*k) * ln;

  else

    ln = log(r(i1)/r0) / log(exp(1));
    DT(i1) = - h0*w^2 / (2*k) * ln;

  end;
end;
plot(r,DT);
```

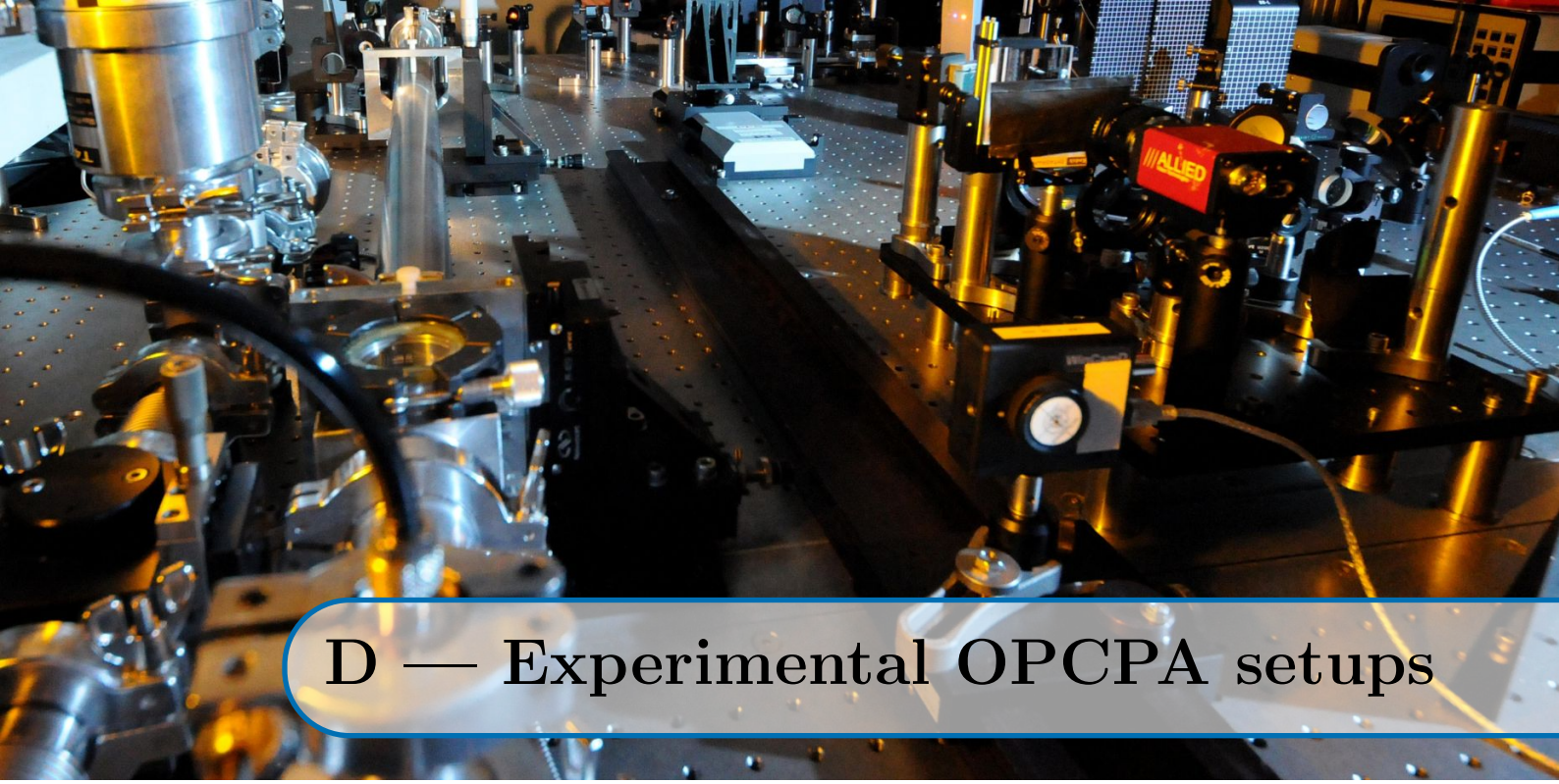

D — Experimental OPCPA setups

This chapter describes the experimental setups used for the OPCPA measurements presented in chapter 7.

D.1 Experimental setup for measurements with DKDP

For the parametric amplification experiments in DKDP presented in section 7.1 a small fraction ($\sim$ 800 μJ) of the total available pump-laser energy at 515 nm was used with a FWHM duration of 2 ps, i.e. slightly longer than the best achievable performance, since in this way the effect of the timing jitter was reduced.

The broadband signal pulses were stretched in time using a double-prism-pair stretcher. The pump pulses were combined with the broadband signal pulses in a DKDP crystal in the non-collinear geometry to allow for the broadest bandwidth and for the separation of the beams after amplification. The crystals used in the experiment had a deuteration level of 96% and a clear aperture of 15 x 15 mm^2. For the amplification measurements the pump and signal beams were focused to obtain near-Gaussian beam profiles in the OPCPA crystal with FWHM beam diameters of $\sim$ 1.5 mm and 1.4 mm, respectively. The pump intensity was limited to 100 $\frac{\mathrm{GW}}{\mathrm{cm}^2}$, which can be regarded as a safe mode of operation. The AR coating of the DKDP crystal (515 nm and 700$-$1400 nm) is the limiting factor in terms of damage in the amplifier stage and its damage threshold was measured to be 300 $\frac{\mathrm{GW}}{\mathrm{cm}^2}$ in the experiment. A schematic sketch of the setup is presented in Figure D.1.

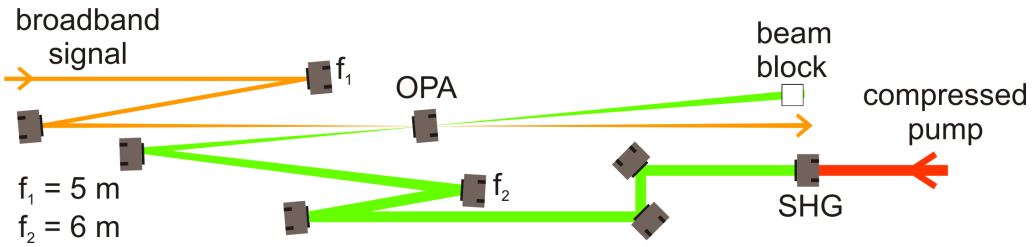

Figure D.1: *Schematic layout of the setup used for the measurements with DKDP. The red beam indicates the beam propagation of the fundamental pump laser, whereas the green beam stands for the frequency-doubled pump. The path of the signal beam is shown as the orange beam.*

D.2 Experimental setup for measurements with two LBO stages in air

Here, the experimental setup used for the measurements with two LBO stages in air presented in section 7.2 is described. The optical arrangement of the two subsequent OPCPA stages is schematically shown in Figure D.2.

Pump laser: The output of the 8-pass Yb:YAG amplifier (H2 in Figure 6.1 and Figure 6.5) was used as the pump since during the time of these experiments the development of the 20-pass imaging amplifier was still ongoing. Compared to the

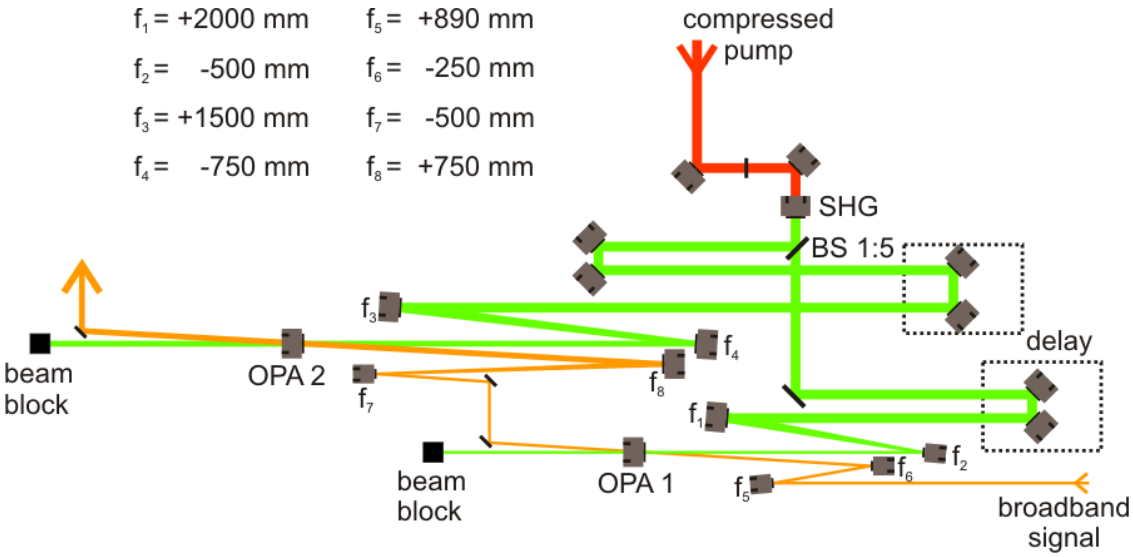

Figure D.2: *Schematic layout of the two-stage-OPCPA chain equipped with LBO. The red beam indicates the beam propagation of the fundamental pump laser, whereas the green beam stands for the frequency-doubled pump. The path of the signal beam is shown as the orange beam.*

DKDP experiments, the clipping of the pump-laser spectrum inside the grating compressor was removed in order to increase the available pump energy. Consequently, the pulse duration after the compressor was shortened to $\sim$ 1.2 ps. The spatial profile was cleaned in a vacuum spatial filter removing stripes on the beam profile imprinted by the compressor gratings. Frequency doubling was performed in a 5 mm thick type II DKDP crystal cut at a phase-matching angle of 54.4° with conversion efficiencies of more than 50% [38]. The pump beam was split into two parts for pumping the first and second stages by a 1 : 5 beam splitter.

A pump energy of 5.3 mJ and 31.3 mJ measured in front of the first and second stages was used for these experiments. Two reflective Galilei-telescopes, one in each pump arm were implemented to adjust the beam sizes for the parametric amplification and to partially counterbalance the effect of SF, i.e. the telescopes were adjusted such that the pump beams were collimated at the nonlinear crystals.

Signal beam: The broadband signal beam generated in two cascaded HCFs (cf. section 6.1) was used to seed the OPCPA stages. Pulse stretching was now performed in a single prism stretcher, since the shorter (1.2 ps) pump pulses require less dispersion for the seed beam. In order to compensate the higher orders of the stretcher and the compressor material (CaF_2), chirped mirrors were installed after the prism stretcher. The chirped mirrors were designed in such a way that after two LBO stages the pulses could be compressed by implementing $\sim$ 30 mm of CaF_2. The beam size of the signal beam was matched to the pump-beam size in the first stage with a Galilei-telescope formed by two silver mirrors. An additional telescope located between the first and second OPCPA stages, magnified the signal-beam size by a factor of 1.5.

D.3 Experimental setup for measurements with two LBO stages in vacuum

For the high energy measurements presented in section 7.3 a vacuum system is necessary in order to avoid energy limiting effects such as SF in air. The vacuum system is designed for a total pump energy of 1 J at 1030 nm delivered by the imaging 20-pass Yb:YAG amplifier described in section 6.2 and [97]. The beam transport of the pump laser is based on imaging, allowing to maintain the beam profile on the OPCPA crystals, which is essential for the usage of future flat-top pump-laser beam profiles. Without imaging beam transport, super-Gaussian beam profiles strongly change their shape and in the worst case experience strong intensity modulations during propagation, leading to intensity enhancements (hot spots), which result in the damage of optics [120, 121].

Figure D.3 presents the schematic layout of this imaging vacuum system and Figure D.4 depicts a 3D model including the vacuum chambers and vacuum tubes. The beam profile of the pump laser at the position of the entrance window of the vacuum system is imaged onto the SHG crystal. The doubling crystal is then imaged onto both the first and second OPCPA stages. Beam foci at different positions inside the vacuum system are unavoidable due to beam imaging. According to [122], the maximum allowed pressure to avoid distortions of the transmitted pulse due to refraction or absorption in the ionized background gas, is 1.5×10^{-3} mbar leading to the necessity to apply turbo molecular pumps. Two TurboVac SL700 (Leybold) are installed, reaching a pressure of 1.0×10^{-4} mbar.

The pump laser enters the vacuum chambers around one meter after its complete compression, i.e. after the second pass on the first grating, in order to reduce the nonlinear beam propagation in air. A periscope adjusts the beam height, after which the pump laser passes trough a spatial filter for beam smoothing. In addition, the spatial-filter telescope consisting of two spherical mirrors with $f = 3000$ mm and $f = 2500$ mm reduces the beam size for the subsequent frequency doubling. A $\lambda/2$ waveplate rotates the polarization of the pump laser to 45°, so that the type II frequency-doubled pump beam is produced with horizontal polarization. SHG is performed under the same conditions as in the case of the experiments with LBO in air (cf. appendix D.2), except a crystal with larger aperture (60 mm) is used to accommodate the higher pump energy. Directly after the SHG the pump is split by a $T = 6\%$ and $R = 94\%$ beamsplitter for pumping the first and second OPCPA stages.

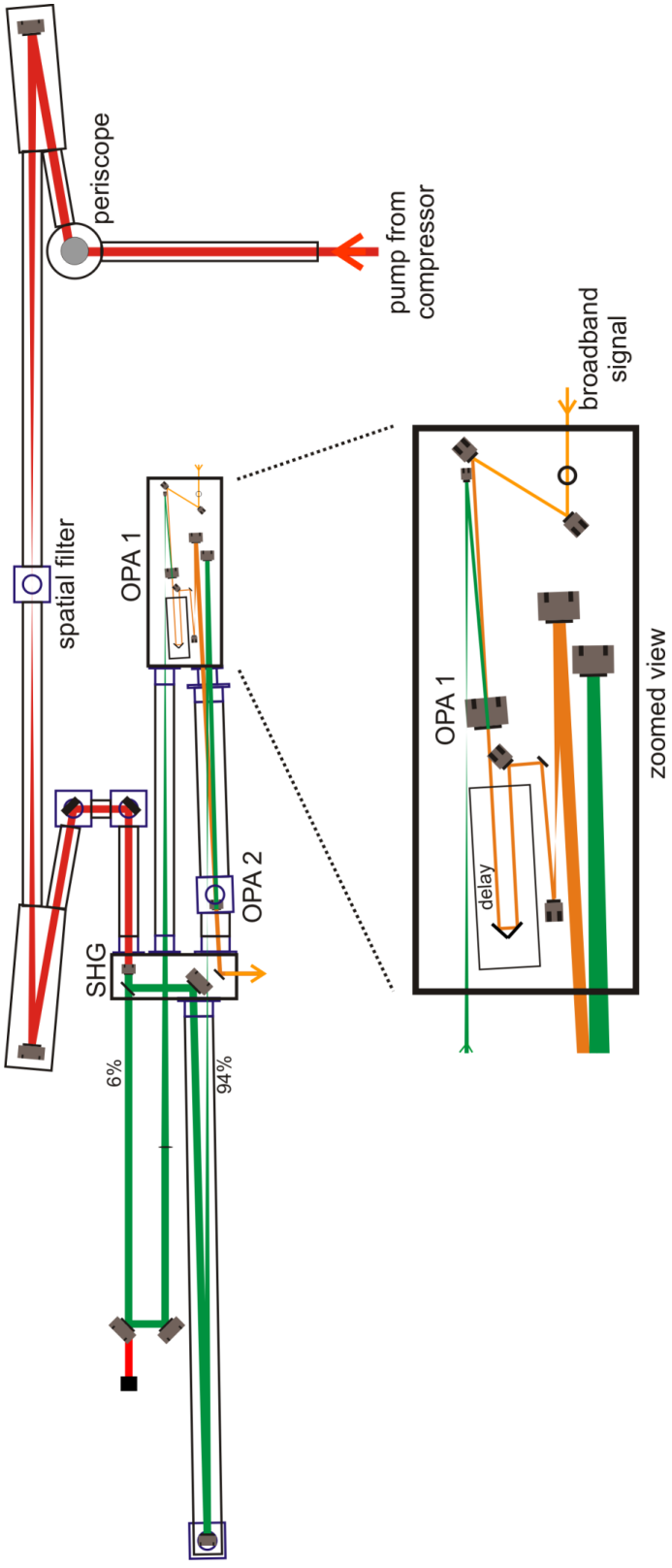

Figure D.3: *Schematic layout of the two-stage OPCPA setup located in vacuum. The pump-laser beam at the entrance of the vacuum system is imaged onto the SHG crystal and subsequently the doubling crystal itself is imaged onto the two OPCPA crystals independently. Detailed information is given in the text.*

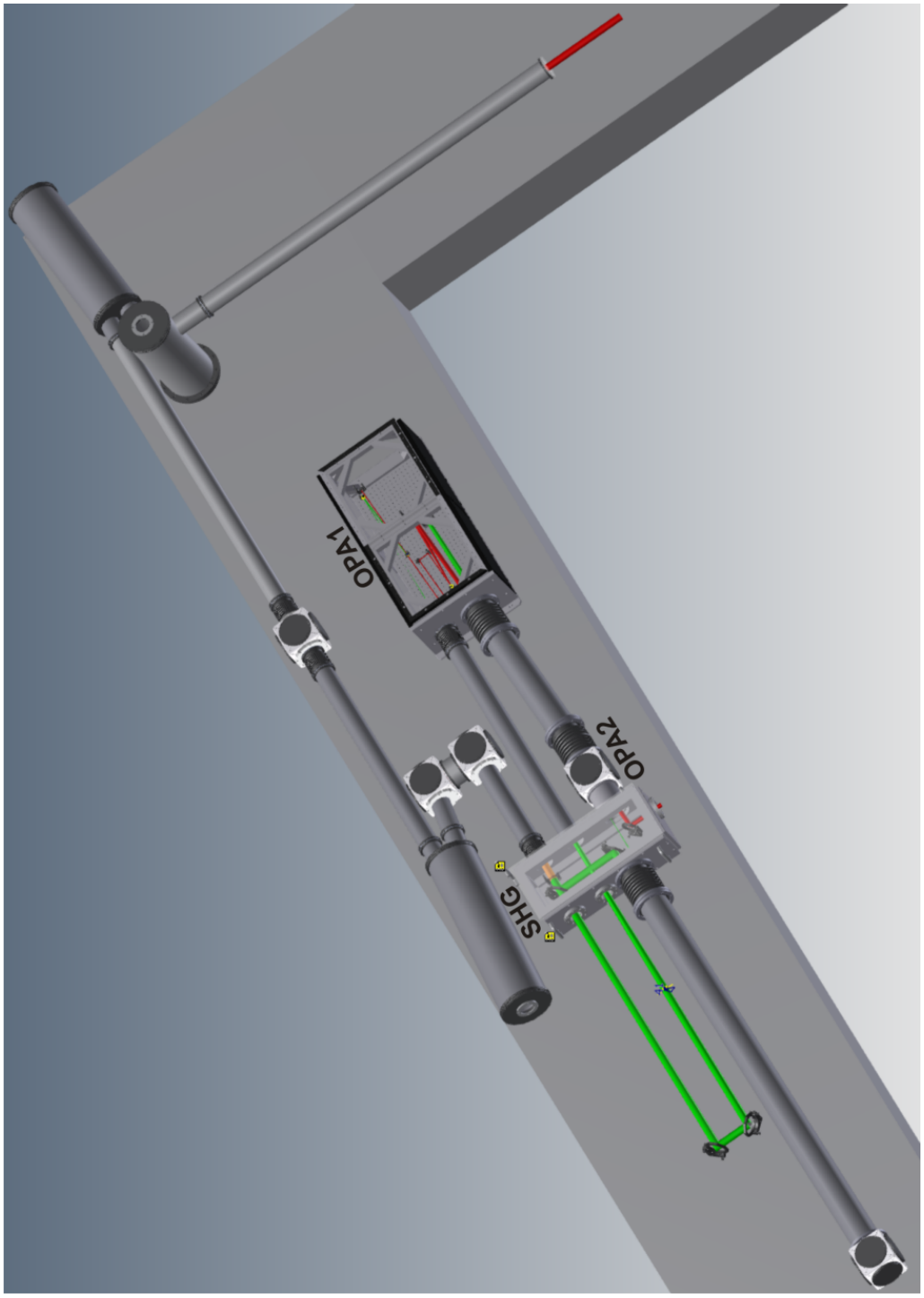

Figure D.4: *3D layout of the OPCPA vacuum system that corresponds to the schematic layout shown in Figure D.3.*

The transmitted part ($\sim 6\%$) is coupled out of the vacuum together with the residual fundamental pump energy. Two high-reflector (HR) mirrors for 515 nm separate the frequency-doubled and fundamental parts, the latter of which is blocked in a water-cooled beam dump. Imaging and adjustement of the pump-beam size for the first OPCPA stage is realized by a telescope consisting of a lens ($f = 3100\,\mathrm{mm}$) and a curved HR mirror ($f = 450\,\mathrm{mm}$). The B-integral introduced by the propagation in air and through the lens material can be neglected since the beam carries only 6% of the total pump energy. Nevertheless, after the focusing lens the pump-laser beam is sent back into vacuum. The above mentioned curved HR mirror recollimates the beam and guides it to the first OPCPA stage.

The second part of the pump-laser beam with higher energy, which is reflected off the beam splitter after SHG ($\sim 94\%$), is used for pumping the second OPCPA stage. The beam transport for this part is fully enclosed in vacuum. A telescope consisting of curved mirrors with $f = 3400\,\mathrm{mm}$ and $f = 1900\,\mathrm{mm}$, respectively, images the SHG crystal onto the second OPCPA crystal and adjusts the pump-beam size. The residual pump energy after amplification is guided back into air and blocked in a beam dump after separation from the signal beam.

The signal beam is aligned with two flat silver mirrors onto the first OPCPA crystal. After the first stage, a motorized delay unit allows for the fine adjustment of the relative timing between signal and pump pulses inside the second crystal. A reflective telescope $f = 100\,\mathrm{mm}$ and $f = 400\,\mathrm{mm}$ increases the beam size after the amplification in the first stage to match the pump-beam size in the second stage. After amplification in the second stage the signal beam is coupled out of the vacuum and separated from the pump beam. A Galilei-telescope, consisting of $f = 400\,\mathrm{mm}$ and $f = -100\,\mathrm{mm}$ silver mirrors, reduces the signal-beam size in order to meet the requirements of the diagnostics.

As mentioned before, the vacuum system was designed to accommodate a pump energy of up to 500 mJ at 515 nm from the 20-pass Yb:YAG imaging amplifier [97]. For the experiments, the pump energy was limited to 90 mJ due to some low-quality coatings in the Yb:YAG amplifier that were replaced only after this campaign (cf. section 6.2). In order to counterbalance the reduced pump energy, the telescope in front of the compressor was rebuilt with a smaller magnification factor guaranteeing to keep the required intensities at the nonlinear crystals.

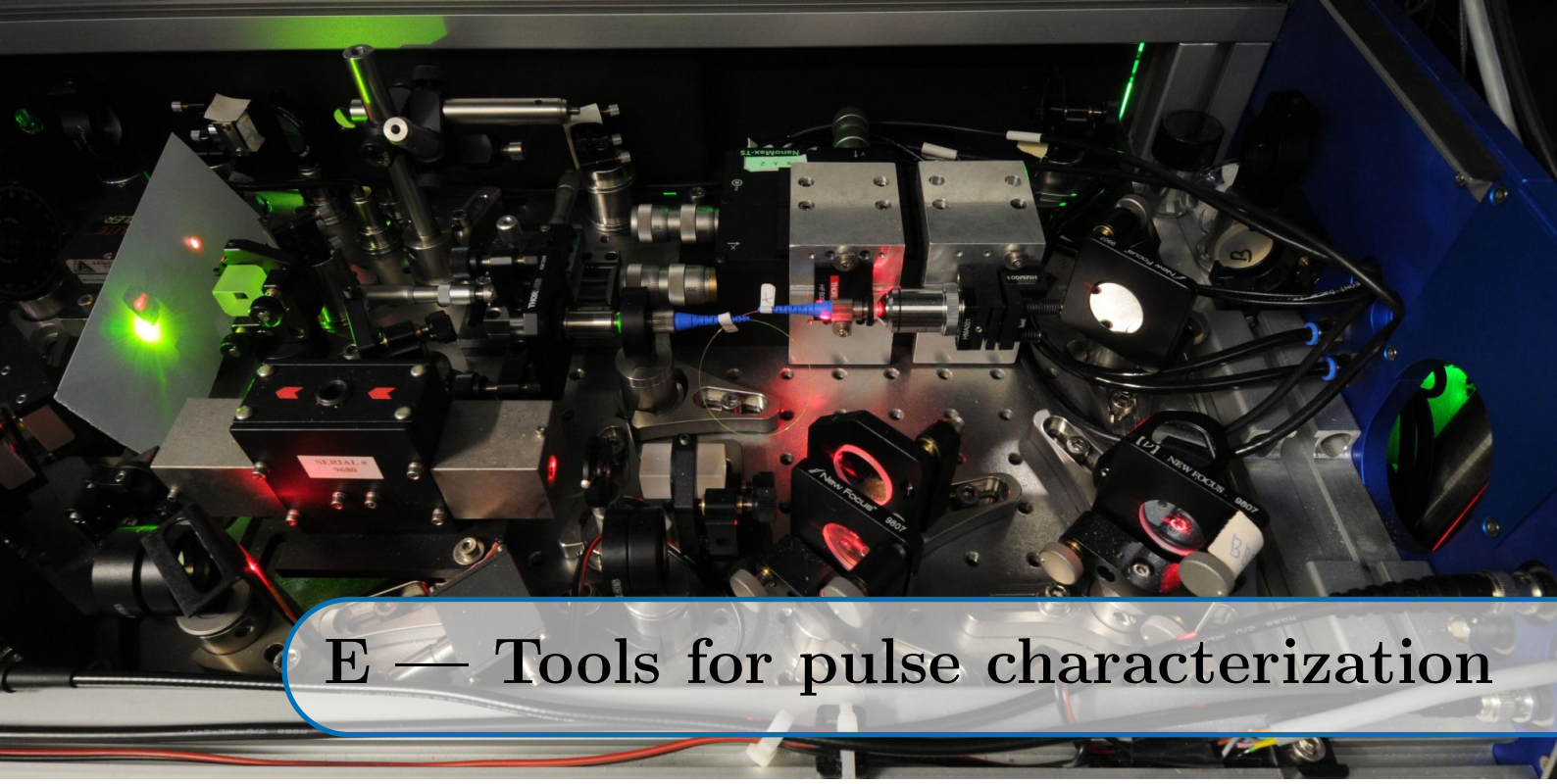

E — Tools for pulse characterization

This section is dedicated to the pulse-characterization tools used in the experiments presented in this thesis. The first part briefly describes the devices used for the measurement of the spectrum, energy and intensity beam profile. The second part introduces the FROG devices used for a complete characterization of the light pulses. In the third part the third order autocorrelator which is used for the characterization of the temporal contrast is described.

E.1 Spectrum, energy and beam profile

The characterization of the spectrum, energy and intensity beam profile of the signal pulse and pump laser is performed with commercially available devices.

- **Spectrum:** The spectrum of the broadband signal is detected with Avantes spectrometers. Since there is no detector material available that covers the full wavelength range of the signal pulse, i.e. $700 - 1400\,\mathrm{nm}$, the signal spectrum is measured with two spectrometers. One spectrometer (AvaSpec-Nir256-1.7) equipped with an InGaAs-detector covers the near infrared spectral part ($1000 - 1800\,\mathrm{nm}$). The second spectrometer (AvaSpec-3648) which uses a Si-detector detects the visible spectral region ($500 - 1000\,\mathrm{nm}$). The specifications of the two spectrometers are listed in Table E.1. A bifurcated fiber splits up the light into two parts containing all spectral information and delivers it to the two spectrometers. Therefore, the full spectrum of a single shot can be measured. Since the measured spectrum is very sensitive to the alignment of the beam into the fiber, the measurements are performed with an additional cosine corrector. The spectrometers are calibrated with an halogen light-source (HL-

	AvaSpec-3648	AvaSpec-Nir256-1.7
# pixel	3648	256
wavelength	$488 - 1027\,\text{nm}$	$973 - 1871\,\text{nm}$
grating	NB	NIRA
slit size	$25\,\mu\text{m}$	$100\,\mu\text{m}$
resolution (FWHM)	0.6 nm	12 nm

Table E.1: *Specifications of spectrometers for the signal characterization [123].*

2000-Cal) from OceanOptics. In the spectral region of $880 - 1000\,\text{nm}$, which is at the end of the sensitivity range of both spectrometers, the obtained spectral information is not reliable as depicted in Figure E.1(a). Here, an amplified broadband signal pulse is measured with the two Avantes spectrometers (red curve) which were meticulously calibrated shortly before. For comparison, the spectrum detected with an OceanOptics NirQuest512 spectrometer is shown. The NirQuest was only a demonstration tool on loan from OceanOptics for a short time. Obviously, the lack of intensity in the range of $890 - 1000\,\text{nm}$ is an artifact introduced by the Avantes spectrometers. Consequently, the measured spectra are interpolated in the wavelength range of $890 - 1000\,\text{nm}$ as indicated by the gray line in Figure E.1(a). Here, the intensity at 890 nm of the visible spectrometer and the intensity at 1000 nm of the infrared spectrometer is taken as references. The intensities between these boundaries are linearly interpolated.

In order to avoid saturation of the detectors in the case of amplified signal pulses, the pulse energy is attenuated by reflection on wedges and with neutral-density filters before entering the spectrometer. Since the transmission of the ND filters is not constant for the broad signal bandwidth in spite of their name, their characteristics are determined by a Varian Cary 500 Scan UV-Vis-NIR Spectrophotometer. These transmission curves are used to correct the data and are presented in Figure E.1(b).

The spectral characterization of the fundamental and frequency-doubled pump laser is performed with two customized Avantes AvaSpec-3648 spectrometers. They have a large spectral resolution in order to observe effects from SPM due to nonlinear beam propagation. Table E.2 gives an overview of the most important specifications of both spectrometers.

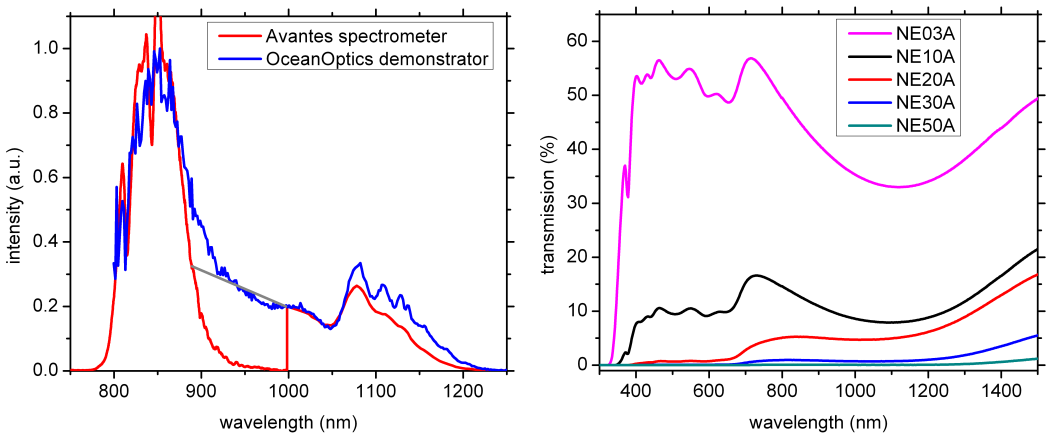

(a) spectrometer test (b) neutral density filters

Figure E.1: *(a) shows a comparison between the used Avantes spectrometers and a demonstration spectrometer from OceanOptics. (b) shows the measured transmission of different neutral density filters used for pulse attenuation.*

	AvaSpec-3648 for $2\omega = 515\,\text{nm}$	AvaSpec-3648 for $\omega = 1030\,\text{nm}$
# pixel	3648	3648
wavelength	$500 - 567\,\text{nm}$	$894 - 1050\,\text{nm}$
grating	VE-grating ($2400\,\frac{1}{\text{mm}}$)	NC-grating ($1200\,\frac{1}{\text{mm}}$)
slit size	$10\,\mu\text{m}$	$10\,\mu\text{m}$
resolution (FWHM)	$0.05\,\text{nm}$	$0.08\,\text{nm}$

Table E.2: *Specifications of spectrometers for the pump-laser characterization [123].*

- **Energy:** The pulse energies are measured with energy sensors and readout units from Coherent. In order to measure small energies, a Coherent J50LP-2A energy sensor is applied in the experiments. It is able to measure energies from $3\,\mu\text{J}$ up to $7\,\text{mJ}$ within a wavelength range of $0.25 - 3\,\mu\text{m}$ [124]. Higher pulse energies are determined by the Coherent J-50MB-YAG energy sensor, which can measure energies from $1.5\,\text{mJ}$ to $3\,\text{J}$ for a wavelength range of $0.27 - 2.1\,\mu\text{m}$. More detailed information about the energy sensor are given in [125]. In order to read out the energy sensors, a Coherent LabMax TOP [126] energy meter is used. It can calculate the standard deviation for a desired number of shots. Furthermore, the device can save longterm trends with the drawback that only approximately one shot per second is taken into account regardless of the repetition rate.

- **Beam profile:** In order to characterize the intensity beam profile of the pulses, a WinCamD Series UCD23 is used. Table E.3 summarizes the most important parameters of this device. More detailed information can be found at [127].

	WincamD Series UDC23
wavelength	350 to 1150 nm
pixel count, HxV	1.4 MPixel, 1360×1024
image area	$8.8\,\text{mm} \times 6.6\,\text{mm}$
pixel dimension	$6.45\,\mu\text{m} \times 6.45\,\mu\text{m}$

Table E.3: *Specifications of the WincamD Series UCD23 [127].*

E.2 Measurement of the pulse duration and phase of the broadband signal

In order to characterize the pulse duration and phase of the broadband seed and the amplified signal, an X-FROG and a single-shot SHG-FROG are used. Since the theoretical background of FROG in general and the specialties of single-shot FROGs are well described in the book of Rick Trebino, "Frequency resolved optical gating" [104], this section deals with the particular setups and the calibration of both FROGs only.

E.2.1 X-FROG

Broadband pulses with high repetition rate and very low energy are characterized with the X-FROG. A schematic sketch of the X-FROG is shown in Figure E.2. Since this device is based on the cross-correlation technique, the broadband pulses are mixed with a high energy compressed reference pulse. This reference pulse is a small part of the well characterized compressed Femtopower output (150 μJ with 25 fs pulse duration at 790 nm). It is compressed at the location of the X-FROG with chirped mirrors (**CM**) and fully characterized with a commercially available Grenouille (Swamp Optics). The reference pulse is delayed relative to the broadband signal pulse at the position of the SFG crystal via a Thorlabs MTS50/M-Z8E motorized linear stage (**delay**), allowing a total time window of 330 ps with a minimum time step of 1 fs. SFG between the reference and the signal pulse is performed in a 10 μm thin BBO crystal in which the SHG process is phase matched

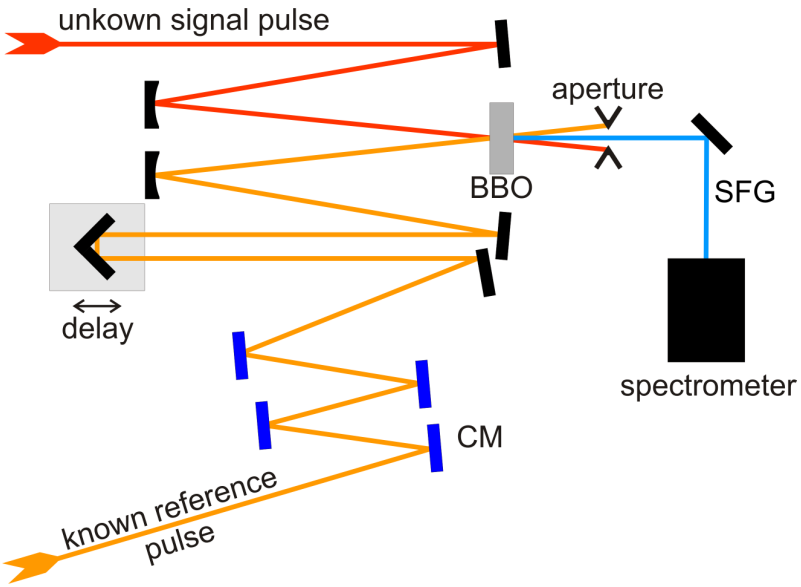

Figure E.2: *Schematic sketch of the X-FROG setup.*

over the entire spectral range of the broadband seed (700−1400 nm) and the reference pulse (760 − 820 nm). The fundamental beams are blocked by an aperture and the SFG signal is detected with an Avantes spectrometer covering the wavelength range of 250 − 600 nm.

Test measurement: In order to test the function of the homebuilt X-FROG, traces of the same pulses before and after having passed two different thicknesses of dispersive material were recorded. The difference in the retrieved GD curves exactly matches the difference in dispersion expected for the two thicknesses. Figure E.3 presents the results of these cross-check measurements. The agreement between theory (blue and green curves) and experiment (red and black curves) is extremely good for both materials over the full wavelength range of the broadband signal. This proves that the spectral phase information provided by the homebuilt X-FROG is reliable.

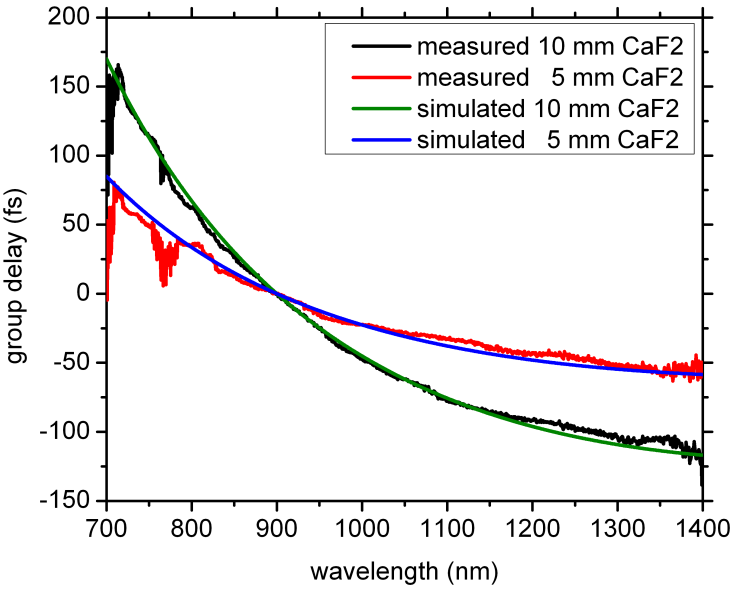

Figure E.3: *Functionality test of the X-FROG. The experimental GD of the materials (red curve and black curve) is the result of the subtraction between the measured traces: one without material and two with additional* 5 mm *and* 10 mm *of* CaF_2*, respectively. The blue and green curves represent the calculated GD for* 5 mm *and* 10 mm CaF_2*, respectively (Sellmeier equations for* CaF_2 *are taken from [128]).*

E.2.2 Single-shot 5 fs SHG-FROG

The amplified pulses of the PFS system are characterized with a homebuilt single-shot FROG. In a single-shot FROG the temporal information is mapped onto one spatial coordinate whereas the spectral information is contained in the other coordinate. The mapping of time onto space is realized by a non-collinear SFG geometry with cylindrically focused beams creating line foci. In order to measure light pulses with pulse durations as short as 5 fs and avoid pulse lengthening due to dispersion, the setup is solely based on reflective components before the SHG crystal.

The schematic layout of the single-shot FROG is shown in Figure E.4. The incoming beam is aligned using two apertures **I1** and **I2**. A vertical D-cut silver mirror **D1** is used to split up the incoming beam into two halves. In one arm of the following interferometer setup a manual delay stage is installed in order to adjust the temporal overlap of both pulses inside the nonlinear crystal. The second D-cut mirror **D2** is installed in a horizontal position introducing an angle between both pulses of 1° in the vertical plane (side view). In the horizontal plane (top view) both pulses are overlapped. A cylindrical gold mirror **F1** generates two line foci on the nonlinear crystal with an FWHM of approx 40 μm. The SFG takes place in a 5 μm thin BBO

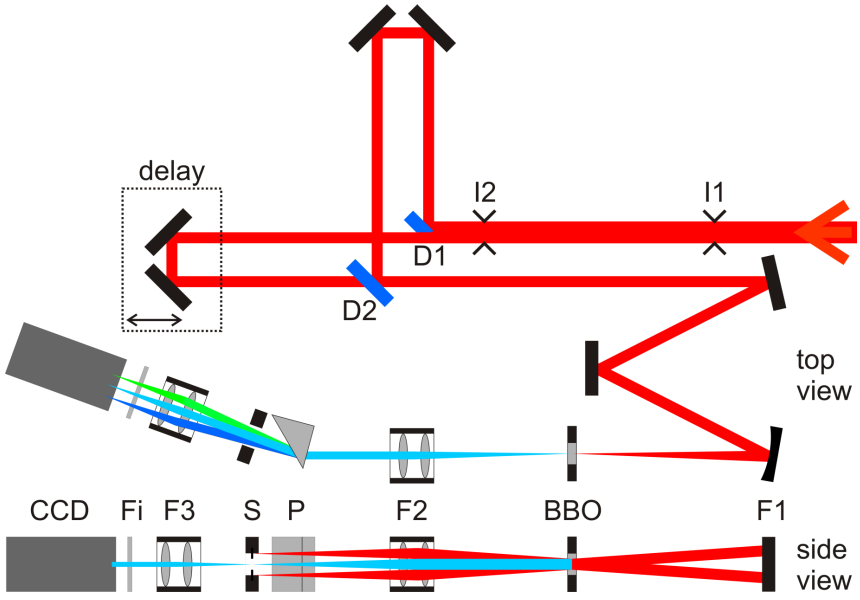

Figure E.4: *Schematic layout of the single-shot SHG-FROG in top view and side view.* ***I1*** *and* ***I2*** *alignment apertures,* ***D1*** *vertical D-cut mirror,* ***D2*** *horizontal D-cut mirror,* ***F1*** *cylindrical mirror with* $f = 100\,\mathrm{mm}$, ***BBO*** *crystal for SFG,* ***F2*** *achromat with* $f = 150\,\mathrm{mm}$, ***P*** *quartz prism,* ***S*** *horizontal slit to block the fundamental beams,* ***F3*** *second achromat with* $f = 50\,\mathrm{mm}$, ***Fi*** *different filters such as color filters and neutral density filters,* ***CCD*** *camera recording the FROG-trace.*

crystal in order to support phase matching for the full bandwidth. However, even a thickness of just 5 μm can not provide a constant conversion efficiency over the full bandwidth of the PFS system [129, 130]. The spectral dependence of the conversion efficiency for the BBO crystal cut at a phase-matching angle of 29.2° is presented in Figure E.5. The measured FROG traces are corrected for this shape. Two achromats **F2** and **F3** image the SFG signal from the nonlinear crystal onto the CCD chip of the camera. The right-angle quartz prism **P** splits up the different wavelengths of the SFG signal. Compared to a grating, the prism offers a higher and relatively constant spectral throughput. The consecutive horizontal slit **S** blocks the fundamental beams and the SHG generated from the fundamentals reducing the stray light on the camera. Different filters **Fi** can be installed in front of the camera. A BG40 color filter (short-pass filter) reduces the stray light of the fundamental beams further. Neutral density filters are implemented to attenuate the SFG signal and suppress light from the surroundings. Beside the effect of the nonlinear interaction on the FROG trace all linear transmission functions from the filters as well as the spectral-camera-response function [131] are taken into account and the measured FROG trace is corrected for these before retrieval.

The measured FROG traces are retrieved with the Femtosoft Frog 3 software [132]. The FROG error quantifies the agreement between the measured trace and the retrieved trace and is therefore a measure for the quality of the retrievals. In general, the FROG error lies in the range of few percents for a good retrieval.

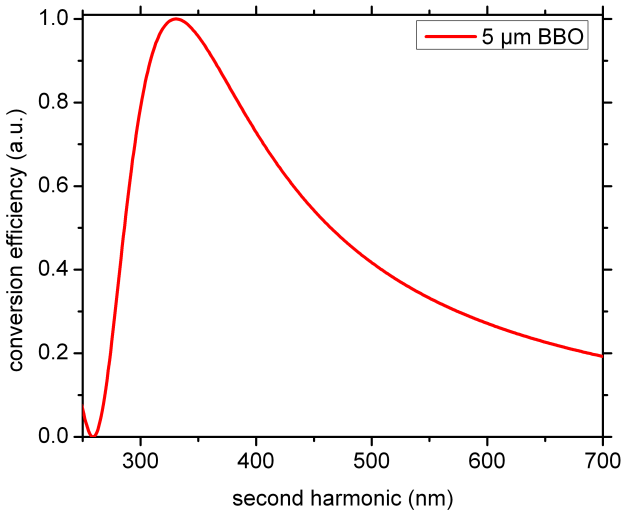

Figure E.5: *Calculated conversion efficiencies for a 5 μm thick BBO crystal with a phase-matching angle of 29.2° and a crossing angle of the fundamental beams of 1°. The formulas used are taken from [130].*

Spectral and temporal calibration: The temporal and spectral calibration of the single-shot SHG-FROG were performed in two independent steps. For the temporal calibration the output of the Femtopower was used. The time axis was determined by generating double pulses via a Dazzler with well controlled delays before the Femtopower. The double pulses were detected by the FROG and the pixel distance between the peaks was compared to the temporal delay set via the Dazzler. By this method the time resolution was measured to be $0.98 \pm 0.04 \, \frac{\text{fs}}{\text{pixel}}$. The full time window of the FROG is approx. 100 fs for a FWHM beam size of 5 mm of the incoming beam.

In order to calibrate the spectral axis, the broadband output of the two cascaded HCFs was used (cf. Figure 6.2). Narrowband pulses at different wavelengths were cut out by two razor blades in the Fourier plane of the prism stretcher and characterized with the two Avantes spectrometers presented in appendix E.1. These narrow-bandwidth pulses were compressed and the position of the second harmonic on the detector of the FROG was measured. With this method its wavelength can be associated with pixel positions. The result of this calibration is presented in Figure E.6.

Test measurement: As in the case of the X-FROG, the functionality of the SHG-FROG was tested with the same measurement procedure. The results are presented in Figure E.7. The strong oscillations in the wavelength range of $700 - 800$ nm are a result of the signal intensity being too low in that spectral range. Nevertheless, the measured curve reproduces the theoretical curve very well. Thus, also the single-shot SHG-FROG is able to characterize the spectral phase and GD in a reliable way.

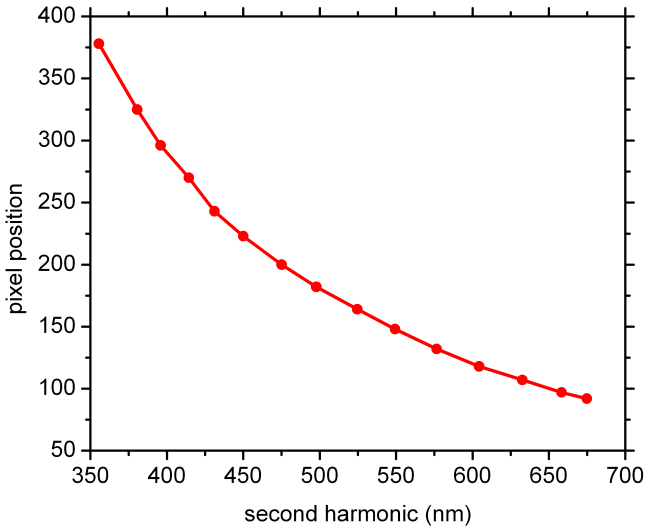

Figure E.6: *Spectral calibration of the single-shot SHG-FROG.*

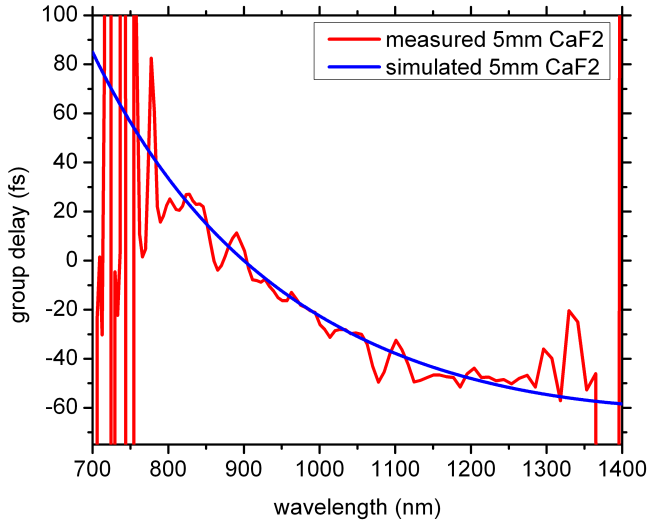

Figure E.7: *Functionality test of the homebuilt single-shot SHG-FROG. The presented GD of the material (red curve) is the result of the subtraction between two measured traces: one without material and one with additional* 5 mm CaF_2. *The blue curve represents the calculated GD.*

E.3 Characterization of the temporal contrast

The temporal contrast of the broadband signal is characterized with a homebuilt third-order autocorrelator. This device was planned and assembled in collaboration with Rocío Borrego-Varillas, Politecnico di Milano, Italy. A schematic sketch of the autocorrelator setup is presented in Figure E.8. The vertically polarized input beam is attenuated by the unit **MA**, consisting of two partially coated silver mirrors mounted on a linear stage. Since 1/3 of one mirror and 2/3 of the other are silver coated, the position of the linear stage determines the level of transmission, which can be 100% (two silver surfaces), 8% (one silver, one glass surface) or 0.64% (two glass surfaces). The pulse is then split into two parts via the pellicle beam splitter (**BS**) with a ratio of $T = 90\%$ and $R = 10\%$. The reflected part can be delayed in time with a 150 mm long delay stage (Physik Instrumente M-505.6dg, **delay**), allowing a scan range of 2 ns in total due to the doubly folded beam path. The transmitted beam is frequency doubled in a 400 μm thick BBO crystal, cut for type I SHG ($\theta = 29.2°$). Two periscopes (**P1** and **P2**) equipped with dichroic mirrors, suppressing the residual fundamental beam, rotate the polarization of the 2ω beam back to the vertical direction in order to have the correct polarization direction in the type I THG crystal. The fundamental and the frequency-doubled beams are

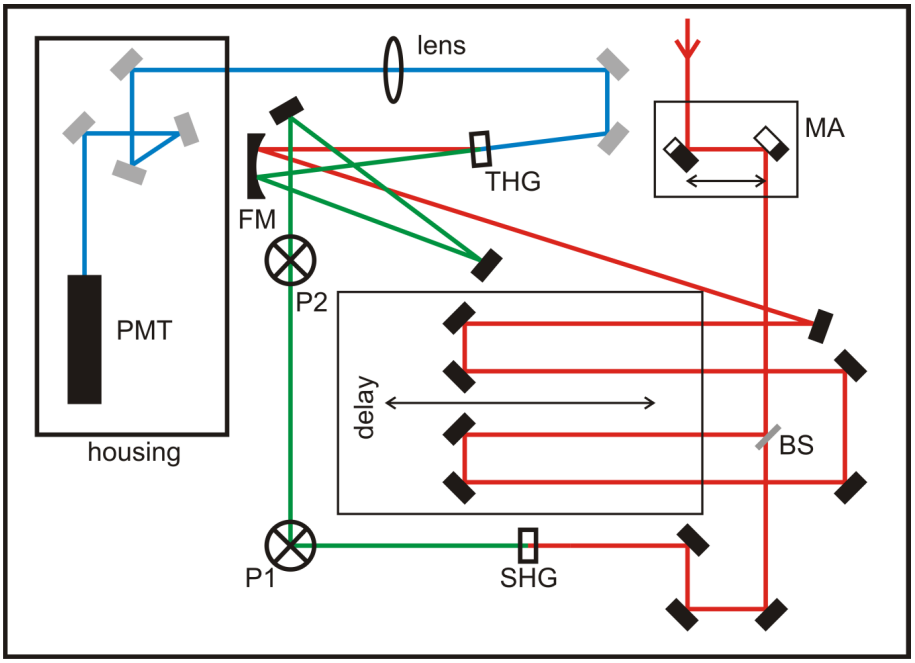

Figure E.8: *Setup of the homebuilt third order autocorrelator used for temporal contrast characterization.* ***MA:*** *linear stage with two partially coated silver mirrors,* ***BS:*** *pellicle beam splitter,* ***delay:*** *motorized delay stage,* ***SHG:*** *BBO crystal used for frequency doubling.* ***P1*** *and* ***P2:*** *periscopes used to rotate beam polarization,* ***FM:*** *focusing mirror,* ***THG:*** *BBO crystal used for THG,* ***PMT:*** *photo multiplier tube,* ***black mirrors:*** *silver coated mirrors,* ***grey mirrors:*** *HR* 3ω *mirrors, acting as dichroic mirrors. More details are given within the text.*

focused into the crystal with a silver mirror $f = 100\,\text{mm}$ (**FM**). The 3ω beam, generated in a $200\,\mu\text{m}$ thick BBO crystal ($\theta = 44.3°$) is guided with dichroic mirrors to the photo multiplier tube (PMT). Owing to the non-collinear geometry of the THG, the background arising from the ω and 2ω signal is suppressed at the position of the PMT. The Hamamatsu R2078 PMT is a solar blind model ($160 - 320\,\text{nm}$) and allows a dynamic range of 10^7 [133]. Combined with the attenuator unit a total dynamic range of 10^{11} is expected at a few hundred μJ of pulse energy.

Since the software for the autocorrelator has not been finished yet, the presented temporal contrast measurements (cf. subsection 7.2.3) were performed with a commercially available Sequoia third-order autocorrelator from Amplitude Technologies. Table E.4 presents the main parameters of this device. More detailed information can be found at [134].

	Sequoia 800
dynamic range	$> 10^9$
temporal range	570 ps
resolution	20 fs
working wavelength	$760 - 840$ nm
minimum pulse energy	1 mJ

Table E.4: *Specifications of the Sequoia third-order autocorrelator.*

However, the new device features advantages compared to the commercial solution such as a higher dynamic range at lower input energies (11-orders of magnitude at 100 μJ), a broader supported bandwidth ($\sim$ 100 nm). Consequently, the software is developed further. It will be finished by the end of August allowing to perform the contrast measurements of the future 1 J-OPCPA with the new device.

F — SHG of the signal beam

The PFS is based on amplification of a broad bandwidth of $700 - 1400\,\text{nm}$. Some spectral components of the signal beam are phase matched for SHG in the nonlinear crystals which can lead to a reduced signal energy. Hence, this effect will be discussed in this paragraph.

As presented in Figure F.1 the k-vector of the SHG of the signal always points in the same direction as the k-vector of the fundamental beam and therefore the phase-matching angle for SHG is $\psi = \theta \pm \alpha$, i.e. 13.35° and 15.55° with $\theta = 14.45°$ and $\alpha = 1.1°$ depending which scheme is used. Figure F.2(a) presents the phase-matching angles in LBO as a function of the signal wavelength for perfectly phase matched SHG, i.e. $\Delta k = 0$. With the calculated values of the phase-matching angle for SHG in the case of PFS, frequency doubling at a signal wavelength of either 1030 nm or 1000 nm is obtained (gray circles in Figure F.2(a)). For DKDP the situation is similar. Here, SHG occurs at 1150 nm or 985 nm. Figure F.2(b) depicts

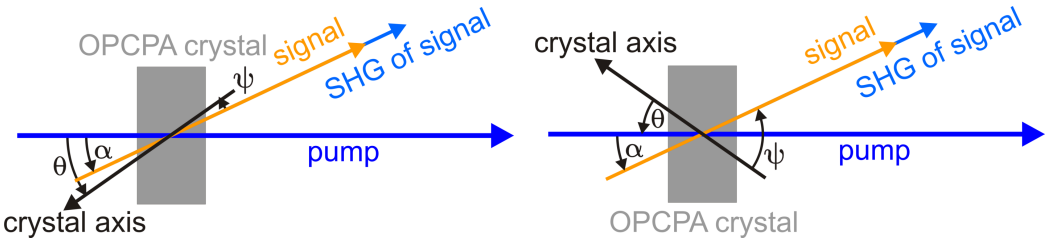

(a) walk-off compensation (b) tangential phase matching

Figure F.1: *Phase-matching angle for SHG for (a) the walk-off compensation scheme and (b) the tangential phase matching scheme.*

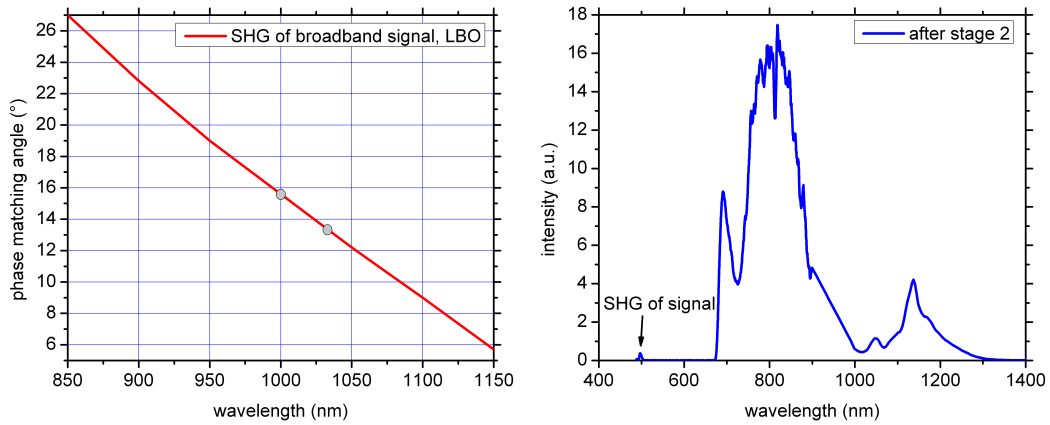

(a) phase matching for SHG (b) SHG of signal beam

Figure F.2: *(a) shows the perfect phase-matching angle for SHG of the broadband signal in LBO. The phase-matching angle for the walk-off compensation as well as the tangential phase-matching scheme are represented by the gray circles, resulting in a frequency-doubled wavelength of* 500 nm *or* 515 nm*, respectively. (b) depicts a measured signal spectrum after amplification in two LBO stages (cf. section 7.3) clearly indicating the SHG of the signal beam. The energy of the SHG amounts to* $\sim 1.8 \times 10^{-4}$ *of the main beam.*

a measured signal spectrum after amplification in two LBO stages (cf. section 7.3) indicating SHG at $\sim 500\,\mathrm{nm}$. The energy ratio between the fundamental and SHG beam is 5.5×10^3 and therefore does not influence the nonlinear amplification at all.

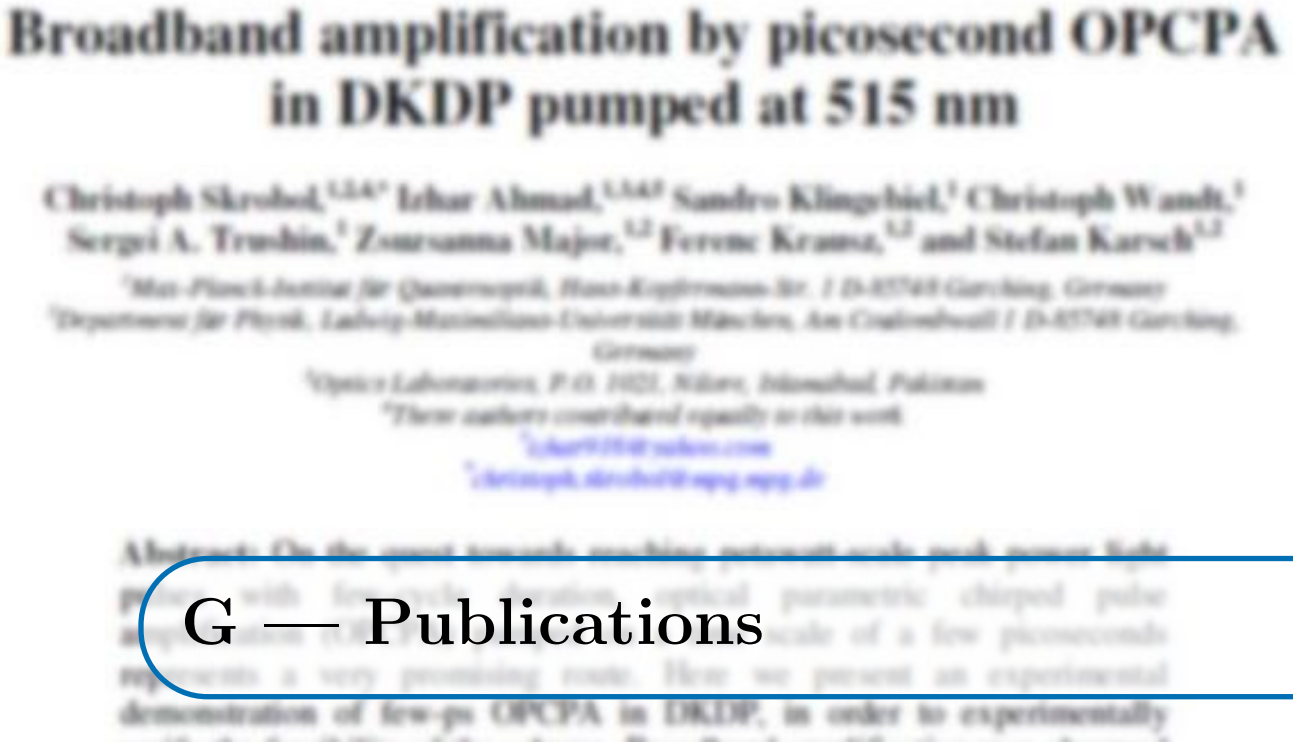

G — Publications

G.1 Broadband amplification by picosecond OPCPA in DKDP pumped at 515 nm

Broadband amplification by picosecond OPCPA in DKDP pumped at 515 nm

Christoph Skrobol,[1,2,4,*] Izhar Ahmad,[1,3,4,5] Sandro Klingebiel,[1] Christoph Wandt,[1] Sergei A. Trushin,[1] Zsuzsanna Major,[1,2] Ferenc Krausz,[1,2] and Stefan Karsch[1,2]

[1]*Max-Planck-Institut für Quantenoptik, Hans-Kopfermann-Str. 1 D-85748 Garching, Germany*
[2]*Department für Physik, Ludwig-Maximilians-Universität München, Am Coulombwall 1 D-85748 Garching, Germany*
[3]*Optics Laboratories, P.O. 1021, Nilore, Islamabad, Pakistan*
[4]*These authors contributed equally to this work*
[5]*izhar916@yahoo.com*
[*]*christoph.skrobol@mpq.mpg.de*

Abstract: On the quest towards reaching petawatt-scale peak power light pulses with few-cycle duration, optical parametric chirped pulse amplification (OPCPA) pumped on a time scale of a few picoseconds represents a very promising route. Here we present an experimental demonstration of few-ps OPCPA in DKDP, in order to experimentally verify the feasibility of the scheme. Broadband amplification was observed in the wavelength range of 830-1310 nm. The amplified spectrum supports two optical cycle pulses, at a central wavelength of ~920 nm, with a pulse duration of 6.1 fs (FWHM). The comparison of the experimental results with our numerical calculations of the OPCPA process showed good agreement. These findings confirm the reliability of our theoretical modelling, in particular with respect to the design for further amplification stages, scaling the output peak powers to the petawatt scale.

OCIS codes: (190.4970) Parametric oscillators and amplifiers; (190.4975) Parametric processes; (190.4410) Nonlinear optics, parametric processes; (190.4223) Nonlinear wave mixing.

References and links

1. J. Faure, Y. Glinec, A. Pukhov, S. Kiselev, S. Gordienko, E. Lefebvre, J. P. Rousseau, F. Burgy, and V. A. Malka, "A laser-plasma accelerator producing monoenergetic electron beams," Nature **431**(7008), 541–544 (2004).
2. S. P. D. Mangles, C. D. Murphy, Z. Najmudin, A. G. R. Thomas, J. L. Collier, A. E. Dangor, E. J. Divall, P. S. Foster, J. G. Gallacher, C. J. Hooker, D. A. Jaroszynski, A. J. Langley, W. B. Mori, P. A. Norreys, F. S. Tsung, R. Viskup, B. R. Walton, and K. Krushelnick, "Monoenergetic beams of relativistic electrons from intense laser-plasma interactions," Nature **431**(7008), 535–538 (2004).
3. C. G. R. Geddes, C. S. Toth, J. Van Tilborg, E. Esarey, C. B. Schroeder, D. Bruhwiler, C. Nieter, J. Cary, and W. P. Leemans, "High-quality electron beams from a laser wakefield accelerator using plasma-channel guiding," Nature **431**(7008), 538–541 (2004).
4. M. Geissler, J. Schreiber, and J. Meyer-ter-Vehn, "Bubble acceleration of electrons with few-cycle laser pulses," New J. Phys. **8**(9), 186 (2006).
5. Y. Nomura, R. Hörlein, P. Tzallas, B. Dromey, S. Rykovanov, Zs. Major, J. Osterhoff, S. Karsch, L. Veisz, M. Zepf, D. Charalambidis, F. Krausz, and G. D. Tsakiris, "Attosecond phase locking of harmonics emitted from laser-produced plasmas," Nat. Phys. **5**(2), 124–128 (2009).
6. D. Strickland and G. Mourou, "Compression of amplified chirped optical pulses," Opt. Commun. **56**(3), 219–221 (1985).
7. A. Dubietis, G. Jonušauskas, and A. Piskarskas, "Powerful femtosecond pulse generation by chirped and stretched pulse parametric amplification in BBO crystal," Opt. Commun. **88**(4-6), 437–440 (1992).
8. V. V. Lozhkarev, G. I. Freidman, V. N. Ginzburg, E. V. Katin, E. A. Khazanov, A. V. Kirsanov, G. A. Luchinin, A. N. Mal'shakov, M. A. Martyanov, O. V. Palashov, A. K. Poteomkin, A. M. Sergeev, A. A. Shaykin, and I. V. Yakovlev, "Compact 0.56 petawatt laser system based on optical parametric chirped pulse amplification in KD*P crystals," Laser Phys. Lett. **4**(6), 421–427 (2007).

#159355 - $15.00 USD Received 2 Dec 2011; revised 14 Jan 2012; accepted 20 Jan 2012; published 9 Feb 2012

9. O. Chekhlov, E. J. Divall, K. Ertel, S. J. Hawkes, C. J. Hooker, I. N. Ross, P. Matousek, C. Hernandez-Gomez, I. Musgrave, Y. Tang, T. Winstone, D. Neely, R. Clarke, P. Foster, S. J. Hancock, B. E. Wyborn, and J. L. Collier, "Development of petawatt laser amplification systems at the Central Laser Facility," Proc. SPIE **6735**, 67350J (2007).
10. S. Adachi, N. Ishii, T. Kanai, A. Kosuge, J. Itatani, Y. Kobayashi, D. Yoshitomi, K. Torizuka, and S. Watanabe, "5-fs, Multi-mJ, CEP-locked parametric chirped-pulse amplifier pumped by a 450-nm source at 1 kHz," Opt. Express **16**(19), 14341–14352 (2008).
11. D. Herrmann, L. Veisz, R. Tautz, F. Tavella, K. Schmid, V. Pervak, and F. Krausz, "Generation of sub-three-cycle, 16 TW light pulses by using noncollinear optical parametric chirped-pulse amplification," Opt. Lett. **34**(16), 2459–2461 (2009).
12. X. Gu, G. Marcus, Y. Deng, T. Metzger, C. Teisset, N. Ishii, T. Fuji, A. Baltuska, R. Butkus, V. Pervak, H. Ishizuki, T. Taira, T. Kobayashi, R. Kienberger, and F. Krausz, "Generation of carrier-envelope-phase-stable 2-cycle 740-μJ pulses at 2.1-μm carrier wavelength," Opt. Express **17**(1), 62–69 (2009).
13. D. Brida, C. Manzoni, G. Cirmi, M. Marangoni, S. Bonora, P. Villoresi, S. De Silvestri, and G. Cerullo, "Few-optical-cycle pulses tunable from the visible to the mid-infrared by optical parametric amplifiers," J. Opt. **12**(1), 013001 (2010).
14. G. Cerullo and S. De Silvestri, "Ultrafast optical parametric amplifiers," Rev. Sci. Instrum. **74**(1), 1–18 (2003).
15. N. Ishii, L. Turi, V. S. Yakovlev, T. Fuji, F. Krausz, A. Baltuska, R. Butkus, G. Veitas, V. Smilgevicius, R. Danielius, and A. Piskarskas, "Multimillijoule chirped parametric amplification of few-cycle pulses," Opt. Lett. **30**(5), 567–569 (2005).
16. S. Witte, R. T. Zinkstok, A. L. Wolf, W. Hogervorst, W. Ubachs, and K. S. E. Eikema, "A source of 2 terawatt, 2.7 cycle laser pulses based on noncollinear optical parametric chirped pulse amplification," Opt. Express **14**(18), 8168–8177 (2006).
17. O. Chalus, P. K. Bates, M. Smolarski, and J. Biegert, "Mid-IR short-pulse OPCPA with micro-Joule energy at 100kHz," Opt. Express **17**(5), 3587–3594 (2009).
18. K. W. Aniolek, R. L. Schmitt, T. J. Kulp, B. A. Richman, S. E. Bisson, and P. E. Powers, "Microlaser-pumped periodically poled lithium niobate optical parametric generator-optical parametric amplifier," Opt. Lett. **25**(8), 557–559 (2000).
19. B. Zhao, Y. Jiang, K. Sueda, N. Miyanaga, and T. Kobayashi, "Ultrabroadband noncollinear optical parametric amplification with LBO crystal," Opt. Express **16**(23), 18863–18868 (2008).
20. V. V. Lozhkarev, G. I. Freidman, V. N. Ginzburg, E. A. Khazanov, O. V. Palashov, A. M. Sergeev, and I. V. Yakovlev, "Study of broadband optical parametric chirped pulse amplification in a DKDP crystal pumped by the second harmonic of a Nd:YLF laser," Laser Phys. **15**, 1319–1333 (2005).
21. Y. Mori, I. Kuroda, S. Nakajima, T. Sasaki, and S. Nakai, "New nonlinear optical crystal: cesium lithium borate," Appl. Phys. Lett. **67**(13), 1818–1820 (1995).
22. B. Zhao, X. Liang, Y. Leng, Y. Jiang, C. Wang, H. Lu, J. Du, Z. Xu, and D. Shen, "Degenerated optical parametric chirped-pulse amplification with cesium lithium borate," Appl. Opt. **45**(3), 565–568 (2006).
23. E. A. Khazanov and A. M. Sergeev, "Petawatt lasers based on optical parametric amplifiers: their state and prospects," Phys. Usp. **51**, 969–974 (2008).
24. S. Karsch, Zs. Major, J. Fülöp, I. Ahmad, T. Wang, A. Henig, S. Kruber, R. Weingartner, M. Siebold, J. Hein, C. Wandt, S. Klingebiel, J. Osterhoff, R. Hörlein, and F. Krausz, "The Petawatt Field Synthesizer: a new approach to ultrahigh field generation," in *Advanced Solid-State Photonics*, OSA Technical Digest Series (CD) (Optical Society of America, 2008), paper WF1.
25. Zs. Major, S. A. Trushin, I. Ahmad, M. Siebold, C. Wandt, S. Klingebiel, T.-J. Wang, J. A. Fülöp, A. Henig, S. Kruber, R. Weingartner, A. Popp, J. Osterhoff, R. Hörlein, J. Hein, V. Pervak, A. Apolonski, F. Krausz, and S. Karsch, "Basic concepts and current status of the Petawatt Field Synthesizer — a new approach to ultrahigh field generation," Rev. Laser Eng. **37**, 431–436 (2009).
26. C. Wandt, S. Klingebiel, M. Siebold, Z. Major, J. Hein, F. Krausz, and S. Karsch, "Generation of 220 mJ nanosecond pulses at a 10 Hz repetition rate with excellent beam quality in a diode-pumped Yb:YAG MOPA system," Opt. Lett. **33**(10), 1111–1113 (2008).
27. S. Klingebiel, I. Ahmad, C. Wandt, C. Skrobol, S. A. Trushin, Zs. Major, F. Krausz, and S. Karsch, "Experimental and theoretical investigation of timing jitter inside a stretcher-compressor setup," submitted to Opt. Express (2011).
28. G. Arisholm, "General numerical methods for simulating second-order nonlinear interactions in birefringent media," J. Opt. Soc. Am. B **14**(10), 2543–2549 (1997).
29. I. Ahmad, S. Trushin, Z. Major, C. Wandt, S. Klingebiel, T. J. Wang, V. Pervak, A. Popp, M. Siebold, F. Krausz, and S. Karsch, "Frontend light source for short-pulse pumped OPCPA system," Appl. Phys. B **97**(3), 529–536 (2009).
30. I. Ahmad, L. Bergé, Zs. Major, F. Krausz, S. Karsch, and S. A. Trushin, "Redshift of few-cycle infrared pulses in the filamentation regime," New J. Phys. **13**(9), 093005 (2011).
31. I. Ahmad, S. Klingebiel, C. Skrobol, C. Wandt, S. Trushin, Z. Major, F. Krausz, and S. Karsch, "Pump-seed synchronization measurements for high-power short-pulse pumped few-cycle OPCPA system," in Advanced Solid-State Photonics, OSA Technical Digest Series (CD) (Optical Society of America, 2010), paper AMB9.

#159355 - $15.00 USD Received 2 Dec 2011; revised 14 Jan 2012; accepted 20 Jan 2012; published 9 Feb 2012

32. Zs. Major, S. Klingebiel, C. Skrobol, I. Ahmad, C. Wandt, S. A. Trushin, F. Krausz, S. Karsch, and D. Dumitras, "Status of the Petawatt Field Synthesizer - pump-seed synchronization measurements," AIP Conf. Proc. **1228**, 117–122 (2010).
33. J. A. Fülöp, Zs. Major, A. Henig, S. Kruber, R. Weingartner, T. Clausnitzer, E.-B. Kley, A. Tünnermann, V. Pervak, A. Apolonski, J. Osterhoff, R. Hörlein, F. Krausz, and S. Karsch, "Short-pulse optical parametric chirped-pulse amplification for the generation of high-power few-cycle pulses," New J. Phys. **9**(12), 438 (2007).

1. Introduction

High-power, few-cycle light pulses are of great interest for studying laser-matter interactions at extreme conditions. A number of applications such as the generation of monoenergetic electron beams or the generation of intense single attosecond pulses from the solid-density plasmas has already emerged from this field [1–5] and call for light sources delivering ever shorter and more powerful pulses. Conventional laser amplification combined with the chirped pulse amplification (CPA) scheme [6], allows for achieving laser pulses with peak-power levels up to the petawatt scale by amplifying a temporally stretched pulse and subsequent compression. However, the pulse duration of the amplified pulses is limited by the laser material to a few tens of femtoseconds. Optical parametric amplification (OPA), which does not suffer from such limitations, has been identified as a promising alternative for generating high power, few-cycle light pulses. Combining the OPA technique with the CPA scheme (OPCPA) enables us to reach ultra high powers [7]. To date, the capability of OPCPA to generate PW-scale pulses on one hand [8,9] and few-cycle pulses on the other [10–12], has been demonstrated. However, it remains a challenge to reach PW-peak powers and few-cycle pulse durations simultaneously.

Since the discovery of OPA a large variety of nonlinear optical crystals have been utilized, newly introduced and engineered in order to optimize the amplification process in terms of the achievable amplification bandwidth. BBO (β-BaB_2O_4), PPLN (periodically poled $LiNbO_3$), LBO (LiB_3O_5) and KTP ($KTiOPO_4$) are most commonly used due to their high nonlinear coefficients, availability and broad gain bandwidths in the visible and NIR spectral range [7,10–19]. A sub-3 cycle, 16 TW light source, which utilizes BBO as an amplification medium, is already in operation [11]. However, these crystals are only available in limited sizes, i.e. present-day technology can provide a maximum aperture of only a few centimeters for BBO and even less for PPLN. In order to generate Joule-scale amplified pulse energies, however, crystal apertures of the order of tens of centimeters are needed to avoid optical damage and unwanted nonlinearities. Alternative crystals such as, KDP (KH_2PO_4), DKDP (KD_2PO_4) [20] and CLBO ($CsLiB_6O_{10}$) [21] become attractive for such systems despite their comparatively lower nonlinearity, since they can be grown in sizes of 40 cm and more in aperture. Since the gain bandwidth of DKDP exceeds that of KDP and CLBO [20,22], this has been the crystal of choice for the final amplification stages in recent high-power projects [8,9,23].

In these petawatt-class systems pulses of 100 ps – ns duration are used to pump the parametric amplifier chain. PW-scale peak powers are reached in pulses with a duration of a few-tens of femtoseconds. However, it is not possible to simply scale this scheme to the few-cycle regime while keeping Joule-scale pulse energies owing to the limited gain bandwidth in thick crystals and optical damage issues. A modified short-pulse pumped OPCPA technique which utilizes high power, few-ps pulses to amplify a broadband signal in thin OPA crystals has been suggested as a viable route towards few-cycle, Joule-scale pulses [24]. The feasibility is also supported by design calculations presented in [25]. Here, the large bandwidth is achieved by using thin OPA crystals, while the high gain and pulse energies are ensured by intense pumping and large crystal size, respectively.

The Petawatt Field Synthesizer (PFS), currently under construction at the Max-Planck-Institut für Quantenoptik (Garching, Germany), will use this short-pulse pumped OPCPA scheme to deliver fully wave-form controlled (i.e. carrier phase stabilized), few-cycle (5 fs) laser pulses with an energy of > 3 J at a repetition rate of 10 Hz. The spectral range of the PFS

#159355 - $15.00 USD Received 2 Dec 2011; revised 14 Jan 2012; accepted 20 Jan 2012; published 9 Feb 2012

pulses will be approximately 700-1300 nm, since especially for the final amplification stages thin DKDP crystals (2-5 mm) will be used in a non-collinear configuration. The special pump source required by the short-pulse pumped OPCPA scheme will deliver 1-2 ps pulses with 15-20 J total pulse energy in the green, i.e. 50 J before frequency doubling, at 10 Hz repetition rate. This pump source is currently under construction [26,27]. According to our design study these high power pump pulses will be used to amplify the μJ-scale broadband signal pulses to the desired ~3 J pulse energy in a chain of 7-8 OPCPA stages. The details of this design and the model of our simulations will be discussed in the following section of this paper.

Although it has been demonstrated that DKDP is suitable for the amplification of narrowband pulses to the PW-level, e.g., 43 fs in 0.56 PW [8], a detailed experimental investigation of its ability to amplify an even broader spectral bandwidth that can support few-cycle pulses, as predicted by theory, is yet to be done. We present here the first experimental findings where we have studied the amplification dynamics of OPA performed in thin DKDP crystals, pumped on the ps timescale. We have measured the broadband small-signal gain as well as the behaviour in saturation and we have compared the results with our OPA simulations. We discuss the implications of these findings in terms of the scalability of short-pulse pumped OPCPA to the PW level.

2. Theoretical modelling

We performed "pseudo 3D" modelling of the process using the Fourier split-step method [28]. The three coupled wave equations, describing the OPA process [14] are solved by a Runge-Kutta solver independently in two dimensions (time and one space coordinate). Dispersion effects as well as the spatial walk-off of both pulses due to the non-collinear geometry are taken into account. The simulation assumes plane and parallel wavefronts of the pump and the signal, which for our relatively small internal non-collinear angle of <1° is justified. The amplified energy is calculated under the assumption of a rotational symmetry in space, hence the term "pseudo 3D". No higher order nonlinear or other parasitic processes are taken into account. To simulate the DKDP crystal, the Sellmeier equations described in [20] are implemented into the code.

Table 1. Parameters used for the Simulations

OPCPA stage	1	2	3	4	5	6	7	8	Σ over stages
pump energy	2 mJ	20 mJ	200 mJ	1 J	3 J	5 J	5 J	5 J	<20 J
crystal length (DKDP)	7.5 mm	7.0 mm	6.3 mm	5.5 mm	4.5 mm	3.5 mm	2.6 mm	2.2 mm	
output signal energy	0.2 mJ	2.2 mJ	22 mJ	123 mJ	452 mJ	1.05 J	1.68 J	2.34 J	2.34 J

For the PFS design studies we have numerically modelled the OPCPA stages with the design pump power of 4 × 5 J at 515 nm. The pump pulse and the OPCPA signal pulse duration (in FWHM) was taken to be 1.2 ps and 1 ps, respectively. Table 1 contains the parameters (pump energy and thickness of the DKDP crystals) for the subsequent OPCPA stages. The pump peak intensity for each stage was fixed to be ~100 GW/cm^2. The non-collinear type-I geometry was used with a phase-matching angle of 37.08° and an internal pump-signal angle of 0.92°. In this design study we used a different non-collinear angle than in the experiments described in this paper due to the fact that the experiments were done with a cut spectrum. These simulations were performed with the experimentally measured signal spectrum without a spectral cut. The signal spectrum and the resulting amplified spectra after each stage for the simulations are depicted in Fig. 1(a), while the extraction efficiency for each stage is presented in Fig. 1(b). It can be seen that in a series of eight amplification

#159355 - $15.00 USD Received 2 Dec 2011; revised 14 Jan 2012; accepted 20 Jan 2012; published 9 Feb 2012

stages, the signal pulses in the spectral range (730-1250 nm, measured at 10% level of maximum intensity) can reach ~2.4 J. The calculated Fourier limited pulse duration supported by the spectrum after the 8th stage is 5.6 fs, corresponding to less than two optical cycles. It is worth noting that these simulations support our simple one dimensional design which has been presented in [25]. The small differences between the simulations are due to dispersion effects, the spatial walk off between pump and signal and the spatial behaviour of the amplification process, which are not considered in the 1D code.

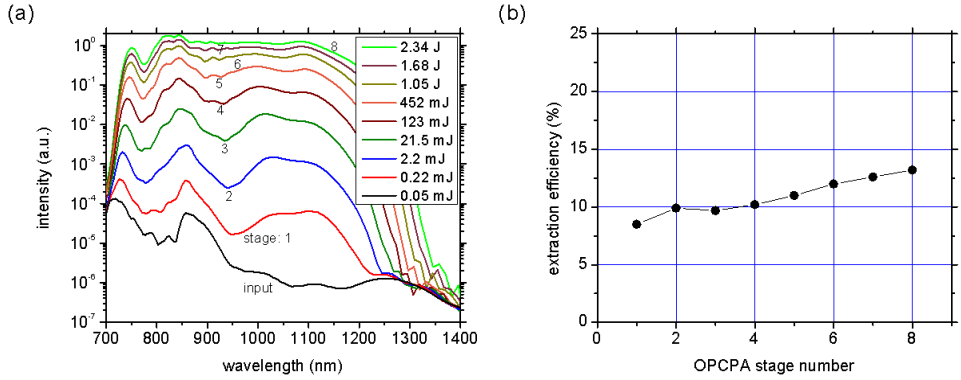

Fig. 1. (a) Calculated amplified spectra for different OPCPA stages of PFS with anticipated pump energy of 20 J. (b) Extraction efficiency $(E^{out}_{signal} - E^{in}_{signal})/E_{pump}$ of these stages.

In order to verify the validity of our "pseudo 3D" simulations we have carried out a comparison between the predictions of our model and the experiment, which are described in the next sections.

3. Methods

3.1 Experimental setup

The parametric amplification experiments were carried out using the available PFS frontend, broadband signal generation stage and first amplifier stages of the ps pump laser chain. The schematic layout of the setup is shown in Fig. 2.

The frontend laser system delivers optically synchronized seed pulses for both the pump laser chain and the OPCPA chain by deriving them from a common "master oscillator" (MO). The broadband OPCPA signal is generated by spectral broadening using a cascaded setup of Ne-filled hollow core fibers (HCF). The resulting spectrum is shown in Fig. 3. The output of the second HCF has 200 μJ of pulse energy, out of which 50 μJ are contained in the spectral range of 700-1400 nm, which is relevant for amplification in DKDP pumped at 515 nm. The frontend architecture and the spectral broadening scheme are described in full detail in [29–32]. The broadband signal pulses are temporally stretched, in order to match their duration to the pump pulses, using a prism-pair stretcher. Thus, the pulses have negative chirp in the OPCPA chain, allowing for high-throughput, simple recompression schemes, such as bulk material in combination with chirped mirrors.

Owing to the target parameters of the pump pulses (ps-scale multi-10-Joule pulses), the pump laser chain itself is a CPA system. The seed pulse for this CPA chain is derived from the master oscillator of the PFS frontend to ensure optical synchronization. Details of the seed generation for the pump laser chain are also given in [29]. The current configuration of the pump laser chain contains two subsequent Yb-doped fiber amplifiers, a grating stretcher, an Yb:glass regenerative amplifier, an Yb:YAG booster amplifier in multipass geometry and a grating compressor. The amplified pulses have a pulse energy of 300 mJ before compression within a bandwidth of ~3.5 nm, which is then temporally compressed to ~1.0 ps at a pulse energy of ~200 mJ. The details of the pump laser configuration used for the present

#159355 - $15.00 USD Received 2 Dec 2011; revised 14 Jan 2012; accepted 20 Jan 2012; published 9 Feb 2012

experiments are described in [26,27]. The compressed output is then frequency doubled in DKDP. For our first OPA experiments we used a fraction of the available pump energy and combined it with our broadband signal pulse in the DKDP OPA crystal in the non-collinear geometry to allow for the broadest bandwidth and to aid the separation of the beams after amplification.

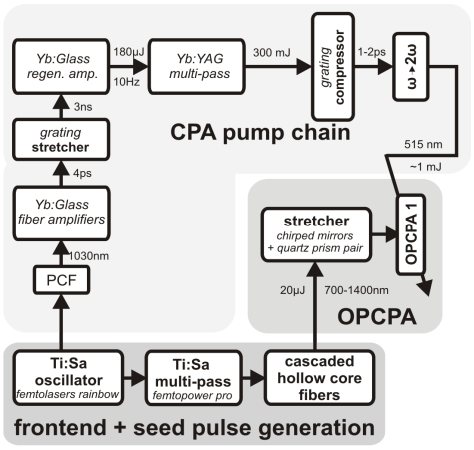

Fig. 2. Experimental setup.

3.2 OPCPA experiments in DKDP

Using the signal and pump pulses described above, we investigated the dynamics of the parametric amplification process in DKDP. For our measurements a small fraction (~800 µJ) of the total available pump laser energy at 515 nm is used with a FWHM duration of ~2 ps, i.e. slightly longer than the best achievable performance, since in this way the effect of the timing jitter can be reduced further. The pump pulse duration was adjusted by clipping the spectrum inside the grating compressor. For the amplification measurements we worked in the focus of both the pump and signal beams and thereby obtained near-Gaussian beam profiles in the OPA crystal of $1/e^2$ beam diameters of 1.3 mm and 1.2 mm, respectively. The signal beam was focused with an f = 5 m silver coated mirror to match the pump beam size. To focus the pump beam a slightly misaligned telescope, consisting of a focusing and defocusing lens, with an effective f-number of ~2000 was used. The pump intensity was limited to ~100 GW/cm^2, which can be regarded as a safe mode of operation, since the AR coating of the DKDP crystal (515 nm and 700-1400 nm) is the limiting factor in terms of damage in the amplifier stage and its damage threshold was measured to be ~300 GW/cm^2 in our experiment. The internal non-collinear angle between the pump and signal was fixed to 0.75°. The broadband signal spectrum after the cascaded HCF is shown in Fig. 3. It has a spike at 720 nm which is of approximately two orders of magnitude higher than the spectral intensity at 1000 nm. This peak will quickly saturate during the OPA process. Moreover it results in saturating the spectrometers and other diagnostics. Therefore in order to measure the small signal gain for the entire wavelength range correctly, we suppressed it by using a 2 mm thick RG1000 bandpass filter. The spectrum after the RG1000 filter is also shown in Fig. 3. The energy of the broadband signal after the RG1000 filter was ~4.5 µJ.

#159355 - $15.00 USD Received 2 Dec 2011; revised 14 Jan 2012; accepted 20 Jan 2012; published 9 Feb 2012

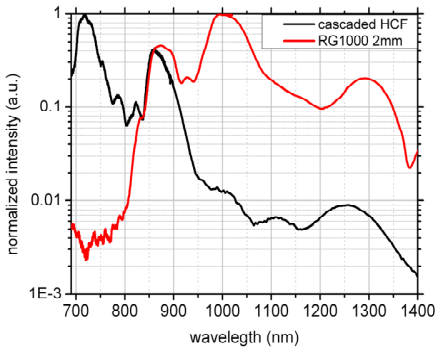

Fig. 3. Broadband OPCPA signal spectra, normalized to the peak values, at the output of cascaded hollow core fibers (black) and after a 2-mm thick bandpass filter (RG1000) shown in red.

Firstly, we investigated the small-signal gain, i.e. the regime where the amplification is far from saturation, at different phase matching angles in a 3 mm thick DKDP crystal (cf. Fig. 4). For this the signal energy was reduced to the nJ-level using a variable neutral density filter in order to avoid saturation of the OPA process. The GD between 700 and 1400 nm of the broadband signal was measured to be 700 fs. The details of the stretcher and characterization of its dispersion are described in [29]. The amplified spectra were measured using a combination of the AvaSpec-3648 and AvaSpec-NIR256-1.7 (Avantes) spectrometers in order to resolve both the visible and the near IR spectral regions.

Secondly, we measured the input signal energy dependence of the OPA gain in order to characterize the amplification behaviour in saturation. We performed this measurement using the pulse before spectral broadening and before stretching as a signal, since in the geometry of our OPA setup the pulse energy of the stretched broadband pulse (~4.5 μJ after the RG1000 filter) would have been too low to achieve saturation. On the other hand the spike of the spectrum without the RG1000 filter would have saturated the OPA process very quickly for parts of the spectrum, which does not represent the real scenario and would have been difficult to model accurately for comparison. The unbroadened signal pulse had a nearly Gaussian-shaped spectrum with a FWHM of 48 nm centered at λ_0 = 780 nm. The pulse duration at the position of the OPA crystal was measured to be 31 fs, using the GRENOUILLE (Swamp optics). The retrieved 2nd order intensity autocorrelation of the pulse by this device is shown in the inset of Fig. 5. For the amplification a 5 mm thick DKDP crystal was used, which was aligned for maximum gain, i.e a phase matching angle of 36.86°. The signal energy was varied using the metallic filter. A high sensitivity power meter (Laser Probe Rm-6600) was used to monitor the signal energy. The amplified signal was slightly focused into a large aperture photodiode for measuring the relative gain (i.e. the ratio of the amplified to the unamplified signal energy). The amplified signal was measured at a position where it was well separated from the pump and idler beams, which were blocked by an iris, in order to minimize their contribution to the measurements.

Finally, in order to determine the extraction efficiency under saturation, for our present experimental conditions, we used a 7 mm DKDP crystal. The signal spectrum after the RG1000 spectrum was stretched in such a way to have a GD of ~1.5 ps for a spectral range of 800-1325 nm, by adjusting the prism separation in the stretcher as shown in Fig. 6. The phase matching angle was adjusted to have amplification in the NIR tail with its maximum at 1100 nm.

#159355 - $15.00 USD Received 2 Dec 2011; revised 14 Jan 2012; accepted 20 Jan 2012; published 9 Feb 2012

4. Results and discussion

In the following we present the results for the experiments described above. The interpretation of these findings is aided by our calculations which we used to model the scenario. In these calculations we have simulated the real scenario by taking the measured pump and signal energies, beam sizes, crystal thicknesses and non-collinear angle. The only adjustable parameter we used is the phase matching angle. Owing to the usual uncertainty in the cut-angle information provided by the crystal manufacturers, this assumption is justified.

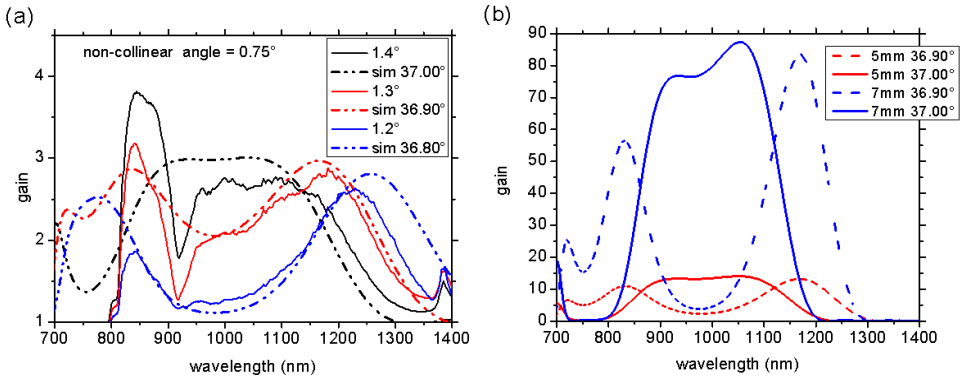

Fig. 4. Investigation of the small-signal gain: (a) Measured gain (solid lines) versus calculated gain (dotted lines) for a 3 mm thick DKDP crystal for three different phase matching angles. The crystal was cut for a phase matching angle of ~37.1°, according to the manufacturer. The angles for the experimental curves are given as the deviation from the nominal cut angle. For the calculation an offset in the phase matching angle has been chosen to achieve the best possible fit with experiment. (b) Calculated gain for 5 mm and 7 mm DKDP crystals for two different phase matching angles.

4.1 Small-signal gain

The measured small-signal gain curves for different phase-matching angles are shown in Fig. 4(a). The gain curves are averaged over 100 shots to eliminate the effect of shot-to-shot instabilities. As can be seen from the measured curves, very broadband amplification was achieved with a significant gain over a bandwidth of ~500 nm for a phase matching angle of 37.00°. Moreover, the gain curve is very sensitive to the phase matching angle and changes its shape significantly when the phase matching angle is slightly detuned. Therefore, when working in the near field, the collimation of the beams should be better than 1 mrad. From our measurements we can see that when the phase matching angle is reduced, the amplification extends more and more into the near infrared region and has even reached 1400 nm in our experimental setup. Since the spectrum of the signal pulse has been artificially suppressed below 800 nm using a bandpass filter, no reliable gain information for this region can be extracted from our experiment. Nevertheless, our calculations predict that the gain curve extends down to 700 nm under these conditions, as shown in Fig. 4(a). In addition, a narrow dip can be observed in the measured gain curves around 920 nm. This is a combination of a very weak seed intensity in this spectral range and the way of spectral detection, since this region is situated at the edge of the sensitivity range of the visible spectrometer which therefore introduces high noise levels and delivers inaccurate measurements.

Alongside the measured small-signal gain curves, Fig. 4(a) also shows the results of our simulations of the experimental scenario, represented by the dotted lines. The calculations agree well with the measured gain curves both in absolute values and shape and the dependence on the phase matching angle is also closely reproduced. The dip in the middle of the gain curves for the phase matching angles of 36.80° and 36.90° respectively, which is due to the characteristic phase matching curve of the DKDP, is also well reproduced.

#159355 - $15.00 USD Received 2 Dec 2011; revised 14 Jan 2012; accepted 20 Jan 2012; published 9 Feb 2012

Based on the good agreement between our experimental observations and the simulations, we have performed further calculations in order to explore the parameter space for the OPA process. Since in experiments that we will discuss later, we used DKDP crystals of 5 and 7 mm thickness, we present in Fig. 4(b) the small-signal gain curves for these crystal thicknesses calculated at different phase matching angles. As expected, the gain bandwidth increases with a decrease in the crystal-thickness for optimum phase-matching conditions. It can be seen that the gain bandwidth changes from ~350 nm to ~400 nm (measured at 10% level of maximum gain) by changing crystal thicknesses from 7 mm to 5 mm for a phase matching angle of 37.00°. We can also see that although the gain bandwidth can be increased by detuning the phase matching angle, the absolute value of the gain drops.

4.2 Saturated gain measurement

As described above, we have used the 31 fs unbroadened signal pulse to investigate the amplification behaviour in saturation. We measured the output pulse energy E_{out} as a function of the input energy E_{in} and determined from this the extracted energy ($E_{out} - E_{in}$). The results are presented in Fig. 5, where it can be seen that in our setup for $E_{in} > 4$ µJ the OPA gain starts to be saturated. The measured temporal profile of the signal pulse is shown in the inset of Fig. 5, clearly indicating the presence of a pre/post-pulse with an intensity of approximately 10% of the main pulse. This pedestal can affect the saturation behaviour. In order to allow for a meaningful comparison between the experiment and our simulations the input pulse has to be modelled as close as possible to the experimental scenario. Since our simulation program is not able to simulate arbitrary pulse shapes in time, we performed two simulations with Gaussian pulse shape. In the first run we assumed a single 31 fs signal pulse containing all the signal energy. The calculated extracted energy for this case is marked in Fig. 5 as red circles. Owing to the fact, that this short 31 fs pulse interacts with a smaller part of the pump energy and includes a higher signal energy, we obtain a smaller extracted energy level in the simulations than we would expect from the real pulse. In our second calculation we considered two Gaussian pulses, which are amplified independently (two different simulation runs), the first one with an amplitude of 10% of the second, and the two pulses separated in time by 50 fs. We assumed, that the two signal pulses, in the simulations, see a "fresh" pump and do not affect each other. This assumption leads to an overestimation of the extracted energy. As can be seen in Fig. 5 the calculated extracted energies from this second model pulse (blue triangles) lie above the measured values. Both model calculations are consistent with the measured data. We can therefore conclude that our simulation program is able to reliably model the saturation behavior of the optical parametric amplification process.

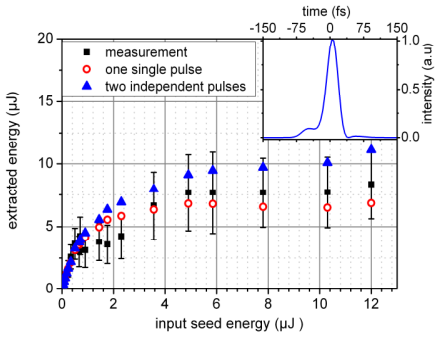

Fig. 5. Extraction energy vs. input signal energy: The black squares represent the measurements using the 31 fs input pulse (the temporal profile of which is shown in the inset). The error bars of the measured data are the standard deviation of 100 shots, which originate both from the temporal jitter and the shot-to-shot pump energy fluctuation. The red circles show the results for the calculation of one single Gaussian pulse, the blue triangles represent the results of the simulation with two independent Gaussian pulses, see details in text.

#159355 - $15.00 USD Received 2 Dec 2011; revised 14 Jan 2012; accepted 20 Jan 2012; published 9 Feb 2012

4.3 Broadband amplification

After having found good agreement in the saturation behaviour between experiment and our theoretical description in the case of the narrowband signal, we investigated the extraction efficiency in saturation using the entire broadband signal pulse. For this study we used a 7 mm DKDP crystal, which corresponds to the calculated crystal length (7.5 mm) of the first stage of the PFS system in Section 2 of this paper. The signal spectrum after the RG1000 filter was matched to the pump pulse duration in order to optimize the extraction efficiency (Fig. 6). The phase matching angle (~36.95° from simulations) was adjusted for amplification in the NIR tail with its maximum at 1100 nm. Figure 7(a) shows the input and the amplified spectrum.

The amplification in DKDP covers the full spectrum from 830 to 1310nm (measured at 10% level of maximum intensity). Below 800 nm no gain can be observed due to the used RG1000 filter. Even without the spectral part from 700 to 800 nm the amplified spectrum supports a Fourier limited pulse duration of ~6 fs which corresponds to a two-cycle pulse. To our knowledge this is the first time that such a broadband amplification in DKDP has been demonstrated. This result confirms that DKDP is appropriate for broadband amplification in ps-pumped OPCPA and supports few-cycle pulse durations.

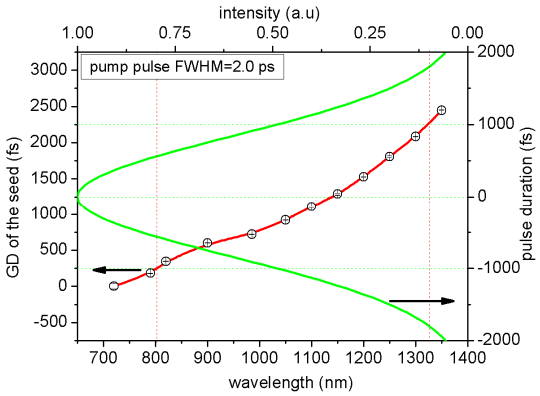

Fig. 6. Measured group delay (GD) of OPCPA signal: The NIR-tail of the signal (800-1325 nm) is stretched to fit in the FWHM duration of the pump pulse.

The broadband gain is shown in Fig. 7(b). The signal energy in the spectral range between 1100–1320 nm is much smaller compared to the energy stored in the rest of the spectrum. Therefore the amplification process is already saturated in the region around 800-1100 nm, while the spectral range between 1100 and 1320 nm experiences a gain of ~30 and is not saturated so far which is similar to the situation in [33]. By injection of 4.4 μJ signal energy, 53 μJ of amplified signal is obtained. This corresponds to an overall gain of 9.6 and an extraction efficiency of 6% from pump to signal.

#159355 - $15.00 USD Received 2 Dec 2011; revised 14 Jan 2012; accepted 20 Jan 2012; published 9 Feb 2012

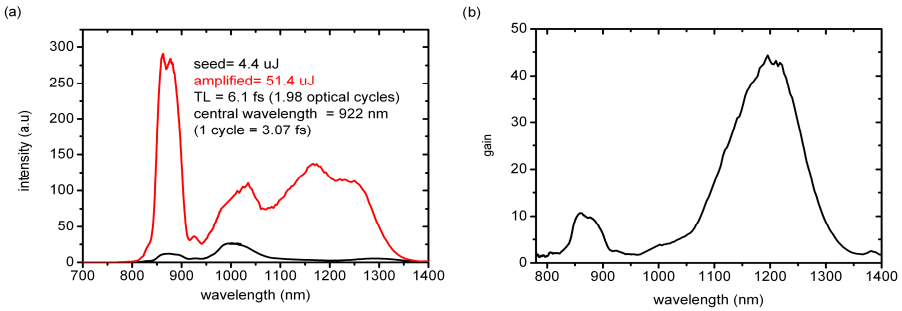

Fig. 7. (a) The amplified and unamplified spectra, using 7 mm DKDP under saturation condition. (b) Spectral gain of the amplification process extracted from (a).

5. Conclusion

We have demonstrated that the short-pulse pumped parametric amplification is feasible to deliver a sufficiently broad spectrum (cf. Fig. 7) to support a few-cycle pulse duration, with reasonable gain to reach high pulse energies up to the J level. It was shown, that DKDP crystals, which can be scaled to large apertures, pumped at 515 nm and with intensities of ~100 GW/cm^2, are able to amplify bandwidth, supporting pulse durations of the order of ~6 fs. Furthermore these experiments demonstrate that the amplification bandwidth, gain and saturation agree well with that obtained from our simulations. This also justifies the validity of the Sellmeier equations [20] used in the code. Moreover this provides strong support to our design of the following OPCPA stages. However, in order to fully verify the feasibility of the PFS approach to high energy few-cycle-pulse generation it is necessary to compress the broadband amplified pulses to few-cycle duration. Measuring the phase of such broadband pulses is connected with difficulties especially for the retrieval of the higher orders in phase. In addition, the expected inherently high contrast still has to be verified experimentally using the first compressed pulses. These immediate further steps in the development of the PFS system are currently under way.

Acknowledgments

This work is funded through the PFS grant of the Max-Planck Society.

#159355 - $15.00 USD Received 2 Dec 2011; revised 14 Jan 2012; accepted 20 Jan 2012; published 9 Feb 2012

G.2 Simulations of petawatt-class few-cycle optical-parametric chirped-pulse amplification, including nonlinear refractive index effects

Simulations of petawatt-class few-cycle optical-parametric chirped-pulse amplification, including nonlinear refractive index effects

Alexandre Thai,[1,*] Christoph Skrobol,[2,3] Philip K. Bates,[1] Gunnar Arisholm,[4] Zsuzsanna Major,[2,3] Ferenc Krausz,[2,3] Stefan Karsch,[2,3] and Jens Biegert[1,5]

[1]*ICFO–Institut de Ciències Fotòniques, Mediterranean Technology Park, 08860 Castelldefels, Barcelona, Spain*

[2]*Max-Planck-Institut für Quantenoptik, D-85748 Garching, Germany*

[3]*Ludwig-Maximilians-Universität München, Am Coulombwall 1, D-85748 Garching, Germany*

[4]*Forsvarets Forskningsinstitutt (Norwegian Defence Research Establishment), P.O. Box 25, N-2027 Kjeller, Norway*

[5]*ICREA–Institució Catalana de Recerca i Estudis Avançats, 08010 Barcelona, Spain*

**Corresponding author: alexandre.thai@icfo.es*

Received July 21, 2010; revised September 13, 2010; accepted September 20, 2010; posted September 27, 2010 (Doc. ID 131829); published October 13, 2010

We present three-dimensional simulations of optical-parametric chirped-pulse amplification stages for a few-cycle petawatt-class laser. The simulations take into account the effects of depletion, diffraction, walk-off, quantum noise, and the nonlinear refractive index (n_2). In the absence of n_2 effects, we show these stages can generate 3.67 J pulses supporting 4 fs transform-limited pulse durations. Adding the nonlinear refractive index to the simulation, the energy output is reduced by ~11% and the bandwidth narrows by ~129 nm, increasing the Fourier limit by ~17.5%.

OCIS codes: 190.4410, 190.4970, 190.7110.

The interest in studying and controlling laser–matter interactions at extreme conditions has been driving the development of new sources of high-power, few-cycle light pulses. Such pulses require a large spectral bandwidth and cannot be achieved using conventional laser amplification, where the level structure of the active medium determines and limits the amplified bandwidth. One promising alternative is optical-parametric chirped-pulse amplification (OPCPA), which has become accepted as the key technology for the amplification of such ultrashort laser pulses. OPCPA uniquely offers the capability for both joule-level energy output and ultrabroad spectral gain, making feasible the generation of petawatt few-cycle pulses. The petawatt capabilities of OPCPA have already been demonstrated for 40–90 fs pulse durations, with systems producing 0.4 PW in 2006 [1] and 0.56 PW in 2007 [2]. Other systems have confirmed the few-cycle ability of OPCPA, directly amplifying huge bandwidths to generate pulses as short as 5.5 [3] and 11.8 fs [4]. Further implementations have used OPCPA to operate over a wide range of wavelengths, with pulses of 7.9 fs at 805 nm [5], 15.7 fs at 2.1 μm [6], and 96 fs at 3.2 μm [7].

In this Letter we simulate four noncollinear OPCPA stages for a petawatt-class system. The parameters we use for these simulations are motivated by the Petawatt Field Synthesizer (PFS) currently under construction at the Max-Planck-Institut für Quantenoptik (Garching, Germany) [8], which aims at delivering pulses with 5 fs and 3 J energy. The design of the system is based on a modified OPCPA scheme where short pump pulses (515 nm) with pulse durations of the order of 1–2 ps are used for pumping the OPCPA chain. Because of high pump intensities, thin DKDP crystals can be used, guaranteeing a large amplification bandwidth and a high gain. The short pump-pulse duration supports only a picosecond-scale time window for the parametric fluorescence, and therefore high-contrast pulses can be expected.

Designing such a system requires a comprehensive understanding of the OPCPA process itself. Many of the current modeling codes operate in one or two spatial dimensions only and thus can miss crucial features of the interactions that limit efficiency and bandwidth. OPCPA is a fundamentally nonlinear process, so accurate modeling must also take into account effects due to a wide range of possible nonlinear optical processes. In this Letter we use a full three-dimensional OPCPA code to calculate the gain and nonlinear interactions for the final stage amplifiers, paying particular attention to the effects of the nonlinear refractive index.

All simulations presented in this Letter have been performed with the nonlinear propagation code Sisyfos, developed at Forsvarets ForskningsInstitutt [9]. This code has already shown its capability to model OPCPA laser systems [10,11]. It includes the effects of depletion, diffraction, walk-off, and dispersion, and it can include multiple second-order nonlinear interactions (e.g., a desired process plus parasitics) in an arbitrary birefringent crystal. Quantum noise is included through the addition of 1/2 photon per signal and idler mode, corresponding to the vacuum energy. Nonlinear refractive index effects are also included. Although some of these effects turn out to be small, we include them because an important part of the design work is to determine which effects are not important. The nonlinear propagation equations are solved in Fourier space using a fourth-order Runge–Kutta algorithm with an adaptive step. The input beams can be defined arbitrarily in tables, and they are not restricted to be separable in space and time.

Current petawatt systems or design proposals generally use DKDP (KD_2PO_4) crystals for their final amplifiers. Although DKDP has lower nonlinearities than BBO (β-BaB_2O_4) and LBO (LiB_3O_5) as used in, e.g., [3,5,12,13], those crystals are unavailable at the large apertures needed for high-energy pulses. Of the crystals

available at large apertures, DKDP offers as large a gain bandwidth as KDP (KH_2PO_4) and CLBO ($CsLiB_6O_{10}$) [14] with a slightly larger transmission spectrum [15].

The PFS final amplifier uses four DKDP crystals in Type I (*ooe*) noncollinear geometry to ensure broad bandwidth. Using the Sellmeier equations for 96% deuterated DKDP defined in [16], and an (internal) noncollinear angle between pump and signal waves of 0.92°, we calculate a phase-matching angle of $\theta = 37.28°$ and $d_{\text{eff}} = 0.224$ pm/V.

We use a 4 J, 515 nm pump pulse with 60 mm FWHM super-Gaussian circular spatial profile and a fluence of 0.14 J/cm^2 for the first stage, while the subsequent stages are pumped by 5 J, 72 mm beam diameter pulses at 120 GW/cm^2. The temporal profile is a 1.2 ps super-Gaussian. The input signal is given by a Gaussian spatial, temporal, and spectral profile pulse at 910 nm with a FWHM bandwidth of 315 nm, sufficient to support a sub-5 fs pulse. The energy is 230 mJ, the duration is 1 ps, and the spatial size is 50 mm FWHM to optimize energy extraction. We assume the idler is blocked and the seed is transmitted without loss between each OPCPA stage.

We calculate the nonlinear interaction in the four crystals initially without nonlinear refractive index effects. The crystal length is optimized to reach the highest pump depletion, where the spatially integrated energy extraction from the pump to the signal is maximal. Figure 1 shows the results for each stage. The conversion efficiency over the four stages, corresponding to the percent of pump energy converted into signal and idler pulses, is 34.2%. The various spectra are shown in Fig. 2. We can see that the spectrum is reshaped during amplification, and energy increases to 3.67 J with bandwidth support for a 4 fs Fourier transform limit. There is no strong evidence of amplified quantum noise, such as high frequency modulations in the spectral domain, and the contributions of diffraction, walk-off, dispersion, and parasitic SHG are minimal. This result confirms that a DKDP-based amplifier chain can generate multijoule pulse energies while still supporting a few-cycle transform limit, thus indicating that OPCPA should be able to extend the generation of petawatt pulse powers to the few-cycle regime.

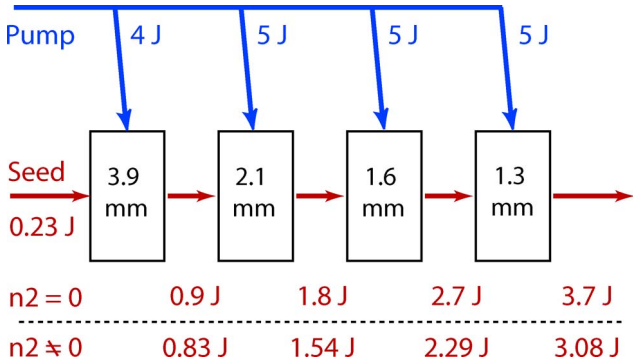

Fig. 1. (Color online) Four last stages of the PFS OPCPA stages, with and without n_2. We use four DKDP crystals with $\theta = 37.28°$, $\alpha = 0.92°$. The idler is filtered out between each stage (not shown). The energy output from each stage with $n_2 = 0$ and nonzero n_2 are shown (see text for values). The final output is 3.7 J with $n_2 = 0$ and 3.29 J when realistic n_2 values are included.

To determine the effect of the nonlinear refractive index (n_2), we reran the same simulation with nonzero n_2. The nonlinear phase shift caused by n_2 gives rise to several phenomena: any transverse variation of the intensity leads to a perturbation of the phase front, while any temporal intensity variation leads to a phase modulation. Both these phenomena can have contributions from the intensity of the beam itself and from other beams, known as self-focusing and self-phase modulation, and cross-focusing and cross-phase modulation, respectively. A further effect, which depends on the intensities themselves rather than on spatial or temporal derivatives, is a nonlinear change of the phase mismatch, which modifies the gain spectrum of the OPA process. A major problem is the lack of accurate n_2 values for DKDP. In the literature, *Z*-scan measurements of the nonlinear refractive index value for DKDP are available at two wavelengths only: n_2 [355 nm] $= 6 - 8 \times 10^{-16}$ cm^2/W [17] and n_2 [1064 nm] $= 3 \times 10^{-16}$ cm^2/W [17,18]. As there is no measured value for n_2 at our 515 nm pump wavelength, we have selected a value of 5×10^{-16} cm^2/*W*, intermediate between the published results at 355 and 1064 nm.

Figure 1 shows the results of the previous simulations rerun with nonzero n_2. By including n_2 effects, the output

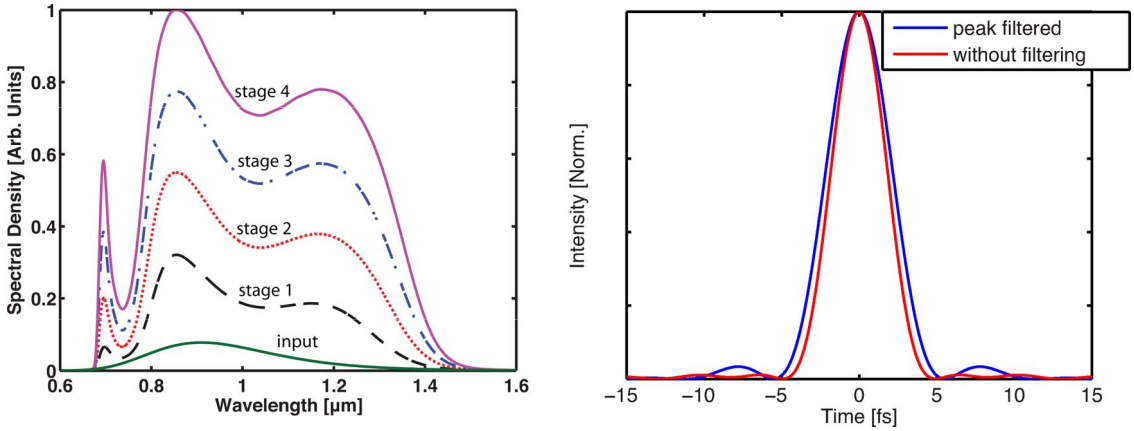

Fig. 2. (Color online) Spectra for the different stages, $n_2 = 0$. Left, input at 910 nm has 315 nm bandwidth, which increases to 540 nm during amplification. The 700 nm peak arises from the phase-matching conditions. Right, in the time domain, the Fourier transform limit duration is 4 fs, with some sidelobes. Filtering out the spectral peak at 700 nm reduces the sidelobes by 10% but increases the pulse duration by ~1 fs.

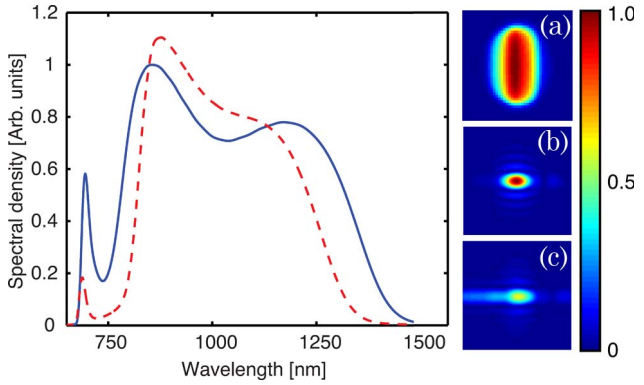

Fig. 3. (Color online) Comparison of the output for the case without n_2 (solid curve) and with n_2 (dashed curve). Left, we observe a narrowing of the spectral bandwidth of 129 nm. With n_2, the bandwidth of the output spectrum (normalized to the $n_2 = 0$ spectrum) represents a Fourier transform limit of 4.7 fs, corresponding to a 17.5% increase in the pulse duration. Right, (a) near field of the output, (b) far field with $n_2 = 0$, and (c) far field with n_2 effects, showing a 30% decrease in peak intensity.

energy is reduced to 3.29 J, corresponding to a conversion efficiency of 30.4% and a reduction in output energy of 11.2%. Additionally, the spectral width narrows (Fig. 3) by ~130 nm, corresponding to a 4.7 fs Fourier transform limit. The near-field spatial profiles show little change due to n_2 effects, with the dominant feature being a narrowing in the plane of the noncollinear interaction due to the phase-front tilt between the pump signal and idler. However, the far-field images are significantly different, and the spatial phase induced by the n_2 effects acts to reduce the peak of the far field by 30% when n_2 effects are included [Figs. 3(a)–3(c)]. A detailed spatio–spectral is quite involved, especially if we wish to separate the different n_2 effects. This is beyond the scope of this Letter and will be addressed in a future work.

In conclusion, we have shown that, in the absence of n_2 effects, a correctly parameterized DKDP crystal is suitable for use in the final amplification stages for a few-cycle petawatt laser system, with output energies of 3.67 J and a transform-limited pulse duration of 4 fs. We demonstrated that the OPCPA interaction is sensitive to the nonlinear refractive index, with a value of $n_2 = 3 \times 10^{-16}$ cm^2/W for the signal and $n_2 = 5 \times 10^{-16}$ cm^2/W for the pump, reducing the output to 3.29 J, a reduction of 11.2% compared to the $n_2 = 0$ case. While the exact percentage depends on the n_2 value chosen, the result clearly shows n_2 effects should be considered when designing OPCPA systems and that further work is needed to accurately determine the n_2 values for pump wavelengths used in OPCPA. Future work will address the mechanisms behind this reduction, including strategies for compensating the observed energy loss. The effect of imperfect input beams will also be studied.

We acknowledge partial support from the Spanish Ministry for Science and Innovation through its Consolider Program Science (SAUUL—CSD 2007-00013), "Plan Nacional" (FIS2008-06368-C02-01), as well as AGAUR 2009-SGR-341 and LASERLAB-EUROPE, grant 228334.

References

1. O. Chekhlov, J. L. Collier, I. N. Ross, P. K. Bates, M. Notley, C. Hernandez-Gomez, W. Shaikh, C. N. Danson, D. Neely, P. Matousek, and S. Hancock, Opt. Lett. **31**, 3665 (2006).
2. V. V. Lozhkarev, G. I. Freidman, V. N. Ginzburg, E. V. Katin, E. A. Khazanov, A. V. Kirsanov, G. A. Luchinin, A. N. Malshakov, M. A. Martyanov, O. V. Palashov, A. K. Poteomkin, A. M. Sergeev, A. A. Shaykin, and I. V. Yakovlev, Laser Phys. Lett. **4**, 421 (2007).
3. S. Adachi, N. Ishii, T. Kanai, A. Kosuge, J. Itatani, Y. Kobayashi, D. Yoshitomi, K. Torizuka, and S. Watanabe, Opt. Express **16**, 14341 (2008).
4. R. Th. Zinkstok, S. Witte, W. Hogervorst, and K. S. E. Eikema, Opt. Lett. **30**, 78 (2005).
5. D. Herrmann, L. Veisz, R. Tautz, F. Tavella, K. Schmid, V. Pervak, and F. Krausz, Opt. Lett. **34**, 2459 (2009).
6. X. Gu, G. Marcus, Y. Deng, T. Metzger, C. Teisset, N. Ishii, T. Fuji, A. Baltuska, R. Butkus, V. Pervak, H. Ishizuki, T. Taira, T. Kobayashi, R. Kienberger, and F. Krausz, Opt. Express **17**, 62 (2009).
7. O. Chalus, P. K. Bates, M. Smolarski, and J. Biegert, Opt. Express **17**, 3587 (2009).
8. Z. Major, S. A. Trushin, I. Ahmad, M. Siebold, C. Wandt, S. Klingebiel, T.-J. Wang, J. A. Fülöp, A. Henig, S. Kruber, R. Weingartner, A. Popp, J. Osterhoff, R. Hörlein, J. Hein, V. Pervak, A. Apolonski, F. Krausz, and S. Karsch, Laser Rev. **37**, 431 (2009).
9. G. Arisholm, J. Opt. Soc. Am. B **14**, 2543 (1997).
10. C. P. Hauri, P. Schlup, G. Arisholm, J. Biegert, and U. Keller, Opt. Lett. **29**, 1369 (2004).
11. P. Schlup, J. Biegert, C. P. Hauri, G. Arisholm, and U. Keller, Appl. Phys. B **79**, 285 (2004).
12. S. Witte, R. T. Zinkstok, A. L. Wolf, W. Hogervorst, W. Ubachs, and K. S. E. Eikema, Opt. Express **14**, 8168 (2006).
13. N. Ishii, L. Turi, V. S. Yakovlev, T. Fuji, F. Krausz, A. Baltuska, R. Butkus, G. Veitas, V. Smilgevicius, R. Danielius, and A. Piskarskas, Opt. Lett. **30**, 567 (2005).
14. Y. Mori, I. Kurado, S. Nakajima, T. Sasaki, and S. Nakai, Appl. Phys. Lett. **67**, 1818 (1995).
15. W. L. Liu, H. R. Xia, X. Q. Wang, Z. C. Ling, D. G. Ran, J. Xu, Y. L. Wei, Y. K. Liu, S. Q. Sun, and H. Han, J. Cryst. Growth **293**, 387 (2006).
16. V. V. Lozhkarev, G. I. Freidman, V. N. Ginzburg, E. A. Khazanov, O. V. Palashov, A. M. Sergeev, and I. V. Yakovlev, Laser Phys. **15**, 1319 (2005).
17. N. A. Kurnit, T. Shimada, M. S. Sorem, A. J. Taylor, G. Rodriguez, T. S. Clement, H. Fearn, D. F. James, and P. W. Milonni, Proc. SPIE **3047**, 387 (1997).
18. I. A. Kulagin, R. A. Ganeev, R. I. Tugushev, A. I. Ryasnyansky, and T. Usmanov, J. Opt. Soc. Am. B **23**, 75 (2006).

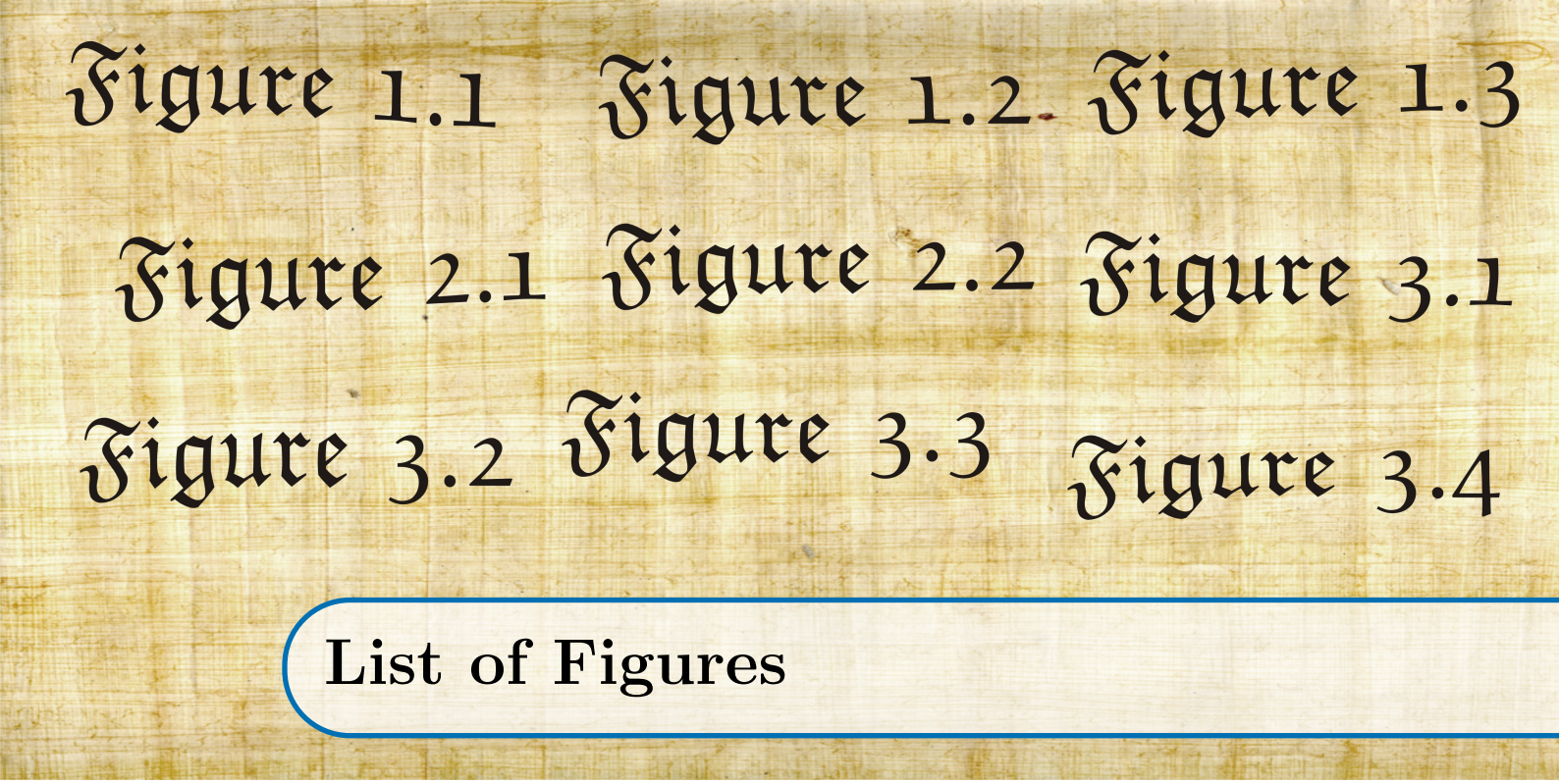

List of Figures

1.1 Scheme showing the proposed experimental configuration for the generation of attosecond pulses using harmonics from overdense plasmas [16]. 2
1.2 Schematic layout of the PFS system [37, 38]. 5

2.1 Schematic picture of the OPA process. 12
2.2 Simulation of the relative pump, signal and idler energy over the crystal length for different ΔkL values. 17
2.3 Simulated small-signal gain and phase mismatch for a 3 mm and 5 mm thick DKDP crystal is shown as a function of signal wavelength. 18
2.4 Schematic sketch of the two geometries used for angle phase matching. . 20
2.5 Phase mismatch for type-I and type-II interaction. 21
2.6 Phase mismatch for different phase-matching and non-collinear angles. . 22
2.7 Picture representing the meaning of the OPA phase. 24

3.1 Schematic scheme of the modeling principle of the SOPAS code. 26
3.2 Comparison between the SOPAS and the Sisyfos code. 29
3.3 Comparison between SOPAS, Sisyfos and measurements. 31

4.1 Walk-off compensation and tangential phase matching geometry. 34
4.2 Spectrum and GD used for the simulations. 36
4.3 Simulation comparing the performance of a BBO and an LBO crystal. . . 38
4.4 Simulations showing the effect of the spectral phase of the signal beam on the spectrum and the energy. 39
4.5 Schematic illustration of the temporal jitter. 40
4.6 Simulations presenting the effect of temporal jitter on the amplified spectrum for different levels of amplification. 41

4.7 Results of a simulation performed with Sisyfos investigating the amount of OPA phase due to amplification for different signal input energies, i.e. levels of back conversion. . . . 43
4.8 Results of a Sisyfos simulation investigating the effect of n_2 on the amplification. . . . 48

5.1 Results of the purely DKDP-based OPCPA design study. . . . 51
5.2 Results of the OPCPA system design study. . . . 53
5.3 Dispersion schemes for the broadband signal of the PFS system. . . . 55

6.1 Projected layout of the PFS system. . . . 60
6.2 Schematic sketch of the frontend system [37]. . . . 61
6.3 Spectrum of the broadband signal pulse after the prism stretcher generated in two cascaded HCF's. . . . 62
6.4 Broadband signal-pulse cleaning by XPW. . . . 63
6.5 Schematic sketch of the pump laser chain [38]. . . . 66
6.6 Measured pump spectra 68
6.7 Photograph of a non-collinear OPA in operation. . . . 69
6.8 Principle of the modified cross correlation technique [102] implemented to characterize the level of temporal synchronization between signal and pump pulse [37]. . . . 70
6.9 Results of the temporal-jitter measurement with the described modified cross-correlation technique [37, 38]. . . . 71
6.10 Temporal-jitter measurement with working active stabilization system [37, 38]. . . . 71

7.1 Broadband seed spectra used for the measurements with DKDP. . . . 75
7.2 Investigation of the small-signal gain [7]. . . . 76
7.3 Measured GD of OPCPA signal [7]. . . . 77
7.4 Results of the saturation measurement in DKDP [7]. . . . 78
7.5 Measured pump-beam profiles at the position of the OPCPA crystals. . . . 79
7.6 Temporal characterization of the seed with the X-FROG. . . . 80
7.7 Measured signal spectra for the unamplifed case, after the first OPCPA stage and the final spectrum after amplification in two LBO stages. . . . 82
7.8 Measured signal-beam profiles without amplification and after amplification. . . . 82
7.9 Comparison between simulations and measurements. . . . 83
7.10 Compression of unamplified signal. . . . 85
7.11 Pulse duration characterization with the single-shot SHG-FROG. . . . 86

7.12 Temporal contrast measurements performed with the Sequoia third-order autocorrelator. . . . 87
7.13 Beam profiles of the pump laser at the position of the SHG crystal. . . . 89
7.14 FROG measurements of the pump laser. . . . 90
7.15 Broadband seed used for the experiments with LBO. . . . 91
7.16 Simulation of the amplified bandwidth for different crystal thicknesses. . . . 92
7.17 Dispersion scheme for the OPCPA measurements in vacuum. . . . 93
7.18 Theoretical GDs of the chirped mirrors used for pulse compression for one reflection. . . . 94
7.19 X-FROG measurements with and without **TOD** mirrors. . . . 95
7.20 Amplification of the broadband seed with installed **TOD** mirrors and without these mirrors. . . . 95
7.21 Results of the amplification in two LBO stages. . . . 96
7.22 Beam profiles of the signal after amplification in two stages. . . . 97
7.23 Comparison between the measurements and a Sisyfos simulation. . . . 98
7.24 X-FROG measurements of the unamplified signal pulse. . . . 100
7.25 Single-shot SHG-FROG measurements of the amplified signal pulse. . . . 101
7.26 Optimized single-shot SHG-FROG measurements of the amplified signal pulse. . . . 102

8.1 Amplification of the output seed of the idler generation setup in two LBO stages. . . . 110
8.2 Schematic layout of the vacuum compressor for the pump laser [38]. . . . 111

A.1 Superposition of monochromatic light waves in time. . . . 116
A.2 Influence of the different dispersion coefficients on the temporal pulse shape and the temporal electric field of a 5 fs Gaussian light pulse with a central wavelength of $\lambda_0 = 920\,\mathrm{nm}$. . . . 118

B.1 Investigation of the small-signal gain. . . . 120
B.2 Extracted energy vs. input signal energy. . . . 121

C.1 Spectrum and GD used for the simulations as input parameters. . . . 124
C.2 The effect of signal input energy on the amplification process. . . . 125
C.3 Simulations presenting the influence of the pump energy on the amplification. . . . 126
C.4 Simulations presenting the influence of the signal-beam and pump-beam size on the nonlinear amplification. . . . 128
C.5 Simulation with smooth and modulated input spectra. . . . 129
C.6 The effect of the signal-pulse duration on the amplification. . . . 130
C.7 Schematic sketch of tilted pulse fronts. . . . 131

C.8 Input parameters for the simulation investigating the difference between parallel pulse fronts of pump and signal and pulse fronts constituting an angle. . . . 133
C.9 Results of the simulation with parallel and non-parallel pulse fronts. . . . 134
C.10 Results of a simulation performed with SOPAS investigating the dependence of the level of superfluorescence on the pump intensity and the crystal length. . . . 136
C.11 Influence of the superfluorescence on the temporal contrast. . . . 137
C.12 Energy ratio between the signal and the superfluorescence for different seed input energies. . . . 138
C.13 Calculation of the heat distribution inside a DKDP crystal. . . . 140
C.14 Measurement of the transmission of DKDP. . . . 140
C.15 Change of the phase mismatch for different crystal temperatures. . . . 141
C.16 Phase-matching curve for two different temperatures. . . . 142

D.1 Schematic layout of the setup used for the measurements with DKDP. . . . 146
D.2 Schematic layout of the two-stage-OPCPA chain equipped with LBO. . . . 146
D.3 Schematic layout of the two-stage OPCPA setup located in vacuum. . . . 149
D.4 3D layout of the OPCPA vacuum system. . . . 150

E.1 Comparison between the Avantes spectrometers and a demonstration spectrometer from OceanOptics. Transmission of neutral density filters. . . . 155
E.2 Schematic sketch of the X-FROG setup. . . . 157
E.3 Functionality test of the X-FROG. . . . 158
E.4 Schematic layout of the single-shot SHG-FROG. . . . 159
E.5 Calculated conversion efficiencies for a 5 μm thick BBO crystal. . . . 160
E.6 Spectral calibration of the single-shot SHG-FROG. . . . 161
E.7 Functionality test of the homebuilt single-shot SHG-FROG. . . . 162
E.8 Setup of the homebuilt third order autocorrelator used for temporal contrast characterization. . . . 163

F.1 Schematic sketch of the phase-matching angle for SHG. . . . 165
F.2 Perfect phase-matching angle for SHG of the broadband signal in LBO. . . . 166

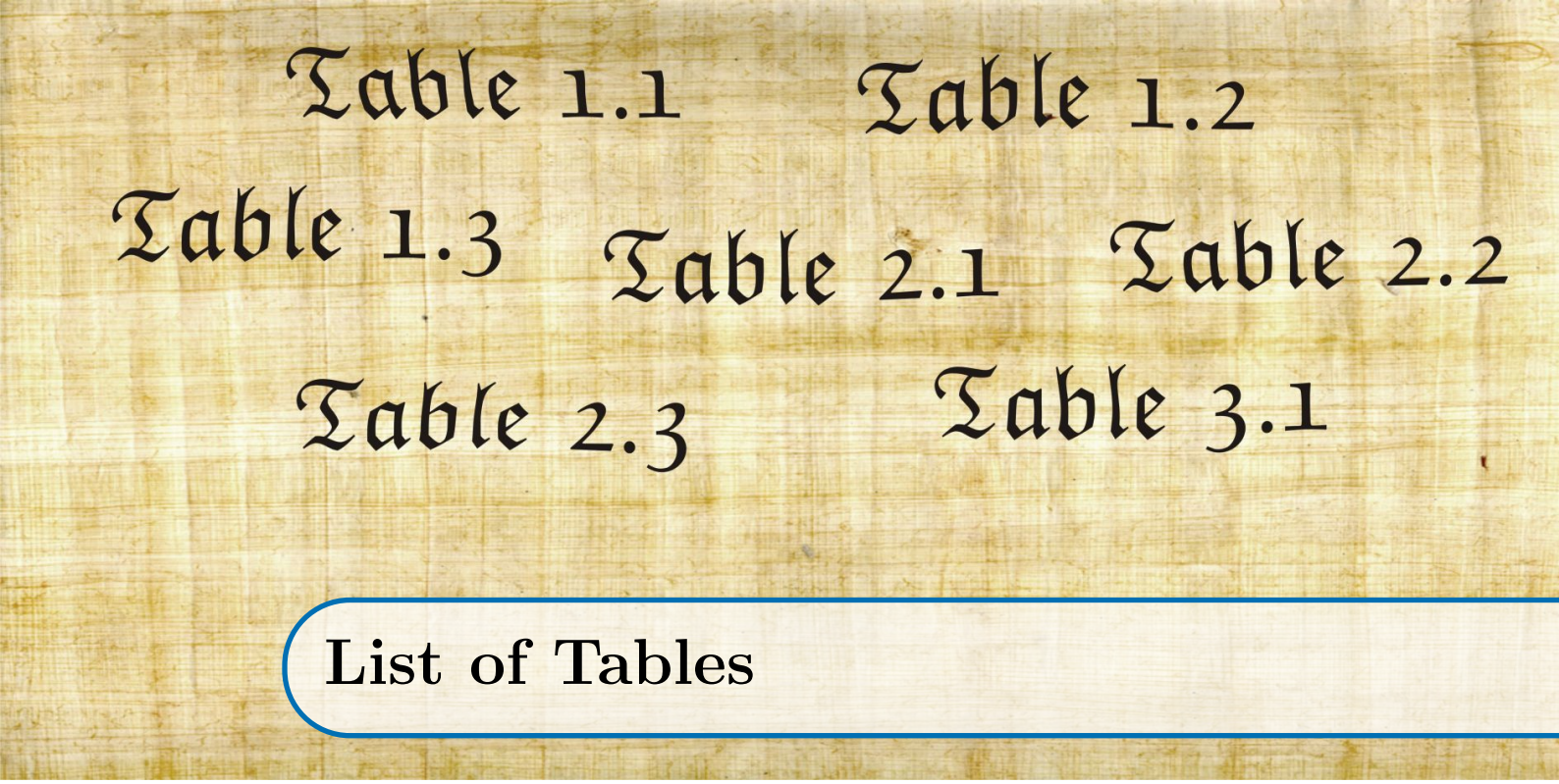

List of Tables

2.1 Phase-matching and non-collinear angles for DKDP and LBO used in the PFS. . . . 22

4.1 Walk-off parameters and beam shift in LBO and DKDP as applied in PFS. 35
4.2 Nonlinear refractive index n_2 for different materials and wavelengths. . . 45
4.3 Estimated B-integral values for a pump beam with an intensity of 100 $\frac{\mathrm{GW}}{\mathrm{cm}^2}$. 46

5.1 Parameters used for the simulations of the system design study using DKDP in all stages. . . . 51
5.2 Parameters used for the simulations of the system design study with a combination of LBO and DKDP crystals. . . . 53

7.1 Temporal contrast measurements with the Sequoia third order autocorrelator. . . . 88

E.1 Specifications of spectrometers for the signal characterization [123]. . . . 154
E.2 Specifications of spectrometers for the pump-laser characterization [123]. 155
E.3 Specifications of the WincamD Series UCD23 [127]. . . . 156
E.4 Specifications of the Sequoia third-order autocorrelator. . . . 164

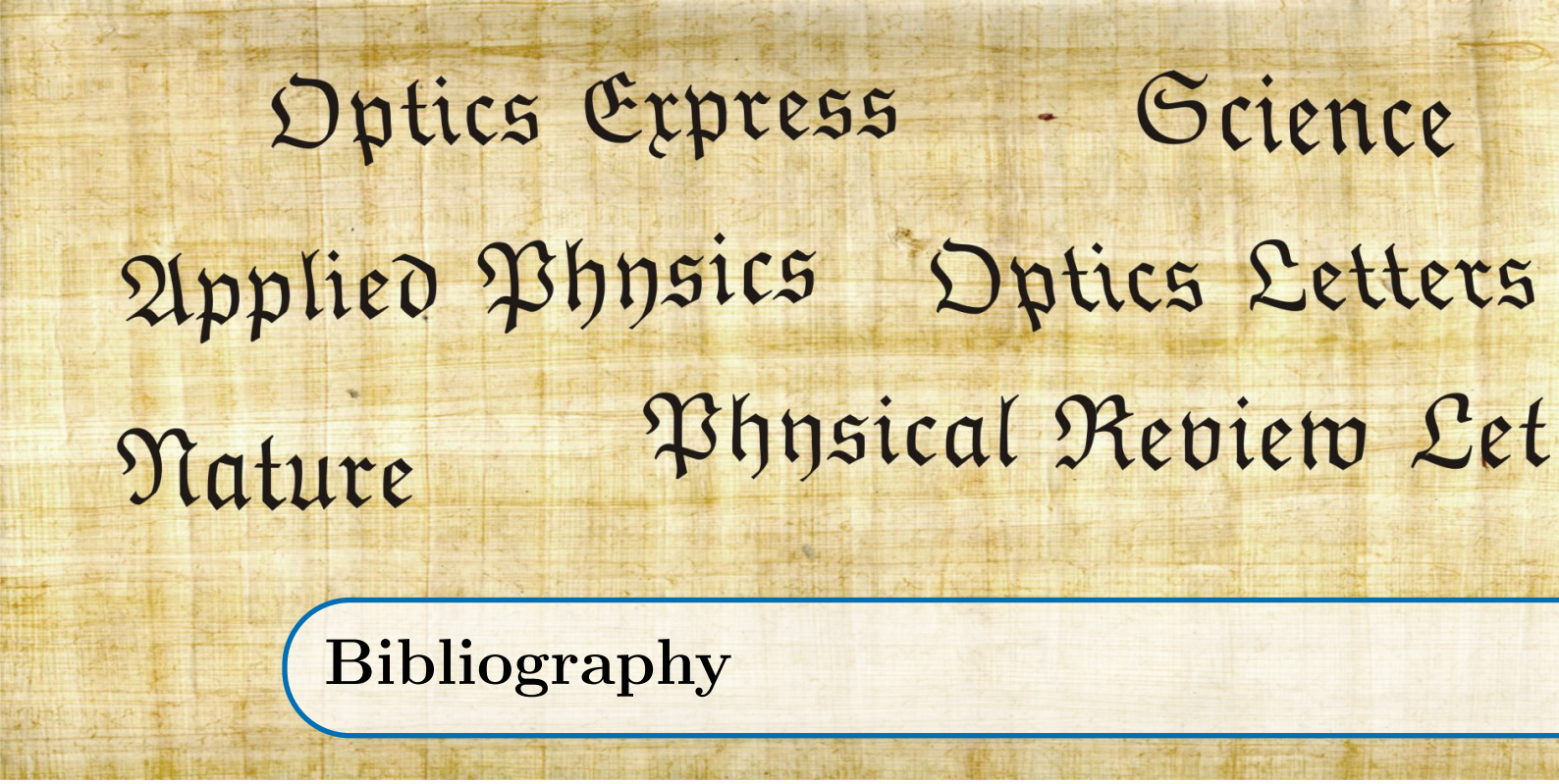

Bibliography

[1] S. Karsch, Z. Major, J. Fülöp, I. Ahmad, T.-J. Wang, A. Henig, S. Kruber, R. Weingartner, M. Siebold, J. Hein, Chr. Wandt, S. Klingebiel, J. Osterhoff, R. Hörlein, and F. Krausz. The petawatt field synthesizer: A new approach to ultrahigh field generation. In *Advanced Solid-State Photonics*, page WF1. Optical Society of America, 2008.

[2] Z. Major, S. A. Trushin, I. Ahmad, M. Siebold, C. Wandt, S. Klingebiel, T.-J. Wang, J. A. Fülöp, A. Henig, S. Kruber, R. Weingartner, A. Popp, J. Osterhoff, R. Hörlein, J. Hein, V. Pervak, A. Apolonski, F. Krausz, and S. Karsch. Basic concepts and current status of the petawatt field synthesizer - a new approach to ultrahigh field generation. *The Review of Laser Engineering*, 37(6):431–436, June 2009.

[3] N. H. Burnett, H. a. Baldis, M. C. Richardson, and G. D. Enright. Harmonic generation in co2 laser target interaction. *Applied Physics Letters*, 31(3):172, 1977.

[4] R. Carman, C. Rhodes, and R. Benjamin. Observation of harmonics in the visible and ultraviolet created in co2-laser-produced plasmas. *Physical Review A*, 24:2649–2663, 1981.

[5] U. Teubner and P. Gibbon. High-order harmonics from laser-irradiated plasma surfaces. *Reviews of Modern Physics*, 81:445–479, 2009.

[6] C. Thaury and F. Quéré. High-order harmonic and attosecond pulse generation on plasma mirrors: basic mechanisms. *Journal of Physics B: Atomic, Molecular and Optical Physics*, 43:213001, 2010.

[7] C. Skrobol, I. Ahmad, S. Klingebiel, Chr. Wandt, S. A. Trushin, Z. Major, F. Krausz, and S. Karsch. Broadband amplification by picosecond opcpa in dkdp pumped at 515 nm. *Opt. Express*, 20(4):4619–4629, Feb 2012.

[8] T.H. Maiman. Stimulated optical radiation in ruby. *Nature*, 187:493, 1960.

[9] P. A. Franken, A. E. Hill, C. W. Peters, and G. Weinreich. Generation of optical harmonics. *Phys. Rev. Lett.*, 7:118–119, 1961.

[10] M. Drescher, M. Hentschel, and R. Kienberger. X-ray pulses approaching the attosecond frontier. *Science*, 291(5510):1923, 2001.

[11] E. Goulielmakis, M. Schultze, M. Hofstetter, V. S. Yakovlev, J. Gagnon, M. Uiberacker, A. L. Aquila, E. M. Gullikson, D. T. Attwood, R. Kienberger, F. Krausz, and U. Kleineberg. Single-cycle nonlinear optics. *Science*, 320(5883):1614–1617, 2008.

[12] A. Wirth, R. Santra, and E. Goulielmakis. Real time tracing of valence-shell electronic coherences with attosecond transient absorption spectroscopy. *Chemical Physics*, 414(0):149 – 159, 2013. Attosecond spectroscopy.

[13] M. Bellini, C. Corsi, and M. Gambino. Neutral depletion and beam defocusing in harmonic generation from strongly ionized media. *Physical Review A*, 64(2):1–10, 2001.

[14] E. Skantzakis, P. Tzallas, J. Kruse, C. Kalpouzos, and D. Charalambidis. Coherent continuum extreme ultraviolet radiation in the sub-100-nj range generated by a high-power many-cycle laser field. *Optics Letters*, 34(11):1732, 2009.

[15] F. Ferrari, F. Calegari, M. Lucchini, C. Vozzi, S. Stagira, G. Sansone, and M. Nisoli. High-energy isolated attosecond pulses generated by above-saturation few-cycle fields. *Nature Photonics*, 4(12):875–879, 2010.

[16] G. D. Tsakiris, K. Eidmann, J. Meyer-ter Vehn, and F. Krausz. Route to intense single attosecond pulses. *New Journal of Physics*, 8(6):19, 2006.

[17] D. H. Sutter, G. Steinmeyer, L. Gallmann, N. Matuschek, F. Morier-Genoud, U. Keller, V. Scheuer, G. Angelow, and T. Tschudi. Semiconductor saturable-absorber mirror assisted kerr-lens mode-locked ti:sapphire laser producing pulses in the two-cycle regime. *Opt. Lett.*, 24(9):631–633, May 1999.

[18] U. Morgner, F. X. Kärtner, S. H. Cho, Y. Chen, H. A. Haus, J. G. Fujimoto, E. P. Ippen, V. Scheuer, G. Angelow, and T. Tschudi. Sub-two-cycle pulses

from a kerr-lens mode-locked ti:sapphire laser. *Opt. Lett.*, 24(6):411–413, Mar 1999.

[19] I. D. Jung, F. X. Kärtner, N. Matuschek, D. H. Sutter, F. Morier-Genoud, G. Zhang, U. Keller, V. Scheuer, M. Tilsch, and T. Tschudi. Self-starting 6.5-fs pulses from a ti:sapphire laser. *Opt. Lett.*, 22(13):1009–1011, Jul 1997.

[20] L. Xu, G. Tempea, Ch. Spielmann, F. Krausz, A. Stingl, K. Ferencz, and S. Takano. Continuous-wave mode-locked ti:sapphire laser focusable to $5 \times 10^{13}\,\mathrm{W/cm^2}$. *Opt. Lett.*, 23(10):789–791, May 1998.

[21] J. H. Sung, S. K. Lee, T. J. Yu, T. M. Jeong, and J. Lee. 0.1 hz 1.0 pw ti:sapphire laser. *Opt. Lett.*, 35(18):3021–3023, Sep 2010.

[22] T. J. Yu, S. K. Lee, J. H. Sung, J. W. Yoon, T. M. Jeong, and J. Lee. Generation of high-contrast, 30 fs, 1.5 pw laser pulses from chirped-pulse amplification ti:sapphire laser. *Opt. Express*, 20(10):10807–10815, May 2012.

[23] M. Nisoli, S. De Silvestri, O. Svelto, R. Szipöcs, K. Ferencz, Ch. Spielmann, S. Sartania, and F. Krausz. Compression of high-energy laser pulses below 5 fs. *Opt. Lett.*, 22(8):522–524, Apr 1997.

[24] G. Steinmeyer, D. H. Sutter, L. Gallmann, N. Matuschek, and U. Keller. Frontiers in ultrashort pulse generation: Pushing the limits in linear and nonlinear optics. *Science*, 286(5444):1507–1512, November 1999.

[25] A. Dubietis, G. Jonusauskas, and A. Piskarskas. Powerful femtosecond pulse generation by chirped and streched pulse parametric amplification in bbo crystal. *Optics Communications*, 88:437–440, 1992.

[26] I. N. Ross, P Matousek, M. Towrie, A. J. Langley, and J. L. Collier. The prospects for ultrashort pulse duration and ultrahigh intensity using optical parametric chirped pulse amplifiers. *Optics Communications*, 144:125–133, December 1997.

[27] G. Cerullo and S. De Silvestri. Ultrafast optical parametric amplifiers. *Rev. Sci. Instrum.*, 74(1):1–18, January 2003.

[28] D. Herrmann, L. Veisz, R. Tautz, F. Tavella, K. Schmid, V. Pervak, and F. Krausz. Generation of sub-three-cycle, 16 tw light pulses by using noncollinear optical parametric chirped-pulse amplification. *Optics Letters*, 34(16):2459–2461, August 2009.

[29] O. D. Muecke, D. Sidorov, P. Dombi, A. Pugzlys, S. Alisauskas, V. Smilgevicius, N. Forget, J. Posius, L. Giniunas, R. Danielius, and A. Baltuska. 10-mj optically synchronized cep-stable chirped parametric amplifier at 1.5 um. *Optics and Spectroscopy*, 108(3):456–462, 2010.

[30] A. Pistelok. *Entwicklung eines OPCPA-Systems zur Verstärkung ultrakurzer Pulse bis in den Terawattbereich.* PhD thesis, Mathematisch-Naturwissenschaftlichen Fakultät der Heinrich-Heine-Universität Düsseldorf, Dezember 2006.

[31] A. Renault, D. Z. Kandula, S. Witte, A. L. Wolf, R. Th. Zinkstok, W. Hogervorst, and K. S. E. Eikema. Phase stability of terrawatt-class ultrabroadband parametric amplification. *Optics Letters*, 32(16):2363–2365, August 2007.

[32] D. Strickland and G. Mourou. Compression of amplified chirped optical pulses. *Optics Communication*, 56:219, 1985.

[33] M. Pessot, P. Main, and G. Mourou. 1000 times expansion/compression of optical pulses for chirped pulse amplification. *Optics Communication*, 62:419, 1987.

[34] R. L. Sutherland. *Handbook of nonlinear optics.* Marcel Dekker, Inc., second edition, 2003.

[35] G. M. Gale, M. Cavallari, T. J. Driscoll, and F. Hache. Sub-20-fs tunable pulses in the visible from an 82-mhz optical parametric oscillator. *Opt. Lett.*, 20(14):1562–1564, Jul 1995.

[36] D. Du, X. Liu, G. Korn, J. Squier, and G. Mourou. Laser-induced breakdown by impact ionization in sio2 with pulse widths from 7 ns to 150 fs. *Applied Physics Letters*, 64(23):3071–3073, 1994.

[37] I. Ahmad. *Development of an optically synchronized seed source for a high-power few-cycle OPCPA system.* PhD thesis, Ludwig-Maximilians-Universität München, 2011.

[38] S. Klingebiel. *Picosecond Pump Dispersion Managment and Jitter Stabilization in a Petawatt-Scale Few-Cycle OPCPA System.* PhD thesis, Ludwig-Maximilians-Universität München, 2013.

[39] R. W. Boyd. *Nonlinear Optics.* Academic Press, third edition, October 2007.

[40] D. Brida, C. Manzoni, G. Cirmi, M Marangoni, S. Bonora, P. Villoresi, S. De. Silvestri, and G. Cerullo. Few-optical-cycle pulses tunable from the visible to the mid-infrared by optical parametric amplifiers. *J. Opt.*, 12:013001, 2010.

[41] M. J. Guardalben, J. Keegan, L. J. Waxer, V. Bagnoud, I. A. Begishev, J. Puth, and J. D. Zuegel. Design of a higly stable, high-conversion-efficiency, optical parametric chirped-pulse amplification system with good beam quality. *Optics Express*, 11(20):2511–2524, October 2003.

[42] G. Arisholm. Quantum noise initiation and macroscopic fluctuations in optical parametric oscillators. *J. Opt. Soc. Am. B*, 16(1):117–127, January 1999.

[43] G. Arisholm. General numerical methods for simulating second-order nonlinear interactions in birefringent media. *J. Opt. Soc. Am. B*, 14(10):2543–2549, October 1997.

[44] V. V. Lozhkarev, G. I. Freidman, V. N. Ginzburg, E. V. Katin, E. A. Khazanov, A. V. Kirsanov, G. A. Luchinin, A. N. Mal'shakov, M. A. Martyanov, O. V. Palashov, A. K. Poteomkin, A. M. Sergeev, A. A. Shaykin, and I. V. Yakovlev. Compact 0.56 petawatt laser system based on optical parametric chirped pulse amplification in kd*p crystals. *Laser Phys. Lett.*, 4(6):421–427, 2007.

[45] J. Schwarz, P. Rambo, M. Geissel, M. Kimmel, E. Brambrink, B. Atherton, and J. Glassman. A hybrid opcpa/nd:phosphate glass multi-terawatt laser system for seeding of a petawatt laser. *Optics Communications*, 281:4984–4992, 2008.

[46] I. N. Ross, P. Matousek, G. H. C. New, and K. Osvay. Analysis and optimization of optical parametric chirped pulse amplification. *J. Opt. Soc. Am. B*, 19(12):2945–2956, December 2002.

[47] D. Herrmann, R. Tautz, F. Tavella, F. Krausz, and L. Veisz. Investigation of two-beam-pumped noncollinear optical parametric chirped-pulse amplification for the generation of few-cycle light pulses. *Opt. Express*, 18(5):4170–4183, Mar 2010.

[48] S. Demmler, J. Rothhardt, S. Hädrich, J. Bromage, J. Limpert, and A. Tünnermann. Control of nonlinear spectral phase induced by ultra-broadband optical parametric amplification. *Opt. Lett.*, 37(19):3933–3935, Oct 2012.

[49] F. Tavella. *Multiterawatt few-cycle pulse OPCPA for applications in high-field physics*. PhD thesis, Ludwig-Maximilians-Universität München, 2008.

[50] L. You, J. Cooper, and M. Trippenbach. Alternative treatment for the initiation of superfluorescence. *J. Opt. Soc. Am. B*, 8(5):1139–1148, May 1991.

[51] H. Fattahi, C. Skrobol, M. Ueffing, Y. Deng, A. Schwarz, Y. Kida, V. Pervak, T. Metzger, Z. Major, and F. Krausz. High efficiency, multi-mj, sub 10 fs, optical parametric amplifier at 3 khz. In *CLEO: Science and Innovations*, page CTh1N.6. Optical Society of America, 2012.

[52] G. Arisholm, J. Biegert, P. Schlup, C. P. Hauri, and Keller; U. Ultra-broadband chirped-pulse optical parametric amplifier with angularly dispersed beams. *Optics Express*, 12(3):518–530, February 2004.

[53] G. Arisholm, G. Rustad, and K. Stenersen. Importance of pump-beam group velocity for backconversion in optical parametric oscillators. *J. Opt. Soc. Am. B*, 18(12):1882–1890, Dec 2001.

[54] G. Arisholm, R. Paschotta, and T. Südmeyer. Limits to the power scalability of high-gain optical parametric amplifiers. *J. Opt. Soc. Am. B*, 21(3):578–590, Mar 2004.

[55] G. Arisholm. General analysis of group velocity effects in collinear optical parametric amplifiers and generators. *Opt. Express*, 15(10):6513–6527, May 2007.

[56] O. Chalus, P. K. Bates, and J. Biegert. Design and simulation of few-cycle optical parametric chirped pulse amplification at mid-ir wavelengths. *Optics Express*, 16(26):21297–21304, December 2008.

[57] G. Rustad, G. Arisholm, and O. Farsund. Effect of idler absorption in pulsed optical parametric oscillators. *Opt. Express*, 19(3):2815–2830, Jan 2011.

[58] A. V. Smith, D. J. Armstrong, and W. J. Alford. Increased acceptance bandwidths in optical frequency conversion by use of multiple walk-off-compensating nonlinear crystals. *J. Opt. Soc. Am. B*, 15(1):122–141, Jan 1998.

[59] C. Homann. *Optical parametric processes to the extreme: From new insights in first principles to tunability over more than 4 octaves*. PhD thesis, Ludwig-Maximilians Universität München, 2012.

[60] N. Ishii, L. Turi, V. S. Yakovlev, T. Fuji, F. Krausz, A. Baltuska, R. Butkus, G. Veitas, V. Smilgevicius, R. Danielius, and A. Piskarskas. Multimillijoule chirped parametric amplification offew-cycle pulses. *Opt. Lett.*, 30(5):567–569, Mar 2005.

[61] S. Witte, R. Th. Zinkstok, A. L. Wolf, W. Hogervorst, W. Ubachs, and K. S. E. Eikema. A source of 2 terawatt, 2.7 cycle laser pulses based on noncollinear

optical parametric chirped pulse amplification. *Optics Express*, 14(18):8168–8177, 2006.

[62] S. Adachi, N. Ishii, T. Kanai, A. Kosuge, J. Itatani, Y. Kobayashi, D. Yoshitomi, K. Torizuka, and S. Watanabe. 5-fs, multi-mj, cep-locked parametric chirped-pulse amplifier pumped by a 450-nm source at 1 khz. *Opt. Express*, 16(19):14341–14352, Sep 2008.

[63] O. Chalus, P. K. Bates, M. Smolarski, and J. Biegert. Mid-ir short-pulse opcpa with micro-joule energy at 100 khz. *Optics Express*, 17(5):3587–3594, March 2009.

[64] X. Gu, G. Marcus, Y. Deng, T. Metzger, C. Teisset, N. Ishii, T. Fuji, A. Baltuska, R. Butkus, V. Pervak, H. Ishizuki, T. Taira, T. Kobayashi, R. Kienberger, and F. Krausz. Generation of carrier-envelope-phase-stable 2-cycle 740-μj pulses at 2.1-μm carrier wavelength. *Opt. Express*, 17(1):62–69, Jan 2009.

[65] K. W. Aniolek, R. L. Schmitt, T. J. Kulp, B. A. Richman, S. E. Bisson, and P. E. Powers. Microlaser-pumped periodically poled lithium niobate optical parametric generator-optical parametric amplifier. *Opt. Lett.*, 25(8):557–559, Apr 2000.

[66] V. V. Lozhkarev, G. I. Freidman, V. N. Ginzburg, E. A. Khazanov, O. V. Palashov, A. M. Sergeev, and I. V. Yakovlev. Study of broadband optical parametric chirped pulse amplification in a dkdp crystal pumped by the second harmonic of a nd:ylf laser. *Laser Physics*, 15(9):1319–1333, 2005.

[67] Y. Mori, I. Kuroda, S. Nakajima, T. Sasaki, and S. Nakai. New nonlinear optical crystal: Cesium lithium borate. *Appl. Phys. Lett.*, 67(13):1818–1820, September 1995.

[68] B. Zhao, X. Liang, Y. Leng, Y. Jiang, C. Wang, H. Lu, J. Du, Z. Xu, and D. Shen. Degenerated optical parametric chirped-pulse amplification with cesium lithium borate. *Applied Optics*, 45(3):565–568, January 2006.

[69] E. A. Khazanov and A. M. Sergeev. Petawatt lasers based on optical parametric amplifiers: their state and prospects. *Physics Uspekhi*, 51(9):969–974, September 2008.

[70] C. Hernandez-Gomez, S. P. Blake, O. Chekhlov, R. J. Clarke, A. M. Dunne, M. Galimberti, S. Hancock, R. Heathcote, P. Holligan, A. Lyachev, P. Matousek, I. O. Musgrave, D. Neely, P. A. Norreys, I. Ross, Y. Tang, T. B.

Winstone, B. E. Wyborn, and J. Collier. The vulcan 10 pw project. *Journal of Physics: Conference Series*, 244(3):032006, 2010.

[71] A. E. Siegman. *Lasers*. University Science Books, 1986.

[72] V. Yu. Fedorov and V. P. Kandidov. A nonlinear optical model of an air medium in the problem of filamentation of femtosecond laser pulses of different wavelengths. *Optics and Spectroscopy*, 105(2):280–287, 2008.

[73] D. Milam. Review and assessment of measured values of the nonlinear refractive-index coefficient of fused silica. *Appl. Opt.*, 37(3):546–550, Jan 1998.

[74] N. A. Kurnit, T. Shimada, M. S. Sorem, A. J. Taylor, G. Rodriguez, T. S. Clement, H. Fearn, D. F. James, and P. W. Milonni. Measurement and control of optical nonlinearities of importance to glass laser fusion systems. *Proc. SPIE*, 3047:387, 1997.

[75] I. A. Kulagin, R. A. Ganeev, R. I. Tugushev, A. I. Ryasnyansky, and T. Usmanov. Analysis of third-order nonlinear susceptibilities of quadratic nonlinear optical crystals. *J. Opt. Soc. Am. B*, 23(1):75–80, Jan 2006.

[76] R. Mohandoss, S. Dhanuskodi, and C. Sanjeeviraja. Optical studies on electron beam evaporated lithium triborate films. *Spectrochimica Acta Part A: Molecular and Biomolecular Spectroscopy*, 96(0):805 – 808, 2012.

[77] S. D. Butterworth, S. Girard, and D. C. Hanna. High-power, broadly tunable all-solid-state synchronously pumped lithium triborate optical parametric oscillator. *J. Opt. Soc. Am. B*, 12(11):2158–2167, Nov 1995.

[78] A. Thai, C. Skrobol, P. K. Bates, G. Arisholm, Z. Major, F. Krausz, S. Karsch, and J. Biegert. Simulations of petawatt-class few-cycle optical-parametric chirped-pulse amplification, including nonlinear refractive index effects. *Opt. Lett.*, 35(20):3471–3473, Oct 2010.

[79] A. Kokh, N. Kononova, G. Mennerat, Ph. Villeval, S. Durst, D. Lupinski, V. Vlezko, and K. Kokh. Growth of high quality large size lbo crystals for high energy second harmonic generation. *Journal of Crystal Growth*, 312:1774–1778, 2010.

[80] M. K. Trubetskov, V. Pervak, and A. V. Tikhonravov. Phase optimization of dispersive mirrors based on floating constants. *Opt. Express*, 18(26):27613–27618, Dec 2010.

[81] V. Pervak. Recent development and new ideas in the field of dispersive multilayer optics. *Appl. Opt.*, 50(9):C55–C61, Mar 2011.

[82] V. Pervak, I. Ahmad, M. K. Trubetskov, A. V. Tikhonravov, and F. Krausz. Double-angle multilayer mirrors with smoothdispersion characteristics. *Opt. Express*, 17(10):7943–7951, May 2009.

[83] F. M. Mitschke and L. F. Mollenauer. Discovery of the soliton self-frequency shift. *Opt. Lett.*, 11(10):659–661, Oct 1986.

[84] X. Liu, C. Xu, W. H. Knox, J. K. Chandalia, B. J. Eggleton, S. G. Kosinski, and R. S. Windeler. Soliton self-frequency shift in a short tapered air–silica microstructure fiber. *Opt. Lett.*, 26(6):358–360, Mar 2001.

[85] I.G. Cormack, D.T. Reid, W.J. Wadsworth, J.C. Knight, and P.S.J. Russell. Observation of soliton self-frequency shift in photonic crystal fibre. *Electronics Letters*, 38(4):167–169, Feb 2002.

[86] C. Y. Teisset, N. Ishii, T. Fuij, T. Metzger, S. Köhler, R. Holzwarth, A. Baltuska, A. M. Zheltikov, and F. Krausz. Soliton-based pump-seed synchronization for few-cycle opcpa. *Optics Express*, 13(17):6550–6557, August 2005.

[87] I. Ahmad, S. A. Trushin, Z. Major, Chr. Wandt, S. Klingebiel, T.-J. Wang, V. Pervak, A. Popp, M. Siebold, F. Krausz, and S. Karsch. Frontend light source for short-pulse pumped opcpa system. *Appl. Phys. B*, 2009.

[88] N. Minkovski, S. M. Saltiel, G. I. Petrov, O. Albert, and J. Etchepare. Polarization rotation induced by cascaded third-order processes. *Opt. Lett.*, 27(22):2025–2027, Nov 2002.

[89] A. Jullien, C.G. Durfee, A. Trisorio, L. Canova, J.-P. Rousseau, B. Mercier, L. Antonucci, G. Chériaux, O. Albert, and R. Lopez-Martens. Nonlinear spectral cleaning of few-cycle pulses via cross-polarized wave (xpw) generation. *Applied Physics B*, 96:293–299, 2009.

[90] Y. Zaouter, L. P. Ramirez, D. N. Papadopoulos, C. Hönninger, M. Hanna, F. Druon, E. Mottay, and P. Georges. Temporal cleaning of a high-energy fiber-based ultrafast laser using cross-polarized wave generation. *Opt. Lett.*, 36(10):1830–1832, May 2011.

[91] L. P. Ramirez, D. N. Papadopoulos, A. Pellegrina, P. Georges, F. Druon, P. Monot, A. Ricci, A. Jullien, X. Chen, J. P. Rousseau, and R. Lopez-Martens. Efficient cross polarized wave generation for compact, energy-scalable, ultrashort laser sources. *Opt. Express*, 19(1):93–98, Jan 2011.

[92] A. Münzer. Development of a high-contrast frontend for atlas ti:sa laser. Master's thesis, Ludwig-Maximilians-Universität München, 2013.

[93] T. Kobayashi and A. Shirakawa. Tunable visible and near-infrared pulse generator in a 5 fs regime. *Appl. Phys. B*, 70:S239–S246, 2000.

[94] T.-J. Wang, Z. Major, I. Ahmad, S.A. Trushin, F. Krausz, and S. Karsch. Ultra-broadband near-infrared pulse generation by noncollinear opa with angular dispersion compensation. *Applied Physics B*, 100(1):207–214, 2010.

[95] A. Kessel, A. Kastner, S. Trushin, C. Skrobol, S. Klingebiel, Chr. Wandt, Z. Major, F. Krausz, and S. Karsch. Noncollinear ultra broaband idler generation for a petawatt class opcpa system. *in preparation*, 2013.

[96] Chr. Wandt, S. Klingebiel, S. Keppler, M. Hornung, C. Skrobol, A. Kessel, S. A. Trushin, Zs. Major, J. Hein, M. C. Kaluza, F. Krausz, and S. Karsch. Development of a joule-class yb:yag amplifier and its implementation in a cpa system generating 1 tw pulses. *Laser & Photonics Reviews*, accepted, 2014.

[97] Chr. Wandt. *Development of a Joule-class Yb:YAG amplifier and its implementation in a CPA system generating 1 TW pulses.* PhD thesis, Ludwig-Maximilians-Universität München, 2013.

[98] Chr. Wandt, S. Klingebiel, M. Siebold, Zs. Major, J. Hein, F. Krausz, and S. Karsch. Generation of 220 mj nanosecond pulses at a 10 hz repetition rate with excellent beam quality in a diode-pumped yb:yag mopa system. *Optics Letters*, 33(10):1111–1113, May 2008.

[99] S. Klingebiel, Chr. Wandt, C. Skrobol, I. Ahmad, S. A. Trushin, Z. Major, F. Krausz, and S. Karsch. High energy picosecond yb:yag cpa system at 10 hz repetition rate for pumping optical parametric amplifiers. *Opt. Express*, 19(6):5357–5363, Mar 2011.

[100] S. Klingebiel, I. Ahmad, Chr.. Wandt, C Skrobol, S. A. Trushin, Z. Major, F. Krausz, and S. Karsch. Experimental and theoretical investigation of timing jitter inside a stretcher-compressor setup. *Opt. Express*, 20(4):3443–3455, Feb 2012.

[101] J. A. Fülöp, Zs. Major, A. Henig, S. Kruber, R. Weingartner, T. Clausnitzer, E-B. Kley, A. Tünnermann, V. Pervak, A. Apolonski, J. Osterhoff, R. Hörlein, F. Krausz, and S. Karsch. Short-pulse optical parametric chirped-pulse amplification for the generation of high-power few-cycle pulses. *New Journal of Physics*, 9:438, 2007.

[102] T. Miura, K. Kobayashi, K. Takasago, Z. Zhang, K. Torizuka, and F. Kannari. Timing jitter in a kilohertz regenerative amplifier of a femtosecond-pulse ti:al2o3 laser. *Optics Letters*, 25(24):1795–1797, December 2000.

[103] P. G. Backes and W. H. Stevenson. A comparison of methods for accurate image centroid position determination with matrix sensors. *Journal of Laser Applications*, 2(2):33–39, 1990.

[104] R. Trebino. *Frequency-Resolved Optical Gating: The Measurement of Ultrashort Laser Pulses*. Kluwer Academic Publishers, 2000.

[105] J. C. Diels and W. Rudolph. *Ultrashort Laser Pulse Phenomena: Fundamentals, Techniques, and Applications on a Femtosecond Time Scale*. Academic Press, second edition, 2006.

[106] O. E. Martinez, J. P. Gordon, and R. L. Fork. Negative group-velocity dispersion using refraction. *J. Opt. Soc. Am. A*, 1(10):1003–1006, Oct 1984.

[107] E. B. Treacy. Optical pulse compression with diffraction gratings. *IEEE Journal of Quantum Electronics*, 5:454, 1969.

[108] W. Dietel, J. J. Fontaine, and J.-C. Diels. Intracavity pulse compression with glass: a new method of generating pulses shorter than 60 fsec. *Opt. Lett.*, 8(1):4–6, Jan 1983.

[109] R. Szipöcs, C. Spielmann, F. Krausz, and K. Ferencz. Chirped multilayer coatings for broadband dispersion control in femtosecond lasers. *Opt. Lett.*, 19(3):201–203, Feb 1994.

[110] A. M. Weiner, D. E. Leaird, J. S. Patel, and J. R. Wullert. Programmable femtosecond pulse shaping by use of a multielement liquid-crystal phase modulator. *Opt. Lett.*, 15(6):326–328, Mar 1990.

[111] P. Tournois. Acousto-optic programmable dispersive filter for adaptive compensation of group delay time dispersion in laser systems. *Optics Communications*, 140:245, 1997.

[112] S.K. Zhang, M. Fujita, M. Yamanaka, M. Nakatsuka, Y. Izawa, and C. Yamanaka. Study of the stability of optical parametric amplification. *Optics Communications*, 184:451 – 455, 2000.

[113] B. R. Mollow and R. J. Glauber. Quantum theory of parametric amplification. *Physical Review*, 160(5):1076–1096, August 1967.

[114] R. L. Byer and S. E. Harris. Power and bandwidth of spontaneous parametric emission. *Phys. Rev.*, 168(3):1064–1068, April 1968.

[115] R. Glauber and F. Haake. The initiation of superfluorescence. *Physics Letters A*, 68(1):29 – 32, 1978.

[116] C. L. Tang. *Quantum Electronics, Volume 1, Nonlinear Optics, Part A*, chapter 6. Academic Press, London, 1975.

[117] V. G. Dmitriev, G. G. Gurzadyan, and D. N. Nikogosyan. *Handbook of Nonlinear Optical Crystals*. Springer, third edition, 1999.

[118] S. Seidel and G. Mann. Numerical modeling of thermal effects in nonlinear crystals for high average power second harmonic generation. *SPIE*, 2989:204–214, May 1997.

[119] M. Xu, Z. Wang, B. Liu, S. Ji, X. Sun, and X. Xu. Study on the properties of the dkdp crystal with different deuterium content. *Proc. of SPIE*, 8206:82062B–3, 2011.

[120] D. L. Shealy and J. A. Hoffnagle. Laser beam shaping profiles and propagation. *Applied Optics*, 45(21):5118, July 2006.

[121] A. A. Tovar. Propagation of flat-topped multi-gaussian laser beams. *J. Opt. Soc. Am. A*, 18(8):1897, August 2001.

[122] J. E. Murray, K. G. Estabrook, D. Milam, W. D. Sell, B. M. Van Wonterghem, M. D. Feit, and A. M. Rubenchik. Spatial filter issues. *Proc. SPIE*, 3047:207, 1997.

[123] Avantes, 2012.

[124] Coherent. J2550lpxa.pdf, January 2003.

[125] Coherent. J-50mb-yag, 2012.

[126] Coherent. Lapmax top, 2012.

[127] DataRay. Wincamd ucd23, 2013.

[128] I. H. Malitson. A redetermination of some optical properties of calcium fluoride. *Appl. Opt.*, 2(11):1103–1107, Nov 1963.

[129] A. Baltuska, M. S. Pshenichnikov, and D. A. Wiersma. Amplitude and phase characterization of 4.5-fs pulses by frequency-resolved optical gating. *Opt. Lett.*, 23(18):1474–1476, Sep 1998.

[130] S. Akturk, C. D'Amico, and A. Mysyrowicz. Measuring ultrashort pulses in the single-cycle regime using frequency-resolved optical gating. *J. Opt. Soc. Am. B*, 25(6):A63–A69, Jun 2008.

[131] Basler. Users manual ace gige, 2012.

[132] Swamp Optics. Femtosoft frog, November 2013.

[133] Hamamatsu. Datasheet of r2078 pmt, 2013.

[134] Amplitude-Technologies. Sequoia third order autocorrelator, Oktober 2013.

Publications by the Author

C. Skrobol, I. Ahmad, S. Klingebiel, Chr. Wandt, S. A. Trushin, Zs. Major, F. Krausz and S. Karsch, *Broadband amplification by picosecond OPCPA in DKDP pumped at 515 nm*, Opt. Express **20**, 4619, **2012**.

S. Klingebiel, I. Ahmad, Chr. Wandt, **C. Skrobol**, S. A. Trushin, Zs. Major, F. Krausz and S. Karsch, *Experimental and theoretical investigation of timing jitter inside a stretcher-compressor setup*, Opt. Express **20**, 3443, **2012**.

H. Fattahi, **C. Skrobol**, M. Ueffing, D. Yunpei, A. Schwarz, Y. Kida, V. Pervak, T. Metzger, Zs. Major and F. Krausz, *High efficiency, multi-mJ, sub 10 fs, optical parametric amplifier at 3 kHz*, Conference on Lasers and Electro-Optics (CLEO) **1**, 6-11, **2012**.

S. Klingebiel, Chr. Wandt, **C. Skrobol**, I. Ahmad, S. A. Trushin, Zs. Major, F. Krausz and S. Karsch, *High energy picosecond Yb:YAG CPA system at 10 Hz repetition rate for pumping optical parametric amplifiers*, Opt. Express **19**, 5357, **2011**.

A. Thai, **C. Skrobol**, P. K. Bates, G. Arisholm, Zs. Major, F. Krausz, S. Karsch and J. Biegert, *Simulations of petawatt-class few-cycle optical-parametric chirped-pulse amplification, including nonlinear refractive index effects*, Opt. Letters **35**, 3471, **2010**.

Zs. Major, S. Klingebiel, **C. Skrobol**, I. Ahmad, Chr. Wandt, S. A. Trushin, F. Krausz and S. Karsch, *Status of the petawatt field synthesizer-pumpseed synchronization measurements*, AIP Conference Proceedings **1228**, 117, **2010**.

Zs. Major, **C. Skrobol**, I. Ahmad, Chr. Wandt, S. Klingebiel, S. A. Trushin, F. Krausz and S. Karsch, *Towards Joule-scale few-cycle pulses - progress and challenges of short-pulse pumped OPCPA*, in Advances in Optical Materials, **HThE1**, **2011**.

I. Ahmad, S. Klingebiel, **C. Skrobol**, Chr. Wandt, S. A. Trushin, Zs. Major, F. Krausz and S. Karsch, *Pump-Seed Synchronization Measurements for High-Power Short-Pulse Pumped Few-Cycle OPCPA System*, Lasers, Sources and Related Photonic Devices, **AMB9**, **2010**.

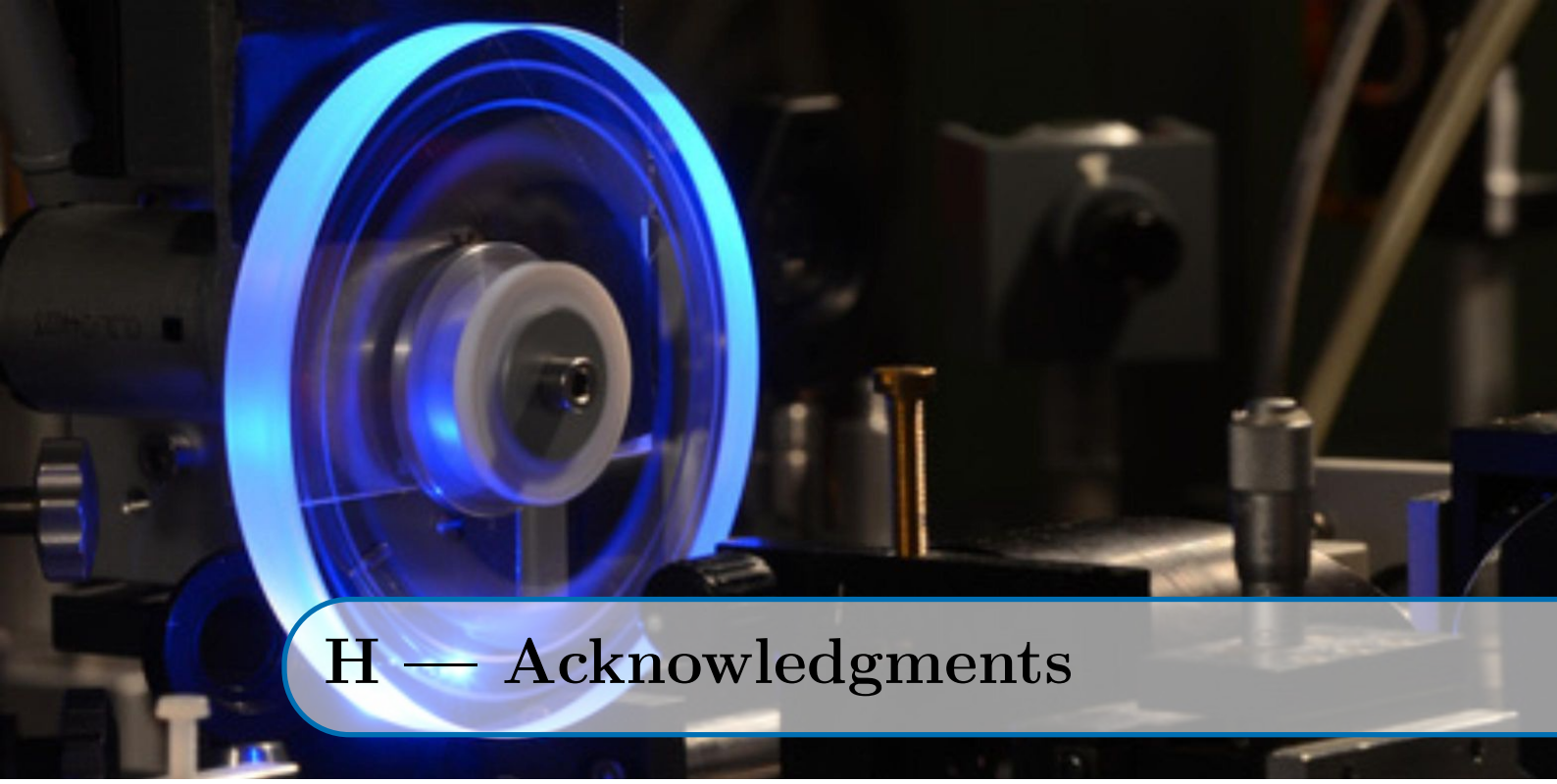

H — Acknowledgments

This work is funded through the PFS grant of the Max-Planck Society.

All pictures of experimental setups which are shown at the beginning of the chapters, underlie the copyright of Thorsten Naeser. I'm grateful that he gave me the permission to present these great photographs from different experiments in our LAP-Group.

The picture of the papyrus paper used as an background for some chapter pictures was created by "freestock" and can be downloaded at: "http://freestock.deviantart.com/art/Papyrus-80121211". The picture was rotated and stretched to the correct size.

The applied template is a slightly modified form of the "The Legrand Orange Book" template by Mathias Legrand (License: CC BY-NC-SA 3.0 (http://creativecommons.org/licenses/by-nc-sa/3.0/)). Compared to the original template the mini table of contents located at the chapter beginnings are removed and the colors are changed.

An dieser Stelle möchte ich mich bei allen bedanken, die zum Gelingen dieser Doktorarbeit beigetragen haben. Mein besonderer Dank gilt:

Prof. Dr. F. Krausz und Prof. Dr. S. Karsch für die freundliche Aufnahme in das LAP-Team, für die Möglichkeit an diesem spannenden Thema und diesem tollen Projekt zu forschen, sowie für die Bereitstellung des fantastischen Equipments und für die Betreuung meiner Doktorarbeit.

Prof. Dr. J. Biegert, Dr. A. Thai and Dr. P. Bates Thank you for the fantastic and fruitful discussions and collaboration.

Dr. G. Arisholm Thank's a lot for the permission to use the Sisyfos code for my numerical investigations. The code is a masterpiece.

Dr. Zsuzsanna Major für die großartige Unterstützung während der gesamten Doktorarbeit und die lustigen Abende in Freising.

Izhar, Sandro, Christoph, Kilian und Alexander vom PFS-Team, für die vielen anregenden physikalischen Diskussionen und die Hilfe beim Lösen von vielen Problemen, sowie für die tollen Stunden die wir auch außerhalb der Arbeit gemeinsam verbracht haben.

Konstantin, Matthias, Johannes, Max und Andi für die legendären Mittagessen in der TU-Mensa und die gemeinsamen abendlichen Streifzüge.

Rocío Gracias por la gran tiempo con usted en el MPQ y en Salamanca.

Dr. Sergei Trushin für die zahlreichen Diskussionen und Ideen und für die hilfreichen Tipps.

Werkstatt des MPQ für die äußerst schnelle und präzise Fertigung der Bauteile und für die zahlreichen Tipps bei der Erstellung der Konstruktionen.

A. Böswald, M. Fischer, H. Haas, A. Horn und T. Kleinhenz für die Hilfe bezüglich Materialien, Bohrungen, Zeichnungen und elektrischen Bauteilen und für viele hilfreiche Ratschläge.

Sekretariat für die schnelle Hilfe bei Urlaubsanträgen, Formularen, Dienstreiseanträgen .... .

allen anderen vom **LAP**-Team, die bislang nicht namentlich erwähnt wurden, für die schöne Zeit am MPQ.

meinen Eltern für die großartige Unterstützung während meines gesamten Studiums und der Doktorarbeit.